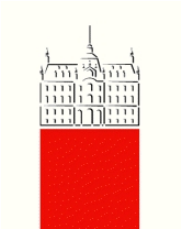

UNIVERSITY OF LJUBLJANA
FACULTY OF MATHEMATICS AND PHYSICS
PHYSICS DEPARTMENT

Boštjan Maček

Measurement of Luminosity in ATLAS Spectrometer with Beam Conditions Monitor

DOCTORAL THESIS

ADVISOR: Prof. Dr. Marko Mikuž
COADVISOR: Dr. Andrej Gorišek

Ljubljana, 2011

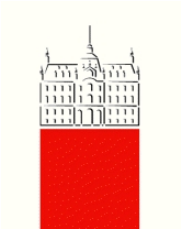

UNIVERZA V LJUBLJANI
FAKULTETA ZA MATEMATIKO IN FIZIKO
ODDELEK ZA FIZIKO

Boštjan Maček

Meritev luminoznosti v spektrometru ATLAS z detektorskim sistemom za spremljanje kakovosti curka protonov

DISERTACIJA

MENTOR: Prof. Dr. Marko Mikuž
SOMENTOR: Dr. Andrej Gorišek

Ljubljana, 2011

Before reading anything else I think the reader should know that the presented effort would not have been possible without many, many, many people. My contribution was only one block, that was put on top of work done by a great team of people that I owe gratitude to.

The biggest THANK YOU! goes to my mentors. To prof. Marko Mikuž, for including me in this great project, for finding the time to steer this young researcher down the path, where he truly gained valuable knowledge and experience. For leading with the example of how things should be done and helping me, not to stray off too far from it. Equal thanks go to Andrej Gorišek for his assistance in both, solving the conceptual problems, and dealing with the down-to-earth things. Without his help many things would not have been done as good as they were (or would not have been done at all)!

I would also like to thank Borut Kerševan for his assistance during my first steps into the world of ATLAS simulation and computing. Many thanks go to Erik Margan, for his occasional but extremely valued advice, that had enabled me not to get electrocuted during my bold endeavors in the world of electronics. I would also like to thank Irena Dolenc Kittelmann for her help and kindness that made my life at CERN easier, and also for introducing me to some very cool people. Thanks also go to Tomi Živko for kindly accepting me into his office and to give quick answers to all my silly questions.

No less valued was the help and the many discussions with Vladimir Cindro, Igor Mandić, Tomaž Podobnik, Marko Zavrtanik, Gregor Kramberger, Andrej Studen, Liza Mijović, Aleš Svetek and with all the rest from our department. I would also like to thank the entire BCM group for collaboration, discussions, and challenges, that enabled us all to build a great detector.

Most importantly, I would like to thank my family, and above all my wonderful parents, for all the support that they have given me from my first day on.

Abstract

The early running period of LHC already provided results from first physics studies and much more is yet to come. Many of these studies, those already performed, and those to come, require an input of the data-sample size and thus rely on independent luminosity measurement.

In order to provide a reliable luminosity measurement for all of the recorded data, the ATLAS experiment at the LHC constructed an independent luminosity measurement infrastructure. To assure the best precision possible many different types of detectors simultaneously measure luminosity and their measurements are compared. Some of these detectors are build specifically for luminosity measurement, while other primarily serve different purposes.

One of the sub-detectors contributing luminosity information is also the Beam Conditions Monitor (BCM). Though conceived as a safety device intended to protect the ATLAS tracking system form potentially dangerous beam losses, its custom-made firmware enabled later adaptation of the system as a luminosity monitor. While still primarily serving ATLAS as a safety device, the BCM has proven to provide very valuable contribution to the ATLAS luminosity measurement. Its excellent timing and signal purity allow luminosity determination for individual bunch pairs with no dead-time. This, combined with dedicated read-out which allows measurements with rates up to few Hz, made the BCM in 2011 the preferred luminosity measurement device within ATLAS.

This thesis describes the design of the BCM and accompanying infrastructure in the view of luminosity monitoring. Its functionality is described in detail. BCM luminosity algorithms are discussed and simulation is used to verify the measurement procedures. All BCM luminosity measurements are relative and the system needs calibration to establish its absolute scale. This is achieved by the van der Meer (vdM) scan that measures the beam parameters from which the absolute luminosity can be determined. The analysis of the last two vdM scans is presented, calibrating the BCM for 2010 and 2011 data. A short overview of the recorded luminosity over the same time period is given at the end.

Keywords:
LHC, ATLAS, beam conditions monitor, pCVD diamond sensors, luminosity, van der Meer scan, calibration

PACS:
29.27.Fh; Beams in particle accelerators: Beam characteristics
85.30.De; Semiconductor-device characterization, design and modeling
25.40.Ep; Nucleon-induced reactions: Inelastic proton scattering

Izvleček

V začetnem obdobju obratovanja trkalnika LHC je bilo dobljenih že kar nekaj rezultatov fizikalnih analiz in pričakovati jih je še mnogo več. Za veliko teh rezultatov, tistih že objavjenih in tistih, ki še pridejo, je potreben podatek o velikosti vzorca podatkov na katerem je bila opravljena analiza. Te analize torej temeljijo na neodvisni meritvi luminoznosti.

V želji, da se zagotovi zanesljiva meritev, je bila znotraj detektorja ATLAS razvita samostojna infrastruktura, namenjena izključno meritvi luminoznosti. Več njegovih pod-detektorjev meri luminoznost hkrati, vendar na različne načine. Nekateri izmed teh so namensko ustvarjeni za meritev luminoznosti, medtem ko drugi prvotno služijo drugim namenom. Vsi pa prispevajo svoje meritve, ki se jih primerja in tako omogoči natančno in zanesljivo meritev.

Eden izmed teh pod-detektorjev je tudi detektorski sistem za spremljanje kakovosti curka protonov, angleško 'Beam Conditions Monitor', okrajšano BCM. Prvotno je bil načrtovan kot varnostna naprava. S pomočjo spremljanja izgub protonskega žarka lahko sklepa na morebitno nevarnost in v izjemnem primeru zaprosi za prekinitev žarka, ter tako varuje notranje dele detektorja ATLAS. Kljub temu pa je njegova namensko narejena elektronska obdelava podatkov omogočila kasnejšo razširitev sistema tako, da prispeva tudi meritev luminoznosti. Njegova izjemna časovna ločljivost in dobra čistost signala omogočata meritev luminoznosti za posamezne gruče protonov, izločitev zaznavnega dela ozadja in ponavljanja celotnih meritev do nekajkrat na sekundo. Kot tak je bil BCM v letu 2011 izbran kot najboljši merilec luminoznosti znotraj detektorja ATLAS.

Ta disertacija opisuje detektor BCM in okoliško infrastrukturo v luči meritve luminoznosti. Podrobno je opisan način delovanja celotnega sistema. Poseben povdarek je na opisu algoritmov za meritev luminoznosti in simulacije, ki je potrdila način merjenja. Vse meritve sistema BCM so relativne, kar pomeni, da je potrebna umeritev sistema. Uporabljen je bil van der Meer postopek (vdM), s pomočjo katerega se izmerijo lastnosti protonskega žarka. Iz teh se lahko nato izračuna luminoznost. Predstavljeni sta analizi zadnjih dveh umerjanj, ki podata umeritvene konstante za podatke nabrane v letih 2010 in 2011. V zaključku so na kratko povzete tudi meritve luminoznosti iz istega časovnega obdobja.

Ključne besede:
LHC, ATLAS, spremljanje kakovosti curka, pCVD diamantni senzor, luminoznost, van der Meer postopek, umerjanje
PACS:
29.27.Fh; Curki delcev v pospeševalnikih: karakteristike curka
85.30.De; Karakterizacija, načrtovanje in modeliranje polprevodniških detektorjev
25.40.Ep; Reakcije nukleonov: Neelastično sipanje protonov

Contents

Chapter 1

Introduction

The aim of any physics research is to deduce general statements from regularities observed in nature. In such a way physics laws are observed, and to systematize them in a concise way theories are built around them. Different theories govern physics at different scales and under different conditions. When studying matter, the theory describing a smaller scale is often used to explain the physics laws governing larger scale phenomena. The beauty in understanding physics at smaller scale is not only to be able to deduce the already known at large scale, but such theories are often more general and usually require less 'ad-hoc' input parameters. In search of rules governing smaller and smaller constituents of matter the humanity traveled the path from materials, to atoms, to nucleons, to quarks and leptons, that are to this day the smallest know building blocks of our universe.

The current knowledge of these basic building blocks is concentrated in a theory called *Standard Model*. It assumes that matter is built of two types of particles: quarks and leptons, which are accompanied with additional force-mediating particles. Conceived in early 1970s, the Standard Model successfully predicted a wide variety of phenomena in the world of particles and it passed decades of experimental testing and verification. This has established it as a well proven theory... with, for now, an honorable exception. The theory helps understanding why different particles have different masses and why some are massless. The underlying mechanism is called the Higgs mechanism and predicts the existence of the yet undiscovered Higgs particle. This is the last missing piece in the Standard Model puzzle. But this is not the only puzzle left! Standard model only describes three out of four elementary forces, leaving the gravitational force outside the box. Additionally there are indications that the model breaks at higher energies where some new physics would start governing our universe...

To tackle these open questions many new experiments have been proposed and the Large Hadron Collider (LHC) is only one of them. LHC was constructed with purpose to extend our horizons to larger energies and with it open an entire specter of new possibilities. It accelerates particles (protons or lead ions) that collide at four different places around the LHC ring in order to provide interactions that can be then measured and studied by the experiments. Six experiments are constructed and positioned around LHC. The smallest two are TOTEM and LHCf that have highly specific designs and are intended for detection of very forward particles. The next two are mid-size, called ALICE and LHCb. They have broader use, but are still

dedicated to measure specific phenomena. Alice measures the Pb-Pb collision products, while LHCb is dedicated to B-physics. The two largest experiments are ALTAS and CMS. These are 'general purpose' spectrometers which allow the broadest coverage of the spectrum of processes to be studied.

The possibilities for new discoveries are truly endless. Not only due to the $7\,\mathrm{TeV}$ energy record promised by LHC, but also due to the frequency of interactions produced. Accordingly ATLAS detector matches the speed of data recording, giving a huge data sample of measured processes. The quantity of the produced data (number of total interactions that LHC produces) and recorded data (interactions that can be analyzed) must be measured. And here is where something called 'BCM' comes in...

This thesis describes the luminosity aspects of Beam Conditions Monitor (BCM) which is one of the ATLAS sub-detectors. In the second chapter the concept of luminosity is explained along with brief motivation as of why this is such an important quantity for the entire experiment and how it influences the physics studies. To give the basic understanding of the origin of luminosity, and a feeling what affects it, the third chapter provides a short intermezzo into accelerator physics. Knowing the reason and the question, the fourth chapter starts diving into the main part of experimentalist's work - designing instrumentations that eventually measures the desired quantity. ATLAS as a whole is described here and special attention is devoted to the luminosity infrastructure. Going into more details is the purpose of the fifth chapter that describes the BCM. Description covers everything from diamond based sensors and read-out electronics to data processing. Here also the BCM's main functionality as a safety system is briefly described. Luminosity algorithms are defined and the entire luminosity data acquisition is described.

Chapter six discusses Monte Carlo simulation of the BCM and explains the correlation between the luminosity being measured, and the numbers that pop-out from the BCM luminosity data stream. An estimation of these numbers is also given on basis of Monte Carlo, giving the basic orientation of what to expect, which was most useful during development. Here the reader also learns that BCM needs calibration, which is the bread and butter of chapter seven. Special procedure called the van dar Meer scan is described, the resulting data analysis is presented, providing the BCM calibration for 2010 and 2011 data. The eigth chapter is a very brief overview of the recorded data and luminosity seen and recorded by ATLAS.

Chapter 2

Luminosity

This chapter deals with the basic concepts that are later elaborated, discussed, and measured. In the first section the term of luminosity will be defined, continuing with the basic principles of measuring this quantity in section three.

2.1 Definition of luminosity

In particle physics performing an experiment typically implies observing particle scattering. There are numerous different types of experiments, but the core of them all usually translates to counting the number of scattered particles in a given solid angle per unit of time. In a simple picture of elastically scattered particles on a fixed target, their number N is scalable with the flux of projectiles. It is useful to write it as a product of two terms:

$$\frac{dN}{d\Omega dt} = L\frac{d\sigma}{d\Omega}. \tag{2.1}$$

In the above formula $\frac{d\sigma}{d\Omega}$ is the differential cross-section for given process – probability density distribution for the particle to be scattered in a given direction, and it describes the physics of particle scattering. The proportionality factor L is the luminosity, usually expressed in units of $cm^{-2}s^{-1}$. It corresponds to the flux of projectiles and describes the *experimental conditions*. Integrating the above formula over the full solid angle gives:

$$R = \frac{dN}{dt} = L\sigma. \tag{2.2}$$

For a physical process with a given cross-section σ the *instantaneous luminosity* is therefore a measure of the observed scattering rate R. If we further integrate the rate over a given time window we get the number of interactions that occurred, and this is usually expressed in terms of the *integrated luminosity* $\mathfrak{L} = \int Ldt$.

2.2 Impact of luminosity on physics studies

Luminosity is a valuable parameter with which one can characterize the performance of a collider. More on beams, optics, and how they condition the luminosity in the next chapter, here let us only note that luminosity is a quantitative measure of collisions produced by the collider. This is called *delivered luminosity*. Due to technical and operational limitations of the detector not all of this data can be recorded. The luminosity produced during the periods, when the detector was active and recording data, is given by *recorded luminosity*. It is obvious that the bigger this quantity is, the better – more data leads to smaller statistical uncertainties in any of the studies of physical processes.

However there is a sensible limit for instantaneous luminosity imposed by the detector. In practice one is often limited with the recording speed and storage of the data. R in equation 2.2 is therefore fixed. Since σ represents the cross-section sum of all processes passing the trigger, one has to trade off between large statistics and broadness of spectrum of physical processes under study.

Additionally another aspect must be considered when dealing with instantaneous luminosity. Along with increasing luminosity the detector occupancy increases. It goes without saying, that above a certain multiplicity the identification, track reconstruction, and calorimetry suffer steep decrease of both efficiency and accuracy, thus hindering possibility for accurate physics analysis.

Once put all together, taking into account statistics, data quality, physical processes under study, and the details of the detector, it is obvious that optimally chosen instantaneous luminosity is a valuable asset. However most stringent limit often comes from the limitations of the collider itself. On the other hand, the recorded luminosity is a never ending race.

2.3 Methods for luminosity measurement and monitoring

The distinction between luminosity measuring and monitoring is somewhat artificial. Its main idea is to distinguish the systematical uncertainties coming from two distinct sources. The *luminosity monitoring* is a relative luminosity measurement and it can be rather accurate. It is often at the percent level, since the precision is limited only by detector systematic uncertainty, while the lack of the absolute scale is its greatest demerit. In contrast, special techniques are available for absolute *luminosity measurements*. Typically these are much more limited with experimental conditions, under which they can be performed and are thus usually used only for calibration of luminosity monitors. The systematical uncertainty of the final absolute luminosity is usually dominated, by the systematics of calibration.

Whatever method one chooses, the task of monitoring and measurement is not straightforward. Even less so, when one considers that luminosity should be known as accurately as possible for time scales from sub-second to years. Therefore many complementary approaches have been used in the past and the majority of them will be implemented in ATLAS. Leaving details aside, all techniques of luminosity measuring and monitoring can be divided among four categories briefly presented in the next subsections.

2.3.1 Low angle elastic scatterings

The total proton-proton cross-section in equation 2.2 is unknown, and would need to be independently measured at energies used at LHC. At this moment no such measurement exists, so in order to measure luminosity one must relay on techniques that do not need the total cross-section. One of such is measurement of scattered particles under very small angles.

Basic scattering theory, in approximation of small momentum transfer between colliding protons (small scattering angles), and the probability conservation law leads us to *optical theorem* [PF95] which is described in appendix A. It corelates the total crossection σ_{tot} with forward scattering amplitude $f(0)$:

$$\sigma_{tot} = \frac{4\pi}{k}\Im\left[f(0)\right], \tag{2.3}$$

where k is the momentum of the projectile. $\Im[x]$ and $\Re[x]$ represent real and imaginary component of x. If $\rho = \Re\left[f(0)\right]/\Im\left[f(0)\right]$ and we use optical theorem for total crossection the following holds true:

$$\frac{d\sigma_{el}}{d\Omega}(\theta = 0) = |f(0)|^2 = \Im^2\left[f(0)\right]\left(1+\rho^2\right) = \frac{\sigma_{tot}}{16\pi^2}\left(1+\rho^2\right). \tag{2.4}$$

Finnaly, using equation 2.2 the luminosity can be expressed as:

$$L = \frac{1}{16\pi}\frac{R_{tot}^2}{dR_{el}/dp|_{p\to 0}}\left(1+\rho^2\right), \tag{2.5}$$

where p is the momentum transfer in proton-proton collisions. To determine the luminosity we therefore have to measure the elastic R_{el} and total rate R_{tot} of interactions.

Of course the protons scattering at zero-angle can not be detected. Therefore the main challenge is the detection of protons scattered under very small angles, and then to extrapolate this to zero-angle. The smaller the measured angle, the smaller the extrapolation needed and better results can be expected. If the LHC goal is to measure the luminosity to 2% of relative accuracy, then a good acceptance for protons' scattering under $14\,\mu\mathrm{rad}$ angles must be provided. This angle is well below the $35\,\mu\mathrm{rad}$ of intrinsic beam spread at high luminosity. *Dedicated runs* with special collider settings are therefore needed to reduce intrinsic spread well under $14\,\mu\mathrm{rad}$ and to allow a precise measurement. This is a big disadvantage of this luminosity measuring tehnique, since it can be used only for calibration and not for real-time measurements.

The greatest challenge in equation 2.5 is usually the total interaction rate. The ATLAS detector, as many in the past, has an insufficient coverage of low angles for the inelastic rate to be measured directly. Therefore a simulation is needed to relate the central region measurements to the total inelastic rate. Here the understanding of the scattering mechanism can be of aid. The main contribution to the elastic scattering at angles relevant to LHC scenario is due to the strong force. If we go to even smaller angles, the contribution due to electromagnetic

interaction increases. The region, where the two contributions are approximately equal is called the Coulomb interference region. Here the elastic scattering rate can be written as:

$$\frac{dR_{el}}{dp} = L\pi \left| f_C + f_N \right|^2 \approx L\pi \left| -\frac{2\alpha}{|p|} + \frac{\sigma_{tot}}{4\pi}(i+\rho)e^{-b|p|/2} \right|^2, \tag{2.6}$$

where f_C is the electromagnetic amplitude with parameter α, f_N is the amplitude arising from strong interaction, which is parametrized with ρ and b. For simplicity the proton form factor and higher order corrections are left out. There is a big advantage of the above formula: it does not include inelastic rate and much greater precision can be expected.

2.3.2 Well calculable processes

Another possibility for a absolute luminosity measurement is to analyze the recorded data itself. Since many processes are recorded, only those that are best known and calculable to highest precision should be selected. The calculations are then compared with the observation rate for this processes and the proportionality factor in-between is the luminosity. This solution is very effective in e^+e^- colliders, where the processes in question are QED processes like Bhabha scattering. The most promising examples of QED process at LHC are $pp \to ppe^+e^-$ and $pp \to pp\mu^+\mu^-$. The main advantage is their high precision cross-section calculation that can be better than 1%. But both have weaknesses. The electrons are produced with low invariant mass and therefore very small transversal momentum. Their almost zero angle direction needs dedicated detectors. On the other hand, muons are produced mainly in the direction of the central detector, and they can be recorded using the standard ATLAS trigger. But this process has a low rate. It will therefore be very challenging to eliminate the background to an acceptable level.

In addition to QED, LHC, being a hadron collider, also has option of QCD processes such as production of W and Z gauge bosons [ZC04]. This process is one of the best known in QCD. Assuming knowledge of parton distribution in protons, it can be calculated to next-to-next-to-leading-order. Main limitations of this method are current uncertainties of the parton distribution function, and a large data sample is needed. On the other hand, it has great advantage – it measures the *parton luminosity* directly and may serve as a normalization of parton luminosity in many other observed processes.

2.3.3 Beam parameters and van der Meer scan

One way to estimate the instantaneous luminosity would be to use the beam parameters of the collider. This discussion could get very involved and one would be required to 'take the collider apart'. Some of the most relevant concepts, along with a more detailed description on systematic uncertainties, will be discussed in the next chapter and more detailed information can be found in [LR04] and [LP07].

The basic idea is that luminosity is a function beam parameters:

$$L = n_b f_r N_1 N_2 \int \rho_1(x,y)\rho_2(x,y)\, dxdy. \tag{2.7}$$

The number of colliding bunch pairs is represented by n_b, N_1 and N_2 are the bunch populations of individual bunches in beams 1 and 2, f_r is the revolution frequency, and $\rho_{1(2)}(x,y)$ represents two dimensional particle density in the plane perpendicular to the beams. This density can be calculated from parameters of the accelerator optics, however the precision of such method would be poor. To avoid these calculations a measurement was proposed by van der Meer [MH68] which came to be known as the *van der Meer scan* or *luminosity scan*. During the scan one of the beams is displaced in given direction and one measures the rate of interacitons $R_{vdM}(x)$ as a function of displacement x. This method will be discussed in more detail in chapter 7. Its asset is that it does not depend on the shape of the distribution. Many detectors can be used for it, as long the non-linearities during scan luminosities are low. On the other hand, it requires dedicated time, and can therefore be used only for calibration.

2.3.4 Luminosity monitoring

Previously mentioned methods yield the absolute luminosity measurement. Such a measurement is necessary in every experiment, but the cost they impose – low luminosity – is unacceptable for normal running of LHC in the ATLAS experiment. Therefore during high luminosity running other methods must be used. In hadron colliders typically the inelastic rate is observed, which means that one counts the average number of proton-proton interactions per bunch-crossing. For counting, high luminosity is preferred, and data samples with 1% of statistical uncertainty can be obtained in times smaller than a millisecond.

Event counting

With event counting, one undertakes the most robust approach to monitoring. Proton-proton interactions within colliding bunches are uncorrelated and the number of these interactions can be described by the Poisson distribution. The simplest way is to count n_{det}, the number of times anything is detected (complementary to empty event counting). One can write:

$$n_{det} = n_{BC}\left(1 - e^{-A_{ec}\cdot L}\right), \tag{2.8}$$

where A_{ec} depends on total cross-section and detector efficiency. At low rates this is the preferred method – it places minimal requirements on detector and the luminosity is proportional to observed rate. However at high luminosity almost every bunch crossing will have some interactions and the difference $n_{BC} - n_{det}$ will be very small.

Particle counting

A second strategy is particle counting. Instead of the relation between luminosity and pp collisions, we can use relation between the luminosity and particle multiplicity:

$$M = C \cdot A_{pc} \cdot L. \tag{2.9}$$

M is the measured average number of particles, and C the average number of detected particles per interaction. In principle C could be determined from simulation, but usually low luminosity calibration is used, where more than one interaction is highly unlikely. This method does not saturate at high luminosities. However, it is used less often than event counting, since it is more stringent on detector, implying more systematical uncertainty that can reduce its predictive power.

As can be seen from equations 2.8 and 2.9, the result relies on knowledge of calibration constants A_{ec} or A_{pc}. These can in principle be obtained from detector simulation, but uncertainty of it is to high for practical usage. Here is where the absolute luminosity measurements, like low angle scattering, are actually used. During low luminosity, when absolute measurements are performed, the luminosity monitoring system can be *calibrated*. After calibration, the LHC is able to run at high luminosity and ATLAS can obtain the luminosity from its luminosity monitoring system.

Chapter 3

The Large Hadron Collider

3.1 Accelerator basics

Before going into the discussion of LHC and its luminosity this section will detour into general accelerator physics. Since it is an enormous field and not the primary focus of the thesis, the discussion here will be limited to its basics – those relevant for understanding the LHC and especially its parameters affecting the luminosity.

Basic principles of particle beam manipulation are extremely simple and an overview can be found in [BO66]. Charged particles change their momentum $\vec{p}$ when moving through electric ($\vec{E}$) or magnetic field ($\vec{B}$) according to expression:

$$\frac{d\vec{p}}{dt} = e\left(\vec{E} + \vec{v} \times \vec{B}\right). \tag{3.1}$$

LHC, as any circular collider, utilizes magnetic field to bend the particle tracks and drive them continuously in circular orbits. Two such orbits are used, both maintaining beam circulation in opposite directions and colliding them at interaction points, around which detectors are built. Since the same hardware is reused every revolution, acceleration can be done gradually with electric field constantly applied. Final achievable energies are thus much higher than in linear accelerators. The actual maximum energy is usually limited by the strength of the orbit-bending magnets and the radius of the collider.

This simple picture, however, is not of much use apart for determining the maximum energy of the collider. For understanding the structure of the beam and limitations in producing collisions a more detailed explanation of particle dynamics is needed.

First let us discuss longitudinal motion. For this the main instrument in an accelerator is a radio-frequency cavity (RF cavity). Herein RF oscillations are provoked in such a manner, that the electric potential V_{RF} has a sinusoidal shape along the beam axis. Particle entering the RF cavity arrives at phase φ relative to the RF wave phase. The ideal case is what is called *synchronous particle*. Its motion is such that $\varphi(t) = \varphi_s$, which is constant. It is always in phase. Unfortunately no particle source is monochromatic and any small deviation of particles' energy during circulation in the collider results in desnychronization and a negative feedback is necessary in order to ensure phase stability. This is achieved by the shape of $V_{RF}(\varphi)$ itself.

The energy variations during a turn are converted in phase variations. Particles energy gain in passing the RF cavity depends on the phase, thus with the proper $V_{RF}(\varphi)$ negative feedback can be achieved. The process (see figure 3.1) is best understood in phase space of energy difference δE compared to the one of synchronous particle and particle relative phase φ to RF wave. For

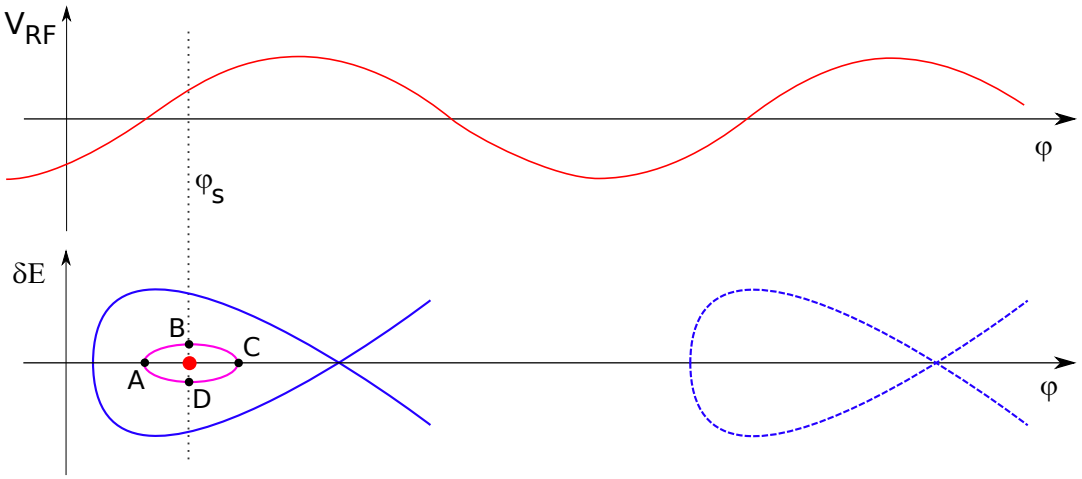

Figure 3.1: *Particle energy difference with respect to that of a synchronous particle (red dot) as a function of their phase differences with respect to RF potential. Periodic potential results in multiple RF buckets separated by the wavelength of the potential. Each bucket is defined with separatrix (blue) which marks the largest particle oscillation before it is lost from the bucket. The violet ring represents the osscilation of a given particle.*

instance, if a particle with energy equal to that of the synchronous particles arrives too late (point A), it will gain an energy greater than of synchronous particle gain. This will speed it up and after some time it will catch up with the synchronous particle (point B). Its energy will be of course greater, thus it will eventually arrive at the RF cavity too early, and its energy will be increased less than energy of synchronous particle. Eventually their energies will again match, but there will be a positive phase shift (point C). The process of decelerating continues, until the particle has smaller energy, but again the same phase (point D), and further to initial situation, of equal energy and smaller phase. The particle will thus oscillate around the synchronous particle with the amplitude dependend on the initial conditions. For simplicity lets assume that initial condition are $\delta E = 0$ and there is a distribution over relative phase of particles in a cloud. Particles with $\varphi - \varphi_s \ll \pi$ will experience linear V_{RF} changes and their trajectories in $\delta E - \varphi$ space will be ellipses, while greater initial phase deviations result in distorted, but still stable oscillations. The limiting case is $\varphi - \varphi_s = \pi$ that defines the RF bucket. All the particles within the bucket will oscillate stably, forming a particle cloud ready to collide, while those outside the bucket will be lost from the cloud. The shape and period of V_{RF} determines bucket dimensions, thus length of the bucket σ_z and the momentum spread of particles. Since V_{RF} is periodic, the next bucket will appear in phase of 2π, 4π, ..., forming a chain of potential particle clouds. The number of buckets is a property of the collider and is usually much greater than the number of colliding bunches. Bunches are usually defined as a set of buckets, where only one is filled,

leaving the rest to accommodate for the detector restoration times. The discussion on how many of them are actually filled, in what order, and how that affects the luminosity of LHC is left for section 3.3. Here, understanding the bunch structure of the beam and bucket z-dimension, the focus should shift to transversal properties of the beam.

While the electrical field plays a dominant role in the longitudinal dimension, accelerating, and structuring of beam, transverse motion of particles is determined by the magnetic field - beam optics. The major part of it focuses on stable orbits for particles revolving around the collider, though this will not be the subject here. In regard to the luminosity the most direct influence comes from the final magnets before the experiments, that focus the beam. The idea of focusing is to achieve minimal transversal size, thus maximum density and therefore higher luminosity. To this end quadrupole magnets are used. If coordinate system is placed so that its z axis is parallel to the beam, than x and y are the transverse coordinates. Particle movement through a single magnet in x direction obeys the equation:

$$\left(\frac{x'}{K}\right)^2 + x^2 = a, \tag{3.2}$$

where K denotes the product of particle charge, its inverse momentum, and magnetic field gradient. s is the coordinate along the particle path so $x' = dx/ds$ represents inclination towards beam axis. Constant a describes initial conditions.

Quadrupole field is differently oriented in case of particle movement in y direction. Here the magnet would defocus the beam. To that end a series of quadrupole magnets is used in an arrangement with alternating orientation. In a given plane, when the particle cloud passes through such system, half of them focuses it, while the other half defocuses it, but the net effect is focusing. Single particles therefore oscillate. The envelope of these oscillation is known as the betatron function $\beta(s)$. It describes the peak excursion of the beam.

Turning the attention back to single particle in a quadrupole and restricting oneself to one dimension, the dynamics is most transparent if represented in $x - x'$ space. The particle movement is represented by an ellipse (dashed ellipses in figure 3.2). Each proton moves this way, the only difference being the initial conditions, which should largely be traced back to the original sin - the particle source. None is monochromatic and perfectly collimated, therefore each bunch covers a finite area in $x - x'$ space. Most times this region (green area in figure 3.2) can also be well approximated by an ellipse and as individual particles move, each on its own ellipse, the total bunch area gets transformed and rotated. The goal of optics is to achieve case d) in figure 3.2 at the interaction point. The transverse bunch distribution is the narrowest, thus the bunch is most dense. The first handle to perfect this is to minimize the bunch area. It is parametrized as $A = \pi\varepsilon$, with *emittance* ε. Due to Liouville's theorem the area remains constant as long as forces do not depend on velocity. Obviously this is broken during acceleration, but the emittance scales inversely to particle momentum along the axis, for this, one usually defines *normalized emittance*:

$$\varepsilon_n = \varepsilon\beta\gamma, \tag{3.3}$$

which is a constant. The second handle for bigger density is the optics, which is parametrized with the betatron function. Its value at the interaction point is usually denoted with β^* and

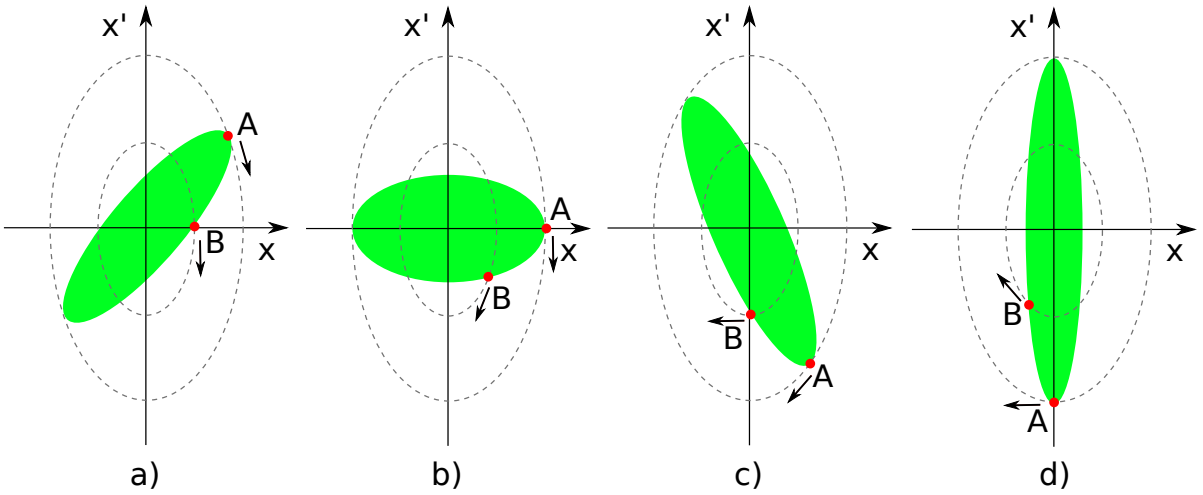

Figure 3.2: *Representation of particle dynamics in a quadrupole magnet. The dashed ellipses represent the path of each individual particle (A and B) and the green-filled areas depict a bunch of particles. The deformation of bunch area results in minimal transverse width of bunch in figure d). This should represent the situation at the proton collision point.*

should be minimized with perfecting the magnets.

Normalized emittance and value of the betatron function at interaction point are the two basic beam parameters entering the luminosity. While the first one describes the intrinsic bunch spread (quality of the beam), the second is defined by the magnet system (quality of the collider). Both together can be used to express the luminosity of two colliding bunches. If N_1 and N_2 are the respective proton populations of the bunches, and f_{rev} is the bunch revolution frequency then

$$L_{bb} = \frac{N_1 N_2 f_{rev} \gamma}{4\pi\varepsilon_n \beta^*}. \tag{3.4}$$

Quantity L_{bb} is single bunch-pair luminosity and is expressed in the above formula under the assumption of symmetrical beams with Gaussian radial profile. More detailed derivation can be found in appendix B. Evaluating the collider, the delivered luminosity is normally stated for the entire beam, meaning in addition a sum over all colliding bunch-pairs is needed.

3.2 LHC description

Knowing the basic concepts of accelerator physics and understanding how they condition luminosity, the focus can be shifted to the specifics of the LHC, that are described to great detail in [LR04]. It is a proton-proton collider at CERN, build in the same $27\,\mathrm{km}$ long tunnel that hosted the LEP collider. Its structure can be divided in eight sectors as shown in figure 3.3. Each octant has an arc and a straight section.

Single arcs are made of 23 regular arc cells, each build of two half cells, short straight section, and three long dipole magnets. Its design has been optimized for maximum integrated

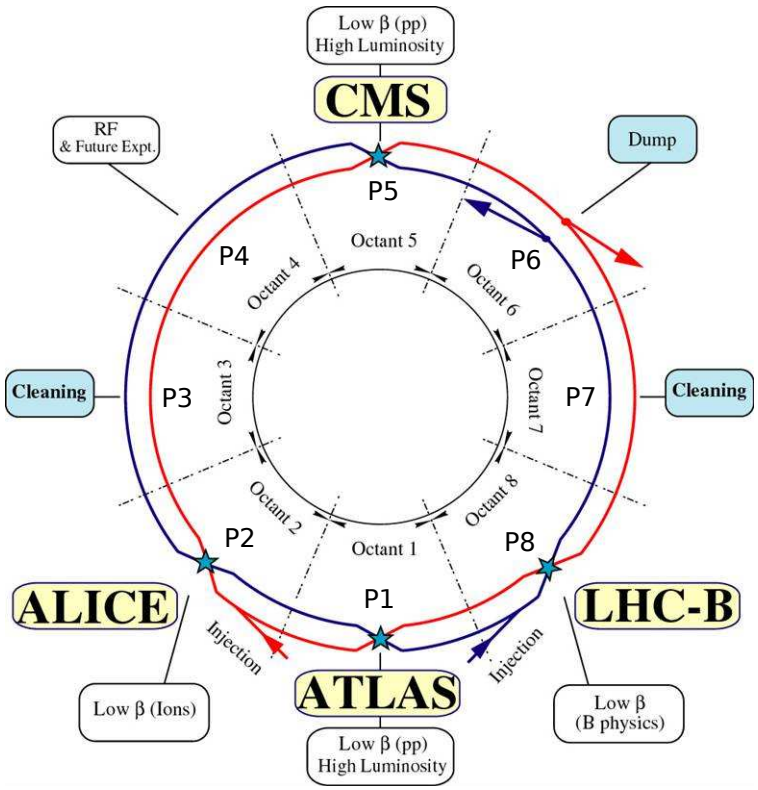

Figure 3.3: *Schematic LHC layout showing its main structure along with experiments positions.*

dipole field. Superconducting magnets provide magnetic fields with strength of $8.4\,\mathrm{T}$. With these the arc defines the maximum bending of the beam and in turn the maximal particle energy of $7\,\mathrm{TeV}$.

Long straight sections of $528\,\mathrm{m}$ length are placed between the arcs. At these points experiments and beam services are installed. The two high luminosity experiments: ATLAS and CMS are placed at P1 and P5, respectively. Being placed on opposite points of the LHC ring, both experiment have same combinations of bunches colliding within them. Beam optics is the same around both experiments which makes the beam conditions as similar as possible and allows LHC to deliver highest luminosity to both simultaneously. ALICE and LHCb detectors are designed for lower luminosities, making their placement easier. They are positioned at P2 and P8, respectively. Corresponding sectors also have injection lines coming from SPS. At P6 a beam abort system is installed. Here each beam separately can be deflected first in horizontal, and afterwards in vertical direction, steering it away from the machine into a separate tunnel where it is absorbed. At P4 the RF insertion is installed, at P3 the betatron cleaning insertion is installed and momentum cleaning insertion resides at P7.

Particles fed to the LHC are pre-acelerated to $450\,\mathrm{GeV}$ in few stages. The acceleration complex is sketched in figure 3.4. First is the Linear accelerator (Linac), then Proton Synchrotron Booster (PSB), followed by Proton Synchrotron (PS) and Super Proton Synchrotron (SPS).

From there particles are injected into LHC. Its dynamic range of proton energies spans from $450\,\mathrm{GeV}$ eventually up to $7\,\mathrm{TeV}$. The lower limit matches the characteristics of SPS, while the upper limit is imposed by the tunnel radius and the strength of beam bending magnets.

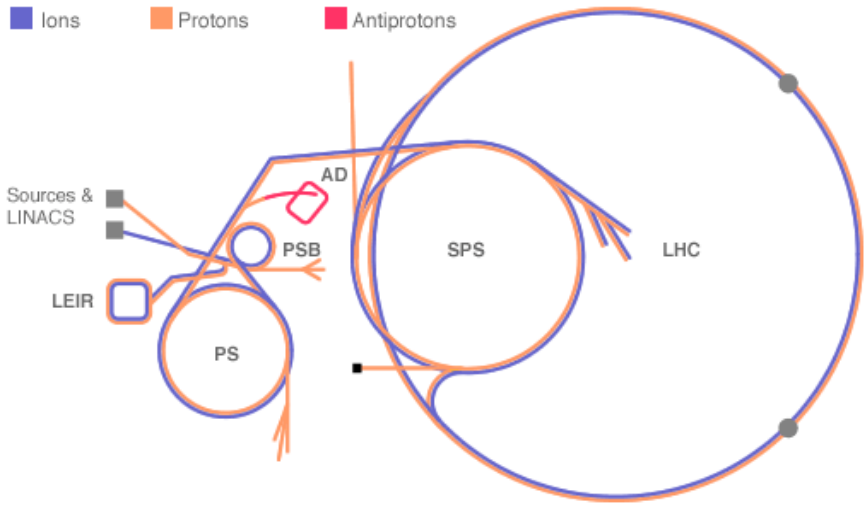

Figure 3.4: *A simplified view of the CERN acceleration complex. Particles start accelerating in Linear accelerator (Linac), then continue through Proton Synchrotron Booster (PSB), Proton Synchrotron (PS) and Super Proton Synchrotron (SPS), which finally injects them in the LHC.*

Steering two counter-rotating beams of equally charged particles requires opposite magnetic fields. 'Twin' magnets were constructed in a way, that the return field of the first half provides the field for the second half of the magnet. Each half can therefore serve its own beam. It should be noted, however, that in this solution the magnet fields are coupled, which also couples both beams, even though they reside within separate beam pipes. Both beam pipes are housed within the same cryostat which uses super-fluid liquid helium to cool the magnets to $1.9\,\mathrm{K}$.

The RF system, as the LHC engine, will work at approx. $400\,\mathrm{MHz}$ thus sizing the bunches in the longitudinal dimension to $8\,\mathrm{cm}$[1]. To allow for the detector dead-time, only every 10th RF-bucket can be filled. This gives 3564 possible bunch places around the LHC ring. These places are numbered with LHC Bunch Crossing IDentifier i.e. BCID, starting from 1. In the transversal direction the RMS of the bunch varies, from over a cm at injection to $16\,\mu\mathrm{m}$ when squeezed at the collision point.

The above characteristics can be extended with nominal bunch population of 1.1×10^{11} protons. With this the nominal luminosity of the machine is defined and in case of ATLAS or CMS this equals $10^{34}\,\mathrm{cm}^{-2}\mathrm{s}^{-1}$. This value corresponds to roughly 25 proton-proton collisions per bunch crossing. Such high instantaneous luminosity will enable to achieve up to $100\,\mathrm{fb}^{-1}$ of integrated luminosity in $10^7\,\mathrm{s}$ of operation in a year, thus enabling high data volume.

[1]The value is the RMS of the longitudinal proton distribution.

3.3 Filling schemes

LHC started its first beams in the machine with the simplest filling scheme of only one bunch per beam. Gradually the pattern of proton bunches became more complex and by August 2010 36 colliding bunches[2] were used. The increase continued up to 1331 bunches by July 2011 [ADS]. In principle many schemes [RF03] can be devised in order to support different modes of LHC operation. These are not "hard-coded" in the machine, but evolve with the better understanding of the collider and its injection chain. In general, all of the schemes must respect following constraints:

- during the rise time of the abort kicker magnet ($3\,\mu\mathrm{s}$) no bunches should be present in it. Due to its gradually increasing magnetic field, the bunches would not be deflected as they should be, but sprayed over the nearby equipment, thus potentially damaging it. This section of the beam, called *beam abort gap*, should therefore always be empty.
- space between subsequent bunch trains injected into LHC must be greater than the LHC injection kicker rise time ($0.95\,\mu\mathrm{s}$),
- LHC injection kicker time must not exceed $7.86\,\mu\mathrm{s}$ limiting bunch train length,
- offset collisions should be provided for LHCb operation,
- bunch pattern should be optimized to reduce the effect of PACMAN[3] bunches [PA98],
- constraints from injection system, like SPS injection kicker rise time ($0.22\,\mu\mathrm{s}$).

Whatever scheme is used, it affects luminosity through the number of bunches in the ring. It has no impact on bunch characteristics like emittance and bunch population. These can still be arbitrary changed within injector chain and LHC limits. The main scheme used for optimizing the luminosity will be the so-called *25 ns scheme*. In this case the beam layout will consist of 39 bunch trains, each built of 72 bunches with $25\,\mathrm{ns}$ spacing, followed by an 8 bunch gap due to SPS injection kicker rise time. Some of these gaps are prolonged for other timing constraints. In total, this scheme will contain 2808 collisions[4] in ATLAS, providing maximum proton population in the collider.

There is a another implication of the filling scheme in luminosity, that is still related to the collider. In the interaction regions, both beams share the same path for $70\,\mathrm{m}$ before and after the collision point. In case of head-on collisions, if one wants to eliminate potential 34 parasitic

[2] This is a number of colliding bunches in all four experiments.

[3] PACMAN bunches are bunches, that during the passage through the interaction region encounter the gap (missing bunches) in the counter-rotating beam. In interaction region, where beams share the beam pipe and are close together, long-range beam-beam interaction plays an important role. Normal bunches are passing bunches of the opposite beam and thus suffer different long-range forces than PACMAN bunches. If the machine is optimized for normal or for average bunch, it will not be optimal for PACMAN bunch which may therefore suffer enhanced losses.

[4] Same filling scheme provides 2808 collisions in CMS, 2736 collisions in ALICE, and 2622 collisions in LHCb.

collisions, only one bunch at a time should be in this region. This gives the limit of 156 bunches in the machine. To avoid parasitic collisions during more populated schemes, the beams must be collided under an angle thus reducing the bunch luminosity. It is also worth mentioning, that the quantity of recorded data does not scale linearly with the number of bunches, since there is detector dead-time after event triggering, that disables the a next few bunch collisions.

3.4 Limitations on delivered luminosity

The maximum luminosity that can in principle be achieved with the current conception of LHC is constrained by seven effects:

- **Beam-Beam limit** is imposed by interaction between protons of the two beams. Here both head-on and long-range interactions have to be considered. During bunch collision a particle passes a strong non-linear filed of the opposite bunch and its dynamics can be strongly distorted. This can also move the particles with large amplitudes closer and closer to the aperture limit where they will be lost. This leads to emittance growth that shortens the beam lifetime. The long-range interaction also causes a PACMAN effect, where the bunches on the end of bunch trains experience only half of the total beam-beam effects and thus have different dynamics inevitably causing an increase in bunch-to-bunch variations. The third effect is also due to the beam-beam force that couples two beams. For this reason coherent modes of oscillation are expected, making the beams oscillate.

- **Mechanical aperture** limits the maximum beam size to $1.2\,\mathrm{mm}$ if one requires 10σ aperture in terms of beam sizes. Combined with the constraints of the β-function along the ring, this limits the maximal transverse beam emittance to $\varepsilon_n = 3.75\,\mu\mathrm{m}$. Taking into account beam-beam interactions this prescribes the maximal bunch population. Additionally the aperture of the triplet magnets limits the β^* and thus the crossing angle.

- **Maximum dipole field** and therefore the energy of the circulating beams depend on temperature margins of the cryo-magnets and on the heat load. The latter is conditioned by the beam losses. A high field therefore implies operation with minimal beam losses.

- **Stored energy** of the circulating beams and in the magnet fields have top values of $362\,\mathrm{MJ}$ and $600\,\mathrm{MJ}$ respectively. In case of beam-abort majority of it must be absorbed safely. The dumping system therefore provides an additional constraint on maximum energy and intensity.

- **Heat load** of the cryogenic system imposed by synchrotron radiation is another possible limit of beam intensities. Additionally a significant amount of electrons can accumulate in the beam pipe. Many processes can create primary electrons. These accelerate in the field of the passing beam and eventually multiply by the secondary emission from the chamber wall. In parallel to degrading the vacuum pressure they can also largely contribute to the head load.

- **Field quality** errors spoil the particle stability. The problem therefore demands high-quality production and installation.
- **Collective beam instabilities** do not include only coherent oscillation effects but also the effect of electromagnetic fields and the conductive boundaries of the vacuum system. Here the geometry and surface properties are equally important. These effects are usually proportional to the beam currents and can therefore impose yet another limit.

3.5 Luminosity lifetime and integrated luminosity

Luminosity is not constant in time but decays during the physics run mostly due to degradation of intensities and emittance growth. Under nominal conditions the decay will be governed by the collisions themselves. Though this is not the only contribution, the discussion here will be limited only to this since it is the most significant effect and highlights the connected issues. Due to collisions the number of particles in the collider N changes:

$$dN = -k\sigma_{tot}Ldt, \tag{3.5}$$

where k is the number of interaction points, σ_{tot} the total cross-section, and L the combined luminosity of the four interaction points. Luminosity is proportional to number of particles squared, and let the proportionality factor A be constant. With this a simplification of constant beam sizes is included and the solution of the previous equation is:

$$N(t) = \frac{N_0}{1 + t/t_0} \quad \text{and} \quad L(t) = \frac{L_0}{(1 + t/t_0)^2}, \tag{3.6}$$

the constants being

$$t_0 = \frac{1}{kN_0\sigma_{tot}A} \quad \text{and} \quad L_0 = AN_0^2. \tag{3.7}$$

This also gives the luminosity lifetime (time for luminosity to drop to $1/e$ of the initial value):

$$\tau_L = t_0(\sqrt{e} - 1). \tag{3.8}$$

Note once again that (3.8) is valid under the assumption that only collisions contribute to luminosity degradation. In reality this is not the only contribution and it becomes dominant only at luminosities above $10^{34}\,\mathrm{cm}^{-2}\mathrm{s}^{-1}$. Most of other contributions have been already mentioned as things imposing the limits of the collider. These are harder to model because they have many interdependencies. Many different mechanisms can contribute to the same type of beam loss, and a lot of parameters would be needed. However it turns out that having a loss proportional to the luminosity is not far from the truth. Therefore in many situations an exponential parametrization:

$$L = L_0 e^{\frac{-t}{\tau_T}} \tag{3.9}$$

perfectly describes the situation with only one parameter – τ_T as the effective luminosity lifetime.

For the luminosity measurement itself the exact functional form of luminosity decay is not essential since the measurements are summed up numerically. However in the interest of physics measurements the luminosity must be maximized and each LHC fill must be put to optimal use. Equation 3.9 shows that there is less and less data with time. Eventually the luminosity drops low enough that a new LHC fill is preferred. For this a *turnaround time* $T_{turnaround}$ is needed. Each full LHC fill requires 12 SPS cycles, and each of those requires 3 to 4 PS cycles. The SPS and PS cycles are $21.6\,\mathrm{s}$ and $3.5\,\mathrm{s}$ respectively. This gives a total filling time of $4\,\mathrm{min}$ per each LHC beam. Additional time is needed for injection setup and human decision making and the low limit for injection becomes roughly $15\,\mathrm{min}$. After injection some time is required to ramp the beam energy from $450\,\mathrm{GeV}$ to $7\,\mathrm{TeV}$. Equal time is needed to ramp the energy back after the beam dump. Adding system checks and human interventions, the total turnaround time approaches $2\,\mathrm{h}$. This being constant and integrated luminosity being:

$$L_{int} = \tau_T L_0 \left(1 - e^{-\frac{t}{\tau_T}}\right), \tag{3.10}$$

one can calculate the total integrated luminosity per unit of time as a function of run length T_{run}:

$$L_{tot} = \frac{t_T L_0}{T_{turnaround} + T_{run}} \left(1 - e^{-\frac{tT_{run}}{\tau_T}}\right). \tag{3.11}$$

The optimal run length is therefore obtained by solving:

$$\ln\left[\frac{T_{turnaround} + T_{run}}{\tau_T} + 1\right] = \frac{T_{run}}{\tau_T}, \tag{3.12}$$

which yields $\sim 7\,\mathrm{h}$ for a lifetime of $14\,\mathrm{h}$, assuming a turnaround time of $2\,\mathrm{h}$.

Chapter 4

ATLAS and luminosity

4.1 ATLAS spectrometer

ATLAS (A Toroidal LHC ApparatuS) is one of the four experiments placed around the LHC. It is located at P1 (see fig. 3.3). As any other general-purpose spectrometer designed for colliding beams, it has a layered structure that is cylindrically symmetrical around the beam pipe. Extensive technical details can be found in [R199], [R299], and in [AT08].

Its symmetry line defines the z-axis of the agreed coordinate system, with positive z-axis oriented in counter-clockwise direction when viewing LHC from the top. The $z > 0$ side of the detector is named A-side, while $z < 0$ side is named C-side of the detector. The x-axis in pointing towards the center of the LHC ring and the y-axis upwards. Due to its symmetrical structure the cylindrical coordinate system is usually used, defining each point with ϕ as the azimuthal angle in x-y plane, coordinate along the z-axis, and polar angle θ. The last coordinate is usually expressed in terms of *pseudorapidity*, defined as $\eta = -\ln[\tan[\theta/2]]$.

Its outer form is a $44\,\mathrm{m}$ long cylinder measuring $25\,\mathrm{m}$ in diameter. It contains the tracking system, calorimeters, and muon chambers. Their placement and structure is shown in figure 4.1.

Inner Detector (ID) is the innermost part of ATLAS and it is designed for efficient tracking of charged particles. The homogeneous magnetic field of $2\,\mathrm{T}$ that curves the particles path is generated by the superconducting solenoid magnet surrounding it. The detector itself is comprised of three sub-detectors. The closest to the beam pipe is the Pixel detector. It is a high resolution silicon detector constructed from three layers (it offers three measurement points) and covers $|\eta| < 2.5$ region. The same coverage has the SemiConductor Tracker which is a silicon strip detector, with abbreviated name SCT. It offers four measured space points. The third layer of Inner detector is the Transition Radiation Tracker (TRT). Its straw tubes detect, in addition to ionization in the gas, transition radiation in the straw wall and typically add more than 30 tracking points. TRT covers the $|\eta| < 2$ region. All three parts combine the information to provide best particle tracking and momentum measurement. Based on transition radiation, TRT also assist calorimeters in electron particle identification.

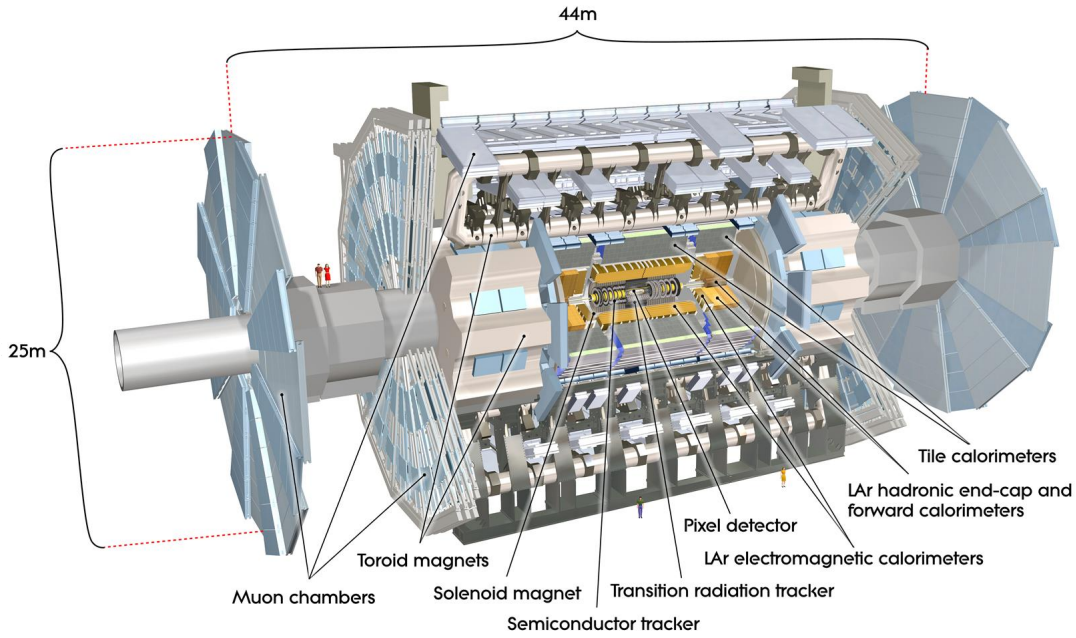

Figure 4.1: *A detailed computer-generated image of the ATLAS detector and it's systems. Source [ATLA].*

Calorimeter system surrounds the central solenoid magnet. Energy measurement as the primary goal is supplemented with particle identification that distinguishes between electrons, photons, and hadronic jets. Energies of the first two particle types are measured by the ElectroMagnetic (EM) calorimeter. It uses lead as absorber material with intermediate sampling planes of liquid argon. Its accordition shape provides full ϕ coverage. Its barrel and end-caps cover $|\eta| < 3.2$ pseudorapidity range. For energy measurement of hadrons more techniques are used, manly due to very different radiation conditions at different η. For the central region of $|\eta| < 1.7$ Tile calorimeter is used. It is a staggered formation of iron and scintillator tiles. The scintillator light output is collected by wavelength shifting optical fiber and measured by photomultipliers. Region $\sim 1.5 < |\eta| < 3.2$ is covered by Hadronic Endcap Calorimeter (HEC) which similarly to EM calorimeter uses liquid argon. However it uses copper instead of lead as passive material. The last region $3.2 < |\eta| < 4.9$ is covered by the Forward liquid-argon CALorimeter (FCAL) and presents most difficult calorimetry measurements due to high radiation. Copper, and at larger z tungsten, is used as the absorber material. In accordance with energy resolution requirements all the calorimeter parts are sufficiently thick in units of radiation length λ_0. At $\eta = 0$ the system is $11\lambda_0$ thick and as such reduces the probability of a punch-through to the muon system to negligible level.

Muon system represents the outer shell of ATLAS and is thus its largest component. Its function is to identify muons with high transverse momentum that signify many

interesting physical processes, to measure the momentum, and to aid the ATLAS data selection with providing trigger information. Its structure is again divided into barrel and two end-caps, while both have three layers of modules. Similarly to calorimeters, different technologies are applied depending both on η and on detector function. The precise momentum measurement is done for the most part by Monitored Drift Tubes (MDT), while at large pseudorapidities Catode Strip Chambers (CSC) are used. This gives the coordinate measurements, that are used to extract momentum, coverage up to $\eta = 2.7$. The magnetic field of $4\,\mathrm{T}$ is provided by a complemented large superconducting toroid magnet with two smaller end-cap magnets. The trigger system has a bit smaller coverage of $|\eta| < 2.4$. Here two different detections are used as well. Resistive Plate Chambers (RPC) are used in the barrel and Thin Gap Chambers are used in the end-caps. Beside triggering this system also provides accurate timing and measures the second coordinate, perpendicular to that measured by precision chambers to resolution of $10\,\mathrm{mm}$.

Once the information is in the sub-detector buffers it is handled by ATLAS Trigger and Data-AcQuisition system (TDAQ). Its main purpose is to filter out the interesting data. Nominal bunch crossing rate is $40\,\mathrm{MHz}$, and at full luminosity this implies interaction rate of $\sim 10^9\,\mathrm{Hz}$. However, event size is expected to be $\sim 1.5\,\mathrm{MBytes}$ thus limiting the event data recording rate to $\sim 200\,\mathrm{Hz}$. Event rejection factor of close to 10^6 is therefore needed, while it is crucial to maintain efficiency for the low cross-section processes under study. This event-selection is done by the trigger system that filters the data online in three sequential steps. Each step refines the event-selection by using more general information and more sophisticated algorithms.

The initial selection is done by level-1 (LVL1) trigger [TG98]. It is completely hardware based and uses information provided by a subset of detectors. These detectors issue trigger bits on basis of local measurement e.g. muon system triggers on high p_T muons, calorimeters trigger on large energy deposits. On basis of these trigger bits the final decision is made by the Central Trigger Processor (CTP). Its decision is based on programmable combination of inputs in coincidence or veto, where a prescale can be applied to each trigger item. CTP also introduces a dead-time to allow for detector and data acquisition dead-time. Once the decision is made, it is broadcasted from CTP to all sub-detectors with the LVL1 accept trigger signal (`L1A`). This signal is distributed by Trigger, Timing, and Control system (TTC) that also distributes LHC-synchronised $40\,\mathrm{MHz}$ bunch-crossing clock, bunch crossing reset, and event counter reset. The latency from actual bunch crossing to `L1A` arrival to sub-detectors is $\sim 2.5\,\mu\mathrm{s}$, demanding at least last 100 bunch crossing information to be stored in sub-detector buffers. Once `L1A` arrives, the detector Read-Out Driver (ROD) transmits the appropriate bunch crossing record to the Read-Out Buffers (ROBs) which constitute a larger unit called Read-Out System (ROS). Overall LVL1 scheme is designed to reduce the rate of interesting events to $75\,\mathrm{kHz}$.

The rest of event filtering is done by the High Level Trigger (HLT) which has two stages: lever-2 trigger (LVL2) and Event Filter (EF). They are both software based, running on dedicated farms of standard PCs. LVL2 uses information stored in ROBs. It is aided by LVL1 which passes Region of Interest (RoI) information, enabling LVL2 to process and move only the data from specific ROBs that contain relevant information. In principle all of the event data with the full precision and high granularity is available to LVL2, however typically only few percent are used in decision making. Once an event is accepted, event building takes place. It moves

all corresponding event fragments from ROBs and moves them to single location accessible by the EF. The $\sim 1\,\mathrm{kHz}$ output rate from LVL2 is low enough for EF to fully process the event. It uses offline algorithms and applies all calibration and alignment. Its output rate is in range $200 - 300\,\mathrm{Hz}$ with which it records the selected events to permanent storage.

This huge volume of information that is produced is stored at CERN and its copies are distributed among many centers throughout the world, enabling distributed computing. This allows for many physicists to perform their physics analyses on large data volumes, without moving the data. The computing model is described in detail in [CR05]. The common analysis software called Athena [AA08] has been developed enabling unified approach to analysis. With this, the Grid [GR09] computing has been used, where the physics analysis (algorithm) moves and is executed on Grid sites that contain the data. This requires only the final results to be moved over the network thus enabling much faster and efficient processing.

4.2 ATLAS approach to luminosity measurement

Luminosity can easily be expressed from equation 2.2:

$$L = \frac{R}{\sigma}. \tag{4.1}$$

Limiting the discussion to a single proton bunch-pair within the collider with revolution frequency f_{rev}, one can express luminosity with the average number of interactions per bunch crossing $\langle\mu\rangle$:

$$L = \frac{\langle\mu\rangle\, f_{rev}}{\sigma}. \tag{4.2}$$

Measuring the ratio $\langle\mu\rangle / \sigma$ thus gives luminosity regardless of the measuring method being particle or event counting. For their simplicity and robustness, at present, ATLAS relies only on the event counting methods. Some of the relevant sub-detectors could be upgraded to provide particle counting. Many systematic effects are under study and achieving better systematic uncertainty than with event counting seems very challenging. Equation 4.2 has a drawback in its form. For measuring $\langle\mu\rangle$ one would need to know detector efficiency ε of a single pp interaction to satisfy the event selection criteria. This efficiency is usually not know precisely. Additionally σ would need to be measured at LHC conditions with an independent measurement. To avoid this, one defines the visible average of interactions μ_{vis} and visible cross-section σ_{vis}:

$$\mu_{vis} = \langle\mu\rangle\, \varepsilon \tag{4.3a}$$

$$\sigma_{vis} = \sigma\varepsilon \tag{4.3b}$$

With this the equation can be rewritten:

$$L = \frac{\langle\mu\rangle\, f_{rev}}{\sigma} = \frac{\mu_{vis} f_{rev}}{\sigma\varepsilon} = \frac{\mu_{vis} f_{rev}}{\sigma_{vis}}. \tag{4.4}$$

The quantity μ_{vis} is now directly measurable and the only unknown is the visible cross-section. It should be stressed, that it depends on the efficiency which in turns depends on

the event selection algorithm. Therefore σ_{vis} which is the only luminosity calibration constant, is dependent both on the detector and the event selection algorithm.

All sub-detectors providing luminosity information follow this measurement scheme, but they all need to be calibrated. In the beginning the raw estimate was done with a Monte Carlo method [AL10]. Full ATLAS simulation was performed that verified the measurement principle and estimated the calibration constants with $\sim 20\%$ systematic uncertainty. This value is dominated by the modeling of diffractive components of the cross-section. To increase accuracy the van der Meer scan method was used to calibrate detectors. In total 6 scans were performed, the first one in April, followed by two in May, and three in October 2010 at different energies. The last three scans were performed in May 2011 at LHC energy $\sqrt{s} = 7\,\mathrm{TeV}$. This method was also used to calibrate the BCM and will be discussed in detail in later chapters as one of the subjects of this thesis. Systematic uncertainties of a few per cent are achievable with this method. The precision will hopefully increase especially in the future when new techniques become available. Studies are underway for determining the luminosity from well calculable electroweak processes, where NNLO calculation exists e.g. W or Z production [LZ11]. Additionally, the ALFA detector [AF08] will provide ATLAS with additional independent calibration method, by measuring the elastic pp scattering under small angles (in the Coulomb-Nuclear Interference region) and employing the optical theorem. However for the time being the vdM method is used as the calibration method of choice.

4.3 Luminosity detectors

In principle many detectors are capable of luminosity measurements, most of them at least with event counting methods. Many of these detectors can even provide multiple event selection criteria – from here on called luminosity algorithms. ATLAS uses available information diversity to its benefit. It includes many systems in its luminosity monitoring scheme and it stores all their measurements. With large number of independent measurements, affected by different systematic effects, ATLAS has a strong handle on assessment of its measurement precision. The detectors themselves are based on different physics principles, have different acceptances, and can provide different algorithms. Detectors that did, or still actively contribute to ATLAS luminosity measurement are listed in table 4.1.

The luminosity aspects of BCM will be described to great detail in the following chapters. Here a short description of other contributors follows:

Minimum Bias Trigger Scintillators or MBTS is built from 32 scintillator paddles. They are equally split between A and C side of the detector. They cover $2.09 < |\eta| < 3.84$ pseudorapidity range in two units, and each of these is segmented into eight parts, together covering the full azimuthal angle ϕ. Scintillator light is guided through wavelength-shifting optical fibers to photomultipliers (PMTs). After shaping and amplification, the signals enter leading-edge discriminators. Their outputs are directly used as trigger bits connected to the CTP and the position of the PMT signal is recorded to the offline data stream with $\sim 3\,\mathrm{ns}$ resolution. The trigger bits are counted by CTP before L1 decision is made, so the counts are not affected by prescale or dead-time. These

Detector	η coverage	no. of readout channels
BCM	$\eta = 4.2$	2×4
LAr	$2.5 < \|\eta\| < 4.9$	35632
LUCID	$5.6 < \|\eta\| < 6.0$	32
MBTS	$2.1 < \|\eta\| < 3.8$	32
ZDC	$\|\eta\| > 8.3$	16

Table 4.1: *Summary of basic characteristics of luminosity detectors that contribute to ATLAS measurements. The number of channels of BCM is written as 2×4 since eight BCM modules are split for the purpose of luminosity measurements into two groups of four, providing two independent luminosity measurements.*

are trigger before prescale (TBP) counters and their value is periodically reported to online database, enabling the MBTS online luminosity measurement. Along with these counters, also the trigger after prescale, and trigger after veto (TAV) counters are recorded. The latter corresponds to the number of accepted events. This gives the possibility of offline analysis. Here the benefit is the timing information on basis of which the background estimation can be done. MBTS was designed for initial ATLAS running at low luminosities ($< 10^{33}\,\mathrm{cm}^{-2}\mathrm{s}^{-1}$), so it was designed to have large efficiency, gaining a lot of statistics which was its huge asset. At present the delivered luminosity at P1 is large enough to saturate the MBTS triggers, thus reducing its value as a luminosity monitor.

LAr electromagnetic calorimeters were briefly described in the previous section. Their tubes are arranged in parallel with beam pipe and filled with liquid argon. Each such tube has a central rod that functions as high voltage electrode that collects the ionization electrons. To maintain a stable electric field a current is being injected to compensate for the ionization created by measured particles. The current injected is correlated to the particle flux which is in turn proportional to the interaction rate. Since all interactions are measured without any filtering, with measuring the current one has a handle on luminosity. In total FCal has 128 high separately monitored voltage lines. The drawback is the calibration. The vdM method is not applicable, since during vdM scan the intensities are much lower that in during normal LHC running and mostly below the FCal minimum sensitivity. Additionally a sufficient precision of current measurement can not be performed with frequency of more than $0.2\,\mathrm{Hz}$, which is too low for $30\,\mathrm{s}$ intervals used in vdM scan. To that end the FCal measurements must be calibrated to another absolute measurement. Additional studies can be done like with MBTS. Its recorded timing information can be used to calculate the time difference between sufficient energy deposits on both A and C side within same event. This timing distributions typically have peaks centered at $\Delta t = 0$ that correspond to pp collisions with smaller peaks with significantly different measured Δt due to different backgrounds. The contribution of these extra peaks is a good measure of the background contribution to luminosity.

Zero Degree Calorimeter or ZDC [ZC08] was primarily designed to monitor the neutral

particle multiplicity at low angles ($|\eta| > 8.3$). Its four modules are designed with tungsten absorber plates and quartz strips for Cherenkov light production. The light signals are read by PMTs and 14-bit ADC conversion evaluates the energy deposition and its position. It measures the neutral particle flow (neutrons and photons) that is proportional to luminosity. It is shown that measured energy is not significantly affected by the charged particle contribution, neither by secondary neutrals.

LUCID abbreviates LUminosity measurement using a Cherenkov Integrating Detector. It has been specifically designed for ATLAS luminosity measurement. It has two detector stations, one on each side, $17\,\mathrm{m}$ from the interaction point, covering $5.6 < |\eta| < 6.0$ region. Both stations are comprised from 16 tubes filled with C_4F_{10} gas. Tubes are pointed towards the interaction point to maximize the particle path within the active volume, thus yielding biggest photon production. The inside tube wall is polished to provide better reflection of Cherenkov light, that is measured with the photomultiplier. Typical photon production is in range 60-70 while another 40 photoelectrons are added by the quartz window. Amplified signals from PMTs are fed to discriminators, to charge-to-digital converters, and to flash analog-to-digital converters. If the discriminator threshold is exceeded the tube has registered a hit. The hit information from all 32 tubes comprises the input to the custom-build back-end electronics where multiple luminosity algorithms are implemented. It is called LUMAT card and integrates LUCID detector into ATLAS framework. It monitors the number of LHC orbits and is synchronous to LHC $40\,\mathrm{MHz}$ clock, enabling LUCID to provide per-bunch information like BCM. It publishes the luminosity information to the ATLAS online framework and also issues trigger signals, enabling LUCID information to be stored in the offline data stream. On luminosity field, LUCID and BCM are rather similar detectors regarding algorithms, data processing functionalities, and ATLAS interfaces. Most significant differences of LUCID compared to BCM are its intrinsic nonlinearity due to PMT gain dependence on photo current, no sub-BCID time resolution, and its signal formation effect called 'migration effect'. At higher luminosities, a significant portion of the light signal is due to secondary particles that contribute differently due to highly anisotropic detector geometry. This particles tranverse the tube mostly almost perpendicularly, having smaller yield of Cherenkov light, however their high multiplicity creates a signal above the threshold. This causes the measured signal to have two different components with different luminosity dependence thus making the measurement non-linear. While the effect is systematic, it is very challenging to model it precisely.

4.4 Luminosity data infrastructure

Along with the BCM, the four detectors described above are the biggest contributors to the luminosity measurement effort. As mentioned, they provide event counting measurements for different algorithms that are marked in table 4.4. The exact definitions for BCM will follow, but generally speaking AND algorithms require coincidence of A-side and C-side hits, OR-A

demands at least one hit on A-side with no condition on C-side, while XOR-A demands A-side hits with nothing detected on C-side. Vice versa for C-side algorithms.

Detector	AND	OR	OR-A	OR-C	XOR-A	XOR-C
BCM	✓	✓			✓	✓
LAr		✓				
LUCID	✓	✓	✓	✓		
MBTS	✓	✓				
ZDC	✓		✓	✓		

Table 4.2: *Different algorithms implemented in the luminosity detectors. For LAr only OR is marked since its measurement is based on current monitoring (effectively OR) and no logic is implemented on the detector level. One should also be aware that when detectors synchronize the readout of all the algorithms, there is no conceptual difference between single sided OR and XOR algorithms if AND algorithm is measured as well. Symbolically: XOR-A = OR-A - AND.*

Data based on all these algorithm/detector combinations must be processed in a coherent way enabling later offline analysis to use the recorded luminosity information. To achieve this, the measured luminosity is stored in the ATLAS conditions database along with all the relevant ATLAS data quality information. The time interval in which the luminosity and data-quality information is assumed to be constant is called *Luminosity Block* (LB). All the ATLAS recorded data is stamped with the Run Number (RN) and the Lumiosity Block Number (LBN). This allows physicists doing the offline analysis to use the conditions data base and select only the portion of data matching their requirements. Once this data is analyzed it can be correlated with the luminosity information that was recorded for analyzed LBs. Length of luminosity blocks is not fixed, however it is usually in the order of minute. The responsibility of declaring new LBs and recording the corresponding timestamps was placed to the CTP. It is a central structure for data acquisition and possesses majority of information required to make this decision. For instance, change in its trigger prescales should initiate a new LB, since these numbers are used to recalculate delivered luminosity to recorded luminosity, including the dead-time and prescales.

The LB information is exchanged over the Information Service[1] (IS) [IS97]. The same service is used as data infrastructure for gathering all 16 independent luminosity measurements from all sub-detectors. It is published at different frequencies and in different formats. In general two criteria are used to distinguish the data: integration time and data granularity. When integration time is kept to its minimum one refers to the data as *instantaneous data*. This data is published by all sub-detectors approximately once per second. The other option is that sub-detectors accumulate different algorithm counts over the entire LB and they publish the *luminosity block average* for the LB that just ended. Most of the sub-detectors are able to provide this. The second criteria is data granularity. Here the distinction is made between luminosity data publications that publish the sum of counts over all BCIDs in LHC ring – *BCID*

[1]This software enables online systems to exchange informations over IS servers, where provider publishes an information that is distributed to all subscribers.

blind publications – and publications holding the entire vector of counts, one for each BCID – *per BCID publications*. At the moment only LUCID and BCM are able to provide *per BCID* informations for their luminosity algorithms. It should be mentioned that *per BCID* information implies being LB averaged in the ATLAS readout scheme, though BCM is capable of providing instantaneous per BCID counts for all of its algorithms.

4.4.1 Online luminosity calculator and data processing

All the luminosity information is monitored by the Online Luminosity Calculator (OLC) [O+11] with frequency of 1 Hz. OLC is a C++ based application, integrated in the ATLAS online environment. It is highly configurable through OKS [OK98], which is a tool for storing class specifications and their instances in XML format. In addition to luminosity sub-detectors it receives information also from CTP, Beam-Pickups (BPTX) via IS, and also from LHCs beam instrumentation via the Data Interchange Protocol[2]. Figure 4.2 shows a schematic view of OLC and its connections to other systems.

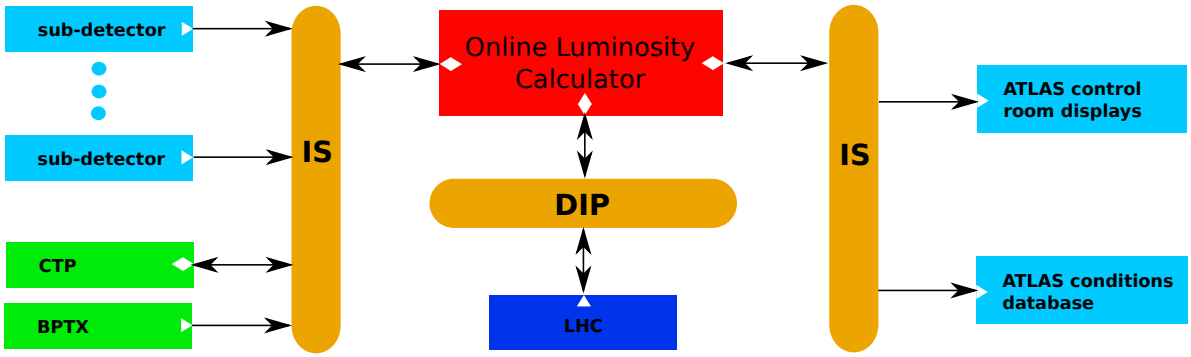

Figure 4.2: *Online luminosity monitoring data infrastructure.*

The LB boundaries published by CTP allow OLC to recalculate the LB average values from instantaneous data. On one hand this enables additional crosscheck with values published by sub-detectors, or publication of these data for sub-detectors that don't provide LB averages. If no per BCID information is available, μ_{vis} for a specific algorithm can be extracted from LB average counts. The integration time (LB duration) is known and the number of colliding bunches is extracted from BPTX bunch intensities published on IS. From these two quantities the number of bunch crossings is known, which, if combined with total number of event counts, gives μ_{vis}. In contrast to this recipe, background contribution can be avoided if per BCID information is published by sub-detector. In this case the LB length information (also published by sub-detectors along with the algorithm data) suffice and μ_{vis} can be calculated for each of the relevant BCIDs separately. After μ_{vis} is calculated OLC applies calibration. Calibration constants defined in OKS help transfering μ_{vis} into LB averaged luminosity.

[2]Simple data transfer system where publishing and subscribing is possible, similar to IS. It is used at LHC and connected experiments.

As the final stage of OLC, the calculated luminosities are distributed. Instantaneous values are published with frequency of $1\,\mathrm{Hz}$, while LB measurements are published in the beginning of the following LB. The primary recipient is of course the ATLAS conditions database. All algorithms from all detectors are stored, enabling later offline crosschecks. Additionally all the OLC published values are displayed by the slow detector control and monitoring system in the ATLAS control room. Several luminosity values are reported via DIP to the LHC for collision optimization purposes. From all luminosity measurements one algorithm of one detector is chosen as the preferred one, and that value is also reported on LHC Page 1 website [LHC1]. From May 2011 on, the BCM OR algorithm was chosen as the ATLAS preferred luminosity measurement.

Chapter 5

Beam conditions monitor

In the first year of operation the LHC reached proton energy of $3.5\,\mathrm{TeV}$ in both beams. During this time also the number of protons increased for few orders of magnitude. Starting with a single bunch populated with approx. 10^9 protons, the fast progress led up to 348 proton bunches, each populated with approx. $1.1 \cdot 10^{11}$ protons by the end of year 2010. Together this yields to roughly $115\,\mathrm{MJ}$ of energy in each beam. This represents the energy frontier of man made particle accelerators, yet this is not the end. Eventually LHC will reach both, the designed number of bunches, and its design energy of $7\,\mathrm{TeV}$ per proton. Given the enormous energies, potential losses of the beam around the interaction point where detectors are located could be dangerous. The lost particles would eventually create showers of secondary particles, delivering huge instant ionization. This could be especially dangerous in the ATLAS Inner Detector. For protection the experiments have chosen to develop their own safety systems, in parallel to one provided by the LHC. In ATLAS, this role has been challenged by the BCM [B+08]. An explanation of all its safety services and its interaction with both LHC and ATLAS will be given in the following subsections.

As will also be detailed, BCM has few unique characteristics, usually not found in such safety systems. The most significant two are its speed, which enables to distinguish individual proton bunches, and its extended dynamic range, allowing single MIP sensitivity while not saturating within the designed range of LHC operation. Along with its positioning and suitable acceptance, these properties are exploited and BCM was also expanded with the functionality of luminosity monitoring. While not its primary goal, it has proven to be a valuable contribution to the ATLAS luminosity measurement effort.

5.1 Basic principle, structure and environment

Since it is primarily a safety system, the BCM has been designed for optimal distinction of background particles from collision induced ones. The main difference between these two contributions is their point of origin. The collisions are produced only at the interaction point (IP) - at the center of the detector. On the other hand, the background has more contributions. Many background sources like beam halo and possible secondary showers created during beam accidents, are very distinct, since they originate outside ATLAS and are topologically different

from collisions. Perhaps the most difficult to spot is the beam gas background since it can also originate from the IP region. This occurs when the accelerated particles collide with the residual gas in the beam pipe.

To make the interactions–background distinction, the BCM uses time-of-flight (TOF) measurements. The two detector stations are placed symmetrically on both sides of the IP, very close to the beam. The positioning, along with the basic principle is sketched in figure 5.1. In case of collisions, final products reach both the detector stations at the same time, t_{BCM} after the collision. The hits registered are called *in-time* hits, and their time difference between the two detector stations equals zero. On the other hand, for the background produced outside ATLAS, the *out-of-time* hits are registered at the incoming side at $-t_{BCM}$ (prior to the collisions), and *in-time* hits at t_{BCM} on the outgoing side of ATLAS. The time difference in this case equals $2t_{BCM}$. The proton bunches collide at maximum every $25\,\mathrm{ns}$, so in order to make best distinction of the background, its time difference must be in between two consecutive collision-induced time differences, so $2t_{BCM} = 12.5\,\mathrm{ns}$. Given the close to light speed of particles, this yields $\sim 1.8\,\mathrm{m}$ as an optimum distance of BCM stations from the IP.

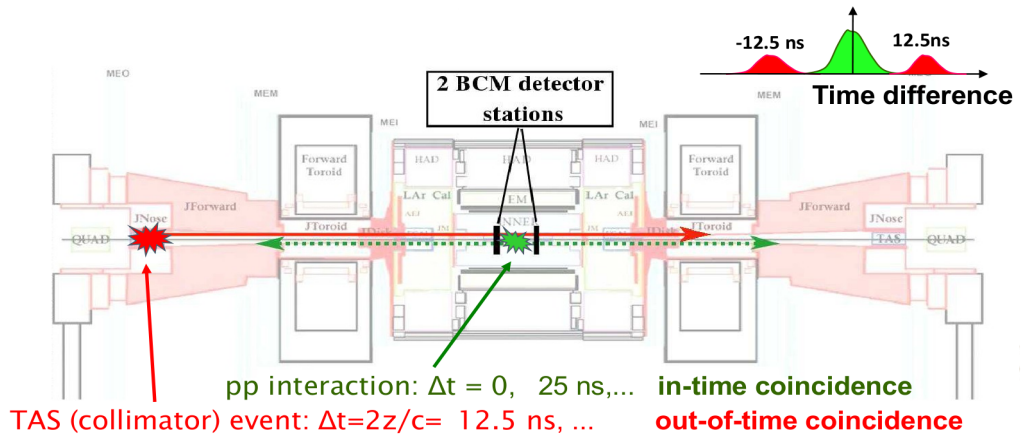

Figure 5.1: *BCM position inside ATLAS and its principle of operation. The red markings indicate the background event which induces signals with detection time difference of* $\pm 12.5\,\mathrm{ns}$ *between the two stations. The green depicts the collision induced signals whose detection time difference equals zero. This indicated, that given sufficient time resolution the time difference between the two stations could be used to distinguish the background from the physics induced signals.*

Each detector station consists of four modules. They are placed around the beam pipe at +x, -x, +y, and -y directions, with their sensors at $z_{BCM} = 184\,\mathrm{cm}$, and at $55\,\mathrm{mm}$ radius. The modules are tilted at 45 with respect to the beam pipe and mounted on the beam pipe support structure along with the Pixel detector (see figure 5.2). This structure also provides the support for the power and signal cables.

The identification of background particles, not only enables BCM to function as a background monitor, but also as a safety system. Multiple beam accidents were considered during development. The two most representative are a case of mis-steered pilot bunch at

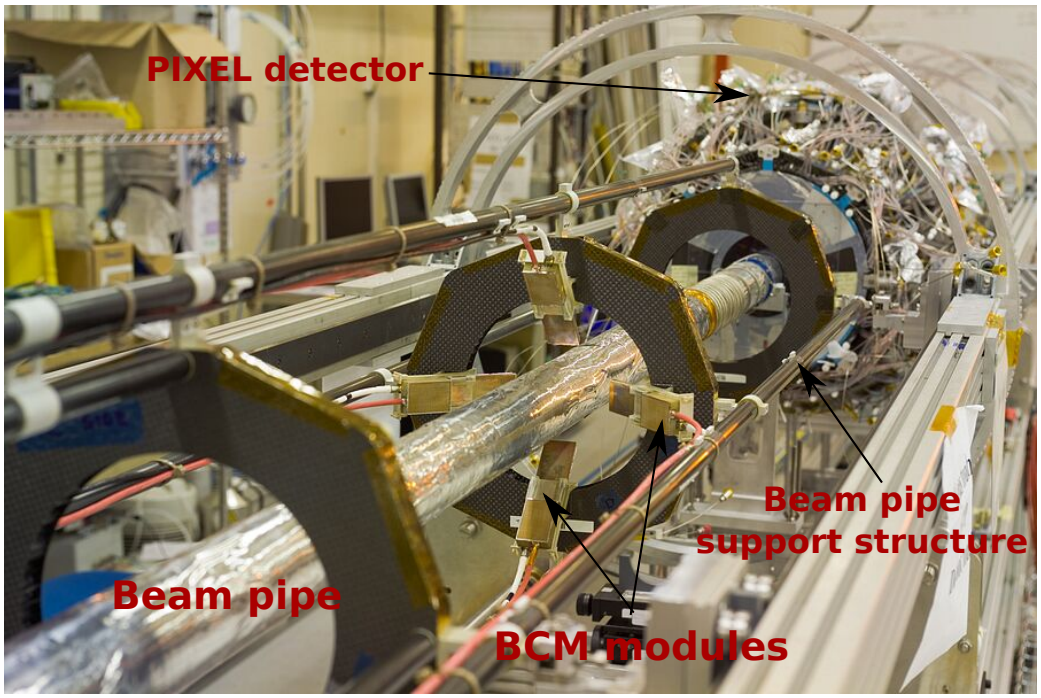

Figure 5.2: *Four BCM modules mounted on the beam pipe support structure along with the Pixel detector.*

$450\,\mathrm{GeV}$ that hits the TAS[1] collimator or the beam pipe, and $7\,\mathrm{TeV}$ protons scraping the TAS collimator. The simulation for pilot bunch estimates an average of 0.06 out-of-time hits in the BCM per proton hitting the TAS, while in the case of $7\,\mathrm{TeV}$ proton this number rises to 1.15 hits per proton. For the pilot bunch beam-pipe scenario simulation predicts 0.14 hits per proton. These numbers indicate, that a significant signal is to be expected with even relatively small beam losses in case of beam failures.

A more sensitive issue is the role of luminosity monitoring. At collision of $7\,\mathrm{TeV}$ protons around 0.37 hits are expected. For this it is required that BCM is sensitive to single Minimum Ionizing Particles (MIPs), and must retain this characteristic throughout ATLAS lifetime. It is positioned in a harsh radiation environment and it is expected that it will have to sustain fluence of approx. 10^{15} particles per cm^2, and receive a total ionization dose of roughly $0.5\,\mathrm{MGy}$ in the expected 10 years of LHC operation. Additionally a fast signal is needed for TOF measurements, so short signals with base-line restoration below $10\,\mathrm{ns}$ are needed.

[1]Target Absorber Secondaries collimators (TAS) are installed at $z = \pm 18\,\mathrm{m}$ for protection of Inner Triplet quadruples against secondaries produced in pp collisions.

5.2 Sensors

Utmost care was dedicated to the heart of the detector - the sensors. In general, silicon is an attractive sensor material, because of good resolution, fast signals and ease of availability. However they are mostly challenged by radiation tolerance. To avoid this pCVD diamond was chosen for its better signal to noise ratio performance after irradiation.

The pCVD diamond sensor material was developed by CERN RD42 collaboration [RD42] in collaboration with Element Six Ltd [E6]. Diamonds are square ($10\,\mathrm{mm} \times 10\,\mathrm{mm}$) surface and $0.5\,\mathrm{mm}$ thick. Cutting produced the edges under a small angle, so viewing from the side the diamonds are of a trapezoidal shape, which enables identification of both sides. Metalization was done by Ohio State University, where $8\,\mathrm{mm} \times 8\,\mathrm{mm}$ radiation hard Ti-Pt-Au contacts were made.

This material was chosen for its radiation hardness. They were tested with fluences up to $1.8 \times 10^{16} p/\mathrm{cm}^2$ after which the signal degraded only by 15% [AD03]. The larger band gap trades off the amount of charge created during MIP passage through the material (factor ~ 2 smaller than in silicon) for lower noise than in silicon. The signals, though smaller, can be fast. For this the relevant quantities are trapping time and drift velocity. To optimize the speed, the sensors are operated at $\pm 1000\,\mathrm{V}$, implying $2\,\mathrm{V}/\mu\mathrm{m}$, thus very close to saturation velocity of $\sim 10^7\,\mathrm{cm/s}$. Under such conditions typical signals have FWHM of $2\,\mathrm{ns}$. The third excellent characteristic is the low leakage current, which has a typical value of $100\,\mathrm{pA}$ at $1000\,\mathrm{V}$ bias voltage. Such a low current brings the power dissipation to extremely low level, allowing the detectors to be operated at room temperature, and eliminating the need for cooling services.

A sample of 20 diamonds was used and complete I-V measurements were performed, characterizing individual sample quality and prefered bias voltage polarity. Complete quality assessment measurements can be found in [ID08]. The best 16 diamonds were chosen and mounted in the installed modules, while the rest were used to build spares.

5.3 Detector modules

Modules are mounted in the innermost part of the ATLAS detector and are therefore extremely hard to access. With this in mind, they were designed in a simple way using highly reliable components to achieve robustness.

To increase the signal, two diamonds are used within one module. They are placed one on top of the other, with their surfaces in parallel. The top diamond is displaced in a way that the line connecting the centers of the diamonds forms 45 angle with the normal to the diamond plane. With this one maximizes the overlap for the collision products due to the 45 tilt of the modules. This tilt reduces the acceptance, however lengthens the most probable particle path in the diamonds, thus increasing the signal for a further factor of $\sqrt{2}$.

Between the diamonds, two Al_2O_3 ceramic pieces are inserted. These spacers have $Au - Pt$ traces to effectively connect the inner two surfaces of this "double-decker" assembly sketched in figure 5.3. The double-decker is then mounted on a ceramic baseboard with metal traces, for wire connections. The whole assembly was done using temperature and radiation resistive

glue. The metal traces on the baseboard connect the inner two planes of the double-decker to ground and this is used as the signal line. The bottom diamond plane is connected via metalized through-hole and the top plane of the upper diamond uses wire bonds to connect to metal traces on the baseboard. Both are connected to the same bias voltage of $\pm 1000\,\mathrm{V}$. This parallel connection is used to sum the signals from both diamonds onto the signal line. This way the ionizing particle, passing through the BCM module diamond, induces a signal with twice the amplitude. The double-decker also increases the noise, however the signal to noise ratio is better than in case of a single diamond.

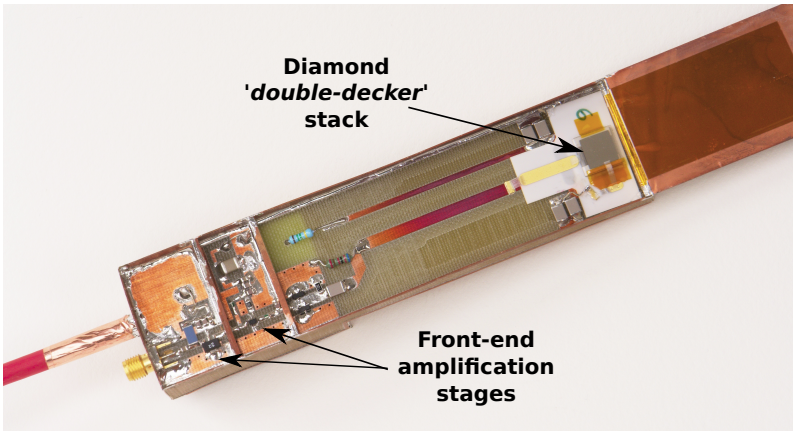

Figure 5.3: *BCM module assembly, showing the two-diamond configuration and the front-end electronic components.*

The diamond ground line is used as signal, and is wired to the $5\,\mathrm{cm}$ long transmission line with 50Ω impedance that transfers the current signal to the front-end electronics that was designed by Fotec [FOT]. The current amplification is done in two stages. For the first stage the $500\,\mathrm{MHz}$ Agilent MGA-62563 GaAs MMIC low noise amplifier is used, while the second stage utilizes Mini Circuit Gali-52 In-Ga-P HBT broadband microwave amplifier. The noise factor is determined by the first stage and has a value of $0.9\,\mathrm{dB}$, while each of the two stages provide $\sim 20\,\mathrm{dB}$ amplification. The amplification stages are AC coupled and diodes protect their inputs from discharges. Additionally each module is equipped with a temperature sensor.

The module housing is built from $0.4\,\mathrm{mm}$ thick G10 plates with single sided copper layer of $35\,\mu\mathrm{m}$. The exception are the base plates hosting the electronics, the diamond holder ceramic platform, and the plates isolating the amplification compartments. These are $1.4\,\mathrm{mm}$ thick. Five of the modules are labeled F40X and three are labeled F42X. The latter differ by the connector wall that is $1.4\,\mathrm{mm}$ thick instead of $0.4\,\mathrm{mm}$ as in the modules.

For operation the modules need supply of $3\,\mathrm{V}$ and $11\,\mathrm{V}$ which is provided by the modified version of SCT detector power supplies [SP01]. The high voltage is provided by floating ISEG units [ISE], which were modified to allow $1\,\mathrm{nA}$ current monitoring resolution. Both supplies reside in the ATLAS USA15 service cavern and share same multi-core cable to connect to modules.

5.4 Digitization and Readout

The modules output signal line is connected to high quality coaxial cable. It is routed $2\,\mathrm{m}$ within the Pixel detector and the next $12\,\mathrm{m}$ stretch leads the signal to PP2 in the toroids, where the digitization electronics is installed.

Before the actual digitization a fourth order high-pass filter is used. The beam tests proved that it improves the signal to noise ratio. Cut-off frequency of $200\,\mathrm{MHz}$ was chosen as an optimal setting. With it, the most probable amplitude is decreased by 35%, but the noise decreases by almost 50%, resulting in the increase of signal-to-noise ratio (SNR) by a factor ~ 1.3. The offline analysis of the signal waveforms recorded during these tests also showed, that a first order filter with cut-off frequency of $200 - 400\,\mathrm{MHz}$ improves the SNR.

The filtered signal is used and digitized with NINO circuits [A04]. NINO chips were originally produced for ALICE RPC TOF measurement. They are produced in $0.25\,\mu\mathrm{m}$ IBM technology that is also radiation tolerant, making them suitable for PP2, where $\sim 10\,\mathrm{Gy}$ of dose is expected in 10 years. Each chip has eight channels. Their digitized output has $\sim 1\,\mathrm{ns}$ rise time with jitter of $\sim 25\,\mathrm{ps}$, thus making NINO the proper choice for BCM. Each channel has the function of amplifier and a discriminator used to deliver a TOT signal. Thus the NINO generates a digital output signal whose width is correlated to the amplitude of the input signal. The relationship is not linear, which makes particle counting a challenge. However, as will be described later, the BCM relies on the hit counting method for all its functionalities, and the energy deposition measurement is used only as an add-on.

In spite having eight channels only two are used with each NINO chip to minimize crosstalk and improve robustness of the system. Both are used for the signal from the same module. A simple resistive splitter is used that splits the signal in two, with their amplitudes sought to be in a ratio of approximately $1:10$. Due to the cross-talk within the chip, the actual ratio was closer to $1:5$. During technical stop at the end of 2010 this ratio was changed to $1:200$ to further expand the dynamic range. Each of these two signals is now fed in a separate NINO and treaded as independent from there on. The smaller signal line is named *high threshold channel*, while the bigger signal reaches the threshold sooner, thus it is named *low threshold channel*. The purpose of this splitting is to expand the dynamic range. Before the hardware change, at the point where the low threshold channel started to saturate, the signal on high threshold channel became measurable. This is a useful feature. The low threshold channels have MIP sensitivity and can therefore contribute to the luminosity measurement, while the high threshold channels produce signals only above the collision induced multiplicities and can therefore be used as a LHC malfunctioning condition signature.

Digitized LVDS signals produced by NINO are used to control radiation hard laser diodes, which send the information over $75\,\mathrm{m}$ optical fibers to USA15 cavern. Once they reach it, the light signals are converted back into electrical PECL signals with the use of photo diodes (Lightron LP3A4-SNC1) on an optical receiver board. The resulting 16 channels are then divided among two processing units. Both modules receive half of high gain and half of low gain channels, both of half of the A and C side modules; the basic idea being the redundancy in case one of the modules would mis-function. In such a case this mapping allows to keep both the expanded dynamic range and possibility for A-C coincidence information, though much of

statistics is lost. The detailed mapping is given in table 5.1.

Module no.	Position	Detector side	Threshold	Channel ID	processing module
0	+X	A	high	0	FPGA1
			low	8	FPGA2
1	+Y		high	1	
			low	9	FPGA1
2	-X		high	2	
			low	10	FPGA2
3	-Y		high	3	
			low	11	FPGA1
4	+X	C	high	4	
			low	12	FPGA2
5	+Y		high	5	
			low	13	FPGA1
6	-X		high	6	
			low	14	FPGA2
7	-Y		high	7	
			low	15	FPGA1

Table 5.1: *Mapping of modules, there positions, and BCM processing modules for both high and low threshold channels.*

5.5 Data processing

Both Data Processing Units (DPUs) are identical in hardware and have the same firmware functionality. They are based on Xilinx ML410 development boards, each hosting Xilinx Vitrex-4 FPGA [XV4] (Field Programmable Gate Array), external 256 MB of DDR2[2] RAM, Ethernet PHY, basic clock sources, etc.

The ML410 boards are connected to a custom made *personality module*, that connects the module to the rest of ATLAS. It serves also as a back-up digital differential $160\,\mathrm{MHz}$ clock source. It uses a PLL that switches between the external clock source (used whenever available) and the on-board oscillator in case the external clock is not provided by ATLAS. Both sources are $40\,\mathrm{MH}z$ and PLL multiplies then by a factor of four. ATLAS provides a reference clock via Local Trigger Processor modules, and the clock is stable only in its configured state. This means that in the absence of ATLAS run, BCM is a standalone system, fully functioning, but not synchronized with other detectors or the LHC. The personality module additionally interfaces the input data from the optical receiver to the FPGA. Its functional schematics is shown in figure 5.4. It enables masking of individual channels and XOR decoding, needed for proper

[2]DDR2 is acronym for Double Data Rate memory type. The '2' on the end indicates its enhanced performance with respect to DDR, since it latches the data on both rising and falling edges of the bus clock signal.

functioning of the sampling circuit. Finally, the personality module is a connection adapter for the rest of signals, except the Ethernet connection, which is hosted by the ML410 board directly.

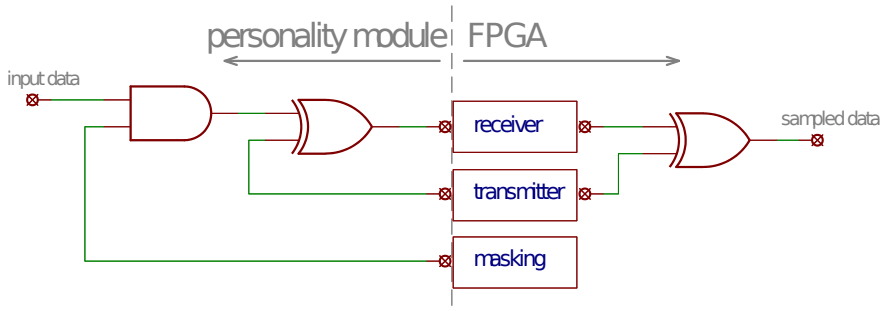

Figure 5.4: *Signal encoding and masking on the personality module and lather decoding within the FPGA to retrieve the original signal. This scheme is necessary for proper functionality of the receiver block in the figure, since it needs regular 0 to 1 toggle.*

The core of the data processing module is the Virtex-4 XC4VFX60-11FFG1152 FPGA [XV4]. It samples the data for 8 channels, passed by NINO, and extracts TOT information. It categorises hits as in-time or out-of-time, does rate counting, monitores the rates and publishes information to different ATLAS data streams. With FPGA as its brain, the BCM provides several services to both ATLAS and LHC. A short list follows, where only basic interfaces are given, while more detail on the internal structure and functionality is left for subsequent subsections:

LHC Beam/Injection Interlock System (BIS) serves as a safety system, protecting the collider and experiments from undesired conditions. BCM is designed to monitor the ATLAS Inner detector conditions, and if unacceptable levels of radiation are reached, the BCM can communicate this to ATLAS CIBU system via two signals, which further propagate to BIS [BI10]. One of these signals (`IP`) can prohibit injection of proton bunches into LHC and the other (`BP`) can dump the already circulating beam.

Post-mortem diagnostics is a key to understanding the conditions that lead to a beam abort. BCM offers the history of its sampled data of approximately 1000 LHC revolutions prior and 100 revolution after the beam abort has been issued.

ATLAS Detector Safety System is a hardware interlock system, offering ATLAS detector components a possibility to react to unwanted situations and protect their hardware. Each BCM data processing module provides two signals, one with severity of warning and one of an error.

ATLAS Detector Control System (DCS) is a detector slow control system that resides in the software world. A dedicated PC is integrated into DCS. Along with receiving the status information and different measured rates from BCM data processing units, it controls power supplies, NINO electronics boards, and monitors the module temperatures.

Though significantly slower than DSS it provides valuable control since it enables more sophisticated decision making and greater flexibility.

Central Trigger Processor is the first and main ATLAS data recording filter. It receives 6 bits (up to 9 bits could be provided) of Level1 trigger information from BCM.

ATLAS Trigger & Data Acquisition is the main ATLAS data stream, dedicated for later physics analysis. This system also accepts a data fragment from BCM (digitized data) and incorporates it into the event if passed by all levels of trigger system. Two arrival times and two time-over-threshold measurements can be recorded in each bunch-crossing for each channel.

Luminosity readout is a separate data stream. Data collected in BCM data processing modules is transfered to a PC application that further processes it and transmits it to a dedicated calibration stream and to the ATLAS online system for collecting data from different luminosity monitors.

All the functionalities mentioned above are implemented in a FPGA fabric using a VHDL language and Xilinx ISE 12.2 tools. The firmware functionality and some important details will be discussed in the following subsections. They all refer to firmware release 3.3.1[3] that was used during the data taking period where data for luminosity analysis presented in this thesis was recorded. The firmware block diagram for this release is shown in figure 5.5.

[3]By accident a second tag 3.3.2 was created for the same version – there is no difference between the two.

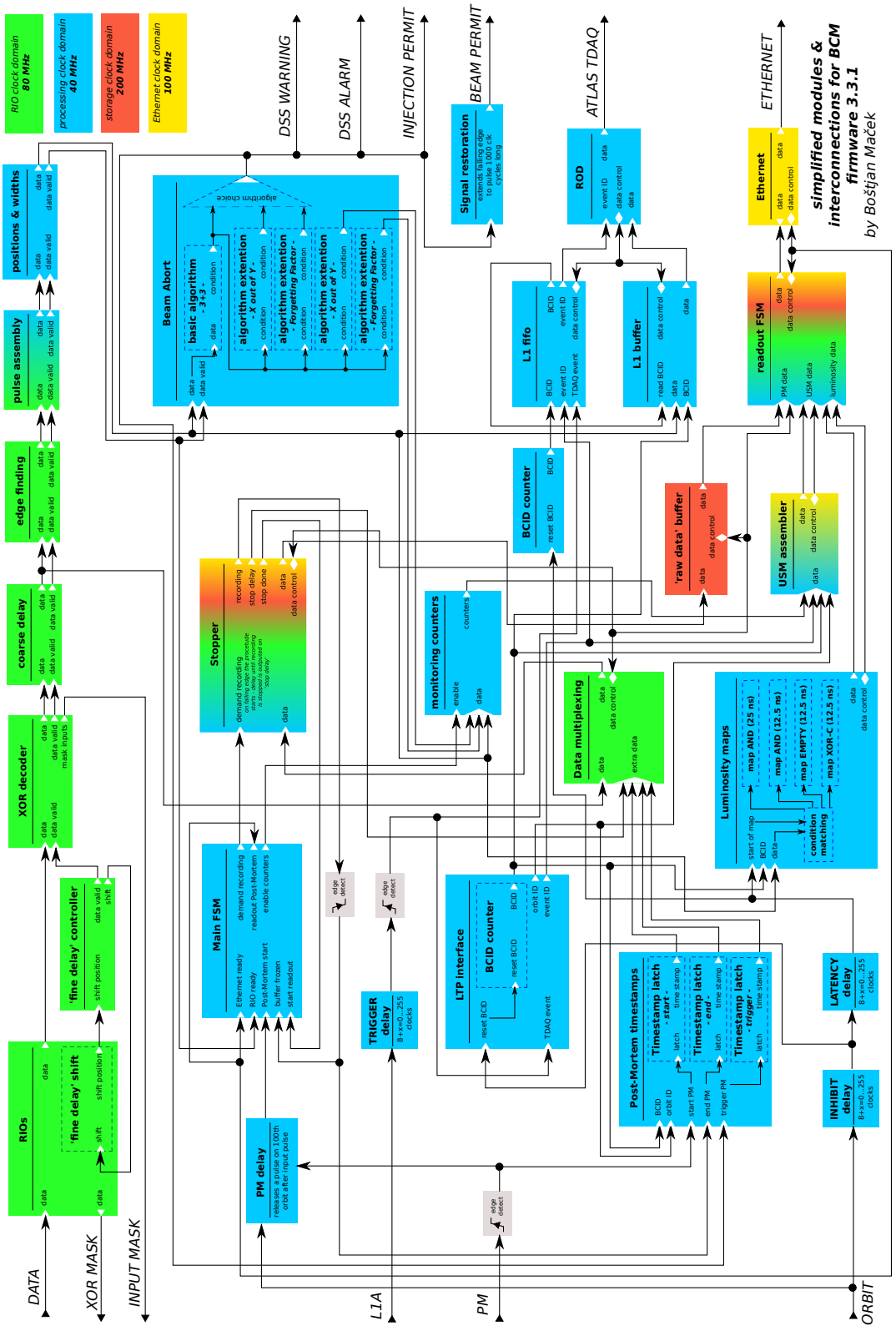

Figure 5.5: *Block diagram for firmware release 3.3.1. Colors label different clock domains as indicated in top right corner of the figure.*

5.5.1 Clocking scheme

The basic thing in any synchronous digital circuity is the clock that drives it. As a rather complex system, BCM firmware uses four major clock regions.

The first two clocks are used for data processing and are derived from the input $160\,\mathrm{MHz}$ clock generated in the personality module. This source is used directly to supply the reference clock for the dedicated sampling circuit. In parallel it is also routed as an input to the Digital Clock Manager (DCM). This device is designed for low jitter output. In this case its output is connected to Phase Matched Clock Divider[4] (PMCD), which is another of silicon hard-coded devices dedicated to clocking. It divides the input clock by powers of two and all the outputs are guaranteed to be phase matched with extremely low skew. Divisions of 2 and 4 are used to generate clocks for the $80\,\mathrm{MHz}$ and $40\,\mathrm{MHz}$ clock regions. They are used for all online data processing, since they are synchronous to the ATLAS clock, and thus to the beam. Here one additional thing must be noted. From the external $40\,\mathrm{MHz}$ coming as input to the personality module, there one generates $160\,\mathrm{MHz}$ which is then divided back to $40\,\mathrm{MHz}$ inside the FPGA. Due to this intermediate stage one could lose the phase shift with the original clock. To ensure that this does not happen, during reset an additional signal is used. Rising edge of the `ORBIT` signal indicates, that the LHC started a new revolution - defines a reference point. This provides an input that is guaranteed to be synchronous with the reference clock. Its rising edge is therefore used to release/start the clock division by PMCD, thus keeping the first tick of the clock in phase with the external clock.

The second input clock is hosted by the ML410 board. It is a $100\,\mathrm{MHz}$ clock that is multiplied to $200\,\mathrm{MHz}$ with the second DCM used inside the FPGA. The slower of these two is used for monitoring circuits and for Ethernet communication, while the $200\,\mathrm{MHz}$ clock region covers data storage in DDR2 module.

All of these clocks, produced by either DCM or PMCD, are than distributed through dedicated global clock lines. These further distribute signals to regional clock networks which spread throughout the FPGA fabric, to ensure the lowest possible skew.

5.5.2 Data sampling and preparation

Data gateway inside the FPGA is the Virtex-4 Multi-Gigabit Transceiver named RocketIO. The chip contains 16 of these, but only 8 are available for data sampling on ML410 board. These circuites are dedicated to serial data transmission at GHz rates, but are not specialized for any protocols. Instead, they are composed from many different modules that can be used or not. The configuration of RocketIOs can be done at compile time, as a part of the firmware or even on-the-fly. Thus these are highly configurable blocks, being able to adapt to both many standardized data transmission protocols as well as to users custom protocol.

In the BCM firmware their main functionality is to sample the input signals, to later interpret their rise times and widths as physics quantities used for different measurements. The signals

[4] As the DCM, the PMCD is a dedicated timing circuit implemented on the chip. Both are extra circuits within FPGA reducing the need of external components for clock management. The implementation varies with the FPGA family and concrete specifications can be found in [XIL].

are expected at most every few tens of nanosecond with a few nanosecond width, however there is no low limit for the rate. Such signals are not adequate for RocketIOs that favor some typical telecommunication concepts. One of these is the concept of digital clock retrieval from the data itself. Each RocketIO channel has a receiver and a transmitter part. Transmitter outputs data on a basis of the reference clock. This is $160\,\mathrm{MHz}$ in BCM case, and is internally multiplied to $2.56\,\mathrm{GHz}$. However, the receiver must stay in-sync with the incoming data. Therefore there is an internal PLL that locks its frequency to the data transition frequency of the incoming data. This clock is then used to sample the data. This of course works well only if there are enough $0 \rightarrow 1$ and $1 \rightarrow 0$ transitions, which is not the case with the native BCM signals coming from the NINO. To remedy this the signals are XOR-ed externally (figure 5.4) and the repeated encoding pattern 1100 is supplied by the transmitting part of the RocketIOs. This introduces sufficient data transitions for the receiving PLL to lock.

Once sampled at $2.56\,\mathrm{GHz}$ frequency, the data enters a barrel-shifter module. It is the only extra RIO functionality that is not bypassed. Here data can be delayed by a maximum of 32 samples. BCM uses this functionality to adjust the relative delays between the channels. The origin of these delays can be different data path length in any of the data processing stages up to the FPGA. These delays can be set individually for each channel and can range from 0 to 31 samples, meaning 0 to 12.5 nanoseconds. These settings are called *fine delays*.

The fine delay basically sets a $t = 0$ reference point. From there onward the sampled data is deserialized and outputted from RocketIO as 32 bit word at $80\,\mathrm{MHz}$. To reconstruct the original data, as it was send by NINO, one more XOR with the exact same pattern is needed. To ensure the correct pattern is used regardless of phase at which the PLL locks special initialization procedure must be followed. It starts with using the mask signal in figure 5.4. During initialization this signal is set to logical false, effectively masking any input. The data sampled by the RocketIOs is therefore exactly the encoding pattern and the pattern for decoding is shifted bit by bit, until the decoded data does not equal zero. Only then the initialization is done, the mask removed to allow the sampling of the real data and the data validity flag is raised. Only the later enables all data processing functionalities within the FPGA.

Additionally, one more functionality must be mentioned. After the XOR decoding, the *coarse delays* are implemented. The goal is the same as with fine delays, only here the unit for the delay is one sampled word, meaning $12.5\,\mathrm{ns}$. Coarse delays can in principle have values[5] 0, and from 7 to 31. Setting the coarse delay to 0 will effectively disable the module, remove its data validity flag and thus stop all FPGA processing. With the combination of both delays one can therefore adjust timing of individual channels over few bunch-crossing intervals in $390\,\mathrm{ps}$ steps.

5.5.3 Raw and processed data

Data at this stage is named *raw data*. It enables unmodified NINO signal reconstruction and is very valuable for diagnostics. For this purpose it is stored in a ring buffer that can be read out at any time. More on this in the next subsection, but in parallel with this, the raw data is further

[5] Values 1 to 6 will not guarantee correct behavior of the delay module.

processed. On each of the 32 bit sample a mask is first applied. It effectively suppresses single spike samples like `'00100'` or `'11011'`. The NINO is not able to produce such short signals and therefore they must have pure noise origin. After this, three rising and three falling edges are searched for and their values encoded in a binary form. Following the data path the next thing is pulse assembly. Here the data crosses to $40\,\mathrm{MHz}$ clock domain, and two consecutive 32 bit samples representing two halfs of the same bunch interval are merged. From combination of rising and falling edge position of both halfs two signals can be reconstructed in each bunch interval. They are described with RIO sample number of rise time (named *pulse position*) and the length of signal in units of RIO samples (named *pulse width*). Pulse position ranges from 0 to 63 (6 bits) and pulse width ranges from 0 to 31 (5 bits). In total 22 bits of information are produced for each channel along with four validity bits, one for each of the values. This data is named *processed data* and is used for monitoring and other BCM services.

A bit of special attention must be devoted to the pulse width encoding. The encoding is straightforward: value 4 is representing a pulse of four samples length ($\approx 1.56\,\mathrm{ns}$). The value 0 is not used, and the only exception is value 1. The previously mentioned mask filters out such signals so the value is used as overflow - for pulses extending over two half-bunch-crossing interval borders. Thus all pulses longer than $12.5\,\mathrm{ns}$ are assigned value of 1.

5.5.4 Safety system functionality

Once the data validity flag is set, the BCM functionality as a safety system becomes operational. The same *beam-abort module* is used to serve the LHC Beam/Injection Interlock System and ATLAS Detector Control System. The decisions are based on processed data. All the pulses with widths of 2 and 3 samples are ignored since the physics part of the pulse width spectra starts at 4. Below noise dominates. The remaining pulses are counted within each bunch-crossing interval. If 3 or more out of 4 low threshold channels and 3 or more out of 4 high threshold channels registered a hit within the same bunch-crossing interval, the *basic condition* has been met. This condition is checked every bunch-crossing interval and was used as the final beam-abort condition during the early running of the LHC. However with increasing luminosity the rates increased, giving greater probability for this condition to be met even when beam conditions were not critical. To add robustness and to suppress possible false aborts two extension algorithms were added:

X out of Y algorithm counts the number of times the basic algorithm has been satisfied within the last Y bunch-crossing intervals. If the count exceeds the threshold value X, the condition is met. Both X and Y are implemented as $16\,\mathrm{bit}$ numbers, giving the possibility of a little more than $1.6\,\mathrm{ms}$ time span for decision making. Even with smaller, around one LHC revolution long time windows one can already become immune to single event scenarios and remain highly sensitive to misbehaving bunches.

Forgetting factor algorithm is the second implemented option for reducing the BCM beam-abort sensitivity. Here the expression

$$V_i = F\,V_{i-1} + C\,R \tag{5.1}$$

is evaluated for each bunch-crossing interval. V_i is the running value of the algorithm on i-th bunch-crossing interval. R represents the current value of basic condition and has a value 0 when condition is not met and value of 1 when it is. C and F are parameters defining the influence of single event upset and the data forgetting rate. Every satisfied basic condition therefore increases the algorithm value which is then slowly decreasing if there are no indication for bad beam conditions. This algorithm is a bit harder to quantify because it does not only depend on the rate at which basic condition is met, but also on the time distribution of such occurrences. However when V_i exceeds the threshold the algorithm condition is met. It should also be noted, that all the values are implemented as $8\,\mathrm{bit}$ numbers. This somehow limits the possible values, especially F which can be viewed as a number between 0 and 1 with granularity of 0.0039.

In the FPGA there are five algorithm signals. One is supplied by the basic condition algorithm and the two extension algorithms are doubled, with all the parameters being settable completely independently.

All five outputs are separately counted and reported to the DCS infrastructure once per second for monitoring. It should be stressed that all of these extensions give a pulse whenever the condition is met, in a same way that the basic condition does. These pulses can therefore last for more than one bunch-crossing interval. E.g. the basic condition is met in more consecutive bunch-crossing intervals or even more likely the X out of Y condition is met for a longer time period. In such cases, for monitoring purposes, their output signals are trimmed to a single clock cycle - thus a continuously met abort condition will yield only one short pulse and a consequent increase of 1 for the counter.

Two of the extension algorithms have only monitoring functionality, while the basic algorithm, one X out of Y and one Forgetting factor algorithm outputs are combined to produce the final beam-abort signal. Here signals are not trimmed! The desired combination can be configured and the possibilities are listed in table 5.2. The entire module can be also disabled.

Name	Logic	Binary conf. code
Basic abort	basic condition	`001`
FF abort	forgetting factor condition	`010`
X/Y abort	X out of Y condition	`011`
AND abort	forgetting factor and X out of Y condition	`100`
OR abort	forgetting factor or X out of Y condition	`101`
Abort disabled	the functionality is disabled	`000`, `110`, or `111`

Table 5.2: *Combining options for the final beam-abort signal. In the rightmost column the configuration string in binary form is given for reference.*

Once different sources are combined into the beam-abort signal this is distributed among outputs connected to LHC Beam/Injection Interlock System and ATLAS Detector Control System. For the Detector Control System both `DSS warming` and `DSS alarm` signals have the same functionality. The signals are raised and latched by the beam-abort signal and manual

acknowledge by a shifter is needed to remove this signals. Both of these signals are connected to the ATLAS DSS infrastructure for both DPUs separately.

The 'Injection permit' signal has the same logic as DSS signals and the same acknowledgement procedure is needed, the only difference being that the signal is defined with inverted logic (is removed on beam-abort condition). The forth, the `Beam permit` signal is also dropped when undesired conditions arise, but it is automatically restored after 1000 bunch crossing interval i.e. $25\,\mu$s. Both of these signals from both DPUs are then combined. To drop the final `Injection permit` signal, either of the DPUs can drop its injection permit, while to drop the `Beam permit` signal, a coincidence of both DPUs beam permit drops is needed. Combined with the timeout, this means, that both halfs of BCM must have had independently registered dangerous beam conditions before a beam-abort would be requested.

5.5.5 Post-Mortem functionality

Once the `Beam permit` has been dropped by any of the enabled LHC safety systems, the beam is to be ejected after three turns. To properly identify the cause of the beam-abort the LHC distributes the `Post-mortem` signal, calling all the sub-detectors capable of diagnostics to contribute their information.

BCM is one of these diagnostic systems. It uses raw data, which are stored in the external $256\,\mathrm{MByte}$ DDR2. This memory functions as a cyclic buffer, being constantly overwritten. Once the request for diagnostics is received, the writing stops and the data is read out to a PC where it is analyzed.

The merged input from all eight channels is $256\,\mathrm{bit}$ word at $80\,\mathrm{MHz}$ and it crosses the border to DDR2 clock domain of $200\,\mathrm{MHz}$ frequency in a dual port RAM. This acts like a FIFO with unsymmetric in/out data bus width. Data from this FIFO is rewritten to DDR2 at $128\,\mathrm{bit}$ per clock cycle, but in a 7+1 burst mode. Each burst consists of four write cycles and there are seven consecutive bursts followed by one pause burst. During this and additional pauses DDR2 has time for internal operations like data refresh. Because of these scheme a care must be taken that at least 28 addresses[6] are filled in the FIFO before the whole block can be written to DDR2.

This is an important requirement during the stop procedure: the recording can be stopped only every 21 bunch-crossing intervals. The `Post-mortem` signal sent by LHC is the initiator of this sequence. Once its rising edge is registered the dedicated delay circuit counts the number of `ORBIT` signals. On 100th `ORBIT` signal after the `Post-mortem` signal the writing sequencer is signaled that the writing should stop. Sequencer waits for multiple of 21st bunch-crossing interval and only then stops recording.

This *stop delay* is random, but measured. Besides the stop delay, orbit counter and BCID are registered (together named time-stamp from here on):

PM start time-stamp is registered on the detection of `Post-mortem` signal.

PM end time-stamp is registered once the data recording stopped.

[6] $7\,(\mathrm{bursts}) \times 4\,(\mathrm{write}\quad \mathrm{opperatios}) = 28\,(\mathrm{addresses})$.

PM trigger time-stamp is registered when BCM dropped `Beam permit` signal. If this happened multiple times, the last time-stamp is remembered, and if this has not happened at all this value equals zero.

All of these timestamps must be communicated to the offline analysis to be able to time-align all the info from both DPUs and from different detectors. Additional info that could be useful and must be recorded is:

- status bit indicating whether or not BCM triggered beam-abort,
- status bit indicating whether beam-abort functionality was enabled or not,
- three bit value indicating the beam-abort algorithm used (see table 5.2 for reference),
- configuration parameters of X out of Y algorithm,
- configuration parameters of Forgetting factor algorithm,
- FirmwareID[7] indicating the firmware version and FPGA that produced the info.

To easily incorporate this data in the readout scheme, the RAM input bus, fed from RocketIOs is multiplexed with this *extra info*. While normally the RocketIO data is the source, during the last three bunch-crossing intervals of the stop sequence the multiplexer is switched to extra info.

To ease the reading the RAM is trimmed to exactly 16777152 addresses which is a common multiple of data write burst length and the readout units length described later. In this way, once the writing has stopped, the reading can resume at the next address, meaning the oldest data is read first, the data alignment remains intact and the last address read corresponds exactly to the last address written. To achieve such a symmetry the above stopping requirement of 21 bunch-crossing intervals was needed.

Read operations are also performed in bursts but here the RAM is not the bandwidth bottleneck and the burst structure can be 1+1: one read burst, one pause burst. Here the data crosses from $200\,\mathrm{MHz}$ to $100\,\mathrm{MHz}$ clock region of PC communication. The translation is again done with FIFO. Once this FIFO has at least $192\,\mathrm{bytes}$ of data, this chunk is encapsulated in the IP/UDP package and send over the Ethernet to the PC, where the data is analyzed and recorded on disk. Each package must be acknowledged by the PCs reading application before the next one is sent. This protocol with limitation of $100\,\mathrm{Mbit}$ Ethernet link defines the bottleneck of the readout, which takes approx. $210\,\mathrm{s}$. Though time consuming, the acknowledge protocol assures that all 1398099 packages are transfered in a well defined sequence summarized in table 5.3.

Additionally the custom protocol defines five packages. Once recording ended and the RAM is ready to be read out FPGA sends a *'ready' package*. After acknowledgement, one can wait an arbitrary amount of time to start the read-out. Once desired, the read-out can be initiated by sending a *'trigger' package* to the FPGA. When this package is received, the FPGA sends

[7] FirmwareID is a eight character hexadecimal string uniquely identifying the firmware. First character indicates whether this is FPGA1 (0x0 for release or 0x2 for debug version) or FPGA2 (0x1 for release or 0x3 for debug version) code. The next three characters denote the version, and the final four match the final four characters of MAC address of the destination ML410 board.

Package number	Data
1	raw data - time interval 1
2	raw data - time interval 2
3	raw data - time interval 3
...	...
1398094	raw data - time interval 1398094
1398095	*extra info*
1398096	raw data - time interval 0
1398097	raw data - time interval 1
1398098	raw data - time interval 2
1398099	raw data - time interval 3

Table 5.3: *Post-mortem data packages sequence. Time ordering of the data is indicated, and the only exception is the* $1398095th$ *package containing extra info. Since the memory is organized in a cyclic manner, three packages are read for a second time at the end, to allow additional check on data-integrity.*

a *'start' package*, then the *'data' packages*, and when the read-out is finished the *'read-over' package* is send. After this package is acknowledged the FPGA returns into the recording mode, again waiting for the `Post-mortem` signal.

On the receiving end, the above described protocol is handled by a program on a single-board-computer VME module. This process is running in the background and once it receives the 'ready' package it acknowledges it, notes the time stamp, and starts polling the data out of DPU. It does this in parallel and completely independently for both DPUs. Once it receives the entire data it writes it without any processing to the backup files. In addition it performs pulse reconstruction, identical to one within FPGAs, and does hit analysis. Once the entire data has been transfered, time alignment can be done and the program finally transmits the analysis results to the LHC. The most important information sent are:

- post-mortem time-stamp,
- BCM abort time-stamp if applicable,
- histograms of number of high/low threshold hits in each module, both versus time (integrated over $40\,\mu$s) and versus bunch number,
- histograms of number of total high/low threshold hits, both versus time (integrated over $40\,\mu$s) and versus bunch number,
- histograms of number of A/C-side high/low threshold hits, both versus time (integrated over $40\,\mu$s) and versus bunch number,
- abort status of the active abort, both versus time (integrated over $40\,\mu$s) and versus bunch number.

It also produces a ROOT [RT] file, containing all the above information along with:

- abort status of all abort algorithms,
- all above histograms done using only hits around $+6\,\mathrm{ns}$, only around $-6\,\mathrm{ns}$, and only at neither of those,
- all histograms over the last 150 LHC turns versus time with only $5\,\mu\mathrm{s}$ integration,
- pulse position and width statistics.

This ROOT file is also published to ATLAS IS online histogramming server, for the shifters to check.

A sample of BCM diagnostic functionality is shown in figure 5.6, where the information produced by the post-mortem analysis is shown for both low and high threshold channels, along with a 3 bunch-crossing interval long detailed plot of raw data. From the later one can observe the signal time difference between side C and A. It is a distinctive background timing signature, indicating an increasing single sided spray of background particles intruding ATLAS.

5.5.6 TDAQ functionality

To help filter out the interesting data that should eventually be recorded, BCM provides trigger bits to CTP. Nine trigger bits are outputted from each data processing unit. With the small solid angle coverage and at high pseudorapidity it is useful as a minimum bias and background trigger. The trigger logic is based on processed data and the functional description for all 9 bits is given in table 5.4.

Both data processing units output 9 bits, and these must be combined before they are passed to CTP. This trigger merging is done in a V1495 CAEN board, a general purpose VME board hosting two FPGAs (one controls the VME side, and the other is dedicated to the user input). In case of trigger bits 1, 2, and 3 a logical OR of the corresponding bits from the two data processing units is performed. The trigger bits 4 to 6 are combined into three final bits named `BCM_MULTI`. They are the sum of the two 2-bit inputs `BCM_Combined` from both processing units. The two `BCM_Att` signals are OR-ed. The logical true result of this OR forces all the bits in `BCM_MULTI` to true, regardless of the `BCM_Combined` input signals. Thus the six BCM signals provided to CTP are: `L1_BCM_AtoC`, `L1_BCM_CtoA`, `L1_BCM_Wide`, and `L1_BCM_MULTI` (3 signals).

In addition to providing triggers, the data processing units also have a functionality of a Read-Out Driver (ROD). Processed data: rising edges (6 bits) and widths (5 bits) of both pulses, are stored in *L1 buffer* along with the corresponding BCIDs. Having 8 channels in one data processing unit gives 192 bits per bunch crossing interval, including four bit padding. L1 buffer is again a circular one, holding information for the last LHC turn. In parallel, *L1 FIFO* is being filled with BCIDs marked with L1A signal provided by the CTP. For each of these BCIDs, data for 31 BCs is read from L1 buffer: 17 BCs prior the L1A marked BC, marked BC, and

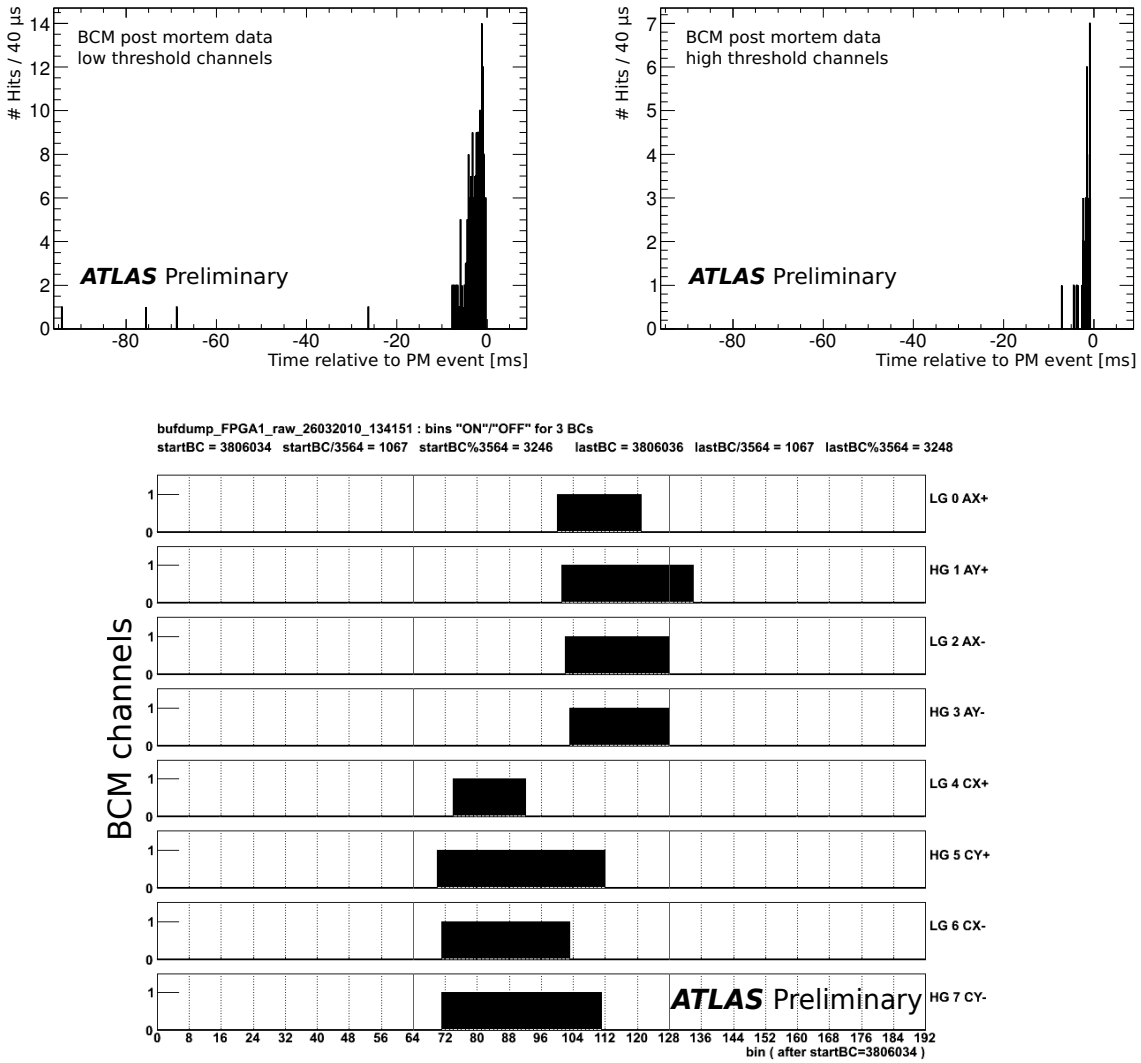

Figure 5.6: *Part of the BCM diagnostic data form BCM-triggered beam-abort on 26.3.2010. Number of hits registered in both data processing modules in low threshold channels (upper-left) and high threshold channels (upper right) is shown. A three bunch-crossing interval long section of raw data from FPGA1 is shown on a bottom plot. The horizontal axis represents the sequential RocketIO sample number. Clear background signature is visible with C modules registering hits* $\sim 12.5\,\mathrm{ns}$ *prior to A side.*

13 BCs after[8]. Along with the appropriate header indicating data version, data source, and Level-1 ID, a ROD fragment is formed. This is send to HOLA S-LINK card mounted on the personality module. It sends the data over the Read-Out Link to Read-Out Subsystem (ROS), which provides this information to the Level-2 trigger. If accepted by level-2 and HLT, this data

[8]The current 17-1-13 structure can be changed. The latency delay and the Trigger delay settings (described in the next subsection) effectively implement pre-trigger. The current value 17 can be changed, effectively moving the triggered BC to anywhere within 31 BC window.

Bit no.:	Name:	Description:
1	BCM_AtoC	At least one out-of-time hit on A side and at least one in-time hit on C side is needed to issue this trigger bit.
2	BCM_CtoA	At least one out-of-time hit on C side and at least one in-time hit on A side is needed to issue this trigger bit.
3	BCM_Wide	A-C coincidence of hits within wide time window. The borders of this interval are set independently from those for in-time and out-of-time windows. The interval is intended to be wider for a more loose trigger.
4	BCM_Combined	Two bit number of low threshold channels that detected a hit in given bunch crossing interval. The binary number `'11'` represents 3 or more hit channels.
5		
6	BCM_Att	For this trigger to fire, a high threshold hit must be detected in any of the four channels.
7	BCM_AtoC	Same as trigger bit 1.
8	BCM_AttA	For this trigger to fire, a high threshold hit must be detected in A side channels.
9	BCM_AttC	For this trigger to fire, a high threshold hit must be detected in C side channels.

Table 5.4: *Description of 9 trigger bits outputted from data processing unit. The trigger bits are determined each bunch crossing interval on the basis of processed data. The time windows for in-time and out-of-time windows can be adjusted at configuration time.*

is incorporated in final event recording, enabling an BCM aware offline analysis of ATLAS data.

5.5.7 Timing, synchronization, and operation within ATLAS

To have proper ROD functionality time synchronization with ATLAS is needed. The data processing clock is supplied by ATLAS so systems are phased matched, but their signals must also correspond to the same bunch-crossing interval. These are identified with the BCIDs and the first one $\mathrm{BCID} = 1$ is marked by rising the edge of the `ORBIT` signal. To allow all sub-detectors to be synchronized in ATLAS, the CTP provides this signal a fixed time prior to the actual bunch-crossing interval. This way any sub-detector specific delay from CTP to the sub-detector itself can be extended by a dedicated delay circuit. By individually setting the delays the sub-detectors achieve synchronization. BCM has three such delay circuits as can be seen in figure 5.5. There are two BCID counters within the BCM firmware. The first one defines the BCID for the in-chip data processing. This time stamp is used for post-mortem, luminosity, and

data recording functionality. The second BCID time stamp is used for time-marking the L1A signal and must therefore be smaller than the first one. The relative delay between ATLAS and both BCID counters is set by *'inhibit delay' setting*, while the relative difference between the two BCID values is controlled with the *'latency delay' setting*. Additionally there is a a *'trigger delay' setting*, that delays the L1A signal. All of these delays can range between 0 and 255 clock cycles in steps of 1.

Once synchronized with ATLAS, BCM can provide event fragments for data recording. To fully rely on its protective and luminosity monitoring services the input signal timing is of essence. The key is to be synchronous with the colliding bunches to be able to interpret the TOF information correctly.

To achieve this more steps were needed. First the relative *delay constants* needed to be measured. These are the relative delays between the bunch collision and and the start of the bunch-crossing interval as sampled by the RocketIOs. As already mentioned this varies between the individual channels due to different signal path lengths. For this, the signal rise time was histogramed during proton-proton collisions and the position of its peak was calculated. This yielded relative delays constants between the channels which are constant.

Additionally the RocketIO's receiving clock PLL locks at random phase in respect to the externally supplied bunch clock. To remedy this, an additional timing procedure must be carried out after each reset or reboot of the firmware. To properly align the signals after reset, BCM must start standalone TDAQ data recording. With it, it configures a pulser in a way, that it transmits a short pulse, synchronous to the bunch clock, every second LHC turn. This signal is split over all 16 BCM channels and or-ed with the signals from the optical receiver board. Once data recording is started, the pulse rise time is histogramed once again. The peaks of these histograms, now appearing at random positions, can be moved to the desired place with properly adjusting fine and coarse delays. One must of course take into account also the delay constants. With this all the proton-proton collision induced signals are guaranteed to appear in the data in the same desired time-position for all channels.

5.5.8 Slow monitoring and detector control

To monitor and control the BCM system as a whole, with status overview of its many functionalities, the system is incorporated into ATLAS Detector Control System (DCS) [DCS]. DCS is build on top of the PVSS framework (Prozessvisualisierungs- und Steuerungs-System) [PV], and it is designed to be a modular and extensible service, providing common interface to all subsystems. Though this data-acquisition branch is the slowest one, it provides a powerful controlling tool. All monitored quantities (e.g. counting rates, status signals) are stored in a database, allowing history to be taken into account in more complex algorithms that finally control the detector. Both monitoring and control, from BCM's point of view, are described in the next paragraphs.

To provide information to DCS, firmware collects the data being monitored, in a module called the Universal Status Message (USM) assembler. Data is provided from almost all firmware modules, thus residing within different clock domain regions. Here all the data is latched once per second and used within $100\,\mathrm{MHz}$ clocking domain. After this, the USM is

constructed. The most relevant information therein:

- **RocketIO parameters** that are monitored for each individual channel are: fine delay, coarse delay, mask status, PLL and ready status signals of both receiver and transmitter part of RocketIO.
- **Hit counts** for all eight channels report the number of reconstructed hits in the processed data.
- **Coincidence counts** help monitor collisions as well as background:
  - *A-C coincidences* require hits in A and in C side modules, with the TOF information within the 'in-time' window,
  - *background A* counter, counts BCs, where a hit in one of the A side modules has TOF information within the 'out-of-time' window, and there is a hit in C side modules with TOF information within the 'in-time' window,
  - *background C* counter, counts BCs, where a hit in one of the C side modules has TOF information within the 'out-of-time' window, and there is a hit in A side modules with TOF information within the 'in-time' window.

  both time windows can be dynamically set and *in-time* and *out-of-time intervals* are also reported as a part of conditions monitoring.
- **Beam abort parameters** that are included:
  - *window and threshold* for both X/Y algorithm extensions,
  - *factor, influence, and threshold* for both Forgetting factor algorithm extensions,
  - *algorithm choice*,
  - *counters* of beam-abort occurrences, for the basic algorithm and all four algorithm extensions implemented in FPGA.
- **Injection and beam permit** status signals, along with the mask status and mask value.
- **DSS warning and DSS abort** status signals, along with the mask status and mask value.
- **ROD status** signals:
  - *L1-buffer, L1-FIFO* state,
  - *HOLA S-Link card* status,
  - *ROD constants* like SourceID, Run number, ROD data version, Extended Event ID.
- **L1-trigger counts** for BCM internal triggers. Nine of these correspond to the triggers propagated to the CTP, while two are purely internal.
  - *wide-time-window* borders for the 'wide-coincidence' trigger,

  - *trigger mask* and its status.

- **Signal delay settings** that are reported are: inhibit delay, trigger delay, and latency delay.
- **General data processing unit status** values:
  - *clock status* indicating the state of the DCMs,
  - *FirmwareID*,
  - *current Orbit counter and BCID*,
  - *error code*, identifying the mis-functioning firmware block.
- **Main FSM state,** indicating the current step in the initialization procedure or operation. The description of all possible states, transition order and conditions are described in table 5.5. This state helps determine the readiness of the detector.

There is a bit more information in USM than it is used in DCS. Some of this data is also needed for slow TDAQ monitoring (much of it actually overlaps). To that end, USM contains union of information needed and the same message is send either to DCS PC or TDAQ PC. With such an approach a great deal of FPGA resources were saved. There is a subtle difference. From TDAQ side, this package must be requested and USM is sent as reply. USM also contains a package serial number, which is not increased if the TDAQ is the recipient. On the other hand DCS receives this packages on a regular basis, with frequency of around $1\,\mathrm{Hz}$ and no request is needed. If DCS is the recipient, the package serial number is incremented each time the package is sent.

The reason for enumerating the packages hides in the treatment of the counting values being reported. Mostly they are implemented as 32 bit counters (beam-abort counters have only 8 bits) that are monotonically increasing and eventually overflowing. No reset is implemented, and their initial value after reboot has no physical meaning. To calculate the hit/event rate useful for monitoring, the DCS must therefore look at the difference between consecutive status messages and potentially correct for overflow. With such approach, and enumerated packages, even with a missed status message, a meaningful result is produced by the next one, since a time average over two readings can still be recovered. All of this is implemented in a custom library installed in DCS. The status messages are send in the form of IP/UDP packages over the Ethernet, and are received and interpreted by this library. This then publishes the resulting values to the PVSS archives, making them available to entire ATLAS.

One of the recipients of the BCM monitored values is also ATLAS FSM, where the status and the operation state of ATLAS is determined on the basis of the sub-detector states. For instance, after the beam-abort all detectors connected to BIS must restore the injection permit in order for the LHC to be able to re-inject the beam. Additional manual intervention of the shift leader is needed, he relies on the status reported by the BCM. Before injection, BCM should be fully operational. It reports 'not ready' during readout of the post-mortem buffers. During this time, the DCS reported value of BCM's FSM states other than 6 vetoes the software injection permit that is implemented in DCS. The beam-abort functionality is still fully functional during this time, but if the abort would happen, BCM would not be able to provide diagnostics. DCS

State 7: *reset*	
Description:	During boot-up of the firmware, this is the initial state. Later, both hardware (DPU front-panel button) and PC induced signal (Ethernet interface) force the FPGA in this state.
End condition:	All DCMs must indicate, that the clock distribution is stable and the reset signal must be removed.
Next state:	State 3: waitEthernet

State 3: *waitEthernet*	
Description:	Ethernet module, capable of sending/receiving IP/UDP packages must properly initialize. In process, it sends 5 Address Resolution Protocol (ARP) packages. With it it announces its MAC and IP addresses to all devices on the local network, enabling them to properly address it. After this Ethernet communication is ready.
End condition:	Ethernet module must end its initialization.
Next state:	State 2: idle

State 2: *idle*	
Description:	Pause in the firmware of the initialization, allowing the components to catch up.
End condition:	2000 clock cycles passed
Next state:	State 1: waitRIO

State 1: *waitRIO*	
Description:	Once the clocks are stable and the reset signal disappears the RocketIOs begin their initialization procedure. This state allows the internal PLLs to lock and XOR decoding pattern to be aligned.
End condition:	All eight RocketIOs end their initialization, and start sampling.
Next state:	State 6: capture

State 6: *capturing*	
Description:	This state indicates the BCM's basic functionality: safety system is operational. In this state, the raw sampled data is written to the circular buffer. If not explicitly disabled, the beam-abort functionality is active.
End condition:	Post-mortem signal.
Next state:	State 14: waitEndSampling

State 14: *waitEndSampling*	
Description:	After the `post-mortem` signal, there conditions described in subsection 5.5.5 must be met to stop the sampling at proper time. During this stop procedure the firmware is in this state.
End condition:	Sampling stopped.
Next state:	State 12: waitReadOut

State 12: *waitReadOut*	
Description:	At the beginning of this state a status message is sent to the PC, indicating that the post-mortem buffer is ready to be read-out. If not acknowledged, the message is resent every 4 seconds.
End condition:	PC triggering the post-mortem buffer readout.
Next state:	State 5: readOut

State 5: *readOut*	
Description:	In this state, the post-mortem buffer is transfered to the PC via Ethernet connection.
End condition:	PC sending read-over signal.
Next state:	State 6: capture

Table 5.5: *States of the main FSM. A short description is given, along with the condition for the FSM to proceed to the next state.*

additionally includes the state of the other parts of BCM (i.e. power supplies, ...) and average noise level into the decision algorithm for the software injection permit.

To be fully functional, the detector must also adapt to the environment and dynamically change its working parameters. Many parameters have been mentioned so far in previous subsections, and most of the parameters included in USM can be set. This is done via an IP/UDP protocol. The integrated Etherenet module not only transmits the data, but also receives them. The data protocol understood by firmware is outlined in table 5.6. With the *data type* field the choice of the parameters being set is done. The corresponding *data* must be appropriately formatted.

Byte no.:	0		1		2		3		4		5		7		...
Nibble :	H	L	H	L	H	L	H	L	H	L	H	L	H	L	...
Field :	length				package number				data type				data		...

Table 5.6: *Data format understood by the firmware. The number of* data *bytes is written in the* length *field. The* package number *can for now be arbitrary, but the* data type *defines which parameters are being set.*

This communication is used usually during ATLAS configuration, if BCM is included in the procedure. During ATLAS startup, at configuration step, the configuration constants are read from OKS database and with the above mentioned protocol communicated to the BCM firmware. With these parameters set, the BCM is fully configured and integrated ATLAS sub-detector. Additionally some of the commands can also be sent from ATLAS FSM, the main being the fine and coarse delay settings, that are determined during time-calibration procedure. The rest are simple command, like disabling the DSS, beam-abort functionality and a reset of the firmware.

In parallel with a reset, which is implemented in firmware, the final thing to mention is also the possibility of a reboot. With this, the FPGA's firmware is wiped clean, and reloaded from scratch. This function can be carried out from ATLAS FSM. It triggers the PVSS data point change, that initiates a callback within a process running on the BCM DCS computer. This process then runs a Xilinx Impact tool, that reloads the firmware to the FPGA via the USB cable.

5.6 Luminosity monitoring

Low threshold channels have single MIP sensitivity and large efficiency, making them suited for physics measurements. The solid angle coverage is extremely small and that can sometimes be of use especially when monitoring the luminosity. Because of all this and its timing capabilities, the BCM contributes an independent luminosity measurement to the ATLAS detector. It is also located in the middle pseudorapidity region ($\eta \sim 4.2$) complementing the coverage of liquid argon calorimeter at low and LUCID at high pseudorapidities.

Having two data processing units, BCM provides two luminosity measurements. The channel mapping as seen in table 5.1, mixes low threshold channels of half of modules, with high threshold channels of the second half of modules. The situation for the second data processing unit is high/low threshold reversed. The unit that is connected to the low threshold channels of horizontal modules ($\pm x$) provides what will be called *BCM-Horizontal luminosity measurement*. The second unit is connect to low thr. channels of vertical modules ($\pm y$) and the measurement is named *BCM-Vertical luminosity measurement*. It should be stressed that also high threshold channels are used in the measurement that will be presented, thus coupling the two measurements.

5.6.1 Luminosity algorithms

In order to provide a robust and reliable luminosity monitoring, the event counting approach has been chosen. Particle counting has its advantages, especially the extended linearity up to higher luminosities, however the systematic uncertainty induced at digitization stage would contribute significantly to the measurement error. In contrast, in hit counting methods the amount of charge collected in the diamond is not the main player, as long as it exceeds a given preset threshold. With sufficient SNR for MIPs this threshold can be set appropriately, allowing both high efficiency and low noise rate. An average noise rate during 2010 for a single low threshold channel was in the order of $10\,\mathrm{Hz}$. Comparing to bunch collision rates that are at least in the order of $10\,\mathrm{kHz}$[9], it is clear that low noise measurements can be obtained.

While hit counting eliminates significant portion of the error, further simplifications can still be made. Instead of counting the number of registered hits, BCM luminosity monitoring employs simple event counting. In general a condition is chosen for an event to satisfy, and if it does, the corresponding counter is increased. The outcome of each event can thus be either 0 or 1. This of course further narrows the linearity range, but since the outcome of the event game is a statistical process, the nonlinearity can be calculated and corrected for. The relevant expressions and methods for this non-linearity correction will be presented in further chapters. Here the focus should stay on the event conditions and BCM measurement approach.

Many different event conditions could be used. Four of them are implemented in the BCM, with the limit imposed by FPGA resources. These four parallel measurements are commonly called *luminosity algorithms*. They were chosen to maximize information that can be obtained, both about collisions and the background. The choice implemented in firmware release 3.3.1 is:

OR algorithm counts the number of events that have any hit registered within the second half of the bunch crossing period. Limiting the discussion to this period, each hit marks the underlying event as OR event. With true collision induced hits this gives the biggest asset of this algorithm - its high statistics. On the other hand each noise or background hit on the underlying empty event (no physics induced hits) falsely classifies it as an OR event, thus making this algorithm most noise/background susceptible.

[9]This rate is a low estimate in case of a single bunch pair in LHC that produces on average one pp collision per bunch crossing. With average of 4 pp per BC and $\sim$ 300 bunches at the end of 2010 this estimate rises by a factor of 10^3.

AND algorithm counts the number of events that registered in both A and C-side modules being hit within the second half of the bunch crossing period. Being the most selective of the algorithms it suffers from low statistics, especially at low luminosities. However, due to low noise rate, it is practically background free and thus provides the cleanest luminosity measurement.

XOR-C algorithm counts the number of events that have at least one hit registered in C-side modules in the second half of the bunch crossing period and none on the A-side modules within the same period. The noise acceptance is a bit reduced, since a noise hit in XOR-A underlying event changes the event to be registered with AND algorithm, thus reducing the effect of C-side noise hits on underlying empty events. This effect is however not significant and highly dependent on detector acceptance and even luminosity itself. More important is its acceptance of the $A \rightarrow C$ background, while rejecting $C \rightarrow A$ background.

AND25 algorithm counts the number of events that registered both A- and C-side modules being hit, where all hits within given bunch crossing interval are taken into account. This algorithm is a redundant addition, and its main purpose is to include the background, that was excluded from previous algorithms because of their narrower time window.

Comparison between AND and AND25 algorithms is not trivial and can serve only as a rough background estimation. The background contributes out-of-time hits as well as in-time hits and is therefore present in both first, and second half of the bunch crossing interval. While all of it is included in AND25 algorithm, only in-time part of the background contributes to the AND. Different background sources contribute differently to this part, making the quantization more challenging.

While AND25 algorithm stands out, the first three have a common timing window, and they were chosen to complement each other in the most orthogonal way. The OR can be viewed as '1 minus empty event' algorithm. If XOR-A algorithm, that demands registered hits only on A-side modules in the second half of BC interval, were added, the probability space would be covered. Every event is bound to be either an empty event(inverted OR), XOR-C, XOR-A, or AND event. This is the additional constraint that enables measurements of three algorithms, while the forth one can be reconstructed off-line. Of course the total number of events must be recorded as well. During development, the AND25 was actually substituted with the XOR-A algorithm. The offline analysis of the recorded data allowed verification of this algorithm-unitarity. In the $250\,\mathrm{h}$ of data recording not a single readout block was found that would violate the constraint, indicating that there were no firmware or readout errors. With this in mind, the decision to use AND25 algorithm instead of XOR-A was made.

The schematics of the BCM luminosity implementation within the firmware can be seen in figure 5.7. The processed data is used by the event condition block, that checks the events versus the algorithm conditions. A single signal line, indicating that algorithm conditions have been met, is outputted for each algorithm. This `algo_valid` signal is updated on BC basis, and used by luminosity maps to count the events, and perform individual bunch statistics. The logic of this block has already been described, but two details remain to be mentioned:

- The $12.5\,\mathrm{ns}$ window used in AND, OR, and XOR-C algorithms is defined as the second half of the RIO sample (sample 32 to sample 63). The timing calibration performed after reset is done in a way that the time, corresponding to earliest physics induced signals ($\sim 6.25\,\mathrm{ns}$), is represented by sample 42. The time window therefore spans from $\sim 2.34\,\mathrm{ns}$ to $\sim 14.84\,\mathrm{ns}$ after proton-proton collision. This way, the in-time hits are accepted, while the background part that produces out-of-time hits ($-6.25\,\mathrm{ns}$) is filtered out.
- All eight channels connected to one data processing unit are used. One unit combines low threshold channels from one half of the detector and high threshold channels from the other half. This should be changed in the next version of firmware, since it couples the two measurements from both data processing units. However this coupling would be present only at high luminosities, where signals would start appearing on high threshold channels. Even more, the coupling would have its source only in events where one module would have high particle multiplicity while the neighboring module on the same side would not detect anything. Such scenario is highly unlikely and the correlation is thus minimal.

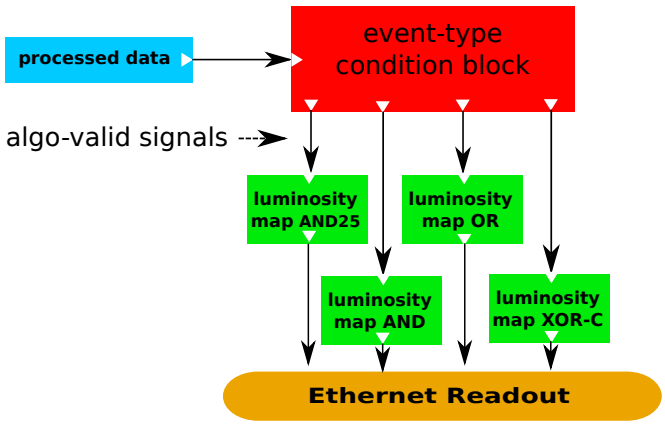

Figure 5.7: *BCM luminosity implementation within the firmware. There are four independent luminosity maps implemented, that are fed information from the condition block, where luminosity algorithms are implement.*

5.6.2 Luminosity maps

The event condition block defines the algorithms and its individual algorithm decisions are for each event passed to the *luminosity map*. Luminosity map is basically data storage for a given algorithm. It behaves as a collection of 3564 counters, thus providing per bunch counting capabilities.

The counters are implemented as a $4\,k$ deep double port RAM. Dual port functionality enables that the data is simultaneously read from and written to the RAM. The read address is by three higher than the write address, giving one clock cycle in between to update the previous

value. The circuity works on BC basis and is increasing both addresses each clock cycle. With such implementation each RAM address holds a counter for one bunch crossing. Its value is incremented if the condition block signals it, otherwise it is left unchanged. The schematics can be seen in figure 5.8.

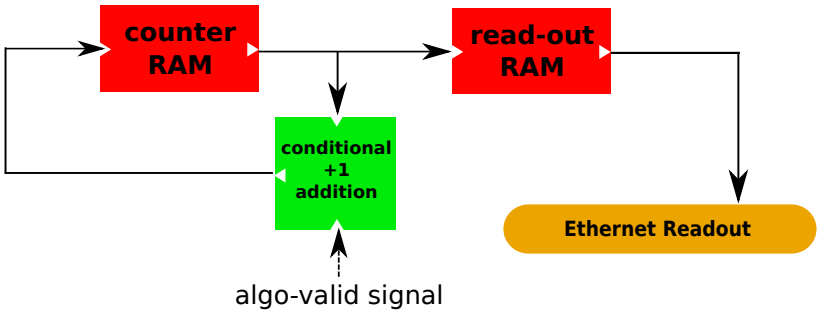

Figure 5.8: *BCM luminosity map implementation with two RAMs allowing read-out with no dead-time.*

ORBIT signal indicates the start of a luminosity map. On its rising edge the read address of RAM is reset to zero and a new round of counters' update starts. In order to make things more robust and to enable easier diagnostics of possible problems the address overflow at address 3563 (last bunch in the orbit) is not implemented. At this value the `ORBIT` signal is expected, and if it is observed, the address resets to 0 and the next round starts. However, if the `ORBIT` is not detected on this clock cycle or if the automatic overflow at address 4096 has occurred, a dedicated counter named *error counter* is increased by one. Monitoring of this counter enables to identify possible hiccups in the `ORBIT` signal or in bunch counting. Any problem in either of these two parts would corrupt the BCID awareness of the of the data if not the data itself. With the current implementation the orbit induced address reset eventually realigns the correct BCID with the start of the map. Additionally the error counter indicates the number of orbits that the system was out of sync. - the maximal error on individual counters. As such it can be used as one of data validity indicators. The presented error counting feature was extensively tested and proven to be fully functional on the development system.

Another feature, called *orbit pause* is implemented in the firmware. It gives a possibility to skip the luminosity counter increase in periods of entire orbits. This would give the chance to eliminate large dead time periods, like detector dead-time. However, this feature is not used. BCM is monitoring luminosity with no dead-time whenever it is running, regardless of any outside condition, like ATLAS running state.

As described, there is no dead-time during the event counting itself. This feature is kept also during the readout. To achieve this a second, equally sized, dual port BRAM is used. When the readout is not in progress each counter read from the counter-BRAM is stored to the same address in the readout-BRAM. This way the readout buffer is regularly updated with the values for the previous LHC turn until the readout is triggered. After the trigger, on beginning of the next orbit, the rewriting is paused and remains that way until the readout is finished. Only then the readout buffer starts refreshing with current values from counter-BRAM that was counting

continuously, thus suffering no dead time even during the readout.

The triggers are issued for all four implemented luminosity maps simultaneously. The data these maps hold therefore represents the same time period for all luminosity maps, making possible to compare the data in the offline analysis, i.e. reconstruct the XOR-A map from XOR-C, OR, and AND. Once the trigger is issued, it not only freezes the readout buffer but registers other quantities important for luminosity readout and later data analysis:

lumiReadoutID is a unique 24-bit number identifying the readout. It consists of two parts: 16-bit sequential counter and 8-bit lumiPeriodID. The counter behaves differently for each of two possible readout modes (described later) but is controlled by the firmware. On the other hand the lumiPeriodID is only user settable via Ethernet interface and enables the user to mark different time periods.

recorded orbits counter holds the total number of orbits during which the luminosity monitoring was active.

error orbits counter holds the total number of orbits in which an error occurred.

paused orbits counter holds the total number of orbits during which the luminosity was in 'pause mode'.

trigger type is a 4-bit number identifying the trigger that started this readout.

reference BCID has the 12-bit BCID corresponding to the first address of the readout-RAM. This value is used in software part of the readout, to deduce the position of data in the read-out luminosity map.

There are two possible sources of luminosity trigger intended for two different modes of operation:

Manual readout-mode is intended for scenarios where a great flexibility regarding readout frequency and data tagging would be needed. Dedicated software reading the data out of data processing units is also responsible for triggering each individual readout. Along with each trigger a lumiPeriodID must be sent, that enables later identification of the data. This allows complex algorithms to fine-tune the readout. The biggest drawback is the time uncertainty of the trigger, since it resides in the software world and must travel by DPU via Ethernet. This eliminates the possibility of single turn resolution in controlling the time periods between the readouts.

Self-triggered readout-mode is intended for more stable running. In this mode an internal trigger source is used. It issues trigger every Nth orbit and this *self-triggering period* can be configured via the Ethernet. The triggers are truly equidistant and besides the initial setting of the self-triggering period no software is needed for readout control. The self-triggering period can be set in units of orbits and must be within the interval $[1, 65535]$, or 0 to disable the feature (this is the default value after the reset/reboot of the firmware). When setting this value the user should take into account the time it takes for all four maps

to be read out. In the case when trigger is issued while the readout is still in progress, it cancels the readout, refreshes the readout-RAM and starts a fresh readout as soon as possible.

5.6.3 Luminosity data-acquisition

In addition to the lower time limit imposed by single read-out duration an upper limit should be taken into account as well. All the counters mentioned so far (unless stated otherwise) are 16 bits wide. Since each LHC turn a counter can be increased only by one, the minimal time for overflow is $\sim 5.4\,\mathrm{s}$. This is therefore the longest time period between two consecutive readouts if data doesn't want to be lost. The counters are not reset during the readout, but are continuously increasing therefore the overflows occur regularly and they must be corrected for in the software. The software must also receive two readings and calculate the difference in order to get the values for a given time period. This offers additional robustness to the system, since if a reading missed is for any reason, the next one still contains all the data, only averaged over a greater time period. Thus any temporary communications blackout shorter than $\sim 5.4\,\mathrm{s}$ does not cause the loss of data.

A data readout is performed over Ethernet using the IP/UDP protocol. A single luminosity map holds $7\,\mathrm{kBytes}$ of data and is split into 14 packages.

After the trigger, when all UDP and IP checksums are pre-calculated, the first package of a luminosity map is sent. Each of these packages must be acknowledged by the readout software. Once it is, the following package of the map is send. The sequence is repeated until the 14th package is acknowledged which ends the readout for the map, and the readout-RAM starts refreshing again. Since all four maps are triggered simultaneously they are also read in parallel. However if multiple packages are waiting to be sent, the one from the map with lowest mapID has the priority. This way any stress on the readout process causes a gradual data loss. Only the last map is therefore send partially if the bandwidth becomes a problem, while the maps before it get transfered completely.

5.6.4 Readout software

The last step in the BCM luminosity data-acquisition chain is the software receiving the data from DPUs. The application is called *lumiReader* and after receiving the data, it optimizes it, stores it to the *BCM private lumi stream*, and also publishes it to IS to be read by OLC. The application communicates with both DPUs[10] but with separate threads, giving total independence of the two readouts.

On basis of functionality the lumiReader can be divided into four parts:

Receiver is the part implementing the protocol described in the last subsection. It receives the packages, acknowledges them and assembles them into *lumiMap*. No data processing is done, and all the counters are still holding total accumulated numbers. At this stage

[10] A technical detail. The receiving ports have been hard-coded and are `0x0FF4` for FPGA1 and `0xFF5` for FPGA2.

each lumiMap is assigned a time-stamp, which is a PC time-stamp on receiving the first package of the readout. All four maps are assigned the same time. Note, that time jitter of milisecond order with respect to the actual lumiTrigger is expected since this is a PC time stamp and additionally the data must be passed through the kernel to the application before the time is forzen. There is additional functionality of this software module, and it is to configure DPU for self-triggered readout-mode. A thread is checking the receiving data rate and if nothing has been received in a given time period it reconfigures the DPU. This way no manual intervention is needed after system startup. The DPU boots-up in manual readout-mode, giving no data. After the lumiReader has been started it auto-configures the DPU on the first timeout. The timeout period and the lumiTrigger period are both settable parameters loaded from the settings file at the program startup. For now the time period of $10\,\mathrm{s}$ and trigger period of 9000 orbits are being used.

Fast data processing takes place immediately once the entire map has been received. The goal is to provide per reading rates with low latency. For this the counters difference between last and second last lumiMap are calculated, yielding the rate information. Counters for all BCIDs are then summed together, providing BCID blind info to two sources. The first one is the private data stream, and the other is the IS. The exact format of the data produced in any part of lumiReader will be described in subsection 5.6.6. Here let's only mention that there is also a fifth IS publication - OR-algorithm data (inverted data of the 'Empty' algorithm that is actually implemented in DPU and is also published).

Event provider is a prestage to slow data processing. The data rate from DPUs is too big for all to be recorded and the per-bunch luminosity is not really needed on $1\,\mathrm{Hz}$ level. To minimize the volume and still provide all relevant information, the *lumi-maps* are accumulated over longer time periods. Only *lumi-accumulations* are then further distributed. The borders of these accumulation periods are defined with *lumi-events*. Since different accumulation periods might be needed for different measurements, and they could also overlap, multiple lumi-events were implemented. Event provider is a common handler for all of them. It receives an event notification from an arbitrary source, creates a lumi-event with the time-stamp, and puts it a into queue.

On every finished lumi-map readout, the reading is (in parallel to fast data processing) put into a reading-buffer. On each insertion, all events from the event-queue are assigned to lumi-maps on the basis of timestamps. Many events have their time-stamp recorded in the software world, and in order to be immune to time-jitter all lumi-maps are kept in the reading-buffer for a minimal amount of time[11]. Once this time is exceeded the lumi-map is removed from the reading-buffer and passed to the slow data processing module.

Currently four lumi-event types are implemented:

event-LB-change is created on each registered new publication of the IS variable `ATLAS:RunParams:LumiBlock`. This signals the start of a new ATLAS

[11] This value can also be set in the settings file. A $3\,s$ timeout proved to be more than enough to catch all events and still provide latency low enough for the OLC to process the information.

luminosity block and caries the time-stamp which is used as a lumi-event time-stamp.

event-PLB-change is created on each registered new publication of the IS variable `initial:RunParams:LumiScanSignal`. This signals the start of a new ATLAS pseudo luminosity block and caries the timestamp which is used as a lumi-event time-stamp.

event-forced is a dedicated lumi-event implemented to provide flexibility to the system. An TCP/IP port in the lumiReader is listening for string messages. If a message is received by lumiReader and if its header is properly formated, a new lumi-event is created. It is given the time-stamp of the message reception and the message text is appended. This gives the possibility to include lumi-accumulations in the data stream that are not yet known. For instance, if one wanted to analyze the effect of threshold change on luminosity measurements, the DCS could be modified to send such message on each threshold setting change. This would automatically cause new accumulation periods at appropriate times. Since the lumi-events are also recorded in the private data stream along with the data, this would enable such offline analysis.

event-nothing is an additional lumi-event signaling internal program events. It is used in two cases:

- In the absence of ATLAS run or vDM calibration there are no (pseudo) luminosity blocks. Since these are the main lumi-event triggers, one can expect long periods without any events. To avoid these periods to be treated as single lumi-accumulation an accumulation timeout is implemented. If no other lumi-event is triggered, an event-nothing is inserted. Currently the settings assure that no lumi-accumulation is longer than $\sim 45\,\mathrm{s}$.
- With the philosophy of 'always expect the unexpected' in mind, the BCM luminosity system was designed to be robust. The weakest point in its chain could be the communication between DPU and lumiReader, since it is UDP-based. To extract the most information in scenarios where some portions of the data are lost it proves optimal to force additional accumulations. For this the event-nothing is used. It should be noted that, because of raw count readout, a communications blackout of less than $5\,\mathrm{s}$ does not cause a problem since the counters cannot overflow. But in this period an lumi-event can occur. There are numerous different possible problematic scenarios. For instance, a reading could potentially be missed only for a single lumi-map, while other three maps are transfered completely. To allow reconstruction of XOR-A all accumulations must be synchronous between the lumi-maps. Therefore, not to lose data, it is sometimes better to divide the accumulation period in two parts: the part where all lumi-maps are received and a part with lack of information. To mark the border an event-nothing is inserted.

It should be noted, that the number of lumi-events should be kept to its minimum, since they increase the data volume size. Therefore the data rate outputted by the

lumiReader can change dynamically. However an upper limit would be produced by a scenario, where an lumi-event would occur each reading. In such case BCM luminosity readout would produce $\sim 70\,\mathrm{kBytes/s}$. This poses no problem for the network, but the accumulated stored data could grow heavily. However such scenario is highly unlikely if not impossible.

Slow data processing is the final stage of data flow within the lumiReader. It accepts the lumi-maps from readout-buffer along with appropriate lumi-events and does the basic lumi-accumulaiton. On every event the current accumulation ends and a new one begins. Each accumulation period starts with the reading that followed the one with the event, and ends with the reading that includes the next lumi-event. Events are recorded along with the lumi-accumulations and the combined data structure is called lumi-entry. These lumi-entries are than dispatched to all lumi-clients. These have specialized functions serving different data streams:

private data stream is meant primarily for calibration, but can also serve for regular data analysis. Additionally it can greatly aid any debugging since it records maximal amount of information. Any lumi-entry is recorded to the file as it is.

LB data stream publishes the luminosity information of the last luminosity block. It merges all lumi-entries on the basis of event-LB-change type of lumi-events. The merging of single LB data is done in a way, that the lumi-entries between the start and end event-LB-change event are summed together, along with linear interpolation of the bordering lumi-entries that contained events. The interpolation is done on timestamp basis of lumi-accumulation interval and lumi-event. Once merged the lumi-entry is published on IS. Note that the publication refers to the LB that ended, therefore the IS publication corresponding to declaration of the start of the first luminosity block in ATLAS run should be ignored. In the first run after lumiReader startup, this publication does not appear, while otherwise it represents data accumulation between two ATLAS runs, and has therefore no meaning.

PLB data stream functions the same as the LB data stream, the difference being the lumi-events that are used for merging the data. Here the type event-PLB-change is used.

All three data streams are filled in parallel and they function independently. The LB information is however valid only when an ATLAS run is ongoing. PLB information is valid only during the vDM scan. Due to its limitations, the OLC can not process both LB and PLB information simultaneously, nor two separate publications. Therefore lumiReader publishes only LB or PLB data-stream information to the same IS variables. The switching between the two sources of publication is also done through the IS. IS command is a text message sent to a chosen IS variable. If command `"SwitchAllBcmRegular"` is send to any of the variables, all publications switch to LB data stream, which is also the default after restart. On `"SwitchAllBcmPseudo"` command the publications switch to PLB data stream.

5.6.5 IS publications

The IS as a source of lumi-events has already been described, so the focus here will be on the publications made by BCM. Their format is imposed by OLC in order to standardize its input from all luminosity sub-detectors.

Instantaneous publications are updated after every readout, and the data fields are:

raw count is the sum of the event counts for all BCID in the current readout,

orbit count is the number of orbits that are included in the reading,

data quality flag is always assigned value 0, since any potential problem would cause a missed reading, causing the values not to be published at all.

Any other fields in the data structure published to IS are undefined and should be ignored. The additional feature is a double publication when the 'EMPTY' algorithm map is received. It is published along with its inversion, 'OR' algorithm map. Per reading rates are published on IS under the names `bcmRaw_X_Y`, where X is either 0 or 1 indicating the DPU, and Y marks the algorithm: 0 for AND25, 1 for AND, 2 for EMPTY, 3 for XOR-C, and 4 for OR.

LB and PLB publications have the same format since they share the same IS variable to be published to. As already described, they are published at the end of each LB/PLB. The data fields are:

raw count vector contains the event counts corresponding to all 3564 BCIDs. Since these values are accumulated over longer periods, a possibility of missed reading somewhere inbetween is taken into account. The fraction of missing time is always known. The event counts are scaled to full-time period and trimmed to integers before filled into the vector.

orbit count contains the number of recorded orbits, again scaled for the missing time if needed, and trimmed to an integer.

data quality flag is assigned 0 (data good), if the fraction of the missing time is below 20%, otherwise the flag equals 1 (data bad).

run and LB numbers are assigned values of the run and luminosity block in question.

Any other fields in the data structure published to IS are undefined and should be ignored. Again the publication doubles in case of 'EMPTY' algorithm map, where 'OR' algorithm map is produced and published. LB/PLB publications are named `bcmBlock_X_Y`, where the same numbering as in the case of per reading publications holds.

5.6.6 Private data stream

Since there are more data than actually published to IS, a private data stream was created. In it one can find the most detailed BCM luminosity data recorded. It allows for data analysis and calibration. These analyses can be done independently of the ATLAS luminosity infrastructure,

providing means for systematic checks on all stages of data processing, from storage to final analysis results. Additionally it proved of great value during the development and debugging.

With storing a detailed information comes a demand of reliability. The stream was designed to write data in raw binary files in form of custom written data structures. This makes analysis a bit more challenging (more software must be written for it). However it gives two advantages: it does not depend on the external software, which makes it more reliable and it is more light-weight, meaning it places a smaller burden on CPU and memory resources. The latter is extremely important for a process like this which is intended to run constantly, especially because this takes place on the same single board computer that also hosts security services for BCM which must not be impaired under any circumstances.

The basic data structure in this stream is lumi-entry. Its identity is marked with lumi-ID, which is unique within one luminosity data of one algorithm, however the lumi-entries for different algorithms, corresponding to the same accumulation period, share the same lumi-ID. This enables easy comparison of different luminosity algorithms under same conditions. It should be noted, that the readout is synchronized only between the lumi-maps of the same DPU. Both DPUs are read independently, thus lumi-IDs cannot be used for comparing data from both DPUs.

Besides lumi-ID each lumi-entry is composed of two data blocks: lumi-event list which contains all corresponding lumi-events, and lumi-period which contains the measurement data. The lumi-event list can be of arbitrary length, even empty, and the collection of possible lumi-event-types has already been given in the preceeding subsections. Lumi-period part of the data can be either of the two things:

- lumi-map period, which contains all the recorded data during luminosity map readout, including all the time stamps.
- lumi-empty period is used in case of readout failure, and includes only the relevant timestamps. This data structure is used to indicate the missing data periods.

The data is written to files sequentially, including the file pointers to the next record. This allows fast storage and immunity against a malformatted data block, however it demands sequential browsing of the files, making data analysis a bit slower. Files are limited with their size and sequentially numbered. After the file is filled it is copied from P1 to CASTOR for permanent storage.

Chapter 6

BCM luminosity response and its simulation

Previous chapter described the BCM from the structural point of view and provided an overview of its functionalities. The aim of this chapter is to detail the luminosity as a measured physics quantity, to describe how raw BCM measurements correlate to LHC delivered luminosity, and to provide basic estimation and verification through Monte Carlo (MC) simulation. It should be stressed from the start that Monte Carlo was used as a very successful tool for proving the basic principles and to give very rough estimation of basic parameters. These were used merely for orientation purposes during development. During actual data taking, no Monte Carlo value is used in data interpretation.

6.1 Luminosity versus BCM luminosity counts

Ideally the measured quantity translates into raw measured values in a linear fashion. If luminosity is discussed, this can certainly be achieved with the particle counting technique. Tracking systems are mostly constructed with enough readout channels that, even at larger luminosities, expected particle multiplicities are low enough for efficient particle counting. This makes particle counting an attractive solution, however it has its drawbacks. For better performance, larger portions of detectors should contribute information, and tracking could be done to distinguish particle signal from the noise and the background. At present this can not be done on bunch-by-bunch basis with no dead-time. Additionally this method usually depends on dE/dx measurements for which much more detailed knowledge of detector characteristics is needed. To achieve optimal precision of the measurement device a trade-off must therefore be done between the method's intrinsic accuracy and its complexity.

To make the luminosity measurements least sensitive to as many detector characteristics as possible the event counting proves to be best. Unlike the particle counting method, it also works with a much simpler detector. Though the BCM in principle also supports dE/dx measurement, the event counting approach has also been chosen for BCM luminosity measurements. However

this approach has its own drawback - each event measurement is limited to 0 or 1, 'true' or 'false'. The end result is the probability for an event to satisfy the given condition. Thus, this method, maps the interval of possible luminosities $[0, \infty)$ to the probability interval $[0, 1]$. The transfer function is nonlinear, it saturates at high luminosities, and is sometimes even non-monotonic.

If the goal is to accurately measure luminosity this transfer function must be well known. In the case of the proposed event conditions: OR, XOR-A, XOR-C, and AND, it can be expressed analytically. The basic parameters are probabilities for these event-types in the case of a single proton-proton (pp) interaction. They will be denoted ε_{OR}, ε_{XOR-A}, ε_{XOR-C}, and ε_{AND}. By definition of event criteria it holds that:

$$\varepsilon_{AND} = \varepsilon_{OR} - \varepsilon_{XOR-A} - \varepsilon_{XOR-C}. \tag{6.1}$$

In reality, on each event (bunch crossing) multiple pp interactions can occur. In the case of i such (uncorrelated) interactions, the probabilities for event types to be observed are:

$$\varepsilon_{OR;i} = 1 - (1 - \varepsilon_{OR})^i \tag{6.2a}$$

$$\varepsilon_{XOR;i} = \sum_{j=1}^{i} \binom{i}{j} \varepsilon_{XOR}^j (1 - \varepsilon_{OR})^{i-j} \tag{6.2b}$$

$$\varepsilon_{AND;i} = \varepsilon_{OR;i} - \varepsilon_{XOR-A;i} - \varepsilon_{XOR-C;i}. \tag{6.2c}$$

Equation (6.2b) holds for both XOR-A and XOR-C. All the interactions within the bunch crossing are independent, thus their number is distributed according to the Poisson distribution. With this the actually measured conditions are described by convolving the above equations with the Poisson distribution having the average of $\langle\mu\rangle$. Including all possible values of i one obtains final expressions (a step by step derivation can be found in appendix C):

$$r_{OR} = 1 - e^{-\langle\mu\rangle\varepsilon_{OR}} \tag{6.3a}$$

$$r_{XOR} = e^{-\langle\mu\rangle\varepsilon_{OR}} \left(e^{\langle\mu\rangle\varepsilon_{XOR}} - 1\right) \tag{6.3b}$$

$$r_{AND} = 1 - e^{-\langle\mu\rangle\varepsilon_{OR}} \left(e^{\langle\mu\rangle\varepsilon_{XOR-C}} + e^{\langle\mu\rangle\varepsilon_{XOR-A}} - 1\right) \tag{6.3c}$$

The r_{OR}, r_{XOR}, and r_{AND} are measured event-type probabilities, while $\langle\mu\rangle$ is a parameter of the bunch crossing. The measured probabilities r_A are calculated from raw counts N_A and number of recorded events N_E. Both of these are extracted from the luminosity maps for each BCID on each readout. For an arbitrary luminosity algorithm A holds:

$$r_A = \frac{N_A}{N_E}. \tag{6.4}$$

Monte Carlo based estimation of BCM measured values r_A as a function of $\langle\mu\rangle$ is plotted in figure 6.1. More on simulation later, here the focus should remain only on the functional form. The OR algorithm is linear at low luminosities and is the most sensitive, but is also the first to saturate. At higher luminosities the AND algorithm promises to be more sensitive

to luminosity changes at the expense of less statistics. This is not an issue during normal running, however it poses a limit during calibration, which will be thoroughly discussed in the next chapter. The XOR algorithms are expected to yield the same measurements. In principle they could be different due to different sensitivity to minimum bias events of A- and C-side (due to difference in detector material distribution and detector efficiency). In the above calculation no detector asymmetry is assumed so this difference does not influence the luminosity measurement precision. The XOR event rates also start to decrease since at higher particle multiplicities the probability for the AND event-type rises at the expense of the XOR event-type probability.

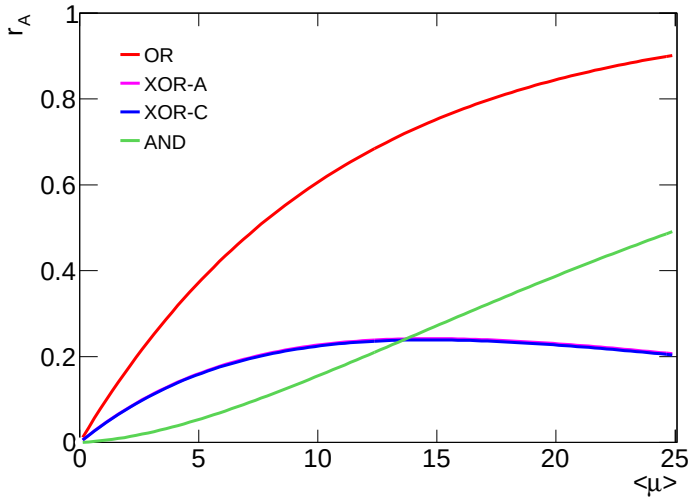

Figure 6.1: *Monte Carlo estimation of BCM measured event-type probabilities. The value* $< \mu >= 25$ *roughly corresponds to the design LHC luminosity of* $10^{34}\,\mathrm{cm}^{-2}\mathrm{s}^{-1}$.

6.2 μ-correction

As described in section 4.2 the luminosity is measured via the measurement of $\langle\mu\rangle$. This in turn is obtained from the BCM measurements of r_A by inverting equations 6.3. These inverse transformations are known as μ-corrections and have an analytical form.

In equations 6.3 $\langle\mu\rangle$ is always multiplied by the relevant algorithm efficiency, so it is natural to use visible cross-section and visible $\langle\mu\rangle$ as defined by 4.3. Since these quantities are algorithm specific it holds:

$$\mu^{vis}_{OR} = \langle\mu\rangle\,\varepsilon_{OR} \quad \text{with} \quad \sigma^{vis}_{OR} = \sigma\varepsilon_{OR} \tag{6.5a}$$

$$\mu^{vis}_{XOR-A} = \langle\mu\rangle\,\varepsilon_{XOR-A} \quad \text{with} \quad \sigma^{vis}_{XOR-A} = \sigma\varepsilon_{XOR-A} \tag{6.5b}$$

$$\mu^{vis}_{XOR-C} = \langle\mu\rangle\,\varepsilon_{XOR-C} \quad \text{with} \quad \sigma^{vis}_{XOR-C} = \sigma\varepsilon_{XOR-C} \tag{6.5c}$$

$$\mu^{vis}_{AND} = \langle\mu\rangle\,\varepsilon_{AND} \quad \text{with} \quad \sigma^{vis}_{AND} = \sigma\varepsilon_{AND}. \tag{6.5d}$$

With this the explicit dependence on efficiency disappears from equations 6.3 and moves to visible cross-sections. This simplifies the inversions and to further simplify the expressions let us also denote:

$$r_0 = 1 - r_{OR}. \tag{6.6}$$

The mathematics needed to invert 6.3 is straightforward, however care must be taken when assigning errors. The measurements r_A are highly anti-correlated; a positive error on the AND algorithm measurement will decrease the XOR algorithm measurements. In the case of independent measurements and under the assumption of constant probability for event detection, the set of measurements: r_0, r_{XOR-A}, r_{XOR-C}, r_{AND} should obey the multinomial distribution. If the collected dataset contains data for N_E events, the variances $Var(r_i)$ and covariances $Cov(r_i, r_j)$ between different measurements are known:

$$Var\left(r_A\right) = N_E r_A (1 - r_A) \tag{6.7a}$$

$$Cov\left(r_A, r_B\right) = -N_E r_A r_B. \tag{6.7b}$$

Using the standard linear error propagation the expressions for all algorithms are (derivation in appendix D):

OR algorithm is the simplest of them all. The inversion of (6.3a) is:

$$\mu_{OR}^{vis} = -\ln\left[r_0\right], \tag{6.8}$$

where the definition 6.5a was used. The corresponding error estimate is:

$$\sigma_{\mu_{OR}^{vis}} = \sqrt{\frac{1}{N_E}\frac{1 - r_0}{r_0}}. \tag{6.9}$$

XOR algorithms can both use:

$$\mu_{XOR}^{vis} = \ln\left[1 + \frac{r_{XOR}}{r_0}\right]. \tag{6.10}$$

It is clear, that both XOR and OR measurements are needed to determine μ_{XOR}^{vis}. Consequently same holds for the error assignment:

$$\sigma_{\mu_{XOR}^{vis}} = \sqrt{\frac{1}{N_E}\frac{r_0 r_{XOR} - 4 r_0 r_{XOR}^2 + r_{XOR}^2}{r_0\left(r_0 + r_{XOR}\right)^2}}. \tag{6.11}$$

AND algorithm measurements are μ-corrected with:

$$\mu_{AND}^{vis} = \ln\left[\frac{r_0}{\frac{r_0}{r_0 + r_{XOR-A}} + \frac{r_0}{r_0 + r_{XOR-C}}}\right]. \tag{6.12}$$

The expression is $A \leftrightarrow C$ symmetrical as it should be since it depends only on coincidences. The unitarity condition 6.1 holds also for the rates so three out of four

measurements are needed to properly μ-correct the AND algorithm measurement. The error assignment is:

$$\sigma_{\mu^{vis}_{AND}} = \sqrt{\frac{1}{N_E}\frac{r_{XOR-A}r_{XOR-C} + r_0^2\left(1 - r_{XOR-A} - r_{XOR-C}\right) - r_0 r_{XOR-A} r_{XOR-C} - r_0^3}{r_0\left(r_0 + r_{XOR-A}\right)\left(r_0 + r_{XOR-C}\right)}}. \tag{6.13}$$

Using the above expressions one linearizes the detector response. Knowing μ^{vis}_A and using equation 4.4 allows the calculation of luminosity for each of luminosity algorithms separately:

$$L = \frac{\mu f_{rev}}{\sigma} = \frac{\mu^{vis}_A f_{rev}}{\sigma^{vis}_A}. \tag{6.14}$$

The only quantities to be determined are the σ^{vis}_A in the denominator. These are the calibration constants and will be the subject of discussion in the next chapter.

6.3 Simulating BCM

The BCM operation does not require any simulation input for any of its functionalities. However, simulation was a valuable tool throughout its entire development and luminosity functionality was no exception. It provided guidelines during development, it offered the start for optimization for running parameters, and was especially useful when evaluating possible luminosity algorithms. All these aspects will be presented in the results of this chapter, while the next sections describe the necessary procedures and infrastructure. Since Monte Carlo detector simulation is a complex field only a brief overview will be given.

6.3.1 ATLAS simulation

Many portions of the simulation code, like physics generators, are independent of ATLAS simulation and can be used standalone, while some are highly ATLAS specific. In the end all modules are incorporated in the Athena framework which is used not only for simulation, but also for recorded data analysis. Athena is an enhanced version of Gaudi framework [GU00], which was designed for a wide range of data-processing physics applications. Athena was designed on principles of component-based architecture, allowing great flexibility. The major groups of components are: algorithms, sequences, tools, transient data stores, services, properties, utilities,... Their functionalities are explained in [CR05] as part of more detailed Athena overview. Here the focus will turn form technicalities to philosophy of simulation in ATLAS. Simplified overall schematic of simulation data flow is seen in figure 6.2.

The first in line are the generators. The initial interaction must be defined, and in case of full ATLAS simulation this is a proton-proton collision at certain energy. With this as their input, the job of the generator is to randomly pick possible physics processes in accordance to their modeled properties. They include physics of hard processes, multiple interactions, initial and final-state radiation, hadronization,... With all this they create the list of final products with

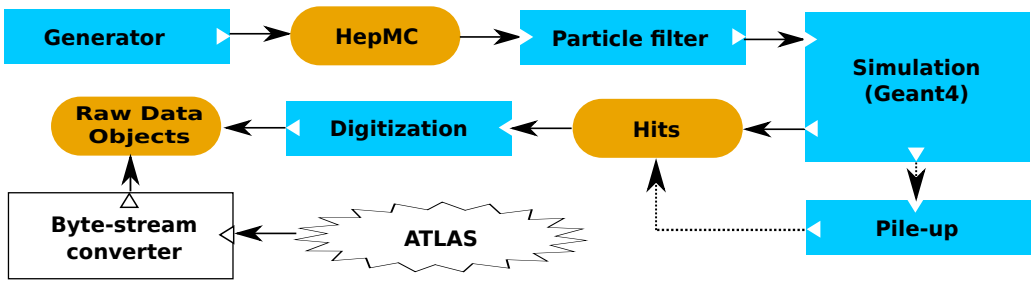

Figure 6.2: *Simplified simulation flow schematic for ATLAS. The dotted lines represent optional use of pile-up. The two empty boxes in the bottom show ATLAS data-taking flow which ends with the Raw Data Objects (RDOs). This are also the final products of simulation, and no matter the source they are used as an input to reconstruction algorithms.*

their physics properties such as direction, energy, momentum. . . - giving the Monte Carlo truth. Athena is able to use any of more than 30 different generators, with all of them providing the same standardized output data-containers called HepMC. The complete list of generators in Athena is available at [GL].

After Monte Carlo truth has been generated it passes through the particle filter implemented in Athena. Selecting only certain particles to be used in simulation allows more specific studies, as well as optimizes the performance by removing the unnecessary work load (e.g. particles that would not reach the sensors due to too low transverse momentum). Particles that passed the filter are then propagated through the detector also taking into account the magnetic field. The main engine for this is the Geant4 toolkit [G4] that models the interaction of passing particle with the surrounding material. Step by step it calculates the trajectory, creates secondary particles, and calculates the energy being deposited in the material. Each such step with energy deposition is named *hit* and Athena records and stores all hit information in the data storage in form of hit containers (each sensor in ATLAS has its own hit container). An additional possibility, after Geant4 produces hits, is the pile-up stage. The simulated events can be overlayed with delayed signals, the background, noise, etc.

Once the hits are finalized for a given event, the digitization takes place. It translates the energy deposition to effective charge that was collected, and on basis of which the signal is produced. Equally the light production is translated into electrical signals as they would be produced by the actual sub-detectors. Here the entire response of readout electronics is taken into account. The final output of digitization step are the Raw Data Objects (RDOs).

RDOs are the final result of the simulation chain. The same data format is produced during ATLAS data recording. Here the raw byte-stream coming from the detector is converted to the RDOs by the byte-stream converter. RDOs are therefore a junction point of data-taking and simulation paths, from where on the same reconstruction and analysis software can be used. This provides the possibility of comparing simulation data with actual measured results thus achieving its main goal.

6.3.2 BCM in ATLAS simulation

To incorporate the BCM into the ATLAS simulation scheme three tasks had to be done:

- BCM geometry and material **detector description** was added to the ATLAS detector description,
- classes for **collecting hits** during Geant4 simulation were written for the sensors,
- **digitization** was implemented to produce the DPU output on the basis of hits.

Additions started with Athena version 12.0.4 and starting with version 14.2.0 the BCM is automatically simulated with the rest of ATLAS. In the following subsections a bit more detailed overview of these three additions is given.

Geometry description

As for the rest of ATLAS, the BCM geometry description is based on the GeoModel toolkit [GM05]. It is a library of geometrical primitives with which one can describe the entire detector, its shape and its material composition. As a data layer it offers creation of nodes that contain information about physical volume and its properties. Each physical volume data-structure consists of:

- *logical volume* that describes the shape and the material. Shape is build as union, subtraction, intersection, etc. of primitive geometrical shapes defined in GeoModel such as cylinders, cubiods, etc. The material properties can also be defined by specifying the material density, its element composition and the mass fractions for each of the elements.
- *list of sub-nodes* provides data links to lower level geometrical structures. Each sub-node is also accompanied with the relative transformation between itself and the parent node. These transformations can be either fixed or alignable transformations. The later allow dynamic alignment later in the data processing.

With such data structuring only the top node is used during initialization. It initializes its sub-nodes and they in turn expand the tree to cover the entire ATLAS detector description. During this procedure the GeoModel checks for possible geometry-clashes, and when initialization is done, offers the geometry to its two main clients: simulation and reconstruction. While reconstruction uses GeoModel directly, Geant4 uses its own native geometry description. A tool called Geo2G4 is therefore needed to translate the GeoModel to Geant4 data structures.

BCM description is implemented in the `BCM_GeoModel` software module. The code is available at [BG]. It is initialized as a Pixel geometry sub-node by instantiating the `BCM_Builder` class, which represents the BCM as a whole. It creates eight sub-nodes, one for each module. The modules themselves are constructed within `BCM_Module` class and have their walls and diamonds as sub-nodes. The outside dimensions of modules are specified in appendix E. The walls are constructed from $1.4\,\mathrm{mm}$ thick G10 material, coated on one side with $35\,\mu\mathrm{m}$ of copper. Diamonds are $10\,\mathrm{mm} \times 10\,\mathrm{mm}$ in size and $0.5\,\mathrm{mm}$ thick with no metalization defined.

The BCM_GeoModel is fully adapted to the Athena environment. Its parts can be turned on/off during simulation and all parameters can be set through initialization options. This parameter manipulation is optional, for cases where one desires a special non-standard simulation setup. During normal simulation the parameters for the entire ATLAS detector description are loaded from the ATLAS Detector Description DataBase (DDDB) [DDB]. This database also includes 15 parameters for each of the eight BCM modules. The list of parameters is:

- TRANS_X, TRANS_Y, and TRANS_Z define the coordinates of the module's geometrical centre within the ATLAS coordinate system.
- Once the translation is performed, ROT_X, ROT_Y, and ROT_Z define the orientation of the module. The rotations are performed in the module's own coordinate system - z axis is along the length of the module, the y axis along its width and the origin is at the center of the module's bounding box. The rotation around z axis is performed first, followed by the rotation around y axis, and ending with the rotation around x axis.
- The lower diamond position within module's coordinate system is defined with DIAM_TRANS_Y and DIAM_TRANS_Z parameters. Its x coordinate is fixed in a way, that the diamond lies on the main board of the module.
- The position of the upper diamond of the double-decker stack is defined with respect to the lower diamond with DIAM_DIAM_X, DIAM_DIAM_Y, and DIAM_DIAM_Z parameters. The values represent the distance between the centres of the two diamond surfaces facing each other.
- DIMESION_Z parameter is used to differentiate between the modules labeled F40x and F42x. The two sets of modules differ by the thickness of the back wall throughout which the cables exit the module. The thickness of G10 material of this wall is written as DIMESION_Z.
- OFF_H, OFF_I, and OFF_J are the z coordinates in the module's coordinate system defining the position of three amplification-compartment separating walls.

The default values for these parameters, as are written in DDDB, are given in appendix F. A view of BCM, constructed with GeoModel, is shown in figure 6.3.

Hit collection

Next stage is Geant4 simulation. For this the BCM diamonds were declared as sensitive volumes in configuration files. This means that all energy depositions produced by Geant4 are reported to a custom callback function in BCM_G4_SD software module. This function collects the following information for each BCM hit:

- *beginning and end coordinates* of the Geant4 step expressed in the diamond coordinate system,

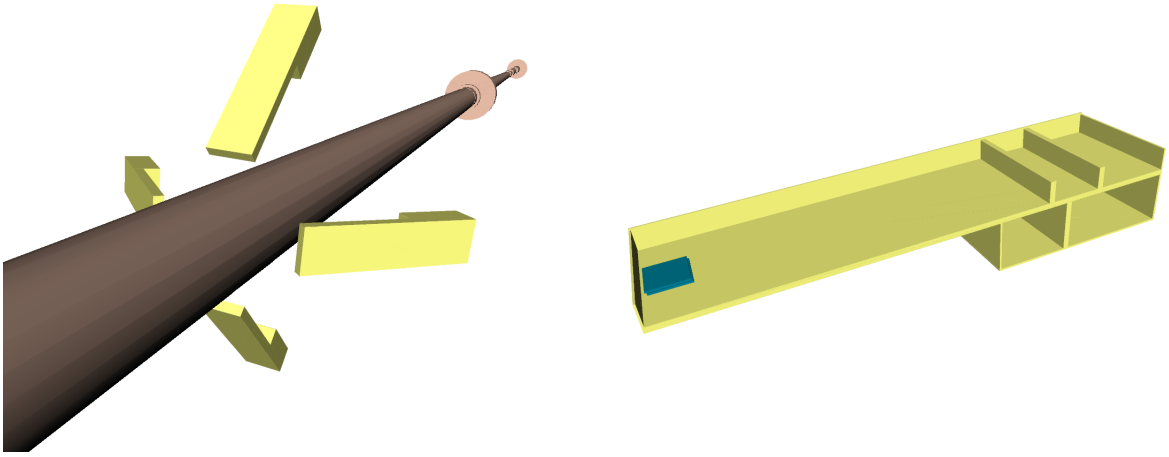

Figure 6.3: Left: *Picture shows C-side BCM modules arranged around the beam pipe. Beam pipe support structure is also seen.* Right: *BCM module as implemented in GeoModel. Top and front wall have been removed so the inner structure is visible. At the very end of the module the diamond stack can be seen (blue). The amplification compartments can be seen on the opposite side. Pictures were generated with the Virtual Point 1 viewing software [VP1].*

- *energy deposition* during this Geant4 step,
- *time* of energy deposition,
- *identity of particle* producing the energy deposit,
- *module number*, identifying the module being hit,
- *diamond* in the module: lower/upper,
- *particle creation flag*, disclosing whether the passing particle is primary or secondary particle. For secondary particles it is also noted whether they have been produced within BCM or outside of it.

All this information is inserted into SiHitCollection data container named `BCMHits`, and exported to transient event storage at the end of Geant4 simulation step.

Digitization

Once the hits have been created digitization takes place. `BCM_Digitization` software package is responsible for translation of hit information into the RDOs. It models the functionality of NINO components as well as functionality of DPUs.

The expected analog pulse is constructed by adding-up multiple pulses[1], one for each hit. Their amplitude is linearly correlated to the hit energy deposit. Once the waveform is assembled

[1] Analog pulses generated by hits are approximated with triangular signals of 2 ns rise time and 3.8 ns fall time. These time constants were measured during beam tests and are reported in [B+08].

Gaussian noise is added and the signal is split in $12:1$ ratio[2], where the split signals correspond to high- and low-threshold channels respectively. Both signals are digitized with a time-over-threshold logic. Position and width of the first two digital pulses is stored into RDO. All 16 RDOs are then packaged together into a container which is saved for later usage.

6.3.3 General simulation results

For the first results presented here hit information, along with part of Monte Carlo truth, was used. This was one of the first BCM simulations. At the time there were no official ATLAS Monte Carlo productions available yet that would include BCM. Therefore full detector was simulated on a local Athena installation. A sample of $51\mathrm{k}$ PYTHIA [PYT] minimum bias proton-proton (pp) collisions at $\sqrt{s} = 14\,\mathrm{TeV}$ was simulated at nominal IP (origin of ATLAS coordinate system). Since colliding bunches are not point-like, original vertices should be distributed in z[3]. This sample had no such distribution. Though not entirely realistic, it enabled orienteering in the world of simulation and to provide a basic quantitative estimation. It also enabled to study the effect of primary vertex displacement with an additionally generated sample under equal conditions, with the exception of primary vertices position which was set to $z = 10\,\mathrm{cm}$.

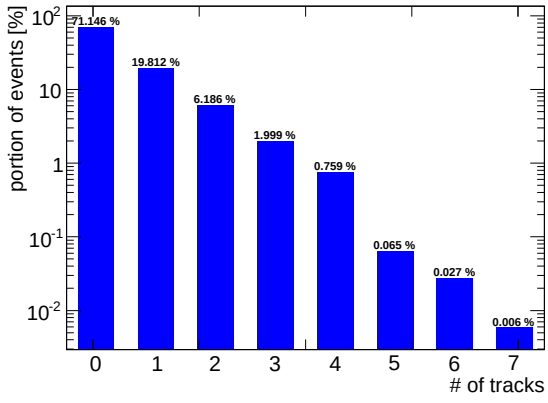

Figure 6.4: *Probability distribution for number of tracks passing through BCM modules within single event (single pp collision). In $\sim 71\%$ of events no particle passes through the BCM diamonds.*

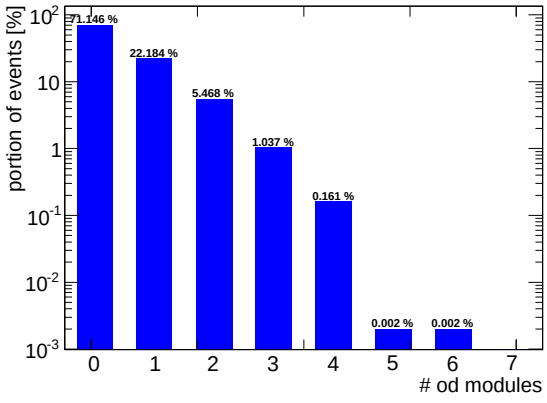

Figure 6.5: *Probability distribution for number of BCM modules being hit within single pp collision.*

[2]This ratio will be changed in the future to adapt the digitization to the hardware modification in circuits preceding NINO modules. These changed the ratio to approx. $100:1$ and verification of this number is needed before the software change is made.

[3]Distributions over x and y are in the order of few ten $\mu\mathrm{m}$ and have no impact on simulation.

Results for z=0 cm sample

First the results obtained from $z = 0\,\mathrm{cm}$ sample. Each pp collision was analyzed separately and no pile-up was added (due to no pile-up, the event represents a single pp collision). The track multiplicities were extracted with the help of Monte Carlo truth information that uniquely labels each track, enabling summation of all hits belonging to the same passing particle. The probability distribution can be seen in figure 6.4. In around $29\,\%$ of events some particle passes the BCM diamonds. It should be stressed that no metalization was taken into account, so in measurements correction factor of 0.64 should be applied[4]. Figure 6.5 is similar, showing the distribution of number of modules being hit. This is a bit closer to luminosity since the module hit status is checked to see if event passes luminosity algorithm criteria. Here the first and very raw estimation for luminosity efficiency can be done. For OR algorithm on half of the detector (since modules are split among two luminosity measurements) one would expect half of events to pass the OR algorithm, giving estimation of $\sim 14\%$. It should be stressed, that no pile-up, digitization or timing cuts were performed and this value is meant only as an order of magnitude prediction.

Focusing back on the simulated sample, one can look at particle types. The list is given in table 6.1. Electrons and pions strongly dominate, while protons and kaons can also be found.

Particle	Fraction [%]
π^-	23.1
π^+	22.7
e^-	23.5
e^+	11.2
p	2.9
K^+	2.8
K^-	2.8
others	11.0

Table 6.1: *Particles passing through BCM diamonds. The values represent fractions of given particle type with respect to all passing particles. Among the particles commonly listed under 'others' muons prevail but one can also find γ, Σ,...*

Another quantity to inspect is the energy deposition. The hit energies have been summed up for each individual module on each event. Obtained energy deposition was histogramed and its distribution can be seen on figure 6.6. Taking MIP ionization loss of $0.47\,\mathrm{MeV/mm}$ [ZH94] for polycrystalline diamond used in BCM, and the effective thickness of BCM diamond stack $\sqrt{2} * 1\,\mathrm{mm}$, the most probable energy loss equals $0.66\,\mathrm{MeV}$. This agrees with simulation. The $\sqrt{2}$ in the thickness calculation is due to the fact that particles coming from IP have ~ 45 angle with respect to the diamond surface. Of coarse not all particles come from the same direction, thus the energy distribution is a smeared Landau distribution. Perhaps the most special feature is the low energy part. Here the main contributors are particles piercing the diamond near

[4]The diamond size is $10\,\mathrm{mm} \times 10\,\mathrm{mm}$, while only $8\,\mathrm{mm} \times 8\,\mathrm{mm}$ area or 64% is metalized.

the edges, piercing both or only one. Additionally some of the particles are generated during G4 simulation as a byproduct of primary particle interactions with matter - these are named *secondary particles*. Some of them are generated within BCM diamond and therefore pass less material and leave less energy before exiting it. Though neither the beam abort logic, nor the luminosity measurements rely on energy deposition measurements, the implicit dependence remains. During digitization thresholds are set, which cut off a portion of low energy signals. This dependence will be further discussed in 6.3.5.

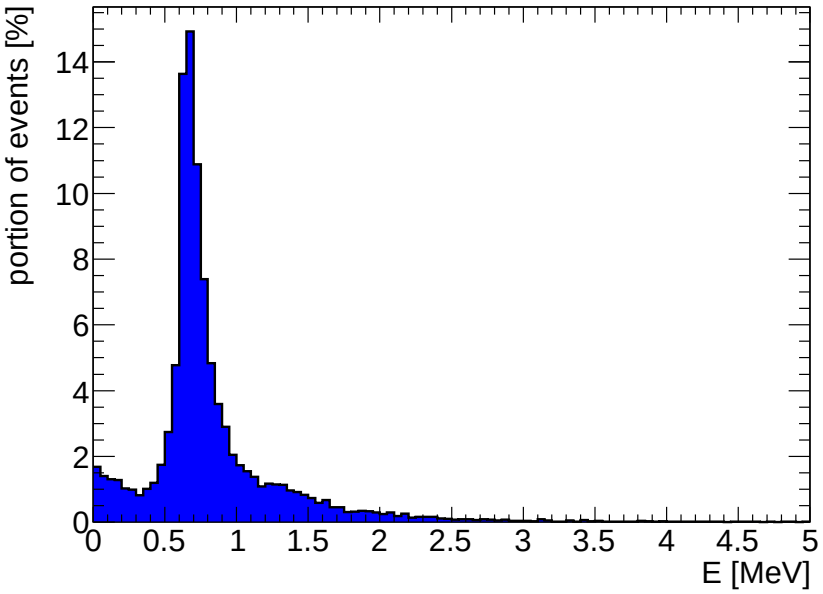

Figure 6.6: *Distribution of energy deposits within a single module. Contribution at small energies is largely due to particles piercing the diamond near the edges and thus passing through it for very short distances. The probability for two particles passing the same diamond stack within the same pp collision is unfortunately too low for the double-energy peak to be clearly visible.*

Due to good timing resolution of the BCM system, another thing worth looking into is the particle timing. The particle arrival time is histogramed in figure 6.7. Time of pp collision is defined as $t = 0$ and the earliest particles are those that follow the straight line from IP to BCM module, arriving at $\sim 1.88\,\mathrm{m}/3 \times 10^8 \frac{\mathrm{m}}{s} = 6.25\,\mathrm{ns}$. One thing to note is that all particles do not arrive to BCM modules at the expected $6.25\,\mathrm{ns}$. A small fraction of particles is delayed, and these are dominantly secondary particles. This hints to two things:

- in figure 6.7 time scale spans over $25\,\mathrm{ns}$ (single BCID). It is clear that the vast majority of particles is detected within the same BCID. However, it is not hard to imagine that some tiny fraction is transfered to the next BCID. Though obviously no disaster, it could offer an additional contribution to luminosity measurement systematics. Once LHC reaches $25\,\mathrm{ns}$ bunch spacing this could add some artificial luminosity to the next bunch. The

contribution is negligible but it should be proven so, and luminosity simulation should be done to estimate this contribution. How this is achieved will be described in the next section and followed up with results in 6.3.5.

- secondly, the larger particle arrival time indicates that these particles have either been strongly scattered or have not been produced near IP-BCM path. This effectively lengthens particles paths and the total time needed to reach the BCM modules.

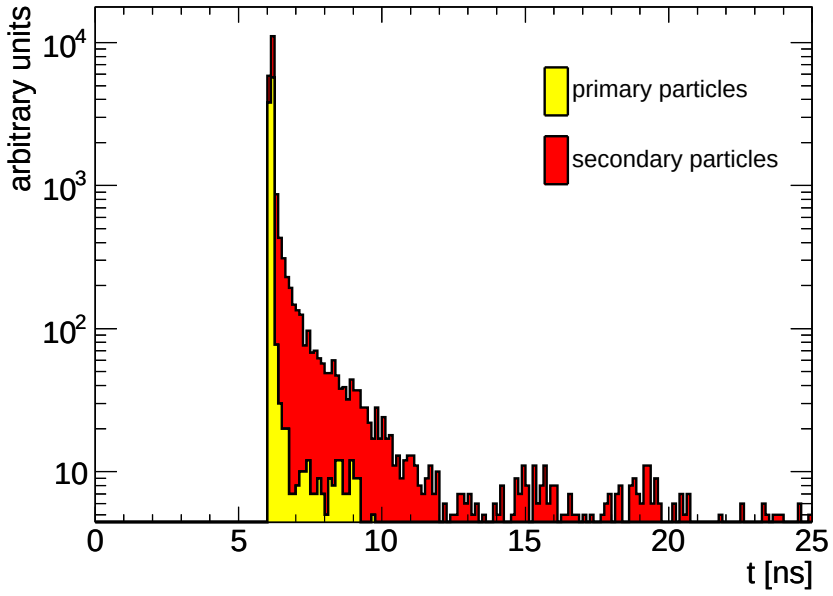

Figure 6.7: *Time of particle's arrival at BCM modules. It is a histogram stack, for primary and secondary particles. A sharp edge shows that most, but not all, particles reach BCM right after minimal time needed. This indicates that the majority of detected particles originates near the IP-BCM path.*

To investigate the particles' origin Monte Carlo truth has been used. Only the particles detected in module no. 3 (A-Y module) were taken and their origins shown in figure 6.8 and 6.9. The former shows the data in the $r - z$ plane, while the latter shows $x - y$ cross-section. Particles coming from IP are primary particles produced by generator, all others are secondary particles. The biggest contributors of those are the beam pipe and the Pixel detector. Beam pipe contributes mostly hits with arrival time close to minimal arrival time, while the Pixel secondaries contribute to the observed tail in the hit time distribution. The contributors of particles are listed in table 6.2. From figure 6.8 one can also see that the amount of particles being scattered from the opposite side of the detector is negligible.

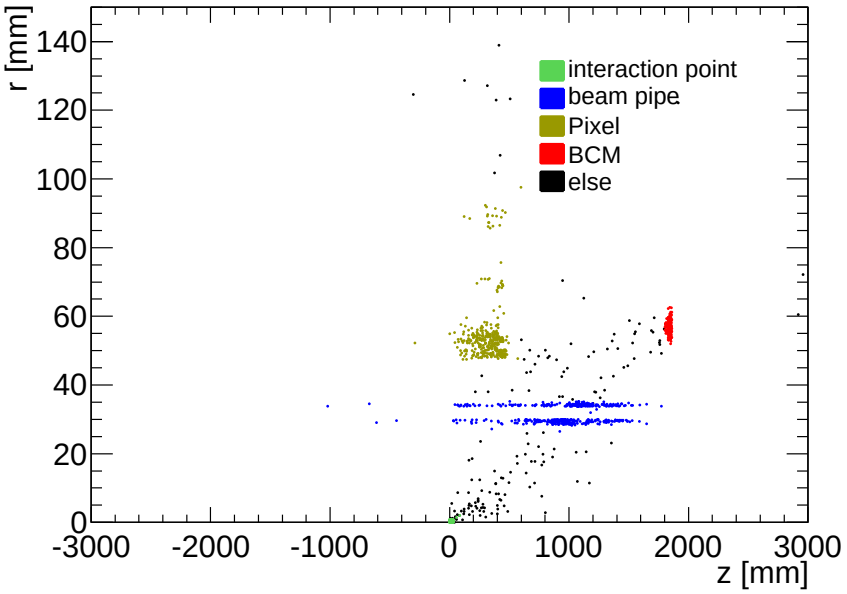

Figure 6.8: *Origins of particles that are detected in A-Y module. Detector components that are sources of secondary particles are colored differently. The biggest contributor of secondary particles is the beam pipe. Its double-wall structure with empty space inbetween is clearly visible. This geometry description has later been updated and double-wall was removed to better describe the real situation. The amount of material, however had not changed significantly, so no big effect was seen in BCM simulation. Layers of Pixel detector are nicely visible. Note the distorted scale, with a blow-up in r.*

Track origin	Fraction[%]	Primary/secondary
IP	45.9	primary (45.9%)
beam pipe	18.9	secondary (54.1%)
Pixel	12.9	
BCM	7.6	
else	14.7	

Table 6.2: *Contributors of particles detected with the BCM. More than half of particles are secondaries, the biggest contribution coming from beam pipe.*

Results for z=10 cm sample

The second simulated sample of 51k pp collisions, with primary vertices displaced to $z = 10\,\text{cm}$ was used to produce the following results. The same analysis procedure was used as with the original sample, and no pile-up was applied either. Results revealed some additional interesting BCM features.

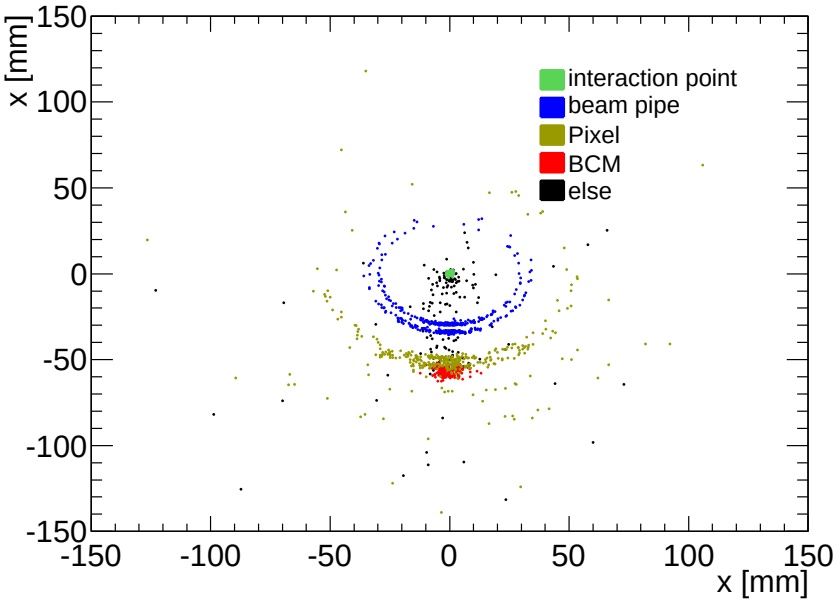

Figure 6.9: *x-y scatter plot of origins of particles that are detected in A-Y module.*

The first is identification of the particle origin. As already described, the BCM timing measurement is used to distinguish the background from interaction induced signals. Figure 6.10 shows the particles arrival time when the vertex has moved. Two peaks correspond to the two detector sides. The A-side detects the particle sooner that at nominal $6.25\,\mathrm{ns}$, while the C-side detects them later. The BCM has not been designed to detect vertex movements of this size. However, even at $10\,\mathrm{cm}$, this two peaks that are roughly $0.7\,\mathrm{ns}$ apart, would in principle have been represented with different bits in sampled data in DPUs. Thus, $10\,\mathrm{cm}$ seems to be a good estimation for the lower limit on BCM space resolution. The actual resolution is a bit worse and more timing characteristics of NINO should be implemented to give a better estimate.

Another interesting observation is the change in the measured particle rates. Simulation shows that if vertex is moved to the A-side ($z+$ side) the measured particle rate decreases on A-side and increases on C-side. Though contra-intuitive at first glance, this phenomenon can be understood by investigating the change of measured rate r_M for a single module. For it, the following equation can be written:

$$\frac{dr_M}{dz_{VX}} = j\frac{d\Omega_{BCM}}{dz_{VX}} + \frac{dj}{dz_{VX}}\Omega_{BCM}, \tag{6.15}$$

where z_{VX} is the primary vertex position, particle density flux distribution is described by j, and Ω_{BCM} is the solid angle covered by the BCM module. The two terms in the above equation describe two different contributions:

- the first term assumes that the particle source has not changed and that the difference

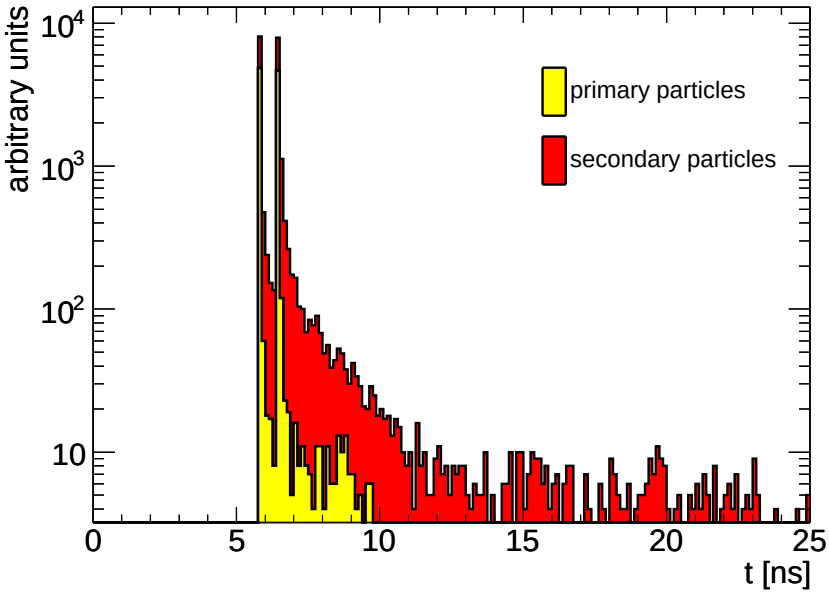

Figure 6.10: *Time of particles arrival at BCM modules when vertex is displaced by* $10\,\mathrm{cm}$ *in* $+z$ *direction. Two distinct peaks are contributed by two sides of the detector.*

comes from changing the distance to the BCM modules and thus changing its coverage. This is obviously the contribution of primary particles. The physics of pp collisions remains the same, but the primary vertex is closer to A-side modules. These modules therefore cover a bigger solid angle, thus it is more likely for particles to pass through them. Equally the rate should decrease on C-side. Due to limited statistics of the simulated sample no strong statement can be made, however the trend is visible in figure 6.11. The rate of primaries for A-side modules (modules 0-3) increased for all four modules, while the rate decreased for all C-side modules (modules 4-7).

- the second term keeps the BCM module coverage constant, but assumes the change of particle source. These are the secondary particles, whose origin distribution changes since they are induced by moved primary particles. The effect can be seen in figure 6.12 where the origin of particles detected in all eight modules is shown for both the original sample (top) and the sample where vertex was moved (bottom). It decreases the rate for modules towards which the vertex moved. As seen, largest secondary particle contribution comes from a region near the IP-module line. If vertex moves towards the module, this line passes the beam pipe under a larger angle, thus shortening the particles path within the beam pipe material. This in turn lowers the chance for production of secondary particles. The opposite is true for the other detector side. The particles must pass the beam pipe under smaller angles, thus transversing more material. The same principle governs the Pixel contribution. One side of Pixel detector moves out of IP-module path, while the other is moving towards the path of primary particles. This term therefore has an effect

opposite to that of the first term in equation 6.15. It is also the larger effect due to the large fraction of secondary particles, as can be seen in figure 6.11.

While the first term of equation 6.15 can be calculated analytically, the second term can only be estimated with Monte Carlo simulation. The outcome of simulation is highly dependent on secondary particle production, and in turn on the precision of material description. This adds additional uncertainty to the simulation.

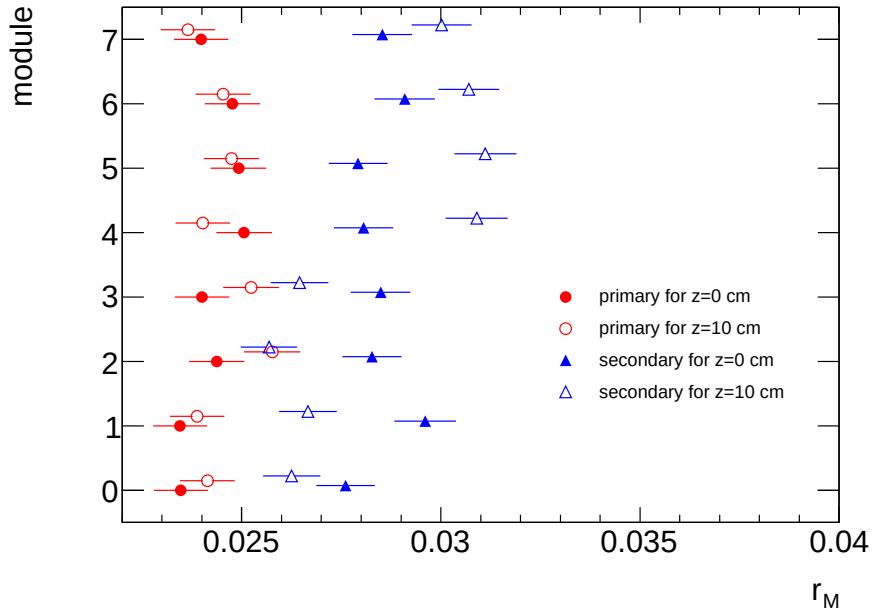

Figure 6.11: *Simulated particle rates for modules. Rates of primary and secondary particles are shown for primary vertex position $z = 0\,\mathrm{cm}$ and $z = 10\,\mathrm{cm}$. It shows that the secondary particles cause different and opposite rate change than primary particles.*

Above observations show that a change of vertex position could also have an impact on the luminosity measurement. To estimate the magnitude of the change for different luminosity algorithms a pile-up was performed. For each event a random number was chosen (according to the Poisson probability distribution) that defined how many pp interactions are going to be overlayed. After pile-up the modules have been checked for hits and luminosity algorithms were evaluated. The results for $\langle\mu\rangle = 1$ simulation can be found in table 6.3. On the available sample, due to limited statistics, no change can be seen neither for the OR algorithm, nor for the AND algorithm. There are opposite changes in the XOR algorithms, with XOR-A algorithm being less probable due to vertex move towards A-side modules. From obtained data one can

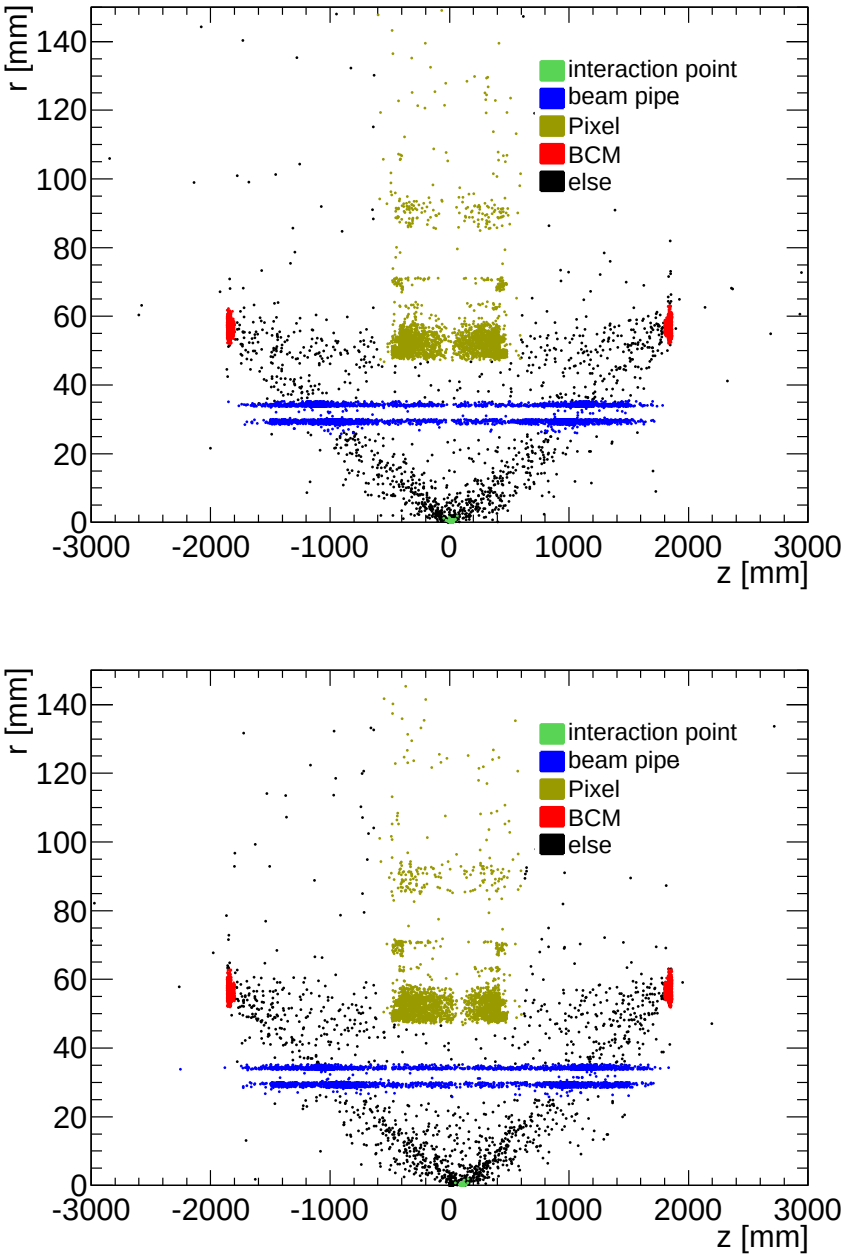

Figure 6.12: *Scatter plot of origins of particles detected in BCM, for primary vertex position $z = 0\,\mathrm{cm}$ (top), and for primary vertex moved to $z = 10\,\mathrm{cm}$ (bottom). A clear asymmetry is seen on a bottom plot, with less particles on the side toward which the vertex moved.*

estimate the sensitivity of XOR algorithms to primary vertex position:

$$\frac{dr_{XOR-A}}{dz_{vx}} = -0.034 \pm 0.023 \frac{1}{\mathrm{cm}}, \tag{6.16a}$$

$$\frac{dr_{XOR-C}}{dz_{vx}} = +0.025 \pm 0.023 \frac{1}{\mathrm{cm}}. \tag{6.16b}$$

Since these values are going to be used for error estimation in chapter 7, the biggest out of two values (one value for each DPU) was used to give the most conservative estimation.

	Fraction of events [%]			
	$z = 0\,\mathrm{cm}$ sample		$z = 10\,\mathrm{cm}$ sample	
Algorithm	vertical lumi.	horizontal lumi.	vertical lumi.	horizontal lumi.
OR	15.41 ± 0.17	15.29 ± 0.17	15.24 ± 0.17	15.32 ± 0.17
XOR-A	6.87 ± 0.12	6.70 ± 0.12	6.52 ± 0.11	6.55 ± 0.11
XOR-C	6.82 ± 0.12	6.86 ± 0.12	7.03 ± 0.11	7.11 ± 0.11
AND	1.72 ± 0.06	1.73 ± 0.06	1.69 ± 0.06	1.66 ± 0.06

Table 6.3: *Fraction of $\langle\mu\rangle = 1$ events for luminosity algorithms on both DPUs. The fractions are consistent between both DPUs for both $z = 0\,\mathrm{cm}$ and $z = 10\,\mathrm{cm}$ samples. The vertex move apparently has the biggest influence on XOR algorithms.*

6.3.4 Luminosity simulation infrastructure

The main goal of the simulation presented in this thesis is to assist in understanding the BCM detector as a luminosity monitor. The basic infrastructure presented in previous chapters was used, however the luminosity simulation deviates a little from normal simulation flow. To save time, resources, and to make simulation more flexible, especially with respect to the pile-up, the normal simulation flow is followed up to the creation of hit containers. As the next step a special Athena algorithm was written that, for each simulated pp collision, outputs the entire hit container to the ROOT files for permanent storage. These files are the input used in a dedicated luminosity simulation outside the Athena framework.

The first in line of this custom made simulation flow is the `bcmHitProvider` and derived classes. This entity is responsible for hit-information extraction from the Athena produced ROOT files. Each hit collection, corresponding to a single pp interaction, is read individually. When more pp collisions are needed in simulation:

- data can be read sequentially from a single file collection[5]. This is managed by `bcmHitRootFileCollection` class instance.
- data can be randomly mixed from different file collections. `bcmHitCollectionMix` class mixes the data from different `bcmHitRootFileCollection` instances. Any number of such instances can be registered with `bcmHitCollectionMix` along with the desired cross-sections. These cross-sections are normalized (sum should equal 1) and used as probability values on basis of which a pp datum is randomly picked form one of the registered collections.

The next stage is the event building, managed by `bcmEventBuilder` class. Independence of pp interactions is assumed, yielding the Poisson probability distribution for interaction

[5] All files in the collection must have common name start, followed by file-to-file increasing number.

multiplicity within a single bunch-crossing. For a given $\langle\mu\rangle$, a random number of interactions is chosen according to this distribution. Data for all these interactions are given by `bcmHitProvider` and pile-up is performed. This collection of overlayed hits is called `bcmDetectorEvent` and is the base for digitization.

Digitization is implemented within `bcmDigitizer` in the same way as it is within Athena. Each hit contributes a triangular signal of $2\,\mathrm{ns}$ rise- and $3.8\,\mathrm{ns}$ fall-time, whose amplitude is proportional to the deposited energy. Once the analog signal is created it is compared to two threshold levels. Digital signals are constructed for the time intervals when the thresholds are exceeded. 64-bit sampling per BCID performed by DPUs is also taken into account, finally producing 64-bit digital samples for each of 16 channels.

To completely mimic the data flow, the firmware stage of pulse reconstruction from the raw data is done as the next simulation step. The implementation is done in `rodProcessing` module and, like firmware, outputs up to two rising edge times and pulse widths for each channel at each BCID. This is then used by `bcmLumiRecorder`, emulating the luminosity-specific firmware components. All channel hit combinations are evaluated for both DPUs where the luminosity algorithm definitions are used. For each event passing the algorithm criteria the corresponding luminosity map counter is increased.

This scheme has the advantage of being able not only to simulate one BCID, but to fill all 3564 luminosity counters within a luminosity map. This is achieved with `beamStructure` component. With it, user can define $\langle\mu\rangle$ for each BCID separately, or flag the BCID with $\langle\mu\rangle_i = 0$ if no collisions are to be simulated for $\mathrm{BCID} = i$. `bcmEventBuilder` starts by building event for $\mathrm{BCID} = 1$ with parameter $\langle\mu\rangle_1$. All the hits within the $[0, 25)\,\mathrm{ns}$ window are passed to `bcmDigitizer`, while any hits with later arrival time remain in hit-overflow buffer. Once the next event is requested by `bcmDigitizer` (now for $\mathrm{BCID} = 2$), it is built with new hit information with parameter $\langle\mu\rangle_2$ and overlayed with any potential hits from hit-overflow buffer that previously corresponded to $[25, 50)\,\mathrm{ns}$. Of course any new delayed hits are added to the hit-overflow buffer and the procedure continues... This procedure can offer simulation of the entire LHC orbit with BCID-to-BCID data flow. The additional asset is the final format, which equals the format of data being recorded by lumiReader. This offers easier further processing and comparison with measured data.

6.3.5 Luminosity simulation results

For the results presented in this chapter the official ATLAS MC production datasets were used. PHOJET generator was used to model pp collision at $\sqrt{s} = 7\,\mathrm{TeV}$. Non-diffractive (ND), single-diffractive (SD), and double-diffractive (DD) components are simulated in separate datasets. Datasets:

- mc10_7TeV.106096.PhojetNdiff.merge.HITS.e574_s932_s946,
- mc10_7TeV.106098.PhojetDdiff.merge.HITS.e574_s932_s946,
- mc10_7TeV.106097.PhojetSdiff.merge.HITS.e574_s932_s946

were used to produce the results that follow. More detailed information on these datasets can be checked on AMI [AMI]. Hit information was extracted and written to ROOT files, followed by the luminosity simulation described in the previous chapter.

Efficiency estimates

The first analysis was done with the goal of estimating the efficiencies for various BCM luminosity algorithms. The simulation was set up as if only one bunch pair was filled and colliding. For a chosen $\langle\mu\rangle$, pile-up was performed and luminosity algorithms were evaluated to extract the event-type probabilities r_{OR}, r_{XOR-A}, r_{XOR-C}, and r_{AND}. Using these values the μ-correction (equations 6.8, 6.10, and 6.12) was performed. Knowing $\langle\mu\rangle$ (the initial parameter) and simulating μ_A^{vis} one can in principle use equations 6.5 to extract the efficiencies ε_A, where A stands for an arbitrary luminosity algorithm. To cover the entire luminosity range $\langle\mu\rangle$ values of 0.2, 0.4, 0.6, 0.8, 1, 2, 4, 6, 8, 10, 12, 14, 16, 18, 20, 22, and 25 were simulated. Since the value of ε_A does not depend on luminosity the plot of μ_A^{vis} vs. $\langle\mu\rangle$ was used to fit the ε_A value.

All three samples were at first analyzed separately and efficiencies for each component were calculated. All this was done with 5000 simulated bunch collisions per each $\langle\mu\rangle$ value. The results for ND sample is shown in figure 6.13, results for SD sample in figure 6.14, and for DD sample in figure 6.15. The efficiency values obtained from fits can be found in table 6.5. The overall efficiency estimates are also included in this table and were done on a mixed sample. The individual samples were mixed prior to digitization, with the relative fractions based on total sample cross-sections given in table 6.4. This simulates the actually measured scenario and the results are presented in figure 6.16.

The efficiency values from table 6.5 could be BCM calibration constants. They show that the same calibration could be used for both the vertical and the horizontal measurements. However caution must be taken when interpreting the given error estimates. These are merely statistical errors and no systematic error is included. From figure 6.16 one could make a very conservative estimation of 4% for μ-correction systematics while other contributions are harder to estimate. One of this kind would be the software description of material distribution within a detector which, as seen, plays an important role through the secondary particle production. Additional, and possibly dominant contribution comes from the event generators. For instance PYTHIA has cross-sections of $48.5\,\mathrm{mb}$, $13.7\,\mathrm{mb}$, and $9.3\,\mathrm{mb}$ for ND, SD, and DD components, respectively, for the same official ATLAS MC production. Not only that the processes are differently modeled, the total cross-section alone differs from the one predicted by PHOJET by 6%. Studies similar to this one were also performed for MBTC and LUCID, where PYTHIA samples were used as well. Results were compared and systematic uncertainty of $\sim 20\%$ was estimated [AS10]. Thus the presented values should be understood as raw estimates and the final calibration should be done by an independent measurement like the van der Meer scan.

Effect of digitization thresholds

Another influence on measured rates and in turn on luminosity excert the thresholds defining the minimum signal being digitized. As described in section 6.3.4, digitization is modeled and

Sample	PHOJET cross-section [mb]	Fraction of total cross-section [%]
non-diffractive	61.6	80.8
single-diffractive	10.7	14.0
double-diffractive	3.9	5.2
Total	76.2	100

Table 6.4: *Cross-sections for simulated samples of pp colliding at $\sqrt{s} = 7\,\mathrm{TeV}$. The fractions on basis of which the mixing was performed are shown in the right-most column.*

Efficiency	ND sample [%]	SD sample [%]	DD sample [%]	mixed sample [%]
$\varepsilon_{OR;V}$	$10.47 \pm 0.06\ (1.28)$	$4.07 \pm 0.03\ (0.52)$	$5.13 \pm 0.03\ (1.38)$	$9.32 \pm 0.04\ (1.96)$
$\varepsilon_{OR;H}$	$10.44 \pm 0.06\ (0.59)$	$4.07 \pm 0.03\ (0.82)$	$5.14 \pm 0.03\ (1.28)$	$9.32 \pm 0.04\ (1.67)$
$\varepsilon_{XOR-A;V}$	$5.10 \pm 0.04\ (0.89)$	$2.03 \pm 0.01\ (2.23)$	$2.54 \pm 0.02\ (1.85)$	$4.55 \pm 0.02\ (1.13)$
$\varepsilon_{XOR-A;H}$	$5.01 \pm 0.04\ (0.71)$	$2.04 \pm 0.01\ (1.54)$	$2.53 \pm 0.02\ (1.88)$	$4.52 \pm 0.02\ (2.09)$
$\varepsilon_{XOR-C;V}$	$5.07 \pm 0.04\ (2.51)$	$1.99 \pm 0.01\ (1.40)$	$2.50 \pm 0.02\ (2.18)$	$4.51 \pm 0.02\ (2.46)$
$\varepsilon_{XOR-C;H}$	$5.03 \pm 0.04\ (0.82)$	$1.97 \pm 0.01\ (1.24)$	$2.53 \pm 0.02\ (2.38)$	$4.53 \pm 0.02\ (1.63)$
$\varepsilon_{AND;V}$	$0.31 \pm 0.03\ (1.01)$	$0.06 \pm 0.01\ (1.43)$	$0.09 \pm 0.01\ (0.79)$	$0.27 \pm 0.02\ (0.78)$
$\varepsilon_{AND;H}$	$0.38 \pm 0.03\ (0.42)$	$0.05 \pm 0.01\ (0.95)$	$0.07 \pm 0.01\ (1.08)$	$0.26 \pm 0.02\ (1.11)$

Table 6.5: *Luminosity efficiencies for all algorithms, for both luminosity measurements (denoted with additional indices V or H for BCM-Vertical or BCM-Horizontal luminosity measurements), and for all samples. Values were obtained by fitting linear function to data presented in figures 6.13, 6.14, 6.15, and 6.16. The values in brackets represent χ^2/NDF for corresponding fits. Values for horizontal and vertical luminosity seem consistent for all algorithms and samples.*

configurable within luminosity simulation. This enabled, that a single bunch pair was simulated again, however this time always for $\langle\mu\rangle = 1$ with different NINO threshold levels. The thresholds of all eight low-threshold channels were equal and varied together. The same mixed PHOJET sample used in the previous section was used to evaluate the event-type probabilities r_A. After that the μ-corrections were made and efficiency was calculated with only one simulated point with the help of equation 6.5. The obtained efficiency trend as a function of threshold is shown in figure 6.17. The horizontal scale is normalized to the threshold needed to suppress the particle with the most probable energy loss (see figure 6.6) - this threshold is denoted by thr_{MP}. From these plots the trend was estimated by performing fit of first order polynomial ($\varepsilon_A^0 + \varepsilon_A^1 \frac{thr}{thr_{MP}}$) in the interval $(0, 0.65)$, where BCM should be operated. The slope values for OR, and XORs algorithms are given in table 6.6. The obtained parameters ε_A^1 are the ratios between the luminosity and threshold fluctuations and will be used in the next chapter. The AND algorithm unfortunately suffers from too low statistics to make any valuable assessment.

Algorithm	ε_A^0	ε_A^1	χ^2/NDF
OR - vertical lumi.	$(8.82 \pm 0.11) \times 10^{-2}$	$(-5.16 \pm 2.90) \times 10^{-3}$	0.47
OR - horizontal lumi.	$(8.85 \pm 0.11) \times 10^{-2}$	$(-7.66 \pm 2.92) \times 10^{-3}$	2.00
XOR-A - vertical lumi.	$(4.34 \pm 0.06) \times 10^{-2}$	$(-3.19 \pm 1.63) \times 10^{-3}$	0.64
XOR-A - horizontal lumi.	$(4.23 \pm 0.06) \times 10^{-2}$	$(-2.05 \pm 1.65) \times 10^{-3}$	4.09
XOR-C - vertical lumi.	$(4.19 \pm 0.06) \times 10^{-2}$	$(-2.01 \pm 1.65) \times 10^{-3}$	1.11
XOR-C - horizontal lumi.	$(4.28 \pm 0.06) \times 10^{-2}$	$(-4.36 \pm 1.65) \times 10^{-3}$	1.69

Table 6.6: *Fit parameters obtained by fitting the simulated data in $(0, 0.65)$ threshold interval. Parameter ε_A^1 gives a measure for luminosity variations with threshold. Efficiency of the AND algorithm is too low to perform a meaningful fit.*

Late hits

It was already mentioned, that some hits could be late, miss the original BCID, and fall into subsequent ones. Having dedicated luminosity simulation allows to inspect such scenario. Again a single bunch pair was set up to collide with $\langle\mu\rangle = 25$ at $\mathrm{BCID} = 100$. The figure 6.18 shows the event-type probabilities r_A as a function of BCID. Apparently some hits arrive up to 500 BCIDs too late. The bottom plot in the figure shows the blow-up near the starting BCID. It is obvious that the contribution is small; signal being already two orders of magnitude lower in the next BCID, with another order of magnitude for the second BCID after the colliding one. This holds for the XOR algorithms, and consequently for the OR, while nothing is observed for the AND algorithm outside the nominal $\mathrm{BCID} = 100$. To quantify the effect, the data for OR algorithm was used to calculate μ_{OR}^{vis} for BCIDs 100 and 101. Table 6.7 shows that the contamination of $\mathrm{BCID} = 101$ does not depend on the simulated value of $\langle\mu\rangle$. This was to be expected, since μ_{OR}^{vis} is proportional to particle multiplicity, whose constant fraction falls into next BCID. From the values it can be concluded that the contamination of the next BCID is $\sim 0.25\%$. In cases of $25\,\mathrm{ns}$ bunch trains more previous bunches contribute and effect could rise up to 0.5%. It is obvious that this is not the dominant contribution to systematic uncertainty and only contributes when a lot of BCIDs are filled with colliding bunches.

Simulated $\langle\mu\rangle$	$\mu_{OR}^{vis}(\mathrm{BCID} = 100)$	$\mu_{OR}^{vis}(\mathrm{BCID} = 101)$	Contamination [%]
25	2.33 ± 0.02	$(5.67 \pm 0.38) \times 10^{-3}$	0.24
10	0.93 ± 0.01	$(2.32 \pm 0.17) \times 10^{-3}$	0.24
1	$(9.19 \pm 0.09) \times 10^{-2}$	$(0.18 \pm 0.04) \times 10^{-3}$	0.20

Table 6.7: *Simulation of μ^{vis} for vertical luminosity measurement. OR algorithm was evaluated for three different $\langle\mu\rangle$ values and contamination of the BCID following the filled one was estimated.*

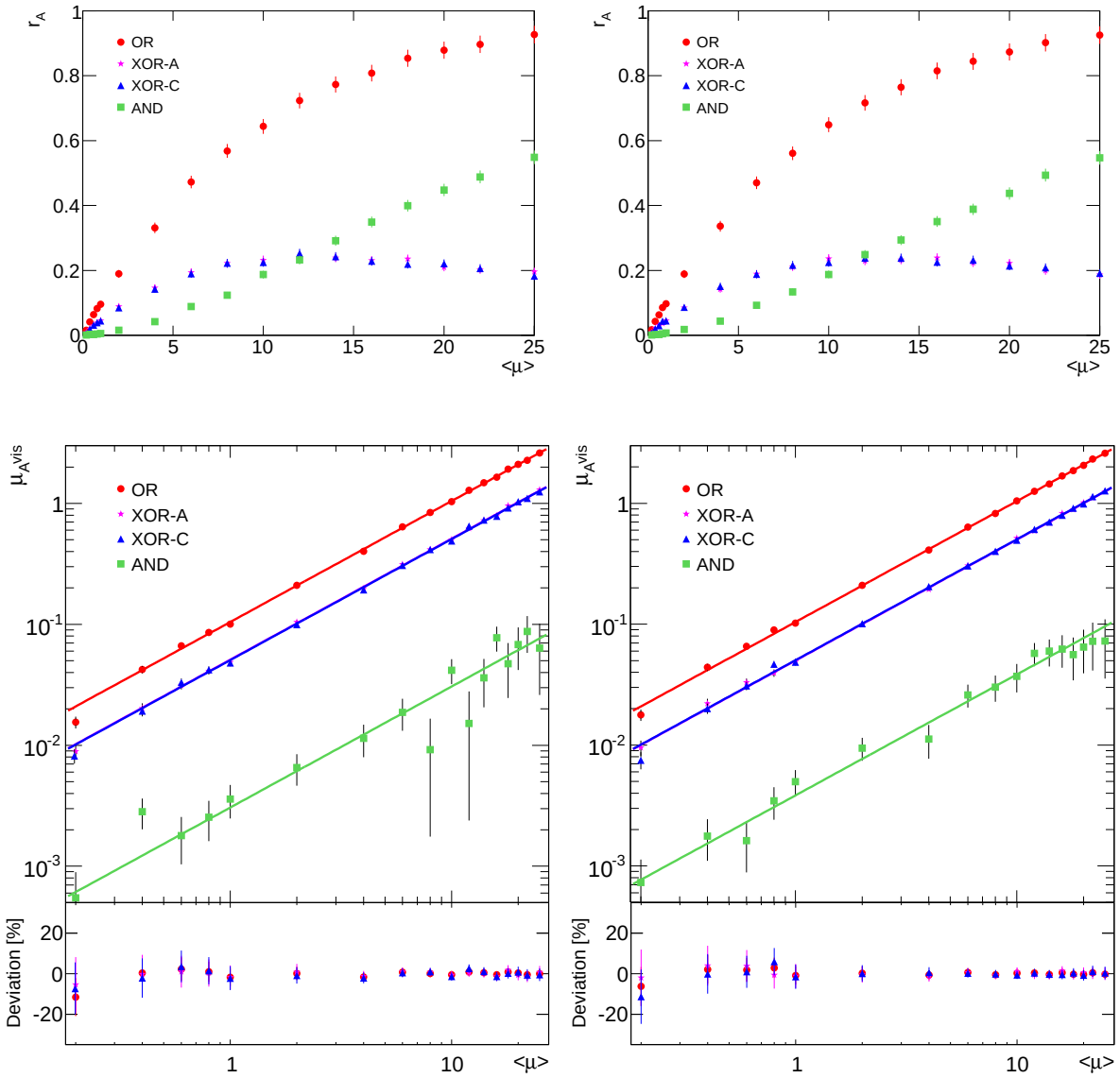

Figure 6.13: *Simulated event-type probabilities r_A (top plots) and μ_A^{vis} (bottom plots) as a function of $\langle\mu\rangle$ for ND PHOJET sample. Left plots show the data for vertical luminosity measurement, while right plots show results for horizontal luminosity measurement. The deviations between simulated and fitted μ_A^{vis} are relatively big for the AND algorithm and they are omitted to make the plots more readable. The two measurements give consistent rates and for both the XOR-A agrees with XOR-C, so no detector asymmetry is visible. In bottom plots the lines represents the efficiency fits for different algorithms.*

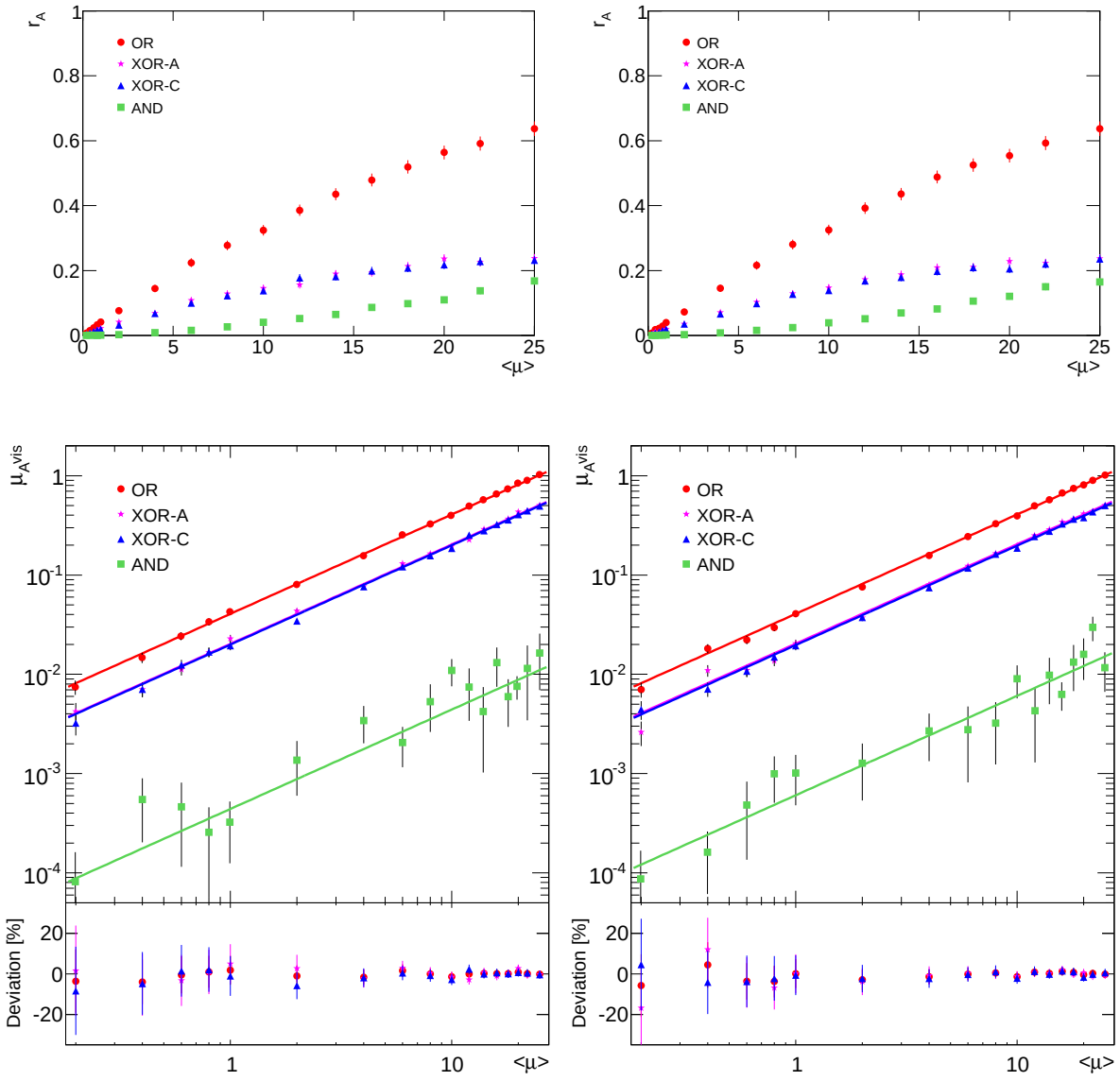

Figure 6.14: *Simulated event-type probabilities r_A (top plots) and μ_A^{vis} (bottom plots) as a function of $\langle\mu\rangle$ for SD PHOJET sample. Left plots show the data for vertical luminosity measurement, while right plots show results for horizontal luminosity measurement. The deviations between simulated and fitted μ_A^{vis} are relatively big for the AND algorithm and they are omitted to make the plots more readable. In bottom plots the lines represent the efficiency fits for different algorithms. This sample seems to have the smallest efficiencies.*

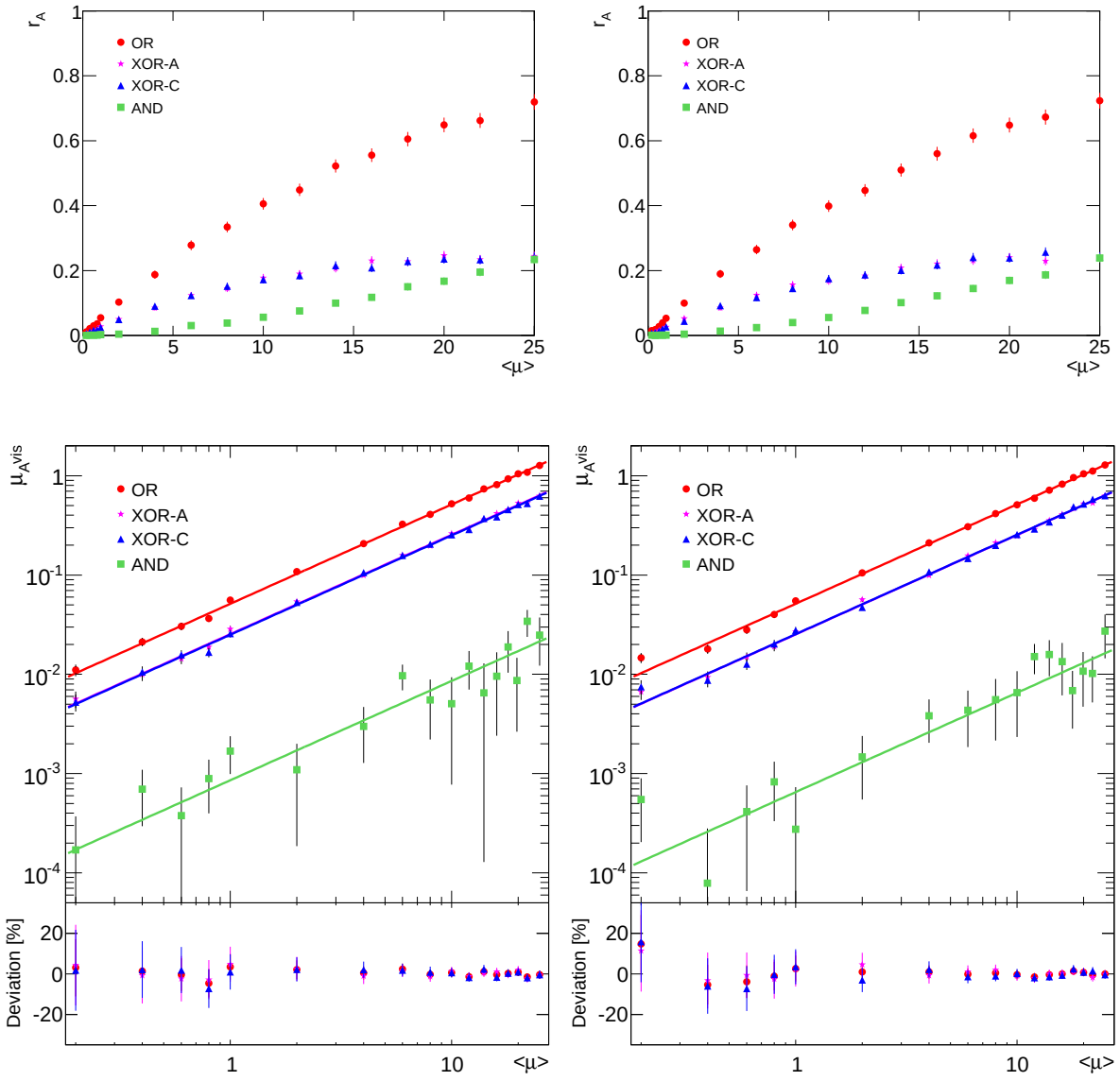

Figure 6.15: *Simulated event-type probabilities r_A (top plots) and μ_A^{vis} (bottom plots) as a function of $\langle\mu\rangle$ for DD PHOJET sample. Left plots show the data for vertical luminosity measurement, while right plots show results for horizontal luminosity measurement. The deviations between simulated and fitted μ_A^{vis} are relatively big for the AND algorithm and they are omitted to make the plots more readable. In bottom plots the line represents the efficiency fits for different algorithms.*

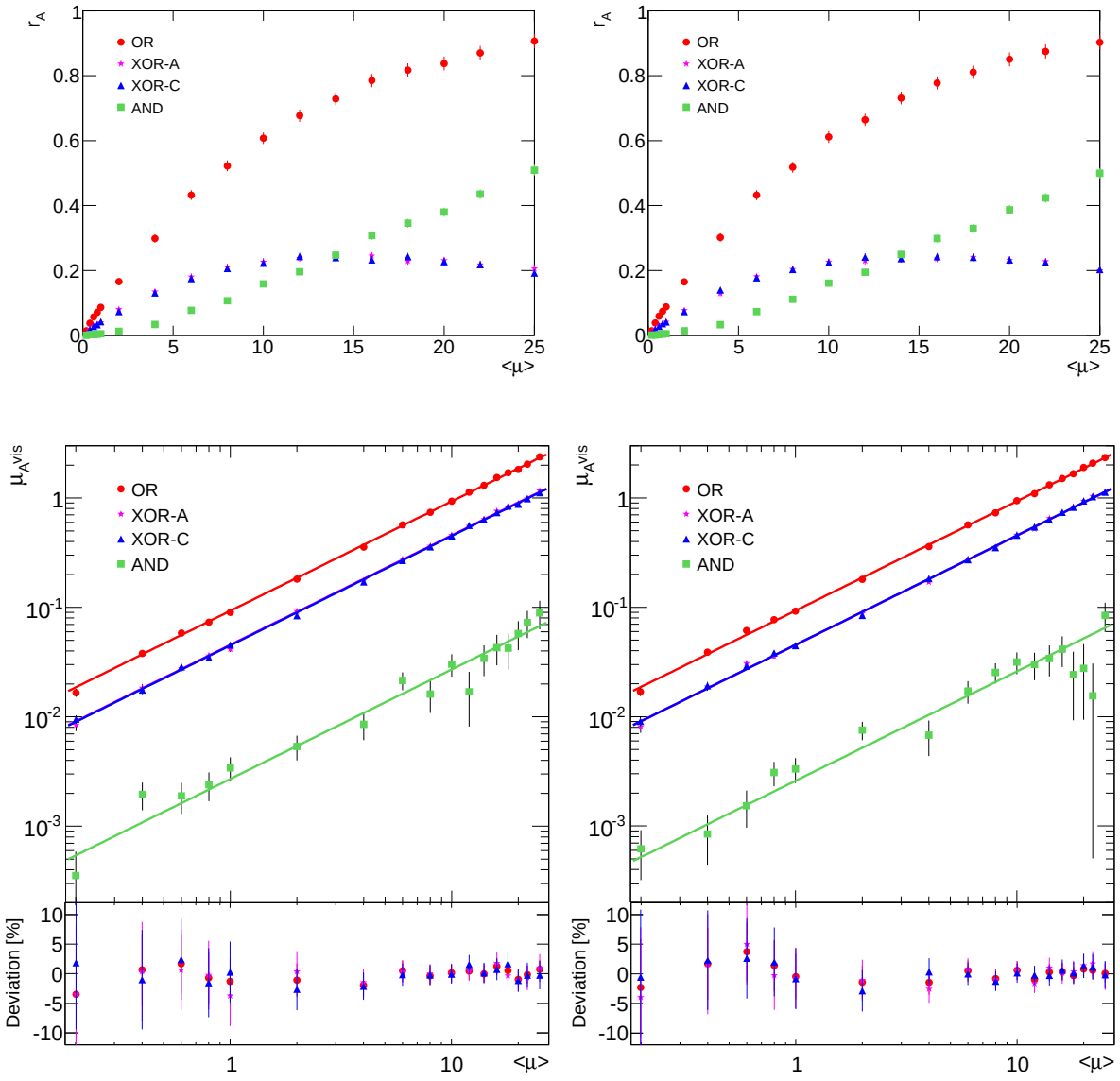

Figure 6.16: *Simulated event-type probabilities r_A (top plots) and μ_A^{vis} (bottom plots) as function of $\langle\mu\rangle$. For this the ND, SD, and DD samples were mixed to give a representative minimum bias sample. The fractions of individual samples are given in table 6.4. Left plots show the data for vertical luminosity measurement, while right plots show results for horizontal luminosity measurement. The deviations between simulated and fitted μ_A^{vis} are relatively big for the AND algorithm and are omitted to make the plots more readable. In bottom plots the line represents the efficiency fits for different algorithms.*

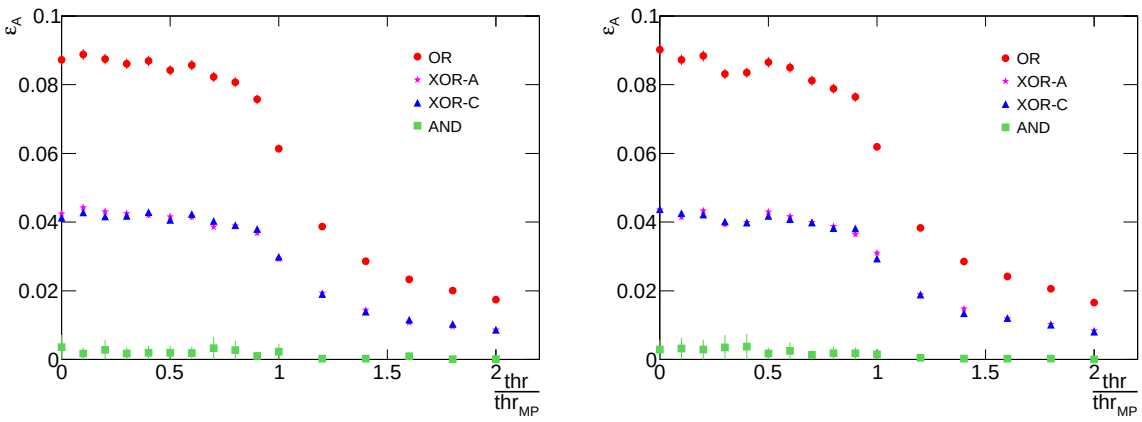

Figure 6.17: *Luminosity algorithm efficiencies as a function of threshold settings. thr_{MP} is defined as a threshold needed to suppress the particle with the most probable energy loss. BCM is operated with the threshold well below thr_{MP}. The AND algorithm data has too low statistics to be usable, since only single events passed the AND criteria at given threshold.*

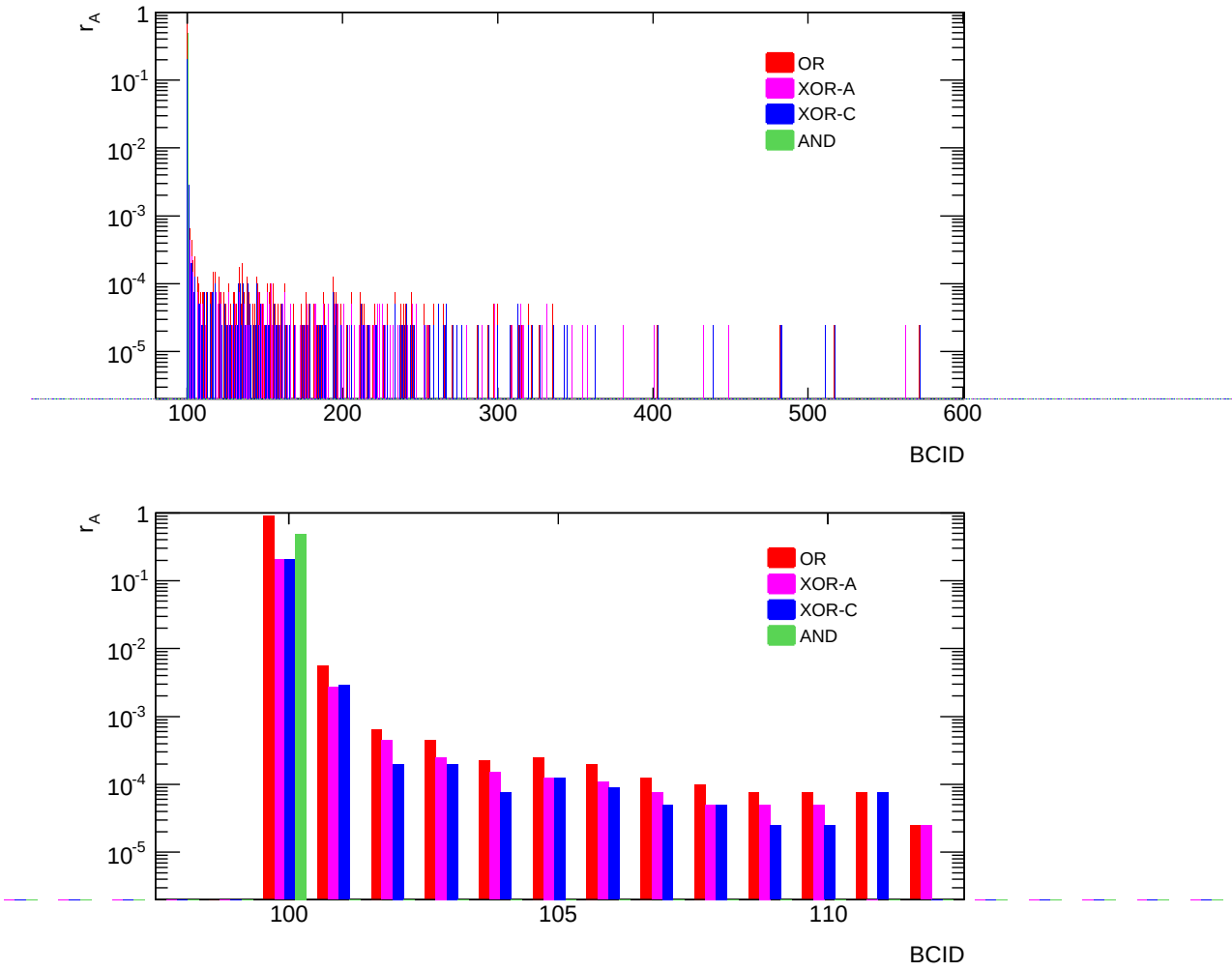

Figure 6.18: *Event-type probabilities r_A for a range of BCIDs simulated under the condition $\langle\mu\rangle = 25$. The bottom plot is a blowup near the filled* $\mathrm{BCID} = 100$*. All algorithms are shown for each BCID. For the AND algorithm all events are detected only in the filled BCID. Unlike the AND, the XOR algorithms have events passing the criteria also in the BCIDs following the filled one.*

Chapter 7

Luminosity calibration of BCM

Understanding the detector response, we now turn focus to the calibration of BCM luminosity scale. To avoid high systematic uncertainty of Monte Carlo based calibration the eventual plan is to calibrate luminosity detectors using the ALFA detector [AF08] measurements of low angle scattering. Until this calibration becomes available all ATLAS sub-detectors that provide luminosity information are calibrated using dedicated *van der Meer (vdM)* scans [1].

This chapter will begin by describing the basic principle of vdM scan. Description of scans performed at IP1 will follow, detailing also the procedures and signals needed to incorporate vdM scans into ATLAS luminosity taking. Afterwards the BCM data will be discussed and extracted calibration constants given, finishing with the discussion of systematic errors.

7.1 Van der Meer principle

One of the possible approaches, mentioned in section 2.3, is to determine luminosity from the beam parameters. Since precise luminosity determination is crucial, a dedicated measurement of these parameters would assure maximal precision. An elegant option was first proposed by S. van der Meer in 1968 [MH68]. Limiting the discussion to a single bunch, a simple expression for luminosity can be written for a collider such as LHC:

$$L = f_{rev} N_1 N_2 \int \rho_1(x,y)\rho_2(x,y)\, dxdy. \tag{7.1}$$

$N_{1(2)}$ are the bunch populations of individual bunches in beams 1(2), f_r is the revolution frequency, and $\rho_{1(2)}(x,y)$ represents the two dimensional particle density in the plane perpendicular to the beam. If one assumes that the distributions are uncorrelated in x and y, they can be factorized and a beam overlap integral can be defined separately for both directions. For x direction it is:

$$\Omega_x\,(\rho_1,\,\rho_2) = \int \rho_1(x)\rho_2(x)\, dx. \tag{7.2}$$

[1] In many other texts they are also referred to as beam-separation or luminosity scans.

The analogue expression holds for y direction. With this, luminosity is expressed:

$$L = n_b f_r N_1 N_2 \Omega_x \Omega_y. \tag{7.3}$$

The basic idea of the vdM scan is to calculate luminosity from measured parameters N_1, N_2, Ω_x, Ω_y and relate it to simultaneously measured rates. During later data taking, this relation is then used as calibration for the relative luminosity measurement of a given detector. The bunch populations $N_{1(2)}$ must be independently measured, while Ω is measured by the vdM method. Its core is the idea that the overlap integral can be extracted from the measurement:

$$\Omega_x\left(\rho_1, \rho_2\right) = \frac{R_x(0)}{\int R_x(\delta)\, d\delta}, \tag{7.4}$$

where $R(\delta)$ is the measured rate as function of beam separation δ, that equals zero when beams are perfectly aligned. Usually one expresses the result with Σ_x - the *effective beam width*:

$$\Sigma_x\left(\rho_1, \rho_2\right) = \frac{1}{\sqrt{2\pi}} \frac{1}{\Omega_x} = \frac{1}{\sqrt{2\pi}} \frac{\int R_x(\delta)\, d\delta}{R_x(0)}, \tag{7.5}$$

and the luminosity expression becomes:

$$L = \frac{f_{rev} N_1 N_2}{2\pi \Sigma_x \Sigma_y}. \tag{7.6}$$

To calculate luminosity two scans are needed - one in each direction perpendicular to the beam. During the scan the beams are displaced in given direction and the rate induced by interactions $R_{x(y)}(\delta)$ is measured as a function of beam displacement. The measured $R_{x(y)}(\delta)$ are bell-shaped curves. Note that the exact shape does not need to be assumed for the vdM method itself. Once $\Sigma_{x(y)}$ are extracted the luminosity can be calculated. It should be stressed, that the vdM method as described assumes linear detector response, thus in case of BCM, the R_{xy} are not the event-type probabilities, but the μ_A^{vis} which are a linear function of luminosity. With μ-corrections the measured peak event-type probability r_A^{peak} translates to $\mu_A^{vis,peak}$ and corresponds to the calculated luminosity. With both luminosity and $\mu_A^{vis,peak}$ measured, the equation 6.14 is used to extract the visible cross-section:

$$\sigma_A^{vis} = 2\pi \Sigma_x \Sigma_y \frac{\mu_A^{vis,peak}}{N_1 N_2}, \tag{7.7}$$

giving the absolute calibration for a luminosity detector.

The asset of the vdM method is that it allows experimental determination of visible cross-section without 'a priori' knowledge of proton-proton cross-section or of detector efficiency. Additionally there is no extra functionality needed so any luminosity aware detector can be calibrated with this method. On the other hand, it requires dedicated time and can therefore be used only occasionally for calibration.

7.2 Van der Meer scans and procedures

The vdM method requires dedicated time because the beam parameters are different and not suited for normal physics data taking. There are no bunch trains, giving a lower total count of filled bunches which also have lower intensities. The main goal of this reduced beam setup is to limit the systematic effects that might otherwise disrupt the calibration.

Table 7.1 summarizes the relevant beam characteristics for all vdM scans performed at IP1. Unfortunately the data transfer infrastructure around the BCM was not entirely finished until June 2010. Up to this time the BCM was taking luminosity data and recording it only in the private data stream, however it was missing the IS interface, making it unaware of pseudo luminosity-blocks. This prevented the BCM from actively participating in the first three vdM scans. The results presented in this chapter will therefore contain the gist of vdM scans IV & V, yielding calibration for 2010 data, and scans VII & VIII calibrating BCM for 2011 data.

The scan procedure itself was basically the same for all of the scans and is described in [VM07] and [VM10]. It starts with centering of the beams with respect to one another. This is achieved with two mini-scans one for each direction in the transverse plane. For each scan direction the beams are moved[2] by $\pm 1\sigma_b$ (σ_b is the transverse beam size) in opposite directions and measured interaction rates are used to determine the positions that give maximal beam overlap.

Following the mini-scans are the full-fledged vdM scans. The same magnets are used for beam displacement as during mini-scans, but this time they go further, up to $\pm 3\sigma_b$ for each individual beam. This gives the scanning interval of $\pm 6\sigma_b$ of relative beam displacement at the IP. The scans start at maximal negative separation and move in $-6\sigma_b \rightarrow 0 \rightarrow +6\sigma_b$ direction[3]. There were 25 scanning points in the entire interval (27 for the first three scans). The beams were left stationary for $20\,\mathrm{s}$ ($30\,\mathrm{s}$ for first three scans) at each of these points, allowing all the ATLAS sub-detectors to collect enough statistics at constant conditions. This was then followed by the period of beam-movement proceeding to the next scan point. The scans followed in close succession, first the horizontal, then the vertical scans. The May 2010 scan consisted of two consecutive horizontal scans followed by two consecutive vertical scans, whereas the the October 2010 and May 2011 procedure consisted of the sequence: horizontal scan, vertical scan, horizontal scan, and the final vertical scan.

During the scan procedures a special application, called *scan-controller* is responsible for synchronizing the ATLAS sub-detectors with the beam states. The information about the beam movement and position is received via DIP. This is the basis for publishing the ATLAS pseudo luminosity blocks (pLBs). After the period of beam movement (once the beams have stopped) a new pLB is declared. The next pLB then declares the end of constant beam position and announces the next beam movement. Here there is a technical difference between the May

[2] A pair of steering dipoles is used to create a distortion in the beam orbit called closed orbit bump. A corresponding dipole pair is located on the opposite sides of the ATLAS IP to correct for the distortion and steer the beam back on its originally intended path. This mechanism allows to move the beams in parallel to itself at the IP in either x or y direction, thus allowing the scan. Both mini-scans and vdM scans are done this way.

[3] Scan I was an exception. The sequence started with aligned beams, moved to $-6\sigma_b$, only then to $+6\sigma_b$, after which it moved back to 0 nominal separation.

2011 scan and those before it. Up to and including scan V the pLB on the beginning of the beam moving period was declared once the beams started moving. This introduces additional systematic uncertainty for BCM, since its firmware readout is not directly coupled with pLBs but occurs independently every given number of orbits. The data is then accumulated in software on the basis of pLBs and the result is transmitted to the OLC. This means that the declared pLB can fall somewhere in the last second of the pLB-accumulation. The interval of data between the pLB announcement and end of accumulation is therefore incorporated into the published data. By itself this is not an issue, however if the pLB is not declared at the exact same time as beams started moving, a small portion of the recorded data represents also the beam-moving period. Since the firmware readout has a frequency of roughly $1\,\mathrm{Hz}$ this effect was eliminated during the May 2011 scans with a time-out procedure in the scan controller. Once the beams are declared to be stable, the expected duration of this state is also given by the LHC. Scan-controller therefore knows when the magnets are going to start moving the beam again and issues the pLB at least $1\,\mathrm{s}$ before. This assures, that the entire BCM accumulation period is during non-moving beams.

During the entire scan sequence the OLC records the published sub-detector data. For each pLB the conditions database is appended with the bunch populations N_1 and N_2 for each bunch, beam displacement δ and beam parameters flag. This gives enough information for later scan analysis. In parallel to the scan-specific data taking the normal ATLAS data acquisition is running, recording events as part of normal data collection. It should be noted, however, that during this time the LB averaged luminosity information is not available, since OLC can process either pLBs or LBs but not both at the same time.

	vdM scan I April 26th, 2010	vdM scan II,III May 9th, 2010	vdM scan IV,V October 1st, 2010	vdM scan VII, VIII May 15th, 2011
BCM included	no		yes	
Scan direction	1 horizontal + 1 vertical scan	2 horizontal scans + 2 vertical scans	$2 \times$ (1 hotrizontal + 1 vertical scan)	
Scan steps per single scan	27	27	25	25
Scan range	$\pm 6\sigma_b$	$\pm 6\sigma_b$	$\pm 6\sigma_b$	$\pm 6\sigma_b$
Scan step duration	30 s	30 s	20 s	20 s
Number of colliding bunches	1	1	6	14
Total number of bunches per beam	2	2	19	38
Number of protons per bunch	$\sim 0.1 \cdot 10^{11}$	$\sim 0.2 \cdot 10^{11}$	$\sim 0.9 \cdot 10^{11}$	$\sim 0.8 \cdot 10^{11}$
β^*-function at IP1 [m]	~ 2	~ 2	~ 3	~ 1.5
Transverse beam size σ_b [μm]	~ 45	~ 45	~ 60	~ 40
Half crossing angle [μrad]	0	0	± 100	± 120
Typical bunch luminosity [$\mu b^{-1}/s$]	$4.5 \cdot 10^{-3}$	$1.8 \cdot 10^{-2}$	0.22	0.38
Typical $\langle\mu\rangle$	0.03	0.11	1.3	2.3

Table 7.1: *Summary of the relevant beam characteristics and scan parameters for vdM scans performed at ATLAS interaction point.*

7.3 Scan data analysis

The analysis results will be presented in the next section, here only the analysis procedure will be described. Most of the things described is valid for analysis of the October 2010 and May 2011 data. Any distinction between manipulation of both data sets will be explicitly given. The analysis was performed on the BCM private stream data. Having the BCM's most verbose luminosity data stream at disposal allowed the analysis of all four luminosity algorithms for both DPUs. This gives in total 8 different calibration constants which should yield the same luminosity measurement during data taking. This redundancy provides a good handle on systematic error estimation. The analysis itself is similar for both October 2010 and May 2011.

7.3.1 Data preparation

An independent analysis was done for each separate BCID, for each algorithm. The measured event-type probabilities have been μ-corrected giving $\mu^{vis}_{X(Y)}$, where X and Y denote the direction of the scan being analyzed. Since each data point requires $20\,\mathrm{s}$ and approximately the same amount of time is needed inbetween them to move the beam, the scan procedure requires some time. It is much less than the beam life time, however not negligible, meaning that the beam intensity decay should be corrected for. As mentioned, the bunch populations are recorded during the scan so the quantity $\mu^{vis}_{X(Y)}/N_1N_2 = \mu^{nr}_{X(Y)}$ expresses the measured visible number of interactions per proton in both bunches. This quantity is therefore insensitive to the beam current decay and the analysis should not be affected by it. Measuring $\mu^{nr}_{X(Y)}$ for each pLB and plotting it against beam displacement gives for the entire analysis a total of 320 vdM scan plots. A few sample plots with already fitted scan curves (next subsection) for $\mathrm{BCID} = 1$ during vdM scan IV are shown in figure 7.1.

7.3.2 Fit model

To calculate the effective beam width (equation 7.5) the integral under the scan curve must be evaluated. The scan itself provides only 25 data points, thus not allowing any simple interpolation model to be applied if higher precision is needed. This requires a choice of parametrized model for the scan curve. During initial analysis different models were tested and combinations of Gaussians for the signal and parametrization of backgrounds as constant yielded best χ^2 for the fits. Parametrizations that follow will be written as a function of x displacement, but analogue expressions hold for y direction scans.

October 2010 data: for OR, XOR-A, and XOR-C data is best described by the double Gaussian plus constant. Both Gaussians can be added like:

$$\frac{C}{\sqrt{2\pi}}\left(\frac{f_1}{\sigma_1}e^{-\frac{(x-x_0)^2}{2\sigma_1^2}} + \frac{1-f_1}{\sigma_2}e^{-\frac{(x-x_0)^2}{2\sigma_2^2}}\right), \tag{7.8}$$

where f_1 represents the area fraction of the first Gaussian with respect to the combined area. Since for calculation of cross-section also the peak value of μ_X^{nr} will be needed it is useful to re-parametrize it to amplitude instead of area. If one defines:

$$\frac{1}{\Sigma_d} = \frac{f_1}{\sigma_1} + \frac{1-f_1}{\sigma_2}, \tag{7.9}$$

then the final parametrization of the scan curve is:

$$\mu_X^{nr}(x) = \mu_X^{nr,peak} \left(\frac{f_1\Sigma_d}{\sigma_1} e^{-\frac{(x-X_0)^2}{2\sigma_1^2}} + \left(1 - \frac{f_1\Sigma_d}{\sigma_1}\right) e^{-\frac{(x-X_0)^2}{2\Sigma_d^2(1-f_1)^2}\left(1-\frac{f_1\Sigma_d}{\sigma_1}\right)^2} \right) + b_X. \tag{7.10}$$

In contrast the AND algorithm data does not need two Gaussians. The main issue for this algorithm is its high selectivity and thus low statistics. With the collected sample, the scan data can be described by a single Gaussian (see bottom of figure 7.1). On the plus side, the background is consistent with zero allowing its elimination from the fit. The parametrization in case of AND algorithm is therefore:

$$\mu_X^{nr}(x) = \mu_X^{nr,peak} e^{-\frac{(x-X_0)^2}{2\Sigma_s^2}}. \tag{7.11}$$

May 2011 data: offers a bit higher statistics also for the AND algorithm, however the parametrization 7.11 remains valid. For the OR, XOR-A, and XOR-C the double Gaussian parametrization does not improve the fit quality. In contrary, the lack of second Gaussian component makes fitting less stable, and a simpler choice was was found satisfactory:

$$\mu_X^{nr}(x) = \mu_X^{nr,peak} e^{-\frac{(x-X_0)^2}{2\Sigma_s^2}} + b_X. \tag{7.12}$$

Both parameters Σ_d and Σ_s were chosen in a way that they also represent the effective beam width, thus removing the need to integrate and simplifying the analysis. Since both parameters have the same meaning they will from now on both be denoted with a simple Σ, omitting the index. This will somewhat shorten the notation in the result tables.

7.3.3 Determination of visible cross-section

Once the fits are performed for both scan directions the parameters Σ_X, $\mu_X^{nr,peak}$, Σ_Y, and $\mu_Y^{nr,peak}$ are at hand. Equation 7.7 is used to extract visible cross-section. For the μ peak value the average of peak values in x scan and y scan direction is taken, thus giving the final calibration recipe:

$$\sigma^{vis} = \pi\Sigma_X\Sigma_Y \left(\mu_X^{nr,peak} + \mu_Y^{nr,peak}\right), \tag{7.13}$$

where the same expression holds for all luminosity algorithms.

In the next subsection the results of the fits and the calculated σ^{vis} will be presented along with their statistical errors. The errors of the fit parameters are given by `MINUIT` which was

used for fitting. The errors are then propagated according to the above expression, where extra care must be taken for $\Sigma \leftrightarrow \mu^{nr,peak}$ pairs from the same fit since they are correlated. Correlation factors $C_{\Sigma-\mu^{vis,\,peak}}$ are extracted from the fit results and used in error propagation. Only correlations between the parameters of a single fit are taken into account, whereas no correlation is assumed between x and y scans.

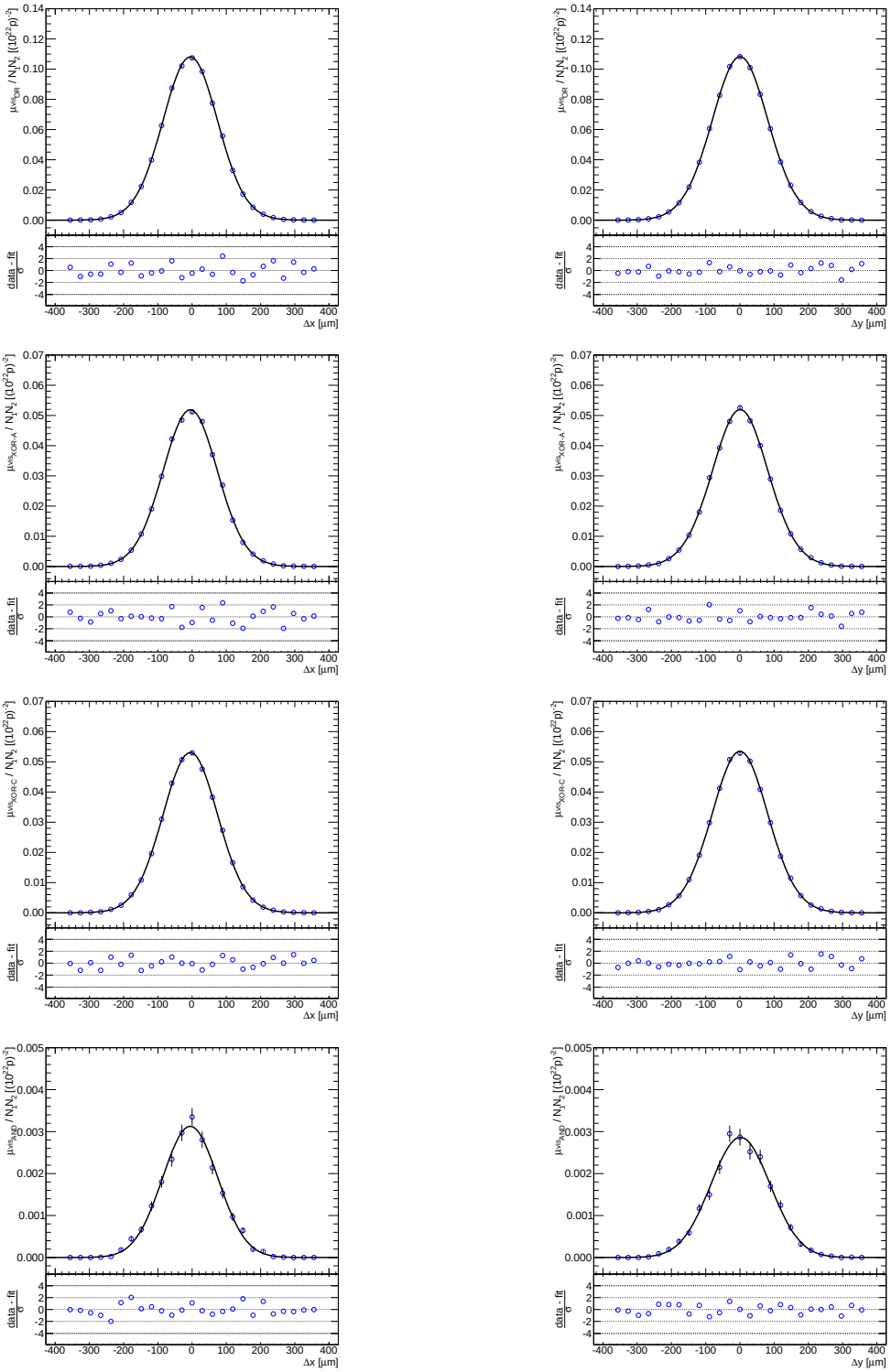

Figure 7.1: *Sample of vdM scan curves for* $\mathrm{BCID} = 1$ *of scan IV for BCM horizontal luminosity. The left column shows the X scan data, while the right column shows the Y scan data. The rows show different algorithms; from top to bottom: OR, XOR-A, XOR-C, and AND. This set of scan curves represents the minimal ensemble needed to extract calibration constants for single BCID and for single DPU.*

7.4 Results

Following the procedure described in the last section all the visible cross-sections were determined. The results will first be presented for the October 2010 scan, then followed by results of May 2011 scan.

7.4.1 Calibration of 2010 data

Due to hardware changes implemented during the 2010/2011 winter shutdown, the calibration performed in October 2010 is valid only for the 2010 data. The following subsections present and discuss the vdM data analysis results.

OR algorithm

Tables 7.3, 7.4, 7.5, and 7.6 show the fit parameters obtained from OR algorithm data for both scan IV and V, for both scan directions. The χ^2 indicates good fits with the double Gaussian. The correlation factor $C_{\Sigma_X - \mu_X^{nr,\,peak}}$ can be seen as another quality parameter in the case of double Gauss parametrization. It shows that the individual Gaussian contributions are not far from each other and that the combined structure is rather constant over BCIDs.

Two parameters that do not enter in the analysis are the background level b and the offset of the centered beams. Looking at the values of b one sees that the background is approximately four orders of magnitude below the peak value of μ^{nr}. Even more useful are offsets X_0 and Y_0 shown in figure 7.3. They represent the beam positioning, and therefore do not depend on algorithm and should thus be the same for all algorithms and both luminosity measurements. As seen they are consistent between the two BCM luminosity measurements, however there is a visible discrepancy between the two scans, showing the limits of scan reproducibility. Fortunately this is not an issue for the vdM since few $\mu\mathrm{m}$ IP displacement in any direction does not change any detector acceptance.

The next fit parameter is the μ^{nr}. Though not required, the two halves of BCM are again consistent, meaning their acceptances are very similar. More importantly, the plotted values in figure 7.4 show that the observed number of interactions is lower in scan V then in scan IV, again holding true for both BCM's halves. Since the beam current decay has already been corrected for, this shows that the emittance growth is observable in both x and y plane during the period of vdM scan.

The last parameter is the effective beam width Σ. Its value is shown in figure 7.5. Bunch to bunch variations are around $5\,\mu\mathrm{m}$, which is expected during physics operation and has its roots in the filling of the LHC or stages before that. The broadening of the beam is also observable, verifying the emittance growth already observed in the μ^{nr} plots.

The discussed fit parameters are then used to extract the visible cross-sections via equation 7.13. The final values are summarized in table 7.2 and show that the results are consistent between the scans. These are the final calibration constants. Their excellent agreement is also exhibited in figure 7.6.

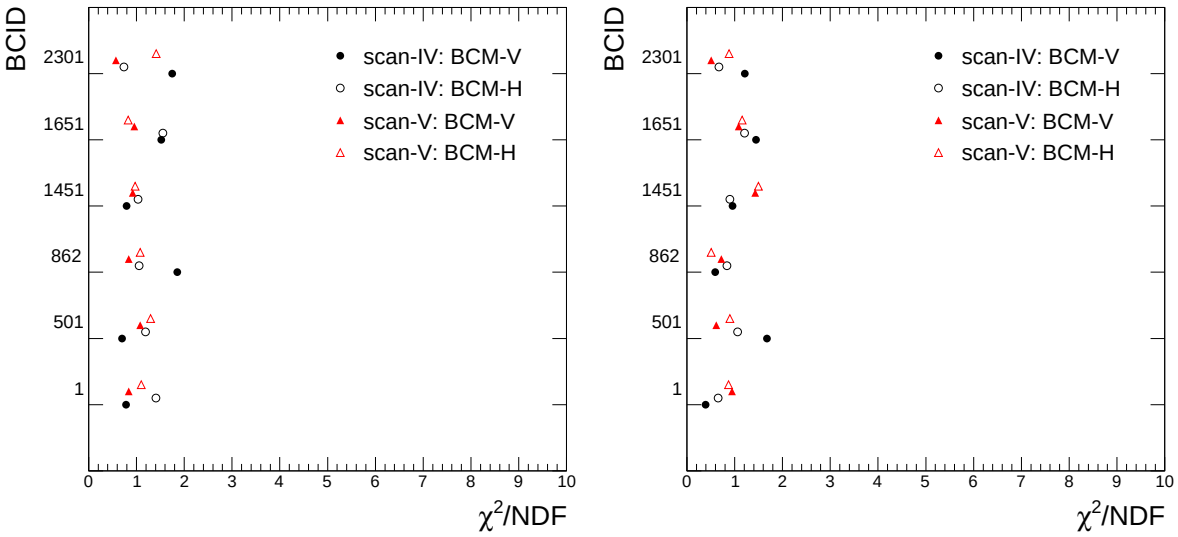

Figure 7.2: *χ^2 evaluation of the x scan (left) and y scan (right) fits for the OR algorithm data of October 2010.*

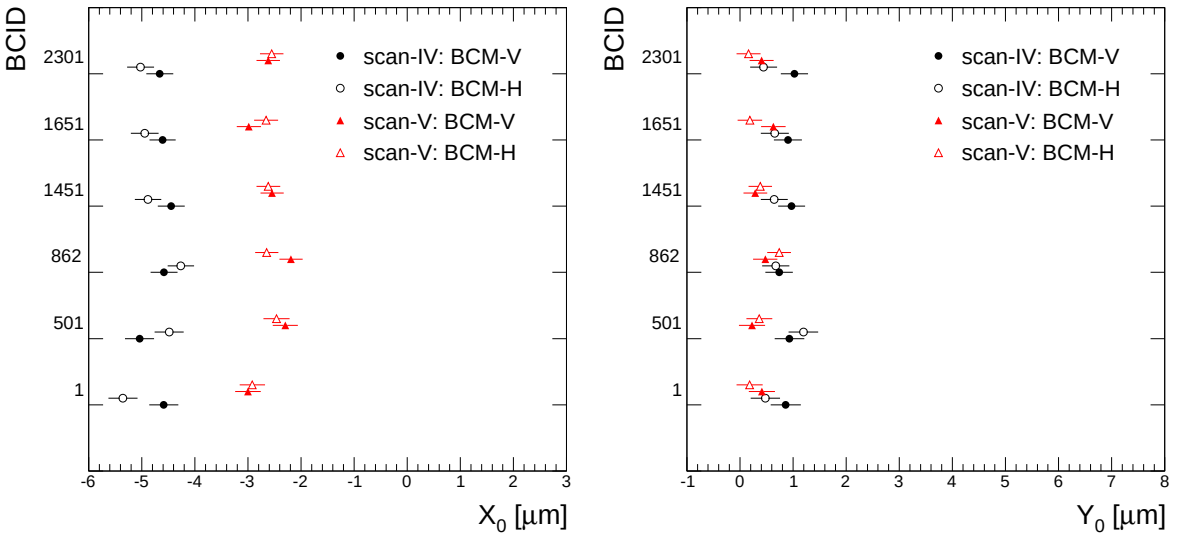

Figure 7.3: *Offset of the centered beams during x scans (left) and y scans (right) for OR algorithm. The data shows consistency between BCM horizontal and BCM vertical luminosity measurements and indicates the limit of scan reproducibility.*

The measured total pp cross-section at $\sqrt{s} = 7\,\mathrm{TeV}$ is $60.3 \pm 2.1\,\mathrm{mb}$ [TS11]. With this value the efficiency of the OR algorithm can be estimated to $(7.62 \pm 0.38)\%$. This is somewhat lower than Monte Carlo prediction [4] of $(9.32 \pm 0.05)\%$. Recognizing the systematic errors of

[4]Remember that at the time of simulation generators presumed pp cross-section of $76.2\,\mathrm{mb}$, which shows the

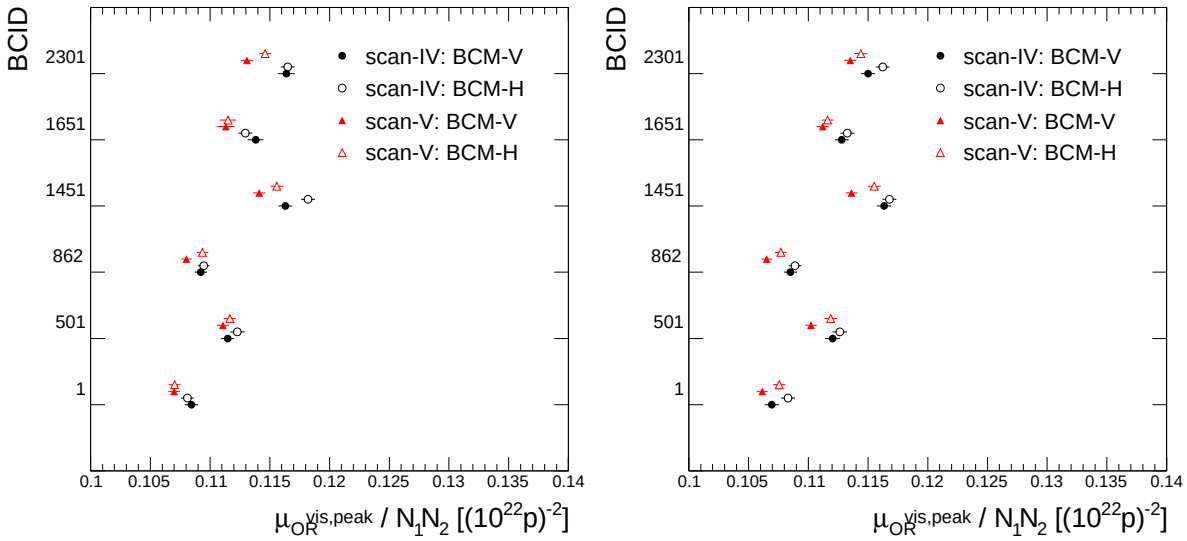

Figure 7.4: *The maximum beam current normalized μ^{vis} during x scans (left) and y scans (right) for OR algorithm. Emittance growth causes lower values for scan V with respect to scan IV, while both BCM's halves are consistent.*

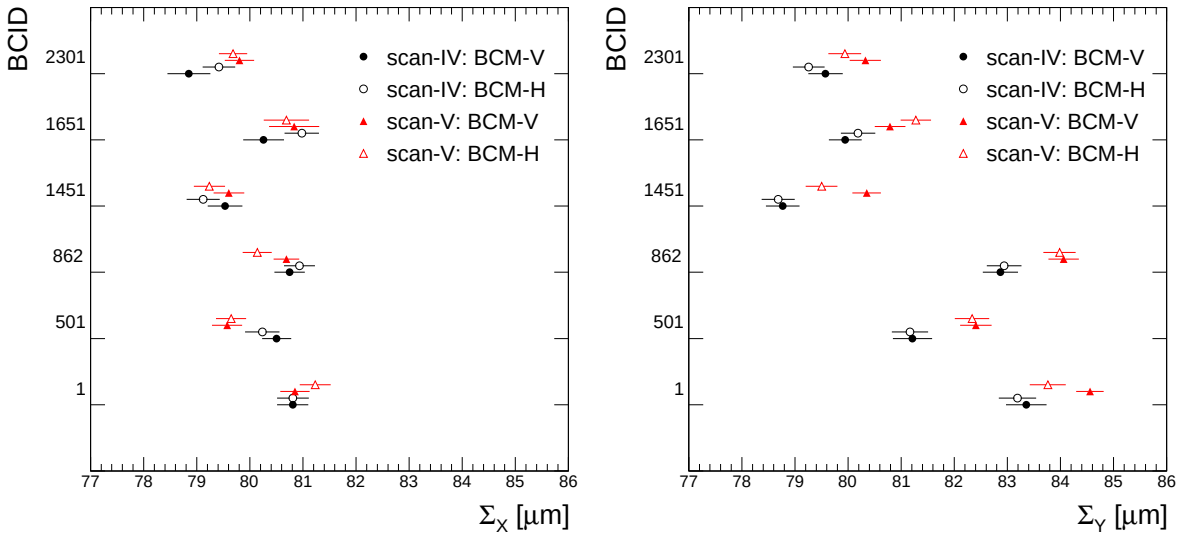

Figure 7.5: *The effective beam width as obtained form the fits of x scans (left) and y scans (right) for OR algorithm. With the exception of* $\mathrm{BCID} = 501$ *for* Σ_X *widening of beams is observable, more so in the y than in the x direction.*

$\sim 20\%$ estimated for the Monte Carlo method the predictions are relatively close.

modeling error, to which one must additionally add uncertainties of ND, SD, DD component mixing.

BCID	Visible cross-section [mb]			
	BCM-Verical		BCM-Horizontal	
	Scan IV	Scan V	Scan IV	Scan V
1	4.558 ± 0.017	4.578 ± 0.014	4.571 ± 0.017	4.587 ± 0.016
501	4.591 ± 0.017	4.559 ± 0.016	4.602 ± 0.018	4.605 ± 0.016
862	4.577 ± 0.016	4.572 ± 0.014	4.605 ± 0.017	4.589 ± 0.015
1451	4.579 ± 0.017	4.576 ± 0.015	4.596 ± 0.017	4.574 ± 0.015
1651	4.568 ± 0.017	4.566 ± 0.018	4.615 ± 0.017	4.597 ± 0.018
2301	4.561 ± 0.018	4.563 ± 0.015	4.602 ± 0.016	4.583 ± 0.015
Average	4.573 ± 0.007	4.569 ± 0.006	4.599 ± 0.007	4.589 ± 0.006
RMS	0.011	0.007	0.013	0.010

Table 7.2: *Calculated visible cross-section for OR algorithm during October 2010 calibration.*

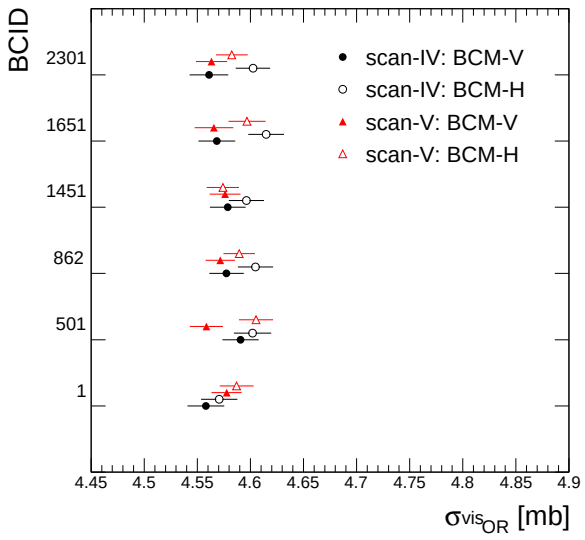

Figure 7.6: *Visible cross-sections for both BCM luminosity measurements, both scans, and all BCIDs. An excellent agreement is obtained for the OR algorithm.*

BCID	Scan	$X_0[\mu m]$	$b_X[10^{-4}\,(10^{22}p)^{-2}]$	$\Sigma_X[\mu m]$	$\mu_X^{nr,\,peak}[(10^{22}p)^{-2}]$	$C_{\Sigma_X-\mu_X^{nr,\,peak}}$	χ^2/NDF
1	IV	-4.59 ± 0.28	0.00 ± 0.07	80.81 ± 0.29	0.1085 ± 0.0005	-0.74	0.78
	V	-3.00 ± 0.24	0.23 ± 0.13	80.85 ± 0.28	0.1070 ± 0.0005	-0.75	0.84
501	IV	-5.04 ± 0.27	0.00 ± 0.05	80.50 ± 0.27	0.1115 ± 0.0005	-0.71	0.70
	V	-2.30 ± 0.24	0.24 ± 0.11	79.57 ± 0.28	0.1111 ± 0.0005	-0.76	1.08
862	IV	-4.58 ± 0.25	0.19 ± 0.12	80.75 ± 0.29	0.1092 ± 0.0005	-0.75	1.86
	V	-2.19 ± 0.22	0.08 ± 0.12	80.69 ± 0.24	0.1080 ± 0.0004	-0.73	0.84
1451	IV	-4.45 ± 0.25	0.17 ± 0.12	79.53 ± 0.33	0.1163 ± 0.0006	-0.79	0.79
	V	-2.55 ± 0.22	0.13 ± 0.08	79.60 ± 0.29	0.1141 ± 0.0005	-0.79	0.92
1651	IV	-4.61 ± 0.25	0.22 ± 0.10	80.26 ± 0.38	0.1138 ± 0.0007	-0.84	1.52
	V	-2.98 ± 0.23	0.08 ± 0.07	80.84 ± 0.47	0.1113 ± 0.0007	-0.90	0.96
2301	IV	-4.66 ± 0.25	0.03 ± 0.07	78.85 ± 0.40	0.1164 ± 0.0007	-0.85	1.75
	V	-2.62 ± 0.22	0.00 ± 0.21	79.80 ± 0.28	0.1131 ± 0.0005	-0.78	0.57

Table 7.3: *Fit parameters obtained for October 2010 X sub-scans of scans IV and V for OR algorithm data from BCM vertical luminoisty.*

BCID	Scan	$Y_0[\mu m]$	$b_Y[10^{-4}\,(10^{22}p)^{-2}]$	$\Sigma_Y[\mu m]$	$\mu_Y^{nr,\,peak}[(10^{22}p)^{-2}]$	$C_{\Sigma_Y-\mu_Y^{nr,\,peak}}$	χ^2/NDF
1	IV	$+0.86 \pm 0.28$	0.47 ± 0.16	83.36 ± 0.38	0.1069 ± 0.0006	-0.80	0.39
	V	$+0.41 \pm 0.25$	0.00 ± 0.24	84.55 ± 0.26	0.1061 ± 0.0004	-0.73	0.94
501	IV	$+0.93 \pm 0.28$	0.03 ± 0.12	81.21 ± 0.37	0.1120 ± 0.0006	-0.80	1.68
	V	$+0.23 \pm 0.25$	0.20 ± 0.25	82.41 ± 0.30	0.1102 ± 0.0005	-0.73	0.61
862	IV	$+0.74 \pm 0.26$	0.30 ± 0.15	82.87 ± 0.33	0.1085 ± 0.0005	-0.78	0.59
	V	$+0.48 \pm 0.23$	0.41 ± 0.15	84.06 ± 0.29	0.1065 ± 0.0005	-0.77	0.72
1451	IV	$+0.97 \pm 0.25$	0.31 ± 0.12	78.77 ± 0.32	0.1163 ± 0.0006	-0.78	0.95
	V	$+0.29 \pm 0.22$	0.16 ± 0.11	80.35 ± 0.27	0.1136 ± 0.0005	-0.77	1.43
1651	IV	$+0.90 \pm 0.26$	0.00 ± 0.30	79.95 ± 0.31	0.1128 ± 0.0006	-0.77	1.45
	V	$+0.63 \pm 0.23$	0.27 ± 0.13	80.79 ± 0.29	0.1112 ± 0.0005	-0.78	1.08
2301	IV	$+1.03 \pm 0.26$	0.14 ± 0.12	79.57 ± 0.32	0.1150 ± 0.0006	-0.78	1.21
	V	$+0.41 \pm 0.23$	0.07 ± 0.14	80.32 ± 0.29	0.1135 ± 0.0005	-0.78	0.51

Table 7.4: *Fit parameters obtained for October 2010 Y sub-scans of scans IV and V for OR algorithm data from BCM vertical luminoisty.*

BCID	Scan	$X_0[\mu m]$	$b_X[10^{-4}\,(10^{22}p)^{-2}]$	$\Sigma_X[\mu m]$	$\mu_X^{nr,\,peak}[(10^{22}p)^{-2}]$	$C_{\Sigma_X-\mu_X^{nr,\,peak}}$	χ^2/NDF
1	IV	-5.35 ± 0.27	0.20 ± 0.16	80.81 ± 0.30	0.1081 ± 0.0005	-0.73	1.41
	V	-2.92 ± 0.24	0.24 ± 0.12	81.23 ± 0.29	0.1070 ± 0.0005	-0.76	1.10
501	IV	-4.48 ± 0.27	0.25 ± 0.14	80.23 ± 0.32	0.1123 ± 0.0006	-0.76	1.19
	V	-2.46 ± 0.25	0.26 ± 0.11	79.65 ± 0.28	0.1117 ± 0.0005	-0.75	1.30
862	IV	-4.26 ± 0.25	0.36 ± 0.20	80.93 ± 0.29	0.1095 ± 0.0005	-0.72	1.06
	V	-2.65 ± 0.22	0.14 ± 0.07	80.14 ± 0.28	0.1094 ± 0.0005	-0.77	1.08
1451	IV	-4.88 ± 0.25	0.17 ± 0.12	79.12 ± 0.31	0.1182 ± 0.0006	-0.78	1.03
	V	-2.62 ± 0.22	0.13 ± 0.07	79.24 ± 0.29	0.1156 ± 0.0005	-0.81	0.97
1651	IV	-4.94 ± 0.26	0.00 ± 0.20	80.98 ± 0.32	0.1130 ± 0.0006	-0.78	1.55
	V	-2.66 ± 0.23	0.17 ± 0.08	80.69 ± 0.43	0.1115 ± 0.0007	-0.88	0.83
2301	IV	-5.02 ± 0.25	0.00 ± 0.07	79.42 ± 0.31	0.1165 ± 0.0006	-0.78	0.74
	V	-2.55 ± 0.22	0.11 ± 0.07	79.68 ± 0.27	0.1146 ± 0.0005	-0.76	1.41

Table 7.5: *Fit parameters obtained for October 2010 X sub-scans of scans IV and V for OR algorithm data from BCM horizontal luminoisty.*

BCID	Scan	$Y_0[\mu m]$	$b_Y[10^{-4}\,(10^{22}p)^{-2}]$	$\Sigma_Y[\mu m]$	$\mu_Y^{nr,\,peak}[(10^{22}p)^{-2}]$	$C_{\Sigma_Y-\mu_Y^{nr,\,peak}}$	χ^2/NDF
1	IV	$+0.48 \pm 0.28$	0.03 ± 0.17	83.19 ± 0.35	0.1083 ± 0.0006	-0.78	0.65
	V	$+0.18 \pm 0.25$	0.33 ± 0.18	83.76 ± 0.34	0.1076 ± 0.0005	-0.79	0.87
501	IV	$+1.20 \pm 0.28$	0.06 ± 0.13	81.17 ± 0.34	0.1126 ± 0.0006	-0.77	1.06
	V	$+0.36 \pm 0.24$	0.38 ± 0.17	82.33 ± 0.32	0.1119 ± 0.0005	-0.79	0.90
862	IV	$+0.67 \pm 0.26$	0.19 ± 0.17	82.94 ± 0.33	0.1089 ± 0.0005	-0.77	0.84
	V	$+0.74 \pm 0.22$	0.40 ± 0.14	83.98 ± 0.30	0.1077 ± 0.0005	-0.79	0.51
1451	IV	$+0.64 \pm 0.25$	0.14 ± 0.12	78.69 ± 0.31	0.1168 ± 0.0006	-0.78	0.90
	V	$+0.38 \pm 0.22$	0.39 ± 0.12	79.50 ± 0.30	0.1155 ± 0.0005	-0.79	1.50
1651	IV	$+0.66 \pm 0.26$	0.21 ± 0.12	80.19 ± 0.32	0.1133 ± 0.0006	-0.78	1.20
	V	$+0.19 \pm 0.23$	0.10 ± 0.18	81.27 ± 0.29	0.1116 ± 0.0005	-0.75	1.16
2301	IV	$+0.44 \pm 0.25$	0.15 ± 0.16	79.26 ± 0.30	0.1162 ± 0.0006	-0.75	0.67
	V	$+0.16 \pm 0.23$	0.26 ± 0.11	79.94 ± 0.31	0.1144 ± 0.0005	-0.81	0.88

Table 7.6: *Fit parameters obtained for October 2010 Y sub-scans of scans IV and V for OR algorithm data from BCM horizontal luminoisty.*

XOR-A algorithm

The XOR-A fit parameters are collected in tables 7.8, 7.9, 7.10, and 7.11. The fits exhibit similar χ^2 as for OR algorithm with a bit more distributed correlation factors $C_{\Sigma_X - \mu_X^{nr,\,peak}}$.

The background levels b_X are again orders of magnitude lower that the peak value of μ^{nr}. Most of them differ from zero no more than their error estimate. A nice thing to plot are the offsets X_0 and Y_0 (figure 7.8). As can be seen, the same values are obtained as in figure 7.3 for the OR algorithm. This shows the stability of the fits, since in this algorithm independent values are reproduced. The statistical uncertainty is understandably higher since the XOR algorithms are more selective.

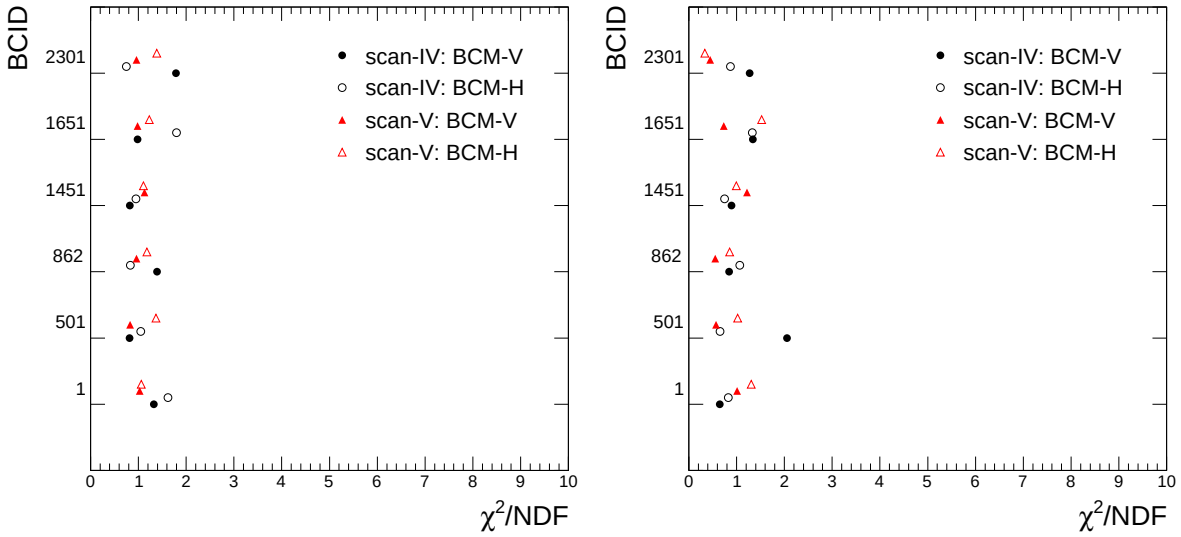

Figure 7.7: *χ^2 evaluation of the x sca (left) and y scan (right) fits of the XOR-A algorithm data from October 2010.*

The μ^{nr} values are shown in figure 7.9. As expected the values are approximately half the values of the OR based fit parameters. The consistency between the two BCM halves remains valid. In the Σ values (figure 7.10) the algorithm independence is seen again, though the values are more distributed due to lower statistics.

The final XOR-A cross-section values are summarized in table 7.7. Their excellent agreement is also shown in figure 7.11.

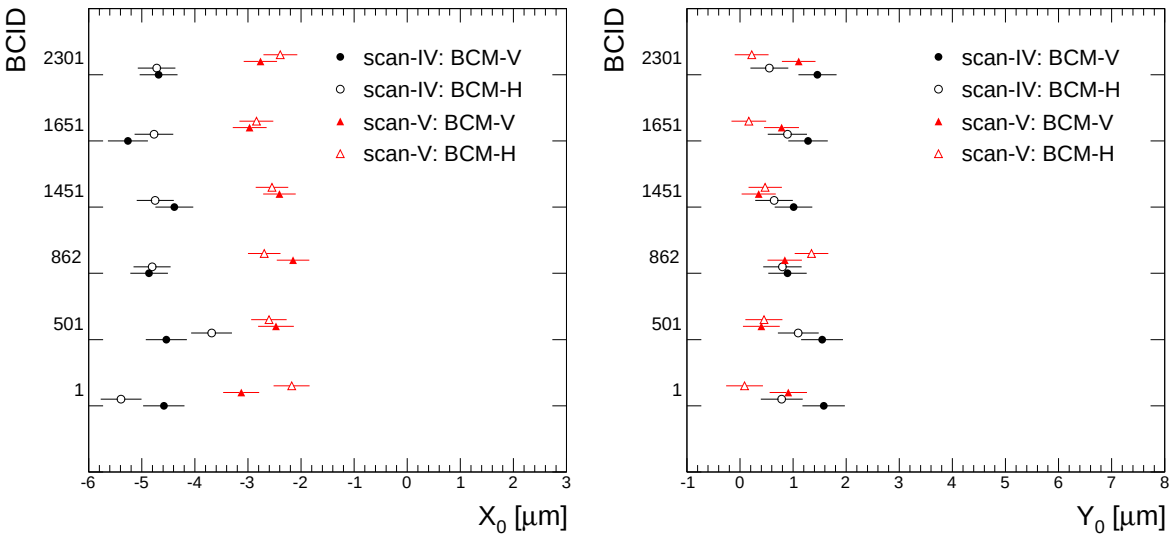

Figure 7.8: *Offset of the centered beams during x scans (left) and y scans (right) for the XOR-A algorithm. It can be compared to figure 7.3 to verify that this parameters are algorithm independent.*

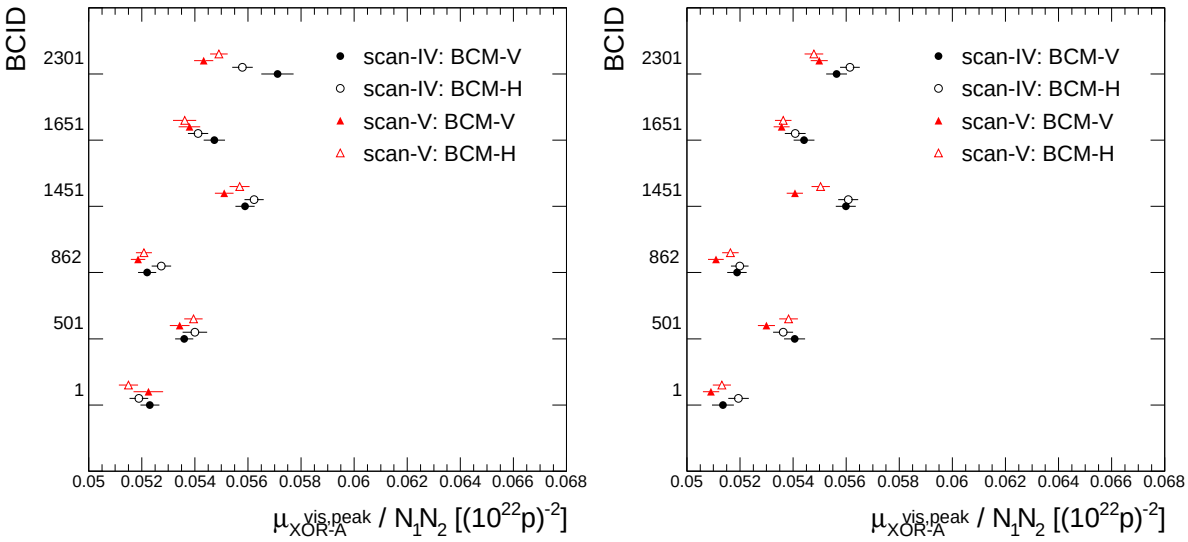

Figure 7.9: *The maximum μ^{vis} (beam population normalized) during x scans (left) and y scans (right) for the XOR-A algorithm.*

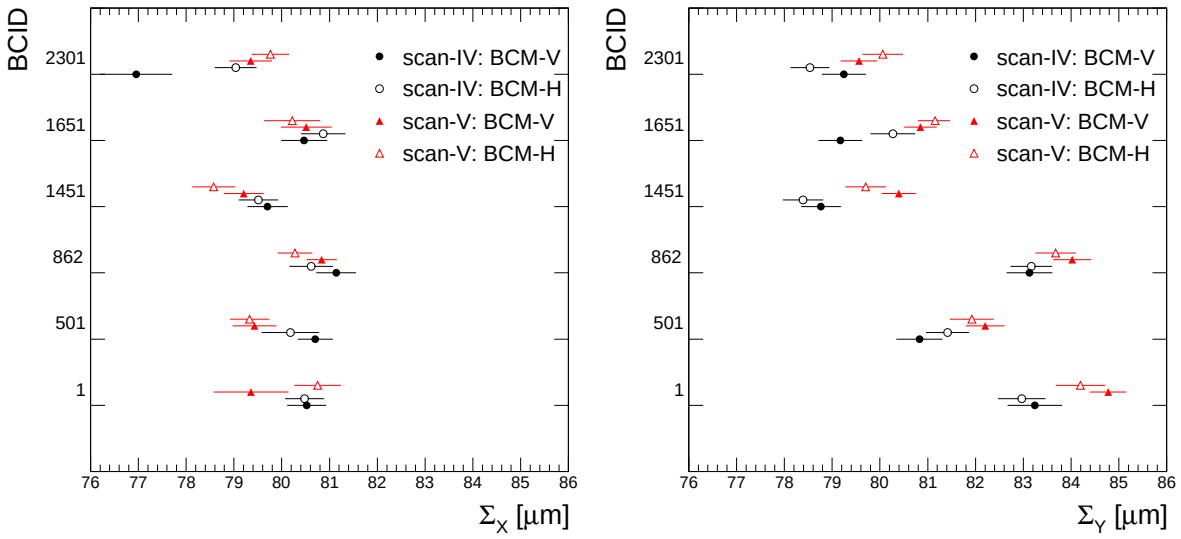

Figure 7.10: *The effective beam width as obtained form the fits of x scans (left) and y scans (right) for the XOR-A algorithm.*

BCID	Visible cross-section [mb]			
	BCM-Verical		BCM-Horizontal	
	Scan IV	Scan V	Scan IV	Scan V
1	2.183 ± 0.012	2.180 ± 0.013	2.178 ± 0.011	2.196 ± 0.012
501	2.206 ± 0.011	2.183 ± 0.011	2.207 ± 0.013	2.201 ± 0.011
862	2.206 ± 0.011	2.197 ± 0.009	2.206 ± 0.011	2.189 ± 0.010
1451	2.206 ± 0.011	2.184 ± 0.010	2.199 ± 0.011	2.178 ± 0.011
1651	2.184 ± 0.012	2.195 ± 0.011	2.207 ± 0.012	2.193 ± 0.011
2301	2.160 ± 0.014	2.168 ± 0.010	2.183 ± 0.011	2.201 ± 0.010
Average	2.193 ± 0.005	2.185 ± 0.004	2.196 ± 0.005	2.193 ± 0.004
RMS	0.017	0.010	0.012	0.008

Table 7.7: *Visible cross-sections extracted for XOR-A algorithm of October 2010 scan.*

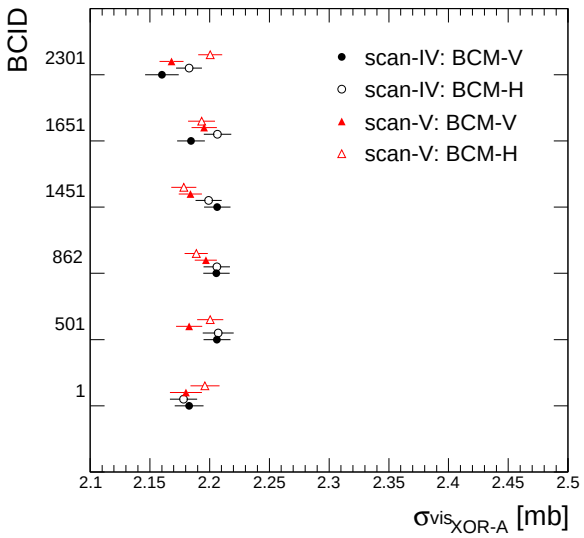

Figure 7.11: *Visible cross-sections for both BCM luminosity measurements, both scans, and all BCIDs. An excellent agreement is obtained for the XOR-A algorithm.*

BCID	Scan	$X_0[\mu m]$	$b_X[10^{-4}\,(10^{22}p)^{-2}]$	$\Sigma_X[\mu m]$	$\mu_X^{nr,\,peak}[(10^{22}p)^{-2}]$	$C_{\Sigma_X-\mu_X^{nr,\,peak}}$	χ^2/NDF
1	IV	-4.58 ± 0.39	0.00 ± 0.10	80.52 ± 0.41	0.0523 ± 0.0004	-0.73	1.33
	V	-3.13 ± 0.34	0.15 ± 0.06	79.36 ± 0.78	0.0522 ± 0.0006	-0.92	1.03
501	IV	-4.54 ± 0.39	0.00 ± 0.07	80.70 ± 0.36	0.0536 ± 0.0003	-0.69	0.82
	V	-2.47 ± 0.34	0.07 ± 0.06	79.43 ± 0.46	0.0534 ± 0.0004	-0.81	0.83
862	IV	-4.86 ± 0.35	0.04 ± 0.07	81.14 ± 0.42	0.0522 ± 0.0003	-0.76	1.39
	V	-2.15 ± 0.31	0.01 ± 0.19	80.84 ± 0.32	0.0519 ± 0.0003	-0.70	0.96
1451	IV	-4.38 ± 0.36	0.01 ± 0.15	79.70 ± 0.42	0.0559 ± 0.0004	-0.74	0.82
	V	-2.41 ± 0.31	0.03 ± 0.04	79.21 ± 0.42	0.0551 ± 0.0004	-0.81	1.13
1651	IV	-5.26 ± 0.38	0.11 ± 0.08	80.47 ± 0.48	0.0547 ± 0.0004	-0.80	0.98
	V	-2.97 ± 0.32	0.00 ± 0.02	80.51 ± 0.53	0.0538 ± 0.0004	-0.86	0.98
2301	IV	-4.68 ± 0.36	0.05 ± 0.07	76.95 ± 0.75	0.0571 ± 0.0006	-0.91	1.79
	V	-2.77 ± 0.31	0.00 ± 0.03	79.35 ± 0.44	0.0543 ± 0.0004	-0.82	0.96

Table 7.8: *Fit parameters obtained for October 2010 X sub-scans of scans IV and V for XOR-A algorithm data from BCM vertical luminoisty.*

BCID	Scan	$Y_0[\mu m]$	$b_Y[10^{-4}\,(10^{22}p)^{-2}]$	$\Sigma_Y[\mu m]$	$\mu_Y^{nr,\,peak}[(10^{22}p)^{-2}]$	$C_{\Sigma_Y-\mu_Y^{nr,\,peak}}$	χ^2/NDF
1	IV	$+1.58 \pm 0.40$	0.19 ± 0.11	83.24 ± 0.57	0.0514 ± 0.0004	-0.81	0.65
	V	$+0.91 \pm 0.35$	0.00 ± 0.08	84.77 ± 0.38	0.0509 ± 0.0003	-0.73	1.01
501	IV	$+1.55 \pm 0.40$	0.00 ± 0.16	80.83 ± 0.48	0.0541 ± 0.0004	-0.77	2.05
	V	$+0.40 \pm 0.35$	0.11 ± 0.17	82.20 ± 0.41	0.0530 ± 0.0003	-0.72	0.57
862	IV	$+0.89 \pm 0.36$	0.27 ± 0.10	83.13 ± 0.48	0.0519 ± 0.0004	-0.79	0.84
	V	$+0.84 \pm 0.32$	0.15 ± 0.11	84.02 ± 0.40	0.0511 ± 0.0003	-0.77	0.55
1451	IV	$+1.01 \pm 0.36$	0.11 ± 0.11	78.77 ± 0.42	0.0560 ± 0.0004	-0.76	0.90
	V	$+0.35 \pm 0.32$	0.17 ± 0.09	80.39 ± 0.36	0.0541 ± 0.0003	-0.74	1.22
1651	IV	$+1.28 \pm 0.37$	0.02 ± 0.07	79.17 ± 0.46	0.0544 ± 0.0004	-0.78	1.34
	V	$+0.78 \pm 0.33$	0.00 ± 0.09	80.85 ± 0.34	0.0536 ± 0.0003	-0.73	0.73
2301	IV	$+1.46 \pm 0.36$	0.10 ± 0.08	79.24 ± 0.46	0.0556 ± 0.0004	-0.79	1.27
	V	$+1.11 \pm 0.32$	0.07 ± 0.10	79.56 ± 0.38	0.0550 ± 0.0003	-0.76	0.45

Table 7.9: *Fit parameters obtained for October 2010 Y sub-scans of scans IV and V for XOR-A algorithm data from BCM vertical luminoisty.*

BCID	Scan	$X_0[\mu m]$	$b_X[10^{-4}\,(10^{22}p)^{-2}]$	$\Sigma_X[\mu m]$	$\mu_X^{nr,\,peak}[(10^{22}p)^{-2}]$	$C_{\Sigma_X-\mu_X^{nr,\,peak}}$	χ^2/NDF
1	IV	-5.39 ± 0.39	0.16 ± 0.11	80.48 ± 0.41	0.0519 ± 0.0003	-0.72	1.62
	V	-2.18 ± 0.34	0.06 ± 0.08	80.75 ± 0.49	0.0515 ± 0.0004	-0.81	1.06
501	IV	-3.69 ± 0.38	0.16 ± 0.10	80.18 ± 0.60	0.0540 ± 0.0005	-0.84	1.05
	V	-2.60 ± 0.33	0.09 ± 0.06	79.33 ± 0.41	0.0539 ± 0.0003	-0.78	1.37
862	IV	-4.80 ± 0.35	0.17 ± 0.07	80.62 ± 0.46	0.0527 ± 0.0004	-0.79	0.83
	V	-2.69 ± 0.31	0.08 ± 0.08	80.28 ± 0.36	0.0521 ± 0.0003	-0.75	1.18
1451	IV	-4.75 ± 0.35	0.11 ± 0.11	79.51 ± 0.41	0.0562 ± 0.0004	-0.75	0.95
	V	-2.55 ± 0.31	0.05 ± 0.04	78.58 ± 0.45	0.0557 ± 0.0004	-0.83	1.11
1651	IV	-4.77 ± 0.36	0.09 ± 0.09	80.87 ± 0.46	0.0541 ± 0.0004	-0.79	1.80
	V	-2.84 ± 0.32	0.03 ± 0.04	80.22 ± 0.59	0.0536 ± 0.0004	-0.88	1.23
2301	IV	-4.72 ± 0.35	0.00 ± 0.06	79.04 ± 0.44	0.0558 ± 0.0004	-0.78	0.75
	V	-2.39 ± 0.32	0.03 ± 0.05	79.76 ± 0.39	0.0549 ± 0.0003	-0.78	1.39

Table 7.10: *Fit parameters obtained for October 2010 X sub-scans of scans IV and V for XOR-A algorithm data from BCM horizontal luminoisty.*

BCID	Scan	$Y_0[\mu m]$	$b_Y[10^{-4}\,(10^{22}p)^{-2}]$	$\Sigma_Y[\mu m]$	$\mu_Y^{nr,\,peak}[(10^{22}p)^{-2}]$	$C_{\Sigma_Y-\mu_Y^{nr,\,peak}}$	χ^2/NDF
1	IV	$+0.79 \pm 0.40$	0.07 ± 0.10	82.97 ± 0.50	0.0519 ± 0.0004	-0.78	0.83
	V	$+0.09 \pm 0.35$	0.20 ± 0.18	84.20 ± 0.52	0.0513 ± 0.0003	-0.79	1.30
501	IV	$+1.10 \pm 0.39$	0.00 ± 0.19	81.41 ± 0.45	0.0536 ± 0.0004	-0.76	0.65
	V	$+0.45 \pm 0.35$	0.27 ± 0.13	81.92 ± 0.46	0.0538 ± 0.0004	-0.78	1.02
862	IV	$+0.80 \pm 0.36$	0.31 ± 0.14	83.17 ± 0.43	0.0520 ± 0.0003	-0.75	1.06
	V	$+1.35 \pm 0.32$	0.17 ± 0.09	83.67 ± 0.42	0.0516 ± 0.0003	-0.80	0.86
1451	IV	$+0.64 \pm 0.35$	0.02 ± 0.08	78.39 ± 0.42	0.0561 ± 0.0004	-0.77	0.75
	V	$+0.47 \pm 0.31$	0.26 ± 0.09	79.70 ± 0.42	0.0550 ± 0.0003	-0.80	1.00
1651	IV	$+0.89 \pm 0.37$	0.07 ± 0.08	80.27 ± 0.47	0.0541 ± 0.0004	-0.79	1.33
	V	$+0.17 \pm 0.32$	0.00 ± 0.03	81.15 ± 0.36	0.0536 ± 0.0003	-0.75	1.52
2301	IV	$+0.55 \pm 0.36$	0.00 ± 0.10	78.54 ± 0.41	0.0561 ± 0.0004	-0.76	0.87
	V	$+0.22 \pm 0.32$	0.16 ± 0.09	80.06 ± 0.42	0.0548 ± 0.0003	-0.80	0.34

Table 7.11: *Fit parameters obtained for October 2010 Y sub-scans of scans IV and V for XOR-A algorithm data from BCM horizontal luminoisty.*

XOR-C algorithm

Four tables: 7.13, 7.14, 7.15, and 7.16 are dedicated to XOR-C algorithm. The plot of offsets X_0 and Y_0 is presented in figure 7.13,the μ^{nr} values are shown in figure 7.9, and the Σ values are shown in 7.15. The final XOR-C cross-section values are summarized in table 7.12. Their agreement is also shown in figure 7.16.

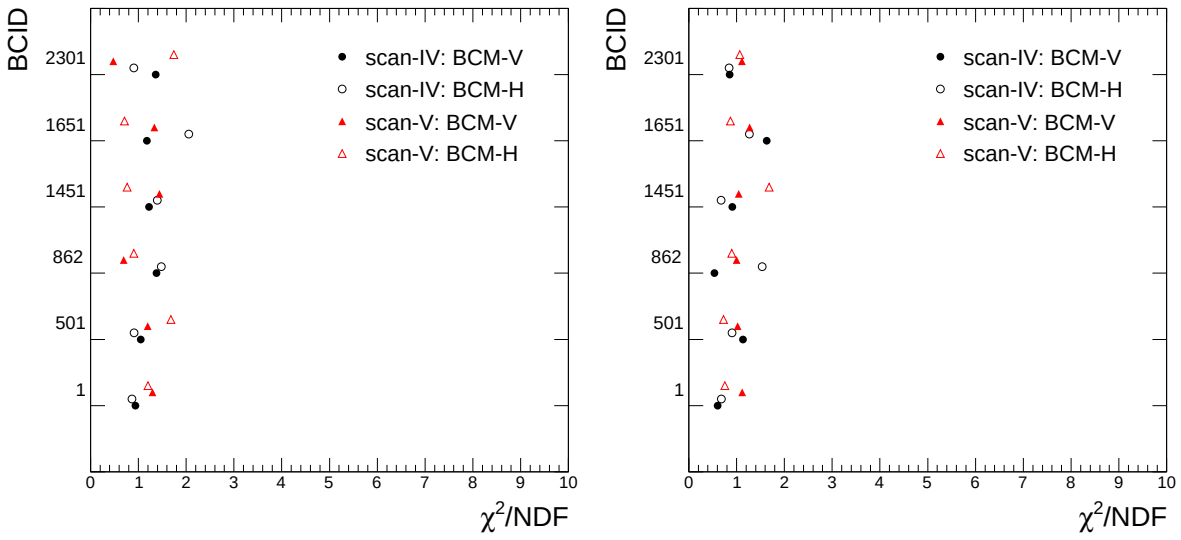

Figure 7.12: *χ^2 evaluation of the x scan (left) and y scan (right) fits.*

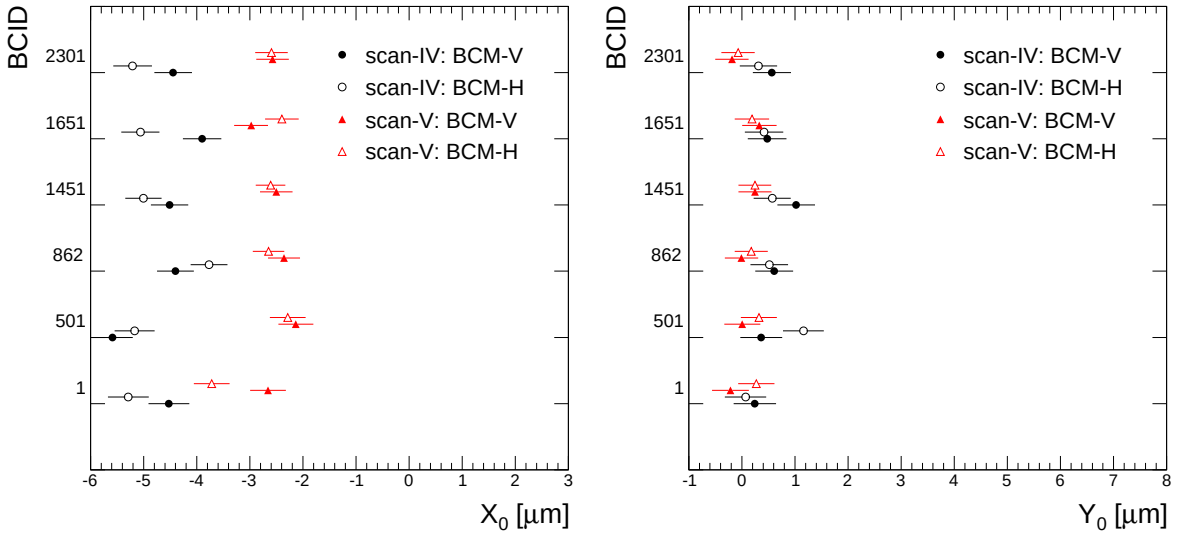

Figure 7.13: *Offset of the centered beams during x scans (left) and y scans (right) for the XOR-A algorithm.*

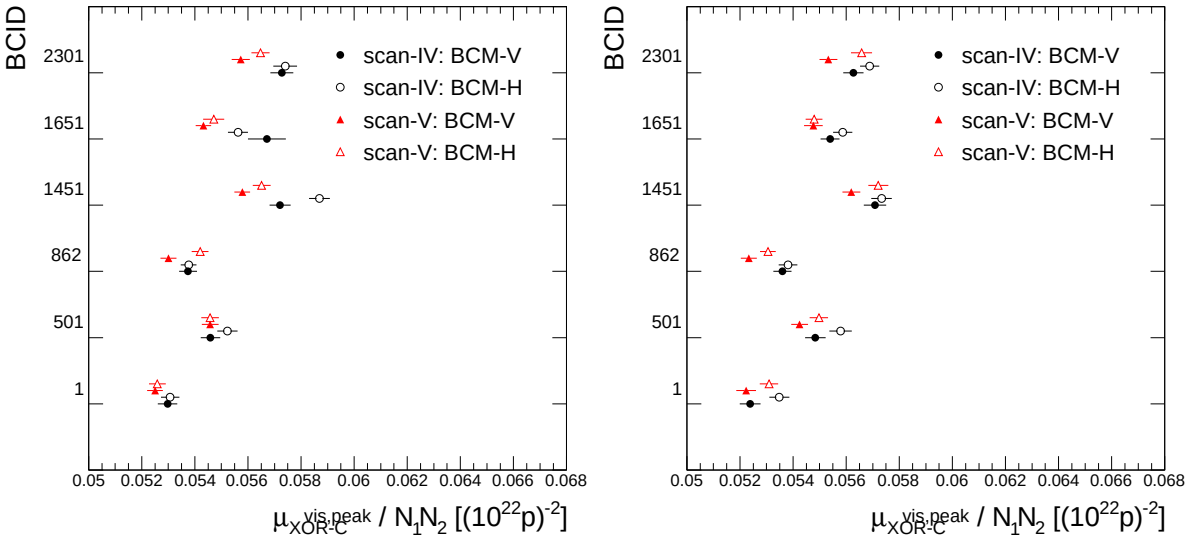

Figure 7.14: *The maximum beam current normalized μ^{vis} during x scans (left) and y scans (right) for the XOR-A algorithm.*

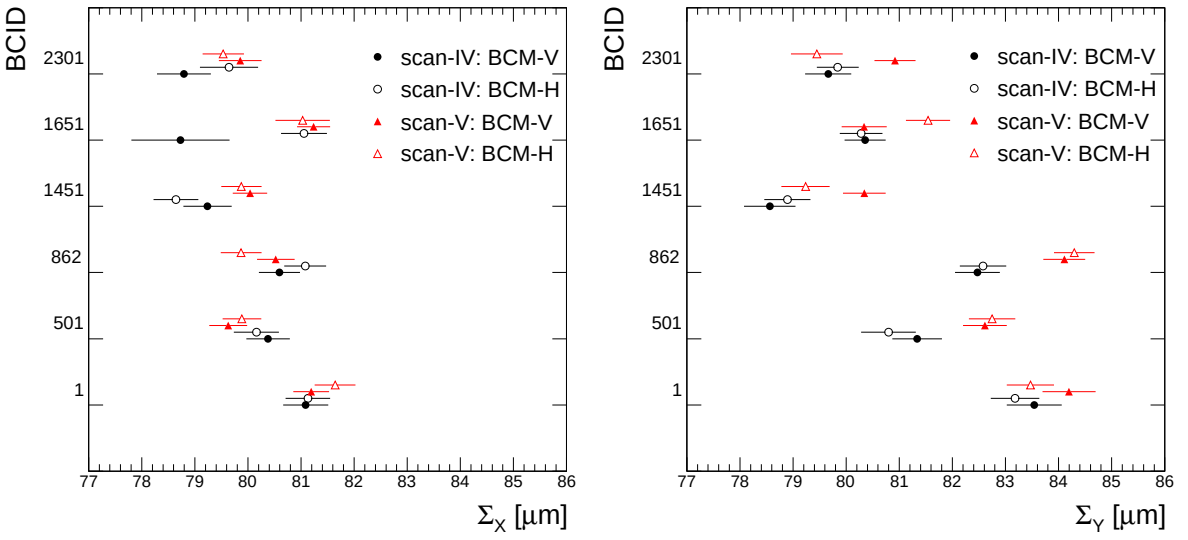

Figure 7.15: *The effective beam width as obtained form the fits of x scans (left) and y scans (right) for the XOR-A algorithm.*

BCID	Visible cross-section [mb]			
	BCM-Verical		BCM-Horizontal	
	Scan IV	Scan V	Scan IV	Scan V
1	2.242 ± 0.012	2.249 ± 0.011	2.259 ± 0.012	2.262 ± 0.011
501	2.247 ± 0.012	2.249 ± 0.011	2.259 ± 0.012	2.275 ± 0.011
862	2.241 ± 0.011	2.241 ± 0.009	2.263 ± 0.012	2.269 ± 0.010
1451	2.235 ± 0.012	2.262 ± 0.010	2.262 ± 0.011	2.261 ± 0.011
1651	2.228 ± 0.016	2.237 ± 0.010	2.279 ± 0.011	2.273 ± 0.012
2301	2.239 ± 0.012	2.255 ± 0.010	2.283 ± 0.012	2.244 ± 0.011
Average	2.240 ± 0.005	2.249 ± 0.004	2.267 ± 0.005	2.264 ± 0.004
RMS	0.006	0.008	0.010	0.010

Table 7.12: *Visible cross-sections extracted for XOR-C algorithm of October 2010 scan.*

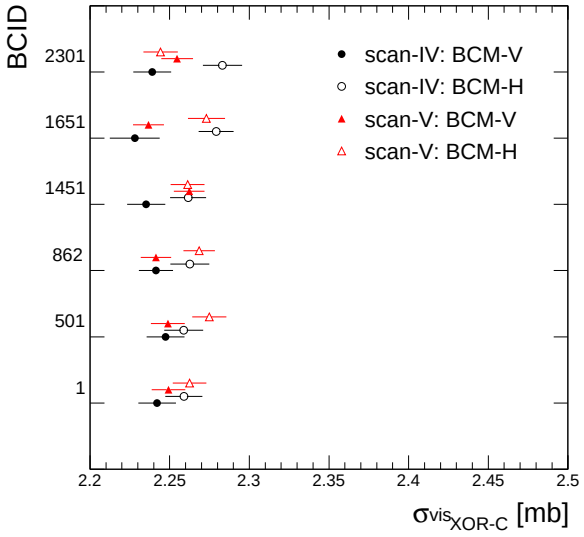

Figure 7.16: *Visible cross-sections for both BCM luminosity measurements, both scans, and all BCIDs.*

BCID	Scan	$X_0[\mu m]$	$b_X[10^{-4}\,(10^{22}p)^{-2}]$	$\Sigma_X[\mu m]$	$\mu_X^{nr,\,peak}[(10^{22}p)^{-2}]$	$C_{\Sigma_X-\mu_X^{nr,\,peak}}$	χ^2/NDF
1	IV	-4.53 ± 0.38	0.00 ± 0.06	81.09 ± 0.42	0.0530 ± 0.0004	-0.74	0.94
	V	-2.66 ± 0.34	0.01 ± 0.19	81.19 ± 0.34	0.0525 ± 0.0003	-0.69	1.29
501	IV	-5.59 ± 0.38	0.02 ± 0.12	80.38 ± 0.41	0.0546 ± 0.0004	-0.71	1.05
	V	-2.13 ± 0.33	0.08 ± 0.10	79.63 ± 0.36	0.0546 ± 0.0003	-0.71	1.19
862	IV	-4.40 ± 0.35	0.13 ± 0.09	80.59 ± 0.39	0.0537 ± 0.0003	-0.73	1.38
	V	-2.36 ± 0.30	0.07 ± 0.06	80.52 ± 0.35	0.0530 ± 0.0003	-0.75	0.69
1451	IV	-4.51 ± 0.35	0.21 ± 0.11	79.24 ± 0.46	0.0572 ± 0.0004	-0.79	1.22
	V	-2.50 ± 0.30	0.00 ± 0.11	80.04 ± 0.32	0.0558 ± 0.0003	-0.72	1.44
1651	IV	-3.90 ± 0.36	0.10 ± 0.06	78.73 ± 0.92	0.0567 ± 0.0007	-0.94	1.18
	V	-2.98 ± 0.32	0.00 ± 0.15	81.24 ± 0.31	0.0543 ± 0.0003	-0.70	1.34
2301	IV	-4.45 ± 0.35	0.07 ± 0.07	78.79 ± 0.51	0.0573 ± 0.0004	-0.82	1.36
	V	-2.57 ± 0.31	0.06 ± 0.05	79.85 ± 0.40	0.0557 ± 0.0003	-0.79	0.48

Table 7.13: *Fit parameters obtained for October 2010 X sub-scans of scans IV and V for XOR-C algorithm data from BCM vertical luminoisty.*

BCID	Scan	$Y_0[\mu m]$	$b_Y[10^{-4}\,(10^{22}p)^{-2}]$	$\Sigma_Y[\mu m]$	$\mu_Y^{nr,\,peak}[(10^{22}p)^{-2}]$	$C_{\Sigma_Y-\mu_Y^{nr,\,peak}}$	χ^2/NDF
1	IV	$+0.24 \pm 0.40$	0.19 ± 0.10	83.54 ± 0.52	0.0524 ± 0.0004	-0.79	0.60
	V	-0.22 ± 0.35	0.00 ± 0.08	84.20 ± 0.50	0.0522 ± 0.0004	-0.83	1.12
501	IV	$+0.36 \pm 0.39$	0.07 ± 0.13	81.34 ± 0.47	0.0548 ± 0.0004	-0.75	1.13
	V	$+0.01 \pm 0.34$	0.04 ± 0.21	82.61 ± 0.41	0.0542 ± 0.0003	-0.71	1.02
862	IV	$+0.61 \pm 0.36$	0.08 ± 0.15	82.47 ± 0.42	0.0536 ± 0.0003	-0.74	0.53
	V	-0.01 ± 0.32	0.23 ± 0.09	84.11 ± 0.39	0.0523 ± 0.0003	-0.77	1.00
1451	IV	$+1.02 \pm 0.35$	0.28 ± 0.10	78.56 ± 0.48	0.0571 ± 0.0004	-0.81	0.91
	V	$+0.25 \pm 0.31$	0.05 ± 0.08	80.34 ± 0.40	0.0562 ± 0.0003	-0.79	1.05
1651	IV	$+0.48 \pm 0.36$	0.00 ± 0.05	80.36 ± 0.39	0.0554 ± 0.0004	-0.73	1.63
	V	$+0.33 \pm 0.32$	0.22 ± 0.08	80.34 ± 0.43	0.0548 ± 0.0004	-0.79	1.27
2301	IV	$+0.57 \pm 0.36$	0.00 ± 0.13	79.66 ± 0.43	0.0563 ± 0.0004	-0.77	0.85
	V	-0.19 ± 0.32	0.00 ± 0.06	80.92 ± 0.39	0.0553 ± 0.0003	-0.79	1.11

Table 7.14: *Fit parameters obtained for October 2010 Y sub-scans of scans IV and V for XOR-C algorithm data from BCM vertical luminoisty.*

BCID	Scan	$X_0[\mu m]$	$b_X[10^{-4}\,(10^{22}p)^{-2}]$	$\Sigma_X[\mu m]$	$\mu_X^{nr,\,peak}[(10^{22}p)^{-2}]$	$C_{\Sigma_X-\mu_X^{nr,\,peak}}$	χ^2/NDF
1	IV	-5.29 ± 0.38	0.00 ± 0.15	81.13 ± 0.42	0.0531 ± 0.0003	-0.70	0.87
	V	-3.72 ± 0.34	0.09 ± 0.08	81.64 ± 0.39	0.0526 ± 0.0003	-0.75	1.20
501	IV	-5.17 ± 0.38	0.08 ± 0.10	80.16 ± 0.43	0.0552 ± 0.0004	-0.74	0.91
	V	-2.29 ± 0.34	0.07 ± 0.12	79.89 ± 0.36	0.0546 ± 0.0003	-0.72	1.68
862	IV	-3.77 ± 0.35	0.02 ± 0.08	81.08 ± 0.39	0.0538 ± 0.0003	-0.50	1.48
	V	-2.65 ± 0.30	0.04 ± 0.05	79.87 ± 0.38	0.0542 ± 0.0003	-0.79	0.91
1451	IV	-5.00 ± 0.34	0.13 ± 0.10	78.64 ± 0.42	0.0587 ± 0.0004	-0.78	1.40
	V	-2.61 ± 0.28	0.06 ± 0.05	79.88 ± 0.38	0.0565 ± 0.0003	-0.78	0.76
1651	IV	-5.06 ± 0.36	0.00 ± 0.05	81.05 ± 0.43	0.0556 ± 0.0004	-0.77	2.06
	V	-2.40 ± 0.32	0.12 ± 0.06	81.03 ± 0.51	0.0547 ± 0.0004	-0.86	0.71
2301	IV	-5.21 ± 0.37	0.09 ± 0.09	79.65 ± 0.55	0.0574 ± 0.0004	-0.84	0.91
	V	-2.59 ± 0.31	0.07 ± 0.05	79.53 ± 0.39	0.0565 ± 0.0003	-0.79	1.74

Table 7.15: *Fit parameters obtained for October 2010 X sub-scans of scans IV and V for XOR-C algorithm data from BCM horizontal luminoisty.*

BCID	Scan	$Y_0[\mu m]$	$b_Y[10^{-4}\,(10^{22}p)^{-2}]$	$\Sigma_Y[\mu m]$	$\mu_Y^{nr,\,peak}[(10^{22}p)^{-2}]$	$C_{\Sigma_Y-\mu_Y^{nr,\,peak}}$	χ^2/NDF
1	IV	$+0.07 \pm 0.39$	0.00 ± 0.07	83.18 ± 0.46	0.0535 ± 0.0004	-0.77	0.68
	V	$+0.27 \pm 0.34$	0.08 ± 0.10	83.47 ± 0.45	0.0531 ± 0.0003	-0.79	0.75
501	IV	$+1.16 \pm 0.38$	0.06 ± 0.10	80.80 ± 0.51	0.0558 ± 0.0004	-0.80	0.90
	V	$+0.32 \pm 0.34$	0.05 ± 0.12	82.75 ± 0.44	0.0550 ± 0.0003	-0.77	0.73
862	IV	$+0.52 \pm 0.35$	0.00 ± 0.02	82.58 ± 0.44	0.0538 ± 0.0004	-0.79	1.54
	V	$+0.18 \pm 0.31$	0.14 ± 0.13	84.30 ± 0.38	0.0531 ± 0.0003	-0.75	0.90
1451	IV	$+0.57 \pm 0.35$	0.09 ± 0.08	78.89 ± 0.43	0.0573 ± 0.0004	-0.78	0.68
	V	$+0.24 \pm 0.31$	0.13 ± 0.08	79.23 ± 0.45	0.0572 ± 0.0004	-0.82	1.68
1651	IV	$+0.42 \pm 0.36$	0.00 ± 0.17	80.28 ± 0.40	0.0559 ± 0.0004	-0.75	1.27
	V	$+0.19 \pm 0.32$	0.02 ± 0.10	81.54 ± 0.42	0.0548 ± 0.0003	-0.74	0.87
2301	IV	$+0.31 \pm 0.35$	0.11 ± 0.10	79.84 ± 0.39	0.0569 ± 0.0004	-0.73	0.84
	V	-0.07 ± 0.31	0.12 ± 0.07	79.45 ± 0.49	0.0566 ± 0.0004	-0.84	1.07

Table 7.16: *Fit parameters obtained for October 2010 Y sub-scans of scans IV and V for XOR-C algorithm data from BCM horizontal luminoisty.*

AND algorithm

To finish the October 2010 data, the AND algorithm fit data is given in tables: 7.18, 7.19, 7.20, 7.21.

The most evident property of the AND algorithm with respect to the rest is its selectivity. It removes the need for the background fit entirely but also drastically reduces the statistics which was clearly visible already from figure 7.1. The graphical overview of the fit parameters is shown in figures 7.18, 7.19, and 7.20. Statistical uncertainties are obviously worse than for the previous algorithms and too big to make some conclusions that were evident before, e.g. emittance growth or beam centering non-reproducibility. Nevertheless, the final gist in table 7.17 and figure 7.21 shows consistency between the scans and DPUs.

The efficiency estimation gives $(0.22 \pm 0.01)\%$, while MC predicts $(0.27 \pm 0.02)\%$. Interesting is the ration of $\varepsilon_{OR} : \varepsilon_{AND}$. According to the Monte Carlo, this ratio is $34.5 : 1$ and the recorded data suggest almost equal value of $34.6 : 1$. As seen in section 6.3.5, different topology requirements of AND and OR algorithms are expressed differently of the ND, SD, DD event subsamples. The consistent efficiency ratios therefore support the Monte Carlo ratios user for mixing ND, SD, DD events into minimum bias sample.

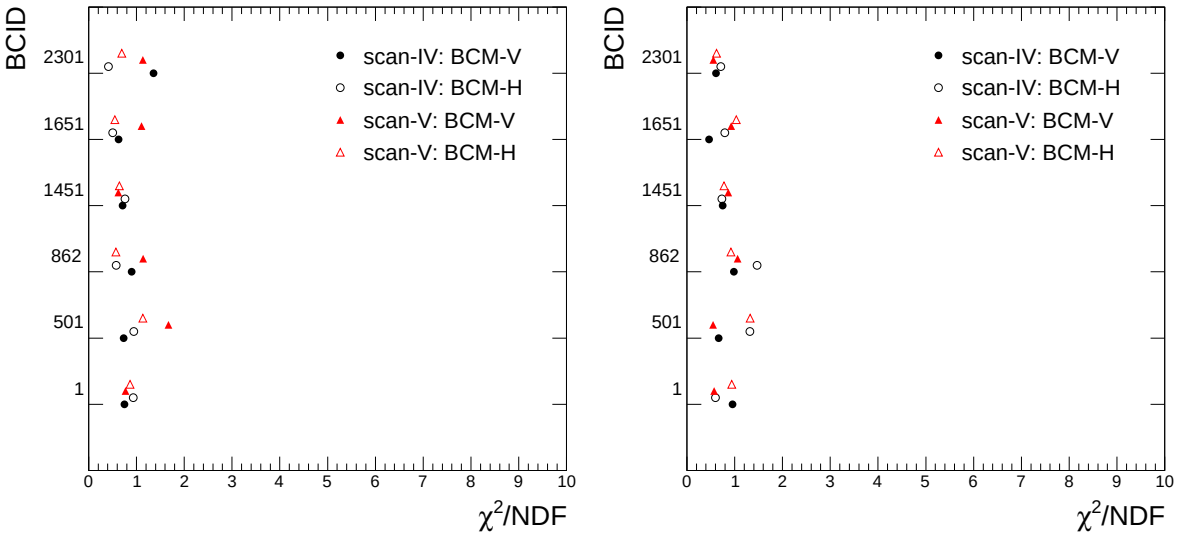

Figure 7.17: *χ^2 evaluation of the x scan (left) and y scan (right) fits for AND algorithm data.*

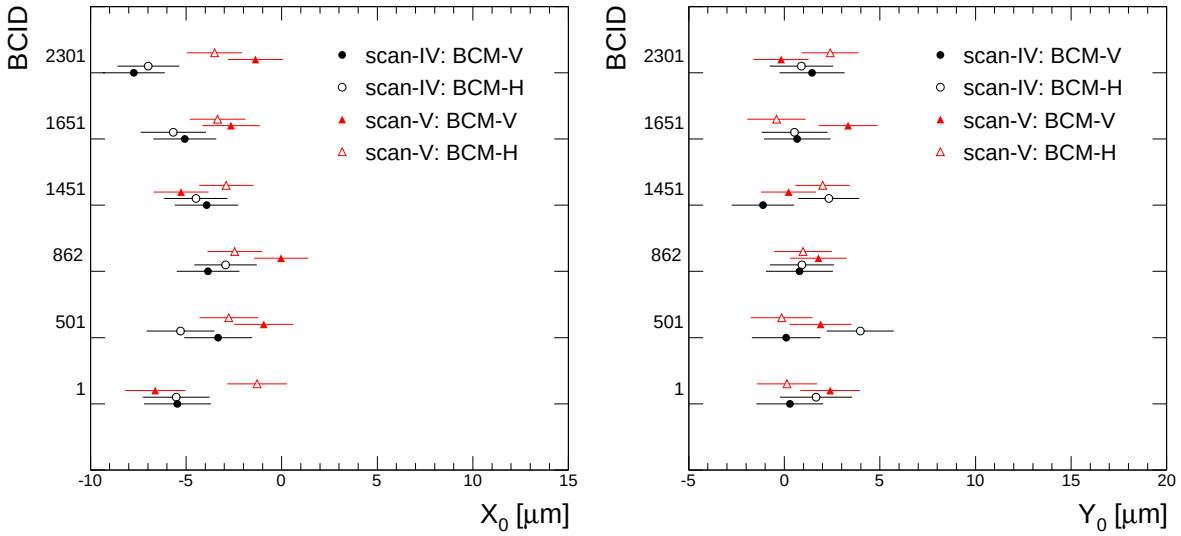

Figure 7.18: *Offset of the centered beams during x scans (left) and y scans (right) for AND algorithm data.*

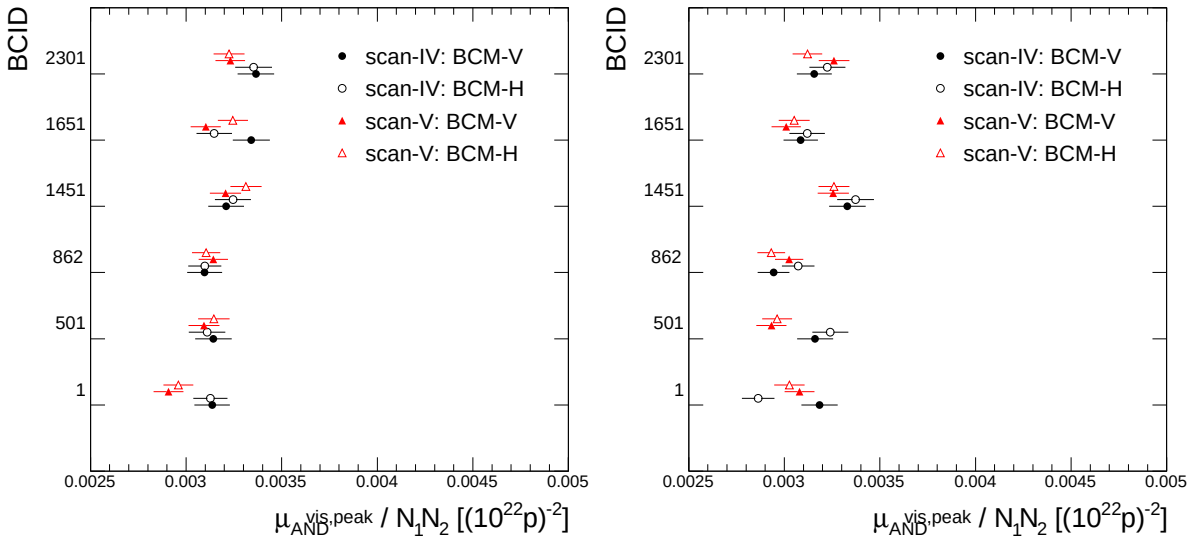

Figure 7.19: *The maximum beam current normalized μ^{vis} during x scans (left) and y scans (right) for AND algorithm data.*

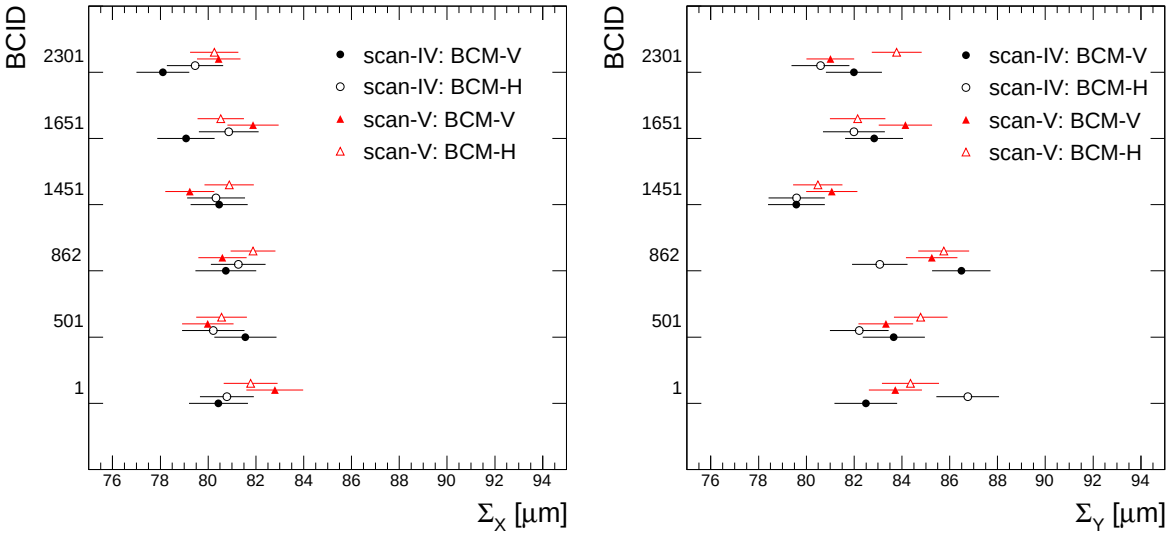

Figure 7.20: *The effective beam width as obtained form the fits of x scans (left) and y scans (right) for AND algorithm data.*

BCID	Visible cross-section [mb]			
	BCM-Verical		BCM-Horizontal	
	Scan IV	Scan V	Scan IV	Scan V
1	0.132 ± 0.002	0.130 ± 0.002	0.132 ± 0.002	0.130 ± 0.002
501	0.135 ± 0.003	0.126 ± 0.002	0.132 ± 0.002	0.131 ± 0.002
862	0.133 ± 0.002	0.133 ± 0.002	0.131 ± 0.002	0.133 ± 0.002
1451	0.132 ± 0.002	0.130 ± 0.002	0.133 ± 0.002	0.134 ± 0.002
1651	0.132 ± 0.002	0.132 ± 0.002	0.131 ± 0.002	0.131 ± 0.002
2301	0.131 ± 0.002	0.133 ± 0.002	0.132 ± 0.002	0.134 ± 0.002
Average	0.132 ± 0.001	0.131 ± 0.001	0.132 ± 0.001	0.132 ± 0.001
RMS	0.001	0.002	0.001	0.002

Table 7.17: *Visible corss-sections extracted for AND algorithm of October 2010 scan.*

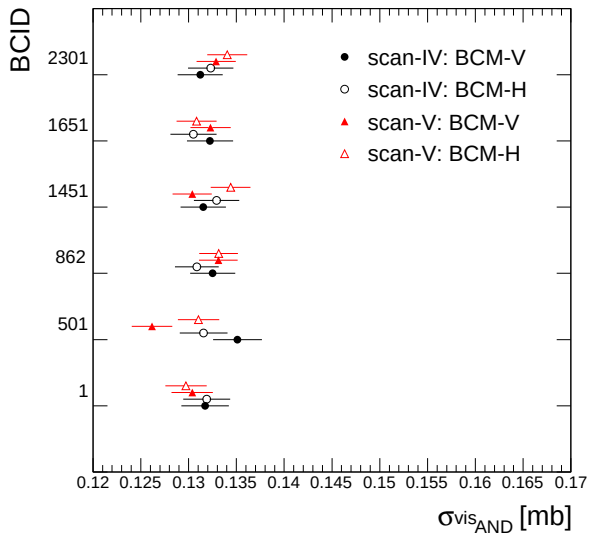

Figure 7.21: *Visible cross-sections for both BCM luminosity measurements, both scans, and all BCIDs. An excelent agreement is obtained for the AND algorithm.*

BCID	Scan	$X_0[\mu m]$	$\Sigma_X[\mu m]$	$\mu_X^{nr,peak}[(10^{22}p)^{-2}]$	$C_{\Sigma_X-\mu_X^{nr,peak}}$	χ^2/NDF
1	IV	-5.46 ± 1.75	80.43 ± 1.23	0.0031 ± 0.0001	-0.61	0.75
	V	-6.62 ± 1.59	82.79 ± 1.19	0.0029 ± 0.0001	-0.63	0.77
501	IV	-3.32 ± 1.78	81.56 ± 1.30	0.0031 ± 0.0001	-0.62	0.73
	V	-0.95 ± 1.55	79.99 ± 1.08	0.0031 ± 0.0001	-0.61	1.67
862	IV	-3.85 ± 1.64	80.74 ± 1.27	0.0031 ± 0.0001	-0.65	0.90
	V	-0.03 ± 1.42	80.60 ± 1.01	0.0031 ± 0.0001	-0.62	1.14
1451	IV	-3.93 ± 1.66	80.46 ± 1.19	0.0032 ± 0.0001	-0.62	0.71
	V	-5.27 ± 1.44	79.23 ± 1.03	0.0032 ± 0.0001	-0.62	0.62
1651	IV	-5.07 ± 1.65	79.07 ± 1.20	0.0033 ± 0.0001	-0.62	0.62
	V	-2.65 ± 1.50	81.88 ± 1.07	0.0031 ± 0.0001	-0.62	1.11
2301	IV	-7.74 ± 1.63	78.11 ± 1.10	0.0034 ± 0.0001	-0.60	1.35
	V	-1.38 ± 1.44	80.44 ± 0.91	0.0032 ± 0.0001	-0.57	1.13

Table 7.18: *Fit parameters obtained for October 2010 X sub-scans of scans IV and V for AND algorithm data from BCM vertical luminoisty.*

BCID	Scan	$Y_0[\mu m]$	$\Sigma_Y[\mu m]$	$\mu_Y^{nr,peak}[(10^{22}p)^{-2}]$	$C_{\Sigma_Y-\mu_Y^{nr,peak}}$	χ^2/NDF
1	IV	$+0.29 \pm 1.76$	82.49 ± 1.31	0.0032 ± 0.0001	-0.63	0.95
	V	$+2.40 \pm 1.56$	83.73 ± 1.11	0.0031 ± 0.0001	-0.61	0.57
501	IV	$+0.10 \pm 1.80$	83.66 ± 1.30	0.0032 ± 0.0001	-0.62	0.67
	V	$+1.89 \pm 1.63$	83.33 ± 1.14	0.0029 ± 0.0001	-0.61	0.55
862	IV	$+0.79 \pm 1.75$	86.49 ± 1.22	0.0029 ± 0.0001	-0.62	0.99
	V	$+1.79 \pm 1.48$	85.25 ± 1.08	0.0030 ± 0.0001	-0.63	1.06
1451	IV	-1.12 ± 1.63	79.58 ± 1.19	0.0033 ± 0.0001	-0.63	0.75
	V	$+0.22 \pm 1.44$	81.06 ± 1.07	0.0033 ± 0.0001	-0.63	0.87
1651	IV	$+0.67 \pm 1.73$	82.83 ± 1.21	0.0031 ± 0.0001	-0.61	0.47
	V	$+3.34 \pm 1.54$	84.14 ± 1.12	0.0030 ± 0.0001	-0.63	0.93
2301	IV	$+1.45 \pm 1.70$	81.99 ± 1.18	0.0032 ± 0.0001	-0.61	0.61
	V	-0.18 ± 1.44	81.00 ± 1.00	0.0033 ± 0.0001	-0.61	0.55

Table 7.19: *Fit parameters obtained for October 2010 Y sub-scans of scans IV and V for AND algorithm data from BCM vertical luminoisty.*

BCID	Scan	$X_0[\mu m]$	$\Sigma_X[\mu m]$	$\mu_X^{nr,peak}[(10^{22}p)^{-2}]$	$C_{\Sigma_X-\mu_X^{nr,peak}}$	χ^2/NDF
1	IV	-5.52 ± 1.74	80.78 ± 1.13	0.0031 ± 0.0001	-0.58	0.93
	V	-1.29 ± 1.57	81.78 ± 1.13	0.0030 ± 0.0001	-0.62	0.86
501	IV	-5.29 ± 1.77	80.22 ± 1.31	0.0031 ± 0.0001	-0.63	0.94
	V	-2.76 ± 1.55	80.56 ± 1.06	0.0031 ± 0.0001	-0.60	1.14
862	IV	-2.94 ± 1.63	81.26 ± 1.14	0.0031 ± 0.0001	-0.61	0.58
	V	-2.46 ± 1.43	81.88 ± 0.94	0.0031 ± 0.0001	-0.59	0.57
1451	IV	-4.49 ± 1.65	80.33 ± 1.21	0.0032 ± 0.0001	-0.63	0.76
	V	-2.90 ± 1.42	80.88 ± 1.03	0.0033 ± 0.0001	-0.62	0.64
1651	IV	-5.67 ± 1.70	80.86 ± 1.25	0.0031 ± 0.0001	-0.63	0.50
	V	-3.35 ± 1.45	80.53 ± 0.97	0.0032 ± 0.0001	-0.59	0.55
2301	IV	-6.98 ± 1.62	79.45 ± 1.18	0.0034 ± 0.0001	-0.62	0.41
	V	-3.51 ± 1.45	80.26 ± 1.01	0.0032 ± 0.0001	-0.61	0.69

Table 7.20: *Fit parameters obtained for October 2010 X sub-scans of scans IV and V for AND algorithm data from BCM horizontal luminoisty.*

BCID	Scan	$Y_0[\mu m]$	$\Sigma_Y[\mu m]$	$\mu_Y^{nr,peak}[(10^{22}p)^{-2}]$	$C_{\Sigma_Y-\mu_Y^{nr,peak}}$	χ^2/NDF
1	IV	$+1.66 \pm 1.89$	86.75 ± 1.31	0.0029 ± 0.0001	-0.60	0.60
	V	$+0.14 \pm 1.58$	84.36 ± 1.19	0.0030 ± 0.0001	-0.64	0.94
501	IV	$+3.97 \pm 1.75$	82.21 ± 1.23	0.0032 ± 0.0001	-0.60	1.32
	V	-0.14 ± 1.62	84.79 ± 1.13	0.0030 ± 0.0001	-0.61	1.32
862	IV	$+0.92 \pm 1.68$	83.07 ± 1.17	0.0031 ± 0.0001	-0.61	1.47
	V	$+0.98 \pm 1.50$	85.75 ± 1.06	0.0029 ± 0.0001	-0.62	0.92
1451	IV	$+2.32 \pm 1.60$	79.59 ± 1.18	0.0034 ± 0.0001	-0.63	0.73
	V	$+2.00 \pm 1.43$	80.48 ± 1.03	0.0033 ± 0.0001	-0.62	0.78
1651	IV	$+0.53 \pm 1.72$	81.99 ± 1.29	0.0031 ± 0.0001	-0.63	0.80
	V	-0.41 ± 1.52	82.14 ± 1.16	0.0031 ± 0.0001	-0.64	1.04
2301	IV	$+0.89 \pm 1.66$	80.59 ± 1.21	0.0032 ± 0.0001	-0.63	0.71
	V	$+2.39 \pm 1.49$	83.78 ± 1.05	0.0031 ± 0.0001	-0.61	0.62

Table 7.21: *Fit parameters obtained for October 2010 Y sub-scans of scans IV and V for AND algorithm data from BCM horizontal luminoisty.*

7.4.2 Calibration of 2011 data

For calibration of 2011 data the May 2011 vdM was used. The following subsections recapitulate its analysis results. Most of the same conclusions as for the October 2010 vdM can be drawn and only the differences will be discussed.

OR algorithm

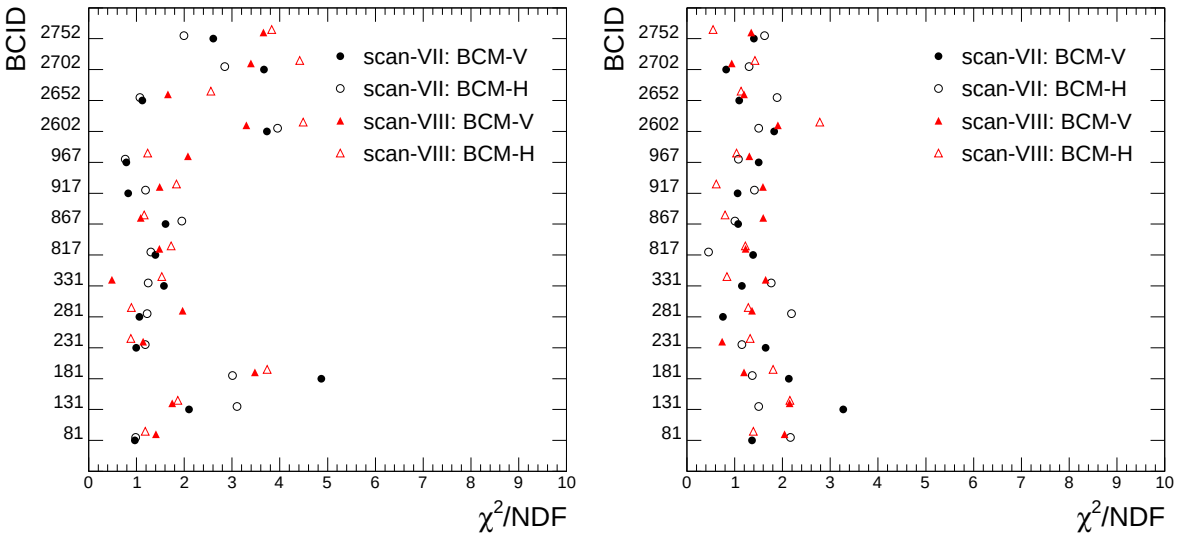

Figure 7.22: *χ^2 evaluation of the x scan (left) and y scan (right) fits for the OR algorithm.*

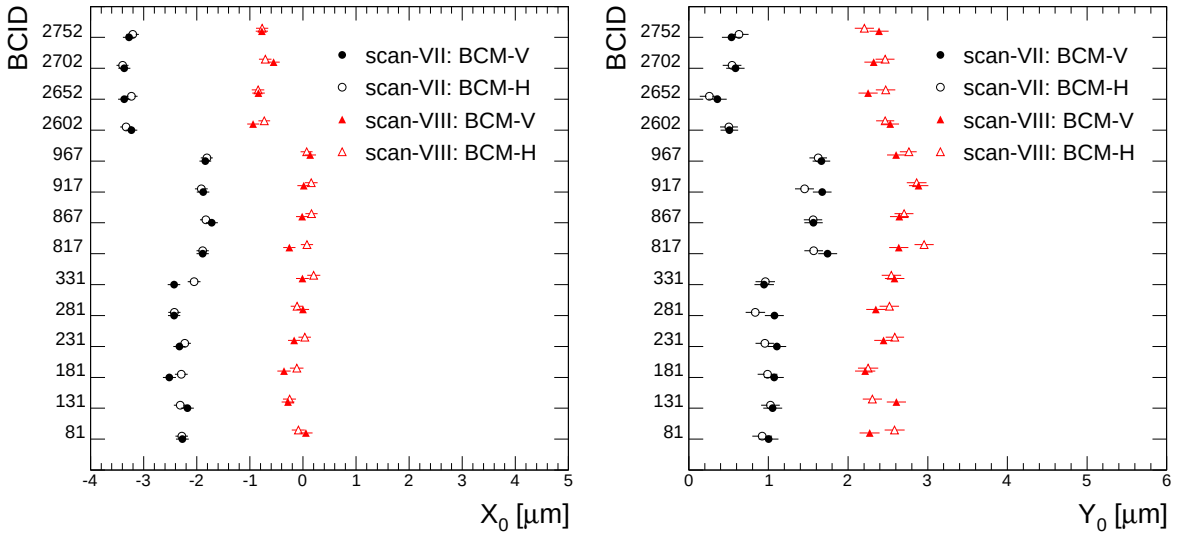

Figure 7.23: *Offset of the centered beams during x scans (left) and y scans (right) for the OR algorithm.*

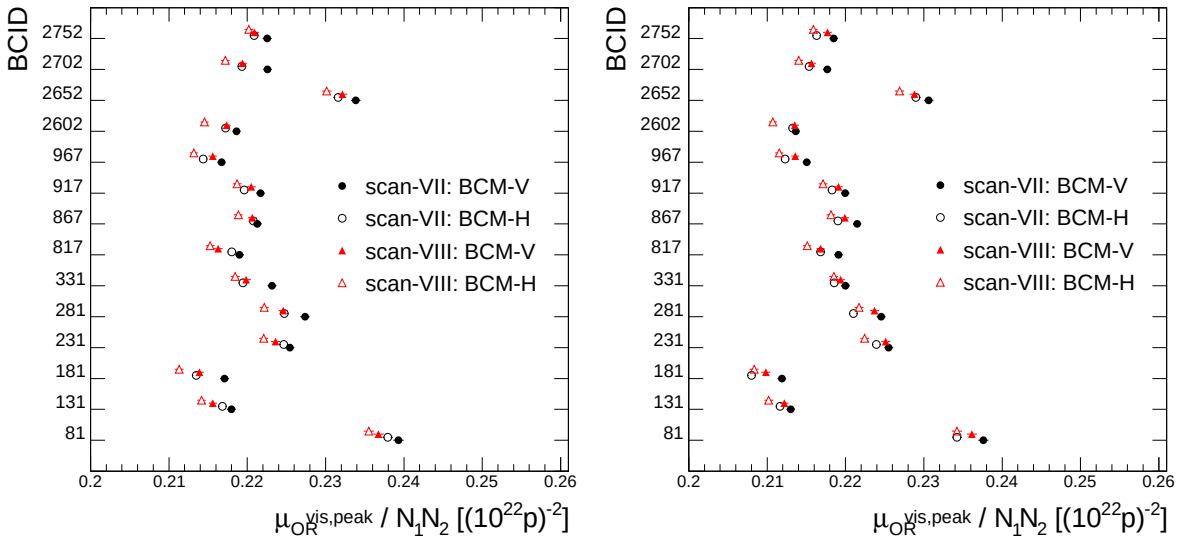

Figure 7.24: *The maximum μ^{vis} (bunch population normalized) during x scans (left) and y scans (right) for the OR algorithm.*

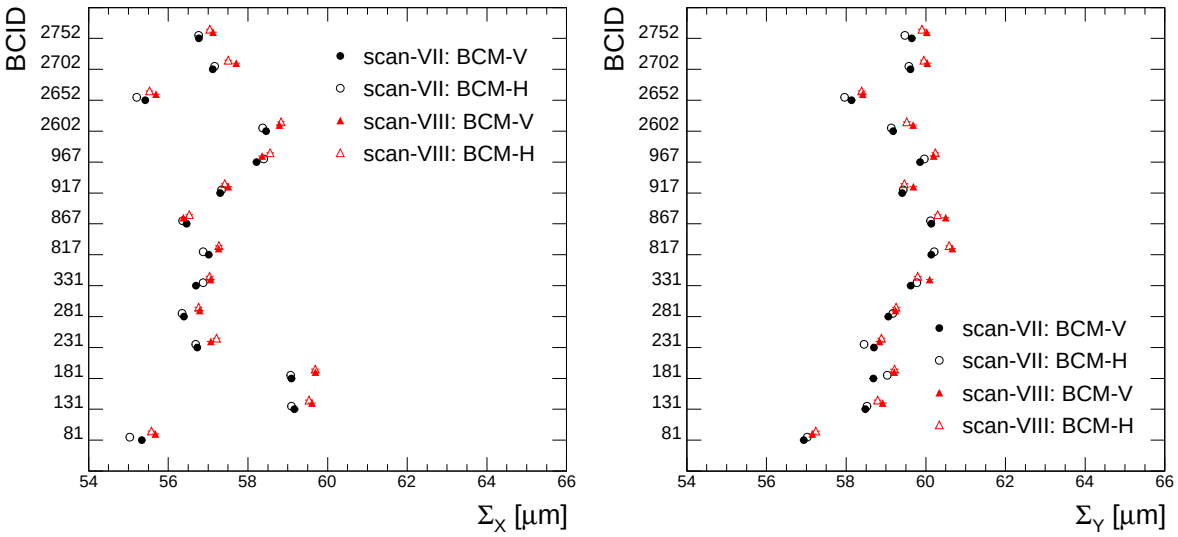

Figure 7.25: *The effective beam width as obtained form the fits of x scans (left) and y scans (right) for the OR algorithm.*

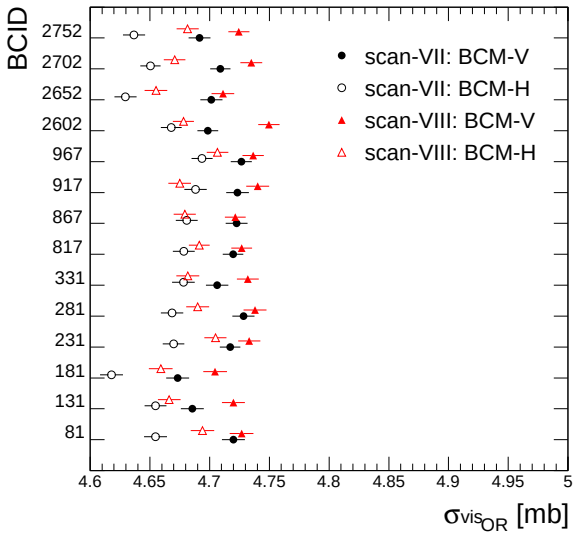

Figure 7.26: *Visible cross-sections for both BCM luminosity measurements, both scans, and all BCIDs. An excelent agreement is obtained for the OR algorithm.*

BCID	Visible cross-section [mb]			
	BCM-Verical		BCM-Horizontal	
	Scan VII	Scan VIII	Scan VII	Scan VIII
81	4.720 ± 0.010	4.727 ± 0.010	4.655 ± 0.010	4.694 ± 0.010
131	4.686 ± 0.010	4.720 ± 0.010	4.655 ± 0.009	4.666 ± 0.009
181	4.673 ± 0.010	4.705 ± 0.010	4.618 ± 0.010	4.659 ± 0.010
231	4.717 ± 0.009	4.733 ± 0.009	4.670 ± 0.009	4.705 ± 0.009
281	4.728 ± 0.009	4.738 ± 0.010	4.669 ± 0.009	4.690 ± 0.010
331	4.706 ± 0.009	4.732 ± 0.009	4.678 ± 0.009	4.682 ± 0.010
817	4.720 ± 0.009	4.727 ± 0.009	4.678 ± 0.009	4.691 ± 0.009
867	4.723 ± 0.009	4.721 ± 0.009	4.681 ± 0.009	4.679 ± 0.009
917	4.723 ± 0.009	4.740 ± 0.010	4.688 ± 0.009	4.675 ± 0.009
967	4.727 ± 0.009	4.736 ± 0.009	4.694 ± 0.009	4.707 ± 0.009
2602	4.698 ± 0.009	4.750 ± 0.009	4.668 ± 0.009	4.678 ± 0.009
2652	4.702 ± 0.009	4.711 ± 0.010	4.630 ± 0.009	4.655 ± 0.009
2702	4.709 ± 0.008	4.735 ± 0.009	4.651 ± 0.008	4.671 ± 0.009
2752	4.692 ± 0.009	4.724 ± 0.009	4.637 ± 0.009	4.682 ± 0.009
Average	4.709 ± 0.002	4.729 ± 0.002	4.662 ± 0.002	4.681 ± 0.002
RMS	0.016	0.011	0.021	0.014

Table 7.22: *May 2011 vissible cross-section obtained for the OR algorithm.*

BCID	Scan	$X_0[\mu m]$	$b_X[10^{-4}\,(10^{22}p)^{-2}]$	$\Sigma_X[\mu m]$	$\mu_X^{vis,peak}[(10^{22}p)^{-2}]$	$C_{\Sigma_X-\mu_X^{vis,peak}}$	χ^2/NDF
81	VII	-2.27 ± 0.12	1.97 ± 0.29	55.34 ± 0.09	0.2393 ± 0.0007	-0.59	0.97
	VIII	$+0.06 \pm 0.12$	3.59 ± 0.35	55.67 ± 0.10	0.2368 ± 0.0007	-0.58	1.41
131	VII	-2.18 ± 0.12	1.44 ± 0.37	59.17 ± 0.10	0.2180 ± 0.0006	-0.55	2.10
	VIII	-0.28 ± 0.12	3.29 ± 0.41	59.61 ± 0.10	0.2156 ± 0.0005	-0.54	1.75
181	VII	-2.52 ± 0.12	0.25 ± 0.35	59.09 ± 0.10	0.2171 ± 0.0006	-0.57	4.87
	VIII	-0.36 ± 0.13	1.77 ± 0.40	59.69 ± 0.10	0.2139 ± 0.0006	-0.56	3.48
231	VII	-2.33 ± 0.11	1.84 ± 0.30	56.73 ± 0.09	0.2254 ± 0.0006	-0.58	0.99
	VIII	-0.17 ± 0.12	3.46 ± 0.34	57.07 ± 0.10	0.2236 ± 0.0006	-0.58	1.14
281	VII	-2.43 ± 0.12	2.31 ± 0.30	56.39 ± 0.09	0.2274 ± 0.0006	-0.59	1.06
	VIII	$+0.00 \pm 0.12$	3.65 ± 0.36	56.79 ± 0.10	0.2246 ± 0.0006	-0.58	1.97
331	VII	-2.43 ± 0.12	2.12 ± 0.31	56.69 ± 0.10	0.2232 ± 0.0006	-0.58	1.58
	VIII	-0.01 ± 0.12	3.83 ± 0.37	57.06 ± 0.10	0.2199 ± 0.0006	-0.58	0.49
817	VII	-1.89 ± 0.12	2.18 ± 0.31	57.02 ± 0.09	0.2190 ± 0.0006	-0.58	1.40
	VIII	-0.26 ± 0.12	2.95 ± 0.33	57.26 ± 0.10	0.2163 ± 0.0006	-0.58	1.48
867	VII	-1.72 ± 0.11	2.40 ± 0.29	56.46 ± 0.09	0.2213 ± 0.0006	-0.59	1.61
	VIII	-0.02 ± 0.12	4.03 ± 0.34	56.38 ± 0.09	0.2207 ± 0.0006	-0.58	1.09
917	VII	-1.88 ± 0.12	2.47 ± 0.34	57.30 ± 0.10	0.2217 ± 0.0006	-0.58	0.83
	VIII	$+0.01 \pm 0.12$	2.59 ± 0.34	57.50 ± 0.10	0.2205 ± 0.0006	-0.58	1.48
967	VII	-1.84 ± 0.11	2.80 ± 0.34	58.21 ± 0.09	0.2167 ± 0.0005	-0.57	0.79
	VIII	$+0.14 \pm 0.11$	3.00 ± 0.34	58.35 ± 0.09	0.2156 ± 0.0005	-0.57	2.08
2602	VII	-3.23 ± 0.11	1.59 ± 0.32	58.46 ± 0.09	0.2186 ± 0.0005	-0.57	3.73
	VIII	-0.94 ± 0.11	1.95 ± 0.34	58.79 ± 0.09	0.2174 ± 0.0005	-0.56	3.30
2652	VII	-3.37 ± 0.12	1.54 ± 0.27	55.42 ± 0.09	0.2339 ± 0.0006	-0.58	1.12
	VIII	-0.84 ± 0.12	2.60 ± 0.31	55.69 ± 0.09	0.2321 ± 0.0006	-0.57	1.66
2702	VII	-3.36 ± 0.11	0.85 ± 0.29	57.11 ± 0.09	0.2226 ± 0.0005	-0.57	3.67
	VIII	-0.55 ± 0.12	2.00 ± 0.33	57.71 ± 0.09	0.2194 ± 0.0006	-0.57	3.39
2752	VII	-3.28 ± 0.12	1.43 ± 0.30	56.77 ± 0.09	0.2225 ± 0.0006	-0.57	2.61
	VIII	-0.77 ± 0.12	1.18 ± 0.30	57.12 ± 0.09	0.2209 ± 0.0006	-0.56	3.66

Table 7.23: *Fit parameters extracted form May 2011 data of the OR algorithm for BCM-Vertical luminosity measurement – X scans.*

BCID	Scan	$Y_0[\mu m]$	$b_Y[10^{-4}\,(10^{22}p)^{-2}]$	$\Sigma_Y[\mu m]$	$\mu_Y^{vis,\,peak}[(10^{22}p)^{-2}]$	$C_{\Sigma_Y-\mu_Y^{vis,\,peak}}$	χ^2/NDF
81	VII	$+1.00 \pm 0.12$	1.48 ± 0.33	56.93 ± 0.10	0.2376 ± 0.0007	-0.59	1.36
	VIII	$+2.27 \pm 0.12$	1.88 ± 0.34	57.15 ± 0.10	0.2361 ± 0.0007	-0.59	2.05
131	VII	$+1.05 \pm 0.12$	0.95 ± 0.32	58.48 ± 0.10	0.2130 ± 0.0006	-0.58	3.27
	VIII	$+2.61 \pm 0.12$	1.36 ± 0.34	58.92 ± 0.10	0.2122 ± 0.0006	-0.59	2.15
181	VII	$+1.07 \pm 0.12$	1.33 ± 0.34	58.68 ± 0.10	0.2119 ± 0.0006	-0.58	2.13
	VIII	$+2.21 \pm 0.13$	1.61 ± 0.36	59.21 ± 0.11	0.2098 ± 0.0006	-0.58	1.19
231	VII	$+1.11 \pm 0.12$	0.00 ± 0.25	58.70 ± 0.08	0.2255 ± 0.0006	-0.59	1.65
	VIII	$+2.45 \pm 0.12$	0.79 ± 0.33	58.84 ± 0.10	0.2251 ± 0.0006	-0.57	0.74
281	VII	$+1.08 \pm 0.12$	1.07 ± 0.35	59.06 ± 0.10	0.2245 ± 0.0006	-0.58	0.76
	VIII	$+2.35 \pm 0.12$	1.08 ± 0.36	59.24 ± 0.10	0.2237 ± 0.0006	-0.58	1.36
331	VII	$+0.95 \pm 0.12$	0.43 ± 0.36	59.62 ± 0.10	0.2200 ± 0.0006	-0.58	1.15
	VIII	$+2.58 \pm 0.12$	0.00 ± 1.27	60.10 ± 0.09	0.2194 ± 0.0006	-0.58	1.65
817	VII	$+1.74 \pm 0.12$	0.00 ± 0.12	60.14 ± 0.08	0.2191 ± 0.0005	-0.59	1.39
	VIII	$+2.64 \pm 0.12$	0.00 ± 0.32	60.67 ± 0.08	0.2168 ± 0.0005	-0.58	1.23
867	VII	$+1.57 \pm 0.11$	0.10 ± 0.34	60.14 ± 0.10	0.2215 ± 0.0005	-0.57	1.07
	VIII	$+2.64 \pm 0.12$	0.00 ± 0.22	60.50 ± 0.08	0.2199 ± 0.0005	-0.59	1.60
917	VII	$+1.68 \pm 0.12$	0.26 ± 0.33	59.41 ± 0.10	0.2200 ± 0.0006	-0.57	1.06
	VIII	$+2.88 \pm 0.12$	0.52 ± 0.35	59.69 ± 0.10	0.2191 ± 0.0006	-0.57	1.59
967	VII	$+1.67 \pm 0.11$	0.37 ± 0.32	59.86 ± 0.09	0.2151 ± 0.0005	-0.58	1.50
	VIII	$+2.60 \pm 0.11$	0.57 ± 0.34	60.20 ± 0.09	0.2136 ± 0.0005	-0.57	1.31
2602	VII	$+0.51 \pm 0.11$	0.99 ± 0.31	59.18 ± 0.09	0.2137 ± 0.0005	-0.57	1.83
	VIII	$+2.53 \pm 0.11$	0.87 ± 0.34	59.68 ± 0.10	0.2135 ± 0.0005	-0.58	1.90
2652	VII	$+0.36 \pm 0.12$	0.83 ± 0.32	58.13 ± 0.10	0.2306 ± 0.0006	-0.58	1.09
	VIII	$+2.25 \pm 0.12$	1.81 ± 0.37	58.42 ± 0.10	0.2288 ± 0.0006	-0.58	1.19
2702	VII	$+0.59 \pm 0.11$	0.00 ± 0.22	59.61 ± 0.08	0.2177 ± 0.0005	-0.59	0.82
	VIII	$+2.32 \pm 0.12$	0.03 ± 0.18	60.04 ± 0.10	0.2157 ± 0.0005	-0.58	0.94
2752	VII	$+0.54 \pm 0.12$	0.27 ± 0.34	59.65 ± 0.10	0.2185 ± 0.0006	-0.58	1.40
	VIII	$+2.39 \pm 0.12$	0.00 ± 0.32	60.02 ± 0.09	0.2177 ± 0.0005	-0.59	1.35

Table 7.24: *Fit parameters extracted form May 2011 data of the OR algorithm for BCM-Vertical luminosity measurement – Y scans.*

BCID	Scan	$X_0[\mu m]$	$b_X[10^{-4}\,(10^{22}p)^{-2}]$	$\Sigma_X[\mu m]$	$\mu_X^{vis,\,peak}[(10^{22}p)^{-2}]$	$C_{\Sigma_X-\mu_X^{vis,\,peak}}$	χ^2/NDF
81	VII	-2.28 ± 0.12	2.99 ± 0.33	55.03 ± 0.10	0.2379 ± 0.0007	-0.58	0.98
	VIII	-0.09 ± 0.12	4.09 ± 0.36	55.58 ± 0.10	0.2355 ± 0.0006	-0.59	1.19
131	VII	-2.31 ± 0.12	0.71 ± 0.34	59.09 ± 0.10	0.2168 ± 0.0005	-0.58	3.10
	VIII	-0.25 ± 0.12	2.90 ± 0.40	59.54 ± 0.10	0.2142 ± 0.0005	-0.57	1.86
181	VII	-2.29 ± 0.12	0.65 ± 0.36	59.07 ± 0.10	0.2135 ± 0.0006	-0.57	3.01
	VIII	-0.12 ± 0.13	2.06 ± 0.41	59.69 ± 0.11	0.2113 ± 0.0006	-0.56	3.74
231	VII	-2.23 ± 0.11	2.33 ± 0.32	56.69 ± 0.09	0.2247 ± 0.0006	-0.58	1.18
	VIII	$+0.03 \pm 0.12$	3.49 ± 0.35	57.21 ± 0.10	0.2221 ± 0.0006	-0.58	0.88
281	VII	-2.42 ± 0.12	2.48 ± 0.31	56.34 ± 0.09	0.2247 ± 0.0006	-0.57	1.22
	VIII	-0.11 ± 0.12	4.42 ± 0.37	56.76 ± 0.10	0.2222 ± 0.0006	-0.58	0.90
331	VII	-2.05 ± 0.12	1.94 ± 0.31	56.87 ± 0.10	0.2194 ± 0.0006	-0.58	1.24
	VIII	$+0.20 \pm 0.12$	3.87 ± 0.36	57.03 ± 0.10	0.2185 ± 0.0006	-0.58	1.53
817	VII	-1.89 ± 0.12	2.93 ± 0.33	56.88 ± 0.09	0.2180 ± 0.0006	-0.58	1.30
	VIII	$+0.07 \pm 0.12$	2.73 ± 0.31	57.27 ± 0.10	0.2153 ± 0.0006	-0.58	1.73
867	VII	-1.83 ± 0.11	3.07 ± 0.31	56.36 ± 0.09	0.2208 ± 0.0006	-0.58	1.95
	VIII	$+0.16 \pm 0.12$	3.17 ± 0.32	56.53 ± 0.09	0.2189 ± 0.0006	-0.58	1.16
917	VII	-1.91 ± 0.12	2.32 ± 0.34	57.34 ± 0.10	0.2196 ± 0.0006	-0.58	1.19
	VIII	$+0.15 \pm 0.12$	2.83 ± 0.35	57.42 ± 0.10	0.2187 ± 0.0006	-0.57	1.84
967	VII	-1.81 ± 0.11	2.48 ± 0.33	58.40 ± 0.09	0.2144 ± 0.0005	-0.57	0.77
	VIII	$+0.07 \pm 0.11$	2.82 ± 0.35	58.56 ± 0.09	0.2132 ± 0.0005	-0.57	1.23
2602	VII	-3.33 ± 0.11	1.78 ± 0.33	58.37 ± 0.09	0.2172 ± 0.0005	-0.56	3.95
	VIII	-0.73 ± 0.11	2.12 ± 0.34	58.83 ± 0.09	0.2145 ± 0.0005	-0.57	4.49
2652	VII	-3.23 ± 0.12	2.21 ± 0.28	55.20 ± 0.09	0.2316 ± 0.0006	-0.58	1.07
	VIII	-0.85 ± 0.12	2.21 ± 0.30	55.53 ± 0.09	0.2302 ± 0.0006	-0.57	2.56
2702	VII	-3.40 ± 0.11	0.89 ± 0.29	57.17 ± 0.09	0.2193 ± 0.0006	-0.57	2.85
	VIII	-0.71 ± 0.12	1.83 ± 0.33	57.51 ± 0.09	0.2172 ± 0.0005	-0.56	4.42
2752	VII	-3.21 ± 0.12	1.27 ± 0.29	56.76 ± 0.09	0.2209 ± 0.0006	-0.57	1.99
	VIII	-0.77 ± 0.12	1.26 ± 0.31	57.04 ± 0.09	0.2202 ± 0.0006	-0.57	3.83

Table 7.25: *Fit parameters extracted form May 2011 data of the OR algorithm for BCM-Horizontal luminosity measurement – X scans.*

BCID	Scan	$Y_0[\mu m]$	$b_Y[10^{-4}\,(10^{22}p)^{-2}]$	$\Sigma_Y[\mu m]$	$\mu_Y^{vis,\,peak}[(10^{22}p)^{-2}]$	$C_{\Sigma_Y-\mu_Y^{vis,\,peak}}$	χ^2/NDF
81	VII	$+0.92 \pm 0.12$	1.64 ± 0.32	57.02 ± 0.10	0.2342 ± 0.0006	-0.59	2.17
	VIII	$+2.58 \pm 0.13$	1.98 ± 0.35	57.23 ± 0.10	0.2342 ± 0.0006	-0.58	1.39
131	VII	$+1.03 \pm 0.12$	0.86 ± 0.31	58.52 ± 0.10	0.2116 ± 0.0006	-0.59	1.50
	VIII	$+2.31 \pm 0.12$	1.55 ± 0.34	58.79 ± 0.10	0.2102 ± 0.0005	-0.58	2.15
181	VII	$+0.99 \pm 0.12$	1.01 ± 0.35	59.03 ± 0.11	0.2080 ± 0.0006	-0.58	1.37
	VIII	$+2.25 \pm 0.13$	1.42 ± 0.37	59.21 ± 0.11	0.2083 ± 0.0006	-0.57	1.80
231	VII	$+0.95 \pm 0.12$	1.10 ± 0.33	58.45 ± 0.10	0.2240 ± 0.0006	-0.58	1.15
	VIII	$+2.59 \pm 0.12$	0.48 ± 0.32	58.88 ± 0.10	0.2225 ± 0.0006	-0.58	1.32
281	VII	$+0.84 \pm 0.12$	1.09 ± 0.36	59.17 ± 0.10	0.2210 ± 0.0006	-0.58	2.19
	VIII	$+2.52 \pm 0.12$	1.48 ± 0.37	59.25 ± 0.10	0.2217 ± 0.0006	-0.58	1.28
331	VII	$+0.96 \pm 0.12$	0.06 ± 0.57	59.77 ± 0.10	0.2186 ± 0.0006	-0.57	1.76
	VIII	$+2.54 \pm 0.12$	1.06 ± 0.38	59.80 ± 0.10	0.2185 ± 0.0006	-0.55	0.84
817	VII	$+1.57 \pm 0.12$	0.26 ± 0.35	60.21 ± 0.10	0.2168 ± 0.0005	-0.57	0.46
	VIII	$+2.95 \pm 0.12$	0.00 ± 0.13	60.58 ± 0.09	0.2151 ± 0.0005	-0.58	1.22
867	VII	$+1.56 \pm 0.11$	0.20 ± 0.35	60.12 ± 0.10	0.2190 ± 0.0005	-0.57	1.00
	VIII	$+2.70 \pm 0.12$	0.97 ± 0.38	60.30 ± 0.10	0.2181 ± 0.0005	-0.58	0.80
917	VII	$+1.45 \pm 0.12$	0.47 ± 0.34	59.43 ± 0.10	0.2183 ± 0.0006	-0.58	1.41
	VIII	$+2.86 \pm 0.12$	1.01 ± 0.35	59.46 ± 0.10	0.2171 ± 0.0006	-0.58	0.61
967	VII	$+1.62 \pm 0.11$	0.33 ± 0.33	59.96 ± 0.09	0.2123 ± 0.0005	-0.57	1.08
	VIII	$+2.76 \pm 0.11$	0.73 ± 0.35	60.24 ± 0.10	0.2115 ± 0.0005	-0.58	1.04
2602	VII	$+0.50 \pm 0.11$	0.73 ± 0.31	59.13 ± 0.09	0.2132 ± 0.0005	-0.58	1.50
	VIII	$+2.46 \pm 0.11$	1.25 ± 0.32	59.52 ± 0.10	0.2107 ± 0.0005	-0.58	2.78
2652	VII	$+0.26 \pm 0.12$	1.38 ± 0.34	57.96 ± 0.10	0.2290 ± 0.0006	-0.58	1.89
	VIII	$+2.47 \pm 0.12$	1.62 ± 0.35	58.39 ± 0.10	0.2269 ± 0.0006	-0.58	1.14
2702	VII	$+0.54 \pm 0.12$	0.00 ± 0.17	59.58 ± 0.08	0.2154 ± 0.0005	-0.58	1.30
	VIII	$+2.46 \pm 0.12$	0.53 ± 0.35	59.95 ± 0.10	0.2140 ± 0.0005	-0.58	1.42
2752	VII	$+0.63 \pm 0.12$	0.48 ± 0.34	59.47 ± 0.10	0.2163 ± 0.0006	-0.58	1.62
	VIII	$+2.20 \pm 0.12$	0.95 ± 0.37	59.90 ± 0.10	0.2159 ± 0.0005	-0.57	0.55

Table 7.26: *Fit parameters extracted form May 2011 data of the OR algorithm for BCM-Horizontal luminosity measurement – Y scans.*

XOR-A algorithm

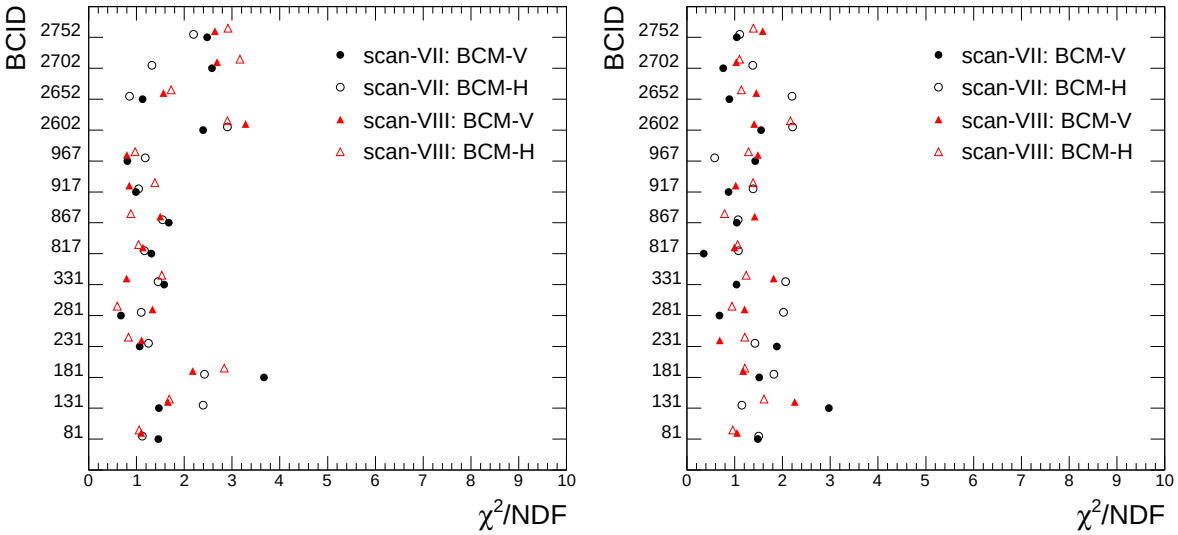

Figure 7.27: *χ^2 evaluation of the x scan (left) and y scan (right) fit for the XOR-A algorithm.*

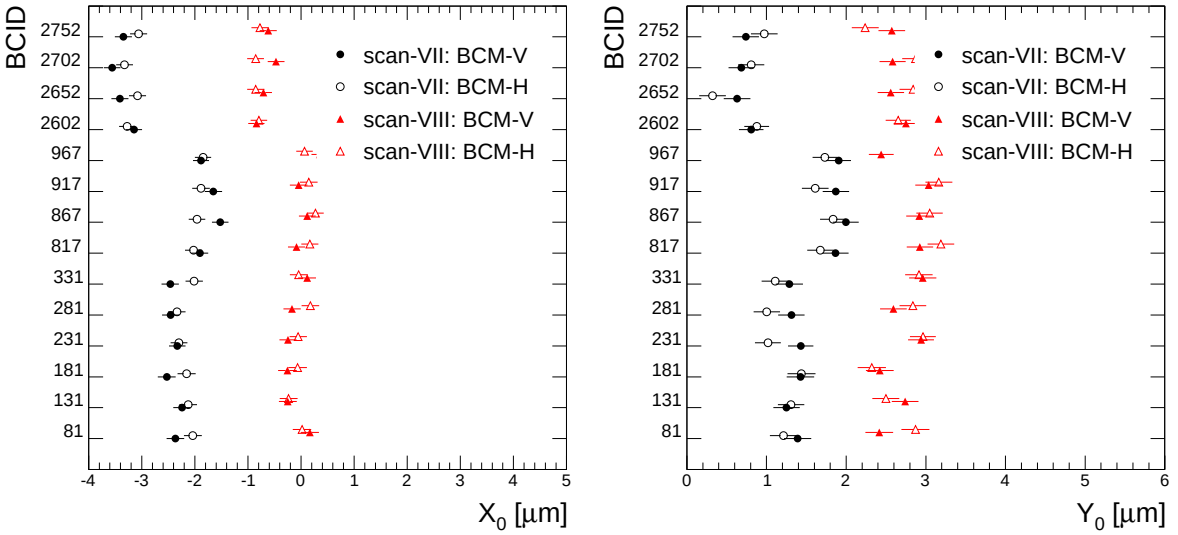

Figure 7.28: *Offset of the centered beams during x scans (left) and y scans (right) for the XOR-A algorithm.*

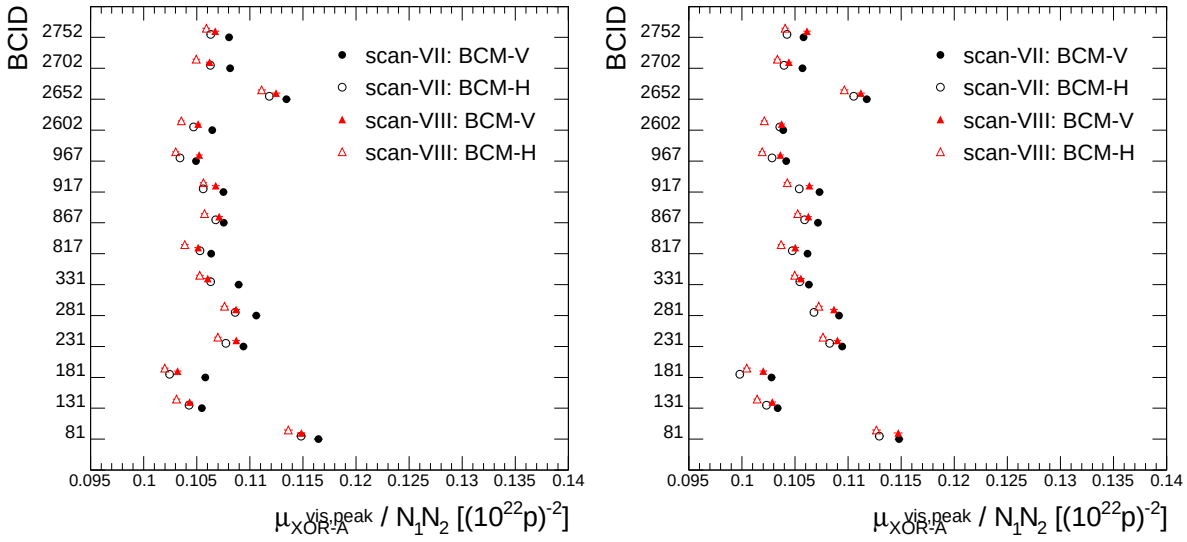

Figure 7.29: *The maximum beam current normalized μ^{vis} during x scans (left) and y scans (right) for the XOR-A algorithm.*

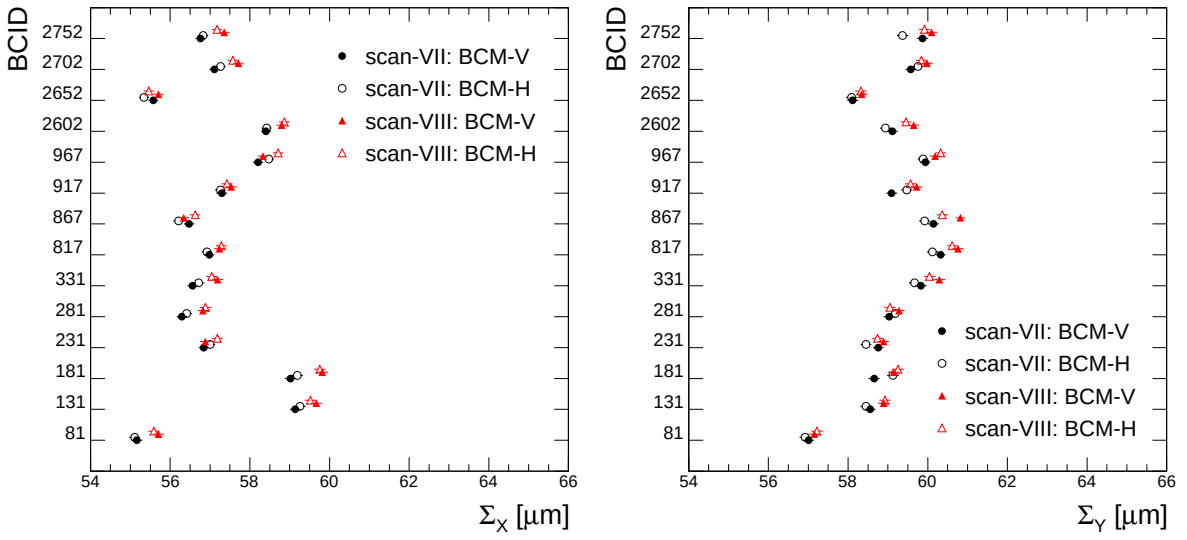

Figure 7.30: *The effective beam width as obtained form the fits of x scans (left) and y scans (right) for the XOR-A algorithm.*

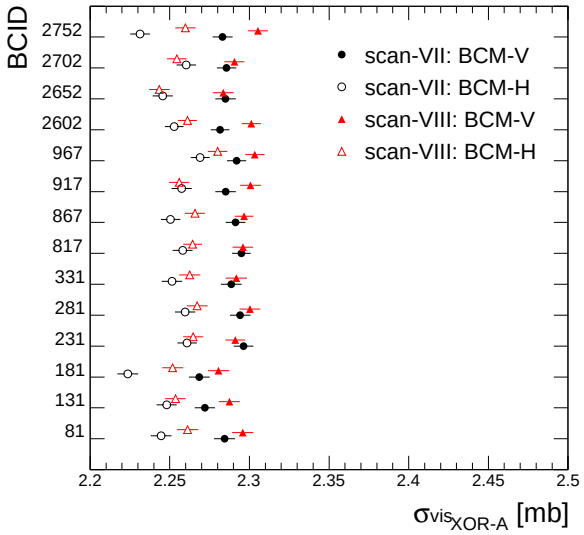

Figure 7.31: *Visible cross-sections for both BCM luminosity measurements, both scans, and all BCIDs. An excelent agreement is obtained for the XOR-A algorithm.*

BCID	Visible cross-section [mb]			
	BCM-Verical		BCM-Horizontal	
	Scan VII	Scan VIII	Scan VII	Scan VIII
81	2.284 ± 0.007	2.296 ± 0.007	2.245 ± 0.007	2.261 ± 0.007
131	2.272 ± 0.006	2.287 ± 0.007	2.248 ± 0.006	2.254 ± 0.006
181	2.269 ± 0.007	2.281 ± 0.007	2.224 ± 0.007	2.252 ± 0.007
231	2.296 ± 0.006	2.291 ± 0.006	2.261 ± 0.006	2.265 ± 0.006
281	2.294 ± 0.006	2.300 ± 0.007	2.260 ± 0.006	2.267 ± 0.006
331	2.289 ± 0.006	2.292 ± 0.007	2.251 ± 0.006	2.263 ± 0.007
817	2.295 ± 0.006	2.296 ± 0.006	2.258 ± 0.006	2.264 ± 0.006
867	2.291 ± 0.006	2.297 ± 0.006	2.251 ± 0.006	2.266 ± 0.006
917	2.285 ± 0.006	2.301 ± 0.007	2.257 ± 0.006	2.256 ± 0.006
967	2.292 ± 0.006	2.303 ± 0.006	2.269 ± 0.006	2.280 ± 0.006
2602	2.282 ± 0.006	2.301 ± 0.006	2.253 ± 0.006	2.261 ± 0.006
2652	2.285 ± 0.006	2.284 ± 0.006	2.246 ± 0.006	2.243 ± 0.006
2702	2.286 ± 0.006	2.291 ± 0.006	2.260 ± 0.006	2.254 ± 0.006
2752	2.283 ± 0.006	2.305 ± 0.006	2.231 ± 0.006	2.260 ± 0.006
Average	2.286 ± 0.002	2.295 ± 0.002	2.251 ± 0.002	2.261 ± 0.002
RMS	0.008	0.007	0.011	0.008

Table 7.27: *May 2011 vissible cross-section obtained for the XOR-A algorithm.*

BCID	Scan	$X_0[\mu m]$	$b_X[10^{-4}\,(10^{22}p)^{-2}]$	$\Sigma_X[\mu m]$	$\mu_X^{vis,\,peak}[(10^{22}p)^{-2}]$	$C_{\Sigma_X-\mu_X^{vis,\,peak}}$	χ^2/NDF
81	VII	-2.37 ± 0.17	1.60 ± 0.23	55.16 ± 0.13	0.1164 ± 0.0004	-0.57	1.46
	VIII	$+0.17 \pm 0.17$	2.11 ± 0.26	55.71 ± 0.14	0.1148 ± 0.0004	-0.57	1.10
131	VII	-2.24 ± 0.16	1.07 ± 0.27	59.14 ± 0.14	0.1055 ± 0.0003	-0.54	1.47
	VIII	-0.25 ± 0.17	2.22 ± 0.31	59.67 ± 0.14	0.1043 ± 0.0003	-0.55	1.66
181	VII	-2.53 ± 0.17	0.41 ± 0.26	59.02 ± 0.14	0.1058 ± 0.0004	-0.55	3.67
	VIII	-0.26 ± 0.18	1.50 ± 0.31	59.82 ± 0.15	0.1032 ± 0.0004	-0.55	2.18
231	VII	-2.33 ± 0.16	1.25 ± 0.22	56.84 ± 0.13	0.1094 ± 0.0004	-0.56	1.07
	VIII	-0.25 ± 0.16	2.25 ± 0.25	56.88 ± 0.13	0.1087 ± 0.0004	-0.57	1.11
281	VII	-2.46 ± 0.16	1.54 ± 0.23	56.29 ± 0.13	0.1106 ± 0.0004	-0.56	0.68
	VIII	-0.17 ± 0.16	2.40 ± 0.27	56.82 ± 0.14	0.1087 ± 0.0004	-0.56	1.33
331	VII	-2.46 ± 0.16	1.43 ± 0.23	56.56 ± 0.13	0.1090 ± 0.0004	-0.57	1.58
	VIII	$+0.11 \pm 0.17$	2.27 ± 0.27	57.19 ± 0.14	0.1060 ± 0.0004	-0.56	0.80
817	VII	-1.91 ± 0.16	1.19 ± 0.22	56.98 ± 0.13	0.1064 ± 0.0004	-0.57	1.32
	VIII	-0.09 ± 0.16	1.71 ± 0.24	57.24 ± 0.13	0.1051 ± 0.0004	-0.56	1.13
867	VII	-1.52 ± 0.16	1.57 ± 0.21	56.48 ± 0.13	0.1075 ± 0.0004	-0.57	1.67
	VIII	$+0.12 \pm 0.16$	2.23 ± 0.24	56.34 ± 0.13	0.1071 ± 0.0004	-0.56	1.50
917	VII	-1.65 ± 0.16	1.76 ± 0.26	57.29 ± 0.14	0.1075 ± 0.0004	-0.55	0.99
	VIII	-0.04 ± 0.17	1.76 ± 0.26	57.53 ± 0.14	0.1068 ± 0.0004	-0.56	0.85
967	VII	-1.88 ± 0.15	1.91 ± 0.25	58.21 ± 0.13	0.1049 ± 0.0003	-0.56	0.81
	VIII	$+0.35 \pm 0.15$	1.71 ± 0.25	58.33 ± 0.13	0.1052 ± 0.0003	-0.56	0.80
2602	VII	-3.14 ± 0.15	1.13 ± 0.24	58.40 ± 0.12	0.1065 ± 0.0003	-0.55	2.40
	VIII	-0.84 ± 0.15	1.31 ± 0.25	58.80 ± 0.13	0.1051 ± 0.0003	-0.55	3.28
2652	VII	-3.41 ± 0.16	0.98 ± 0.20	55.57 ± 0.13	0.1134 ± 0.0004	-0.56	1.13
	VIII	-0.71 ± 0.16	1.62 ± 0.23	55.70 ± 0.13	0.1125 ± 0.0004	-0.56	1.56
2702	VII	-3.56 ± 0.16	0.77 ± 0.22	57.11 ± 0.12	0.1081 ± 0.0003	-0.55	2.58
	VIII	-0.47 ± 0.16	1.37 ± 0.24	57.71 ± 0.13	0.1062 ± 0.0003	-0.55	2.69
2752	VII	-3.35 ± 0.16	1.00 ± 0.22	56.76 ± 0.13	0.1081 ± 0.0004	-0.56	2.48
	VIII	-0.62 ± 0.16	0.76 ± 0.23	57.36 ± 0.13	0.1067 ± 0.0004	-0.56	2.64

Table 7.28: *Fit parameters extracted form May 2011 data of the XOR-A algorithm for BCM-Vertical luminosity measurement – X scans.*

BCID	Scan	$Y_0[\mu m]$	$b_Y[10^{-4}\,(10^{22}p)^{-2}]$	$\Sigma_Y[\mu m]$	$\mu_Y^{vis,\,peak}[(10^{22}p)^{-2}]$	$C_{\Sigma_Y-\mu_Y^{vis,\,peak}}$	χ^2/NDF
81	VII	$+1.39 \pm 0.17$	0.96 ± 0.24	57.01 ± 0.14	0.1148 ± 0.0004	-0.55	1.48
	VIII	$+2.42 \pm 0.17$	1.41 ± 0.26	57.15 ± 0.14	0.1147 ± 0.0004	-0.57	1.05
131	VII	$+1.25 \pm 0.17$	0.78 ± 0.24	58.55 ± 0.14	0.1034 ± 0.0003	-0.56	2.97
	VIII	$+2.74 \pm 0.17$	0.89 ± 0.24	58.89 ± 0.14	0.1029 ± 0.0003	-0.57	2.26
181	VII	$+1.43 \pm 0.17$	1.07 ± 0.26	58.65 ± 0.14	0.1028 ± 0.0004	-0.56	1.51
	VIII	$+2.42 \pm 0.17$	1.21 ± 0.27	59.14 ± 0.15	0.1020 ± 0.0004	-0.56	1.18
231	VII	$+1.43 \pm 0.16$	0.26 ± 0.23	58.76 ± 0.13	0.1094 ± 0.0004	-0.56	1.88
	VIII	$+2.94 \pm 0.16$	0.54 ± 0.23	58.89 ± 0.13	0.1090 ± 0.0004	-0.58	0.69
281	VII	$+1.31 \pm 0.17$	0.88 ± 0.25	59.03 ± 0.14	0.1092 ± 0.0004	-0.56	0.68
	VIII	$+2.59 \pm 0.17$	0.87 ± 0.26	59.28 ± 0.14	0.1087 ± 0.0004	-0.57	1.21
331	VII	$+1.29 \pm 0.17$	0.46 ± 0.27	59.83 ± 0.14	0.1063 ± 0.0004	-0.56	1.04
	VIII	$+2.96 \pm 0.17$	0.42 ± 0.28	60.29 ± 0.15	0.1056 ± 0.0004	-0.56	1.82
817	VII	$+1.87 \pm 0.16$	0.00 ± 0.20	60.33 ± 0.12	0.1062 ± 0.0003	-0.57	0.35
	VIII	$+2.93 \pm 0.16$	0.10 ± 0.27	60.76 ± 0.14	0.1050 ± 0.0003	-0.55	0.99
867	VII	$+1.99 \pm 0.16$	0.91 ± 0.27	60.15 ± 0.14	0.1072 ± 0.0003	-0.56	1.04
	VIII	$+2.92 \pm 0.16$	0.00 ± 0.21	60.82 ± 0.12	0.1062 ± 0.0003	-0.57	1.42
917	VII	$+1.87 \pm 0.17$	0.60 ± 0.25	59.09 ± 0.14	0.1073 ± 0.0004	-0.56	0.87
	VIII	$+3.04 \pm 0.17$	0.47 ± 0.26	59.72 ± 0.14	0.1064 ± 0.0004	-0.56	1.02
967	VII	$+1.91 \pm 0.15$	0.44 ± 0.23	59.94 ± 0.13	0.1042 ± 0.0003	-0.56	1.43
	VIII	$+2.44 \pm 0.16$	0.78 ± 0.26	60.19 ± 0.14	0.1036 ± 0.0003	-0.56	1.48
2602	VII	$+0.81 \pm 0.15$	0.90 ± 0.23	59.11 ± 0.13	0.1039 ± 0.0003	-0.56	1.55
	VIII	$+2.75 \pm 0.16$	0.70 ± 0.25	59.65 ± 0.13	0.1037 ± 0.0003	-0.56	1.41
2652	VII	$+0.63 \pm 0.17$	0.80 ± 0.24	58.12 ± 0.14	0.1118 ± 0.0004	-0.56	0.89
	VIII	$+2.56 \pm 0.17$	1.52 ± 0.28	58.34 ± 0.14	0.1112 ± 0.0004	-0.56	1.45
2702	VII	$+0.68 \pm 0.16$	0.25 ± 0.24	59.57 ± 0.14	0.1057 ± 0.0003	-0.56	0.76
	VIII	$+2.58 \pm 0.16$	0.37 ± 0.25	59.98 ± 0.14	0.1044 ± 0.0003	-0.56	1.03
2752	VII	$+0.74 \pm 0.17$	0.49 ± 0.26	59.87 ± 0.14	0.1058 ± 0.0004	-0.56	1.05
	VIII	$+2.57 \pm 0.17$	0.17 ± 0.26	60.10 ± 0.14	0.1061 ± 0.0004	-0.56	1.59

Table 7.29: *Fit parameters extracted form May 2011 data of the XOR-A algorithm for BCM-Vertical luminosity measurement – Y scans.*

BCID	Scan	$X_0[\mu m]$	$b_X[10^{-4}\,(10^{22}p)^{-2}]$	$\Sigma_X[\mu m]$	$\mu_X^{vis,\,peak}[(10^{22}p)^{-2}]$	$C_{\Sigma_X-\mu_X^{vis,\,peak}}$	χ^2/NDF
81	VII	-2.04 ± 0.17	1.68 ± 0.24	55.11 ± 0.14	0.1148 ± 0.0004	-0.58	1.12
	VIII	$+0.02 \pm 0.17$	2.34 ± 0.26	55.59 ± 0.14	0.1136 ± 0.0004	-0.56	1.06
131	VII	-2.12 ± 0.16	0.53 ± 0.25	59.26 ± 0.14	0.1043 ± 0.0003	-0.55	2.40
	VIII	-0.24 ± 0.17	1.84 ± 0.29	59.52 ± 0.14	0.1031 ± 0.0003	-0.56	1.69
181	VII	-2.16 ± 0.17	0.66 ± 0.27	59.19 ± 0.14	0.1024 ± 0.0004	-0.55	2.43
	VIII	-0.06 ± 0.18	0.95 ± 0.28	59.75 ± 0.15	0.1020 ± 0.0004	-0.56	2.83
231	VII	-2.30 ± 0.16	0.92 ± 0.22	57.00 ± 0.13	0.1077 ± 0.0004	-0.57	1.25
	VIII	-0.05 ± 0.16	2.20 ± 0.26	57.18 ± 0.14	0.1070 ± 0.0004	-0.56	0.83
281	VII	-2.34 ± 0.16	1.25 ± 0.22	56.42 ± 0.13	0.1086 ± 0.0004	-0.57	1.10
	VIII	$+0.17 \pm 0.17$	2.35 ± 0.27	56.88 ± 0.14	0.1076 ± 0.0004	-0.56	0.60
331	VII	-2.01 ± 0.17	1.49 ± 0.23	56.72 ± 0.14	0.1063 ± 0.0004	-0.57	1.45
	VIII	-0.04 ± 0.17	2.26 ± 0.26	57.04 ± 0.14	0.1053 ± 0.0004	-0.57	1.53
817	VII	-2.02 ± 0.16	1.38 ± 0.22	56.92 ± 0.13	0.1053 ± 0.0004	-0.56	1.17
	VIII	$+0.17 \pm 0.16$	1.68 ± 0.24	57.29 ± 0.13	0.1039 ± 0.0003	-0.57	1.04
867	VII	-1.96 ± 0.16	1.57 ± 0.21	56.21 ± 0.13	0.1068 ± 0.0004	-0.57	1.55
	VIII	$+0.27 \pm 0.16$	1.70 ± 0.23	56.62 ± 0.13	0.1057 ± 0.0004	-0.57	0.88
917	VII	-1.89 ± 0.16	1.55 ± 0.25	57.26 ± 0.14	0.1056 ± 0.0004	-0.56	1.04
	VIII	$+0.14 \pm 0.17$	1.64 ± 0.25	57.43 ± 0.14	0.1056 ± 0.0004	-0.56	1.39
967	VII	-1.85 ± 0.15	1.56 ± 0.25	58.47 ± 0.13	0.1034 ± 0.0003	-0.56	1.18
	VIII	$+0.07 \pm 0.15$	1.52 ± 0.25	58.71 ± 0.13	0.1030 ± 0.0003	-0.56	0.97
2602	VII	-3.28 ± 0.15	1.00 ± 0.24	58.42 ± 0.13	0.1047 ± 0.0003	-0.55	2.91
	VIII	-0.79 ± 0.15	1.15 ± 0.24	58.87 ± 0.13	0.1035 ± 0.0003	-0.56	2.90
2652	VII	-3.08 ± 0.16	1.39 ± 0.22	55.34 ± 0.13	0.1118 ± 0.0004	-0.57	0.85
	VIII	-0.85 ± 0.16	1.48 ± 0.23	55.46 ± 0.13	0.1111 ± 0.0004	-0.56	1.72
2702	VII	-3.32 ± 0.16	0.74 ± 0.22	57.27 ± 0.13	0.1063 ± 0.0003	-0.55	1.32
	VIII	-0.86 ± 0.16	1.14 ± 0.24	57.57 ± 0.13	0.1050 ± 0.0003	-0.55	3.17
2752	VII	-3.06 ± 0.16	0.90 ± 0.21	56.83 ± 0.13	0.1063 ± 0.0004	-0.55	2.20
	VIII	-0.77 ± 0.16	1.00 ± 0.23	57.17 ± 0.13	0.1059 ± 0.0004	-0.55	2.91

Table 7.30: *Fit parameters extracted form May 2011 data of the XOR-A algorithm for BCM-Horizontal luminosity measurement – X scans.*

BCID	Scan	$Y_0[\mu m]$	$b_Y[10^{-4}\,(10^{22}p)^{-2}]$	$\Sigma_Y[\mu m]$	$\mu_Y^{vis,\,peak}[(10^{22}p)^{-2}]$	$C_{\Sigma_Y-\mu_Y^{vis,\,peak}}$	χ^2/NDF
81	VII	$+1.21 \pm 0.17$	0.96 ± 0.24	56.92 ± 0.14	0.1129 ± 0.0004	-0.56	1.50
	VIII	$+2.87 \pm 0.17$	1.30 ± 0.25	57.22 ± 0.14	0.1127 ± 0.0004	-0.57	0.96
131	VII	$+1.31 \pm 0.17$	0.94 ± 0.23	58.45 ± 0.14	0.1023 ± 0.0003	-0.57	1.15
	VIII	$+2.50 \pm 0.17$	0.98 ± 0.25	58.92 ± 0.14	0.1014 ± 0.0003	-0.57	1.62
181	VII	$+1.44 \pm 0.18$	0.59 ± 0.25	59.13 ± 0.15	0.0998 ± 0.0004	-0.56	1.82
	VIII	$+2.32 \pm 0.18$	1.14 ± 0.27	59.25 ± 0.15	0.1005 ± 0.0004	-0.56	1.21
231	VII	$+1.02 \pm 0.16$	0.83 ± 0.24	58.45 ± 0.13	0.1083 ± 0.0004	-0.56	1.42
	VIII	$+2.96 \pm 0.16$	0.72 ± 0.24	58.74 ± 0.14	0.1076 ± 0.0004	-0.56	1.21
281	VII	$+1.00 \pm 0.17$	0.88 ± 0.26	59.19 ± 0.14	0.1068 ± 0.0004	-0.56	2.02
	VIII	$+2.84 \pm 0.17$	1.21 ± 0.27	59.05 ± 0.14	0.1072 ± 0.0004	-0.56	0.94
331	VII	$+1.11 \pm 0.17$	0.40 ± 0.27	59.67 ± 0.14	0.1055 ± 0.0004	-0.56	2.07
	VIII	$+2.91 \pm 0.17$	0.78 ± 0.28	60.05 ± 0.15	0.1050 ± 0.0004	-0.56	1.24
817	VII	$+1.68 \pm 0.16$	0.49 ± 0.25	60.12 ± 0.14	0.1047 ± 0.0003	-0.56	1.08
	VIII	$+3.19 \pm 0.17$	0.00 ± 0.13	60.61 ± 0.12	0.1037 ± 0.0003	-0.57	1.06
867	VII	$+1.84 \pm 0.16$	0.39 ± 0.25	59.92 ± 0.14	0.1059 ± 0.0003	-0.56	1.07
	VIII	$+3.05 \pm 0.16$	0.79 ± 0.28	60.37 ± 0.14	0.1053 ± 0.0003	-0.56	0.79
917	VII	$+1.61 \pm 0.17$	0.43 ± 0.24	59.47 ± 0.14	0.1054 ± 0.0004	-0.57	1.39
	VIII	$+3.16 \pm 0.17$	0.75 ± 0.26	59.57 ± 0.14	0.1043 ± 0.0004	-0.56	1.39
967	VII	$+1.73 \pm 0.16$	0.35 ± 0.23	59.88 ± 0.13	0.1029 ± 0.0003	-0.56	0.58
	VIII	$+3.15 \pm 0.16$	0.82 ± 0.26	60.32 ± 0.14	0.1019 ± 0.0003	-0.56	1.29
2602	VII	$+0.88 \pm 0.16$	0.76 ± 0.23	58.94 ± 0.13	0.1036 ± 0.0003	-0.56	2.21
	VIII	$+2.65 \pm 0.16$	1.17 ± 0.25	59.45 ± 0.13	0.1021 ± 0.0003	-0.56	2.17
2652	VII	$+0.32 \pm 0.17$	1.18 ± 0.26	58.09 ± 0.14	0.1105 ± 0.0004	-0.57	2.20
	VIII	$+2.84 \pm 0.17$	1.17 ± 0.26	58.32 ± 0.14	0.1096 ± 0.0004	-0.56	1.14
2702	VII	$+0.81 \pm 0.16$	0.21 ± 0.24	59.75 ± 0.14	0.1040 ± 0.0003	-0.56	1.38
	VIII	$+2.87 \pm 0.17$	0.60 ± 0.25	59.84 ± 0.14	0.1033 ± 0.0003	-0.56	1.10
2752	VII	$+0.97 \pm 0.17$	0.72 ± 0.26	59.36 ± 0.14	0.1042 ± 0.0004	-0.56	1.10
	VIII	$+2.24 \pm 0.17$	0.76 ± 0.27	59.92 ± 0.14	0.1041 ± 0.0003	-0.56	1.39

Table 7.31: *Fit parameters extracted form May 2011 data of the XOR-A algorithm for BCM-Horizontal luminosity measurement – Y scans.*

XOR-C algorithm

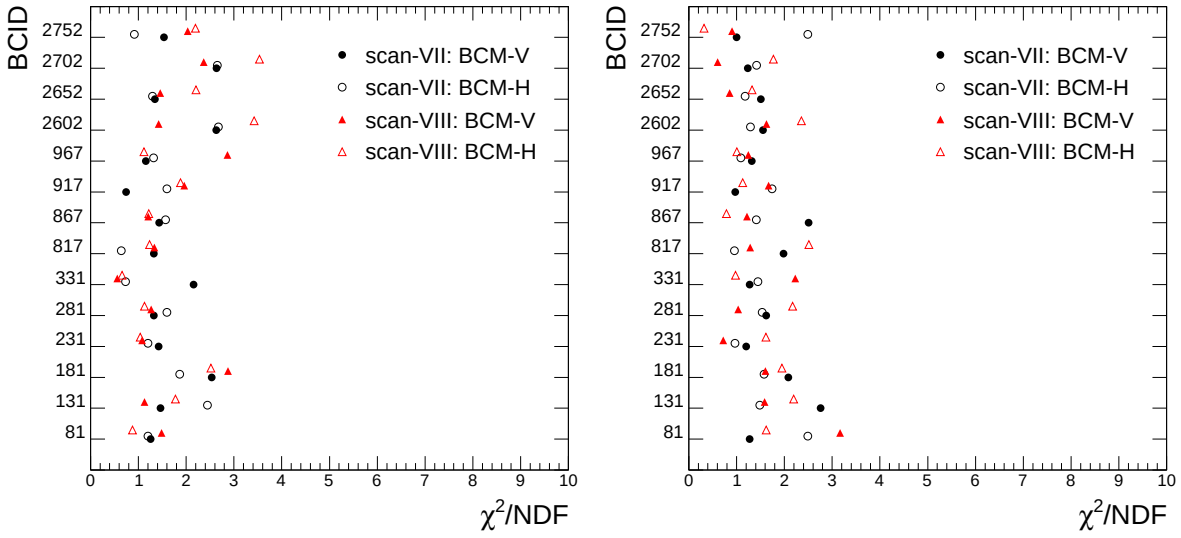

Figure 7.32: *χ^2 evaluation of the x scan (left) and y scan (right) fits for the XOR-C algorithm.*

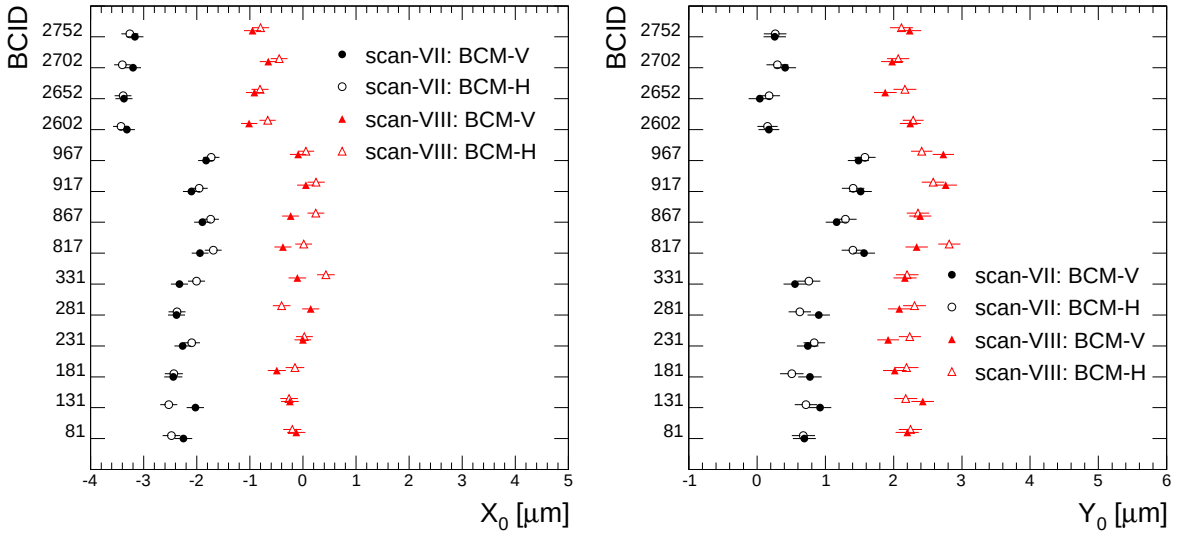

Figure 7.33: *Offset of the centered beams during x scans (left) and y scans (right) for the XOR-C algorithm.*

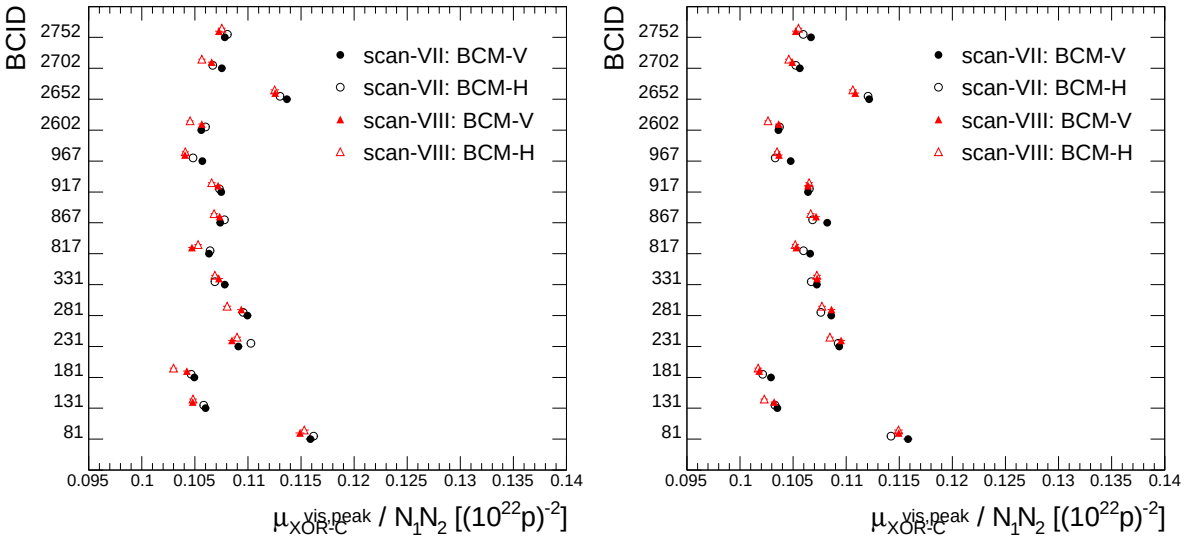

Figure 7.34: *The maximum beam current normalized μ^{vis} during x scans (left) and y scans (right) for the XOR-C algorithm.*

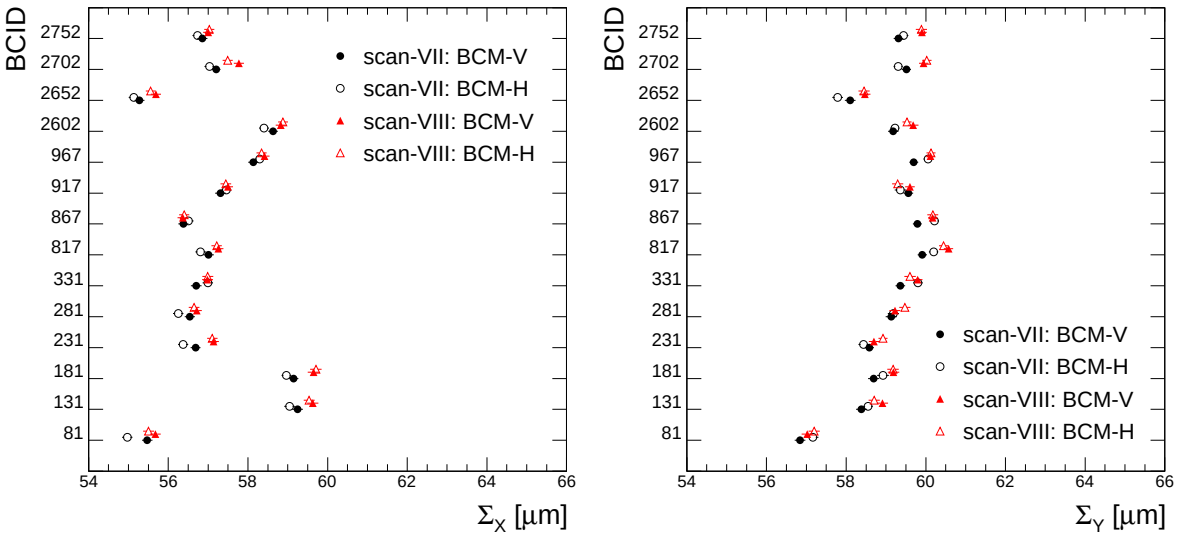

Figure 7.35: *The effective beam width as obtained form the fits of x scans (left) and y scans (right) for the XOR-C algorithm.*

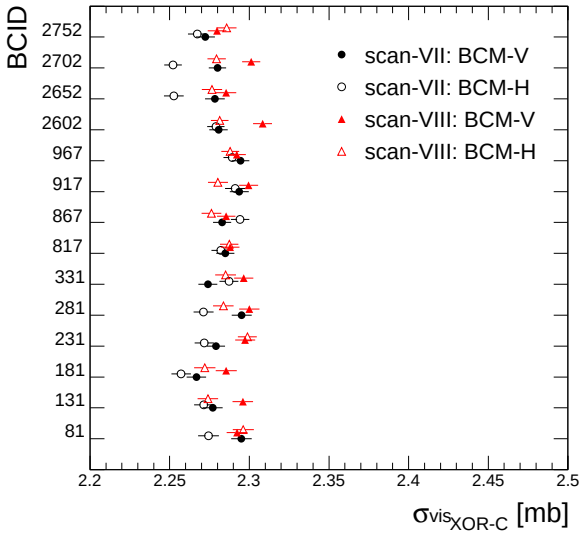

Figure 7.36: *Visible cross-sections for both BCM luminosity measurements, both scans, and all BCIDs. An excelent agreement is obtained for the XOR-C algorithm.*

BCID	Visible cross-section [mb]			
	BCM-Verical		BCM-Horizontal	
	Scan VII	Scan VIII	Scan VII	Scan VIII
81	2.295 ± 0.006	2.292 ± 0.007	2.274 ± 0.007	2.296 ± 0.007
131	2.277 ± 0.006	2.296 ± 0.006	2.271 ± 0.006	2.274 ± 0.006
181	2.267 ± 0.006	2.285 ± 0.007	2.257 ± 0.006	2.272 ± 0.007
231	2.279 ± 0.006	2.297 ± 0.006	2.272 ± 0.006	2.299 ± 0.006
281	2.295 ± 0.006	2.300 ± 0.006	2.271 ± 0.006	2.284 ± 0.006
331	2.274 ± 0.006	2.296 ± 0.006	2.287 ± 0.006	2.285 ± 0.006
817	2.285 ± 0.006	2.288 ± 0.006	2.282 ± 0.006	2.287 ± 0.006
867	2.283 ± 0.006	2.285 ± 0.006	2.294 ± 0.006	2.276 ± 0.006
917	2.294 ± 0.006	2.300 ± 0.006	2.291 ± 0.006	2.280 ± 0.006
967	2.294 ± 0.006	2.292 ± 0.006	2.289 ± 0.006	2.288 ± 0.006
2602	2.281 ± 0.006	2.308 ± 0.006	2.279 ± 0.005	2.281 ± 0.006
2652	2.278 ± 0.006	2.285 ± 0.006	2.253 ± 0.006	2.277 ± 0.006
2702	2.280 ± 0.005	2.301 ± 0.006	2.252 ± 0.006	2.279 ± 0.006
2752	2.272 ± 0.006	2.280 ± 0.006	2.267 ± 0.006	2.286 ± 0.006
Average	2.282 ± 0.002	2.293 ± 0.002	2.275 ± 0.002	2.283 ± 0.002
RMS	0.009	0.008	0.013	0.008

Table 7.32: *May 2011 vissible cross-section obtained for the XOR-C algorithm.*

BCID	Scan	$X_0[\mu m]$	$b_X[10^{-4}\,(10^{22}p)^{-2}]$	$\Sigma_X[\mu m]$	$\mu_X^{vis,\,peak}[(10^{22}p)^{-2}]$	$C_{\Sigma_X-\mu_X^{vis,\,peak}}$	χ^2/NDF
81	VII	-2.25 ± 0.17	0.19 ± 0.17	55.47 ± 0.13	0.1159 ± 0.0004	-0.58	1.26
	VIII	-0.13 ± 0.17	1.17 ± 0.21	55.68 ± 0.13	0.1149 ± 0.0004	-0.59	1.48
131	VII	-2.02 ± 0.16	0.27 ± 0.24	59.25 ± 0.14	0.1060 ± 0.0003	-0.56	1.46
	VIII	-0.25 ± 0.17	0.95 ± 0.27	59.63 ± 0.14	0.1048 ± 0.0003	-0.56	1.13
181	VII	-2.44 ± 0.17	0.00 ± 0.13	59.15 ± 0.12	0.1049 ± 0.0004	-0.56	2.53
	VIII	-0.49 ± 0.17	0.09 ± 0.25	59.65 ± 0.14	0.1043 ± 0.0004	-0.55	2.88
231	VII	-2.27 ± 0.16	0.46 ± 0.19	56.68 ± 0.13	0.1091 ± 0.0004	-0.56	1.43
	VIII	$+0.00 \pm 0.16$	1.19 ± 0.22	57.14 ± 0.13	0.1085 ± 0.0004	-0.56	1.08
281	VII	-2.38 ± 0.16	0.59 ± 0.19	56.54 ± 0.13	0.1100 ± 0.0004	-0.57	1.32
	VIII	$+0.15 \pm 0.16$	1.17 ± 0.22	56.71 ± 0.13	0.1094 ± 0.0004	-0.56	1.27
331	VII	-2.33 ± 0.16	0.64 ± 0.20	56.70 ± 0.13	0.1078 ± 0.0004	-0.57	2.16
	VIII	-0.10 ± 0.17	1.39 ± 0.24	56.98 ± 0.14	0.1073 ± 0.0004	-0.57	0.56
817	VII	-1.94 ± 0.16	0.89 ± 0.20	57.01 ± 0.13	0.1063 ± 0.0004	-0.57	1.32
	VIII	-0.38 ± 0.16	1.19 ± 0.22	57.25 ± 0.13	0.1047 ± 0.0004	-0.56	1.33
867	VII	-1.90 ± 0.16	0.70 ± 0.18	56.38 ± 0.13	0.1074 ± 0.0004	-0.57	1.44
	VIII	-0.23 ± 0.16	1.64 ± 0.22	56.36 ± 0.13	0.1073 ± 0.0004	-0.57	1.21
917	VII	-2.10 ± 0.16	0.50 ± 0.20	57.31 ± 0.13	0.1075 ± 0.0004	-0.57	0.74
	VIII	$+0.05 \pm 0.16$	0.64 ± 0.21	57.49 ± 0.13	0.1072 ± 0.0004	-0.57	1.96
967	VII	-1.82 ± 0.15	0.92 ± 0.22	58.13 ± 0.13	0.1057 ± 0.0003	-0.56	1.16
	VIII	-0.09 ± 0.15	1.07 ± 0.22	58.42 ± 0.13	0.1041 ± 0.0003	-0.56	2.86
2602	VII	-3.32 ± 0.15	0.25 ± 0.20	58.63 ± 0.12	0.1056 ± 0.0003	-0.55	2.63
	VIII	-1.01 ± 0.15	0.58 ± 0.22	58.82 ± 0.13	0.1056 ± 0.0003	-0.56	1.43
2652	VII	-3.37 ± 0.16	0.46 ± 0.17	55.28 ± 0.12	0.1137 ± 0.0004	-0.57	1.35
	VIII	-0.92 ± 0.16	0.92 ± 0.20	55.69 ± 0.13	0.1126 ± 0.0004	-0.56	1.46
2702	VII	-3.20 ± 0.15	0.00 ± 0.24	57.20 ± 0.11	0.1075 ± 0.0003	-0.56	2.64
	VIII	-0.66 ± 0.16	0.51 ± 0.21	57.77 ± 0.13	0.1066 ± 0.0003	-0.56	2.37
2752	VII	-3.16 ± 0.16	0.33 ± 0.19	56.85 ± 0.13	0.1078 ± 0.0004	-0.54	1.53
	VIII	-0.95 ± 0.16	0.33 ± 0.19	57.00 ± 0.13	0.1073 ± 0.0004	-0.55	2.03

Table 7.33: *Fit parameters extracted form May 2011 data of the XOR-C algorithm for BCM-Vertical luminosity measurement – X scans.*

BCID	Scan	$Y_0[\mu m]$	$b_Y[10^{-4}\,(10^{22}p)^{-2}]$	$\Sigma_Y[\mu m]$	$\mu_Y^{vis,\,peak}[(10^{22}p)^{-2}]$	$C_{\Sigma_Y-\mu_Y^{vis,\,peak}}$	χ^2/NDF
81	VII	$+0.69 \pm 0.17$	0.45 ± 0.21	56.84 ± 0.14	0.1158 ± 0.0004	-0.58	1.27
	VIII	$+2.20 \pm 0.17$	0.46 ± 0.21	57.02 ± 0.14	0.1149 ± 0.0004	-0.57	3.17
131	VII	$+0.92 \pm 0.16$	0.16 ± 0.21	58.39 ± 0.13	0.1035 ± 0.0003	-0.56	2.76
	VIII	$+2.43 \pm 0.17$	0.30 ± 0.23	58.91 ± 0.14	0.1032 ± 0.0003	-0.57	1.59
181	VII	$+0.77 \pm 0.17$	0.11 ± 0.21	58.69 ± 0.14	0.1029 ± 0.0004	-0.57	2.09
	VIII	$+2.02 \pm 0.17$	0.36 ± 0.23	59.19 ± 0.15	0.1018 ± 0.0004	-0.57	1.61
231	VII	$+0.74 \pm 0.16$	0.00 ± 0.04	58.58 ± 0.11	0.1094 ± 0.0004	-0.57	1.20
	VIII	$+1.92 \pm 0.16$	0.30 ± 0.23	58.70 ± 0.13	0.1095 ± 0.0004	-0.56	0.72
281	VII	$+0.90 \pm 0.17$	0.07 ± 0.23	59.13 ± 0.14	0.1086 ± 0.0004	-0.57	1.62
	VIII	$+2.08 \pm 0.17$	0.12 ± 0.23	59.22 ± 0.14	0.1086 ± 0.0004	-0.57	1.03
331	VII	$+0.55 \pm 0.17$	0.00 ± 0.62	59.36 ± 0.12	0.1072 ± 0.0004	-0.59	1.27
	VIII	$+2.17 \pm 0.17$	0.00 ± 0.03	59.80 ± 0.12	0.1073 ± 0.0004	-0.56	2.23
817	VII	$+1.57 \pm 0.16$	0.00 ± 0.08	59.91 ± 0.12	0.1066 ± 0.0003	-0.57	1.98
	VIII	$+2.34 \pm 0.16$	0.00 ± 0.10	60.57 ± 0.12	0.1053 ± 0.0003	-0.57	1.28
867	VII	$+1.17 \pm 0.16$	0.00 ± 0.02	59.79 ± 0.11	0.1082 ± 0.0003	-0.56	2.50
	VIII	$+2.39 \pm 0.16$	0.00 ± 0.16	60.17 ± 0.12	0.1072 ± 0.0003	-0.57	1.22
917	VII	$+1.52 \pm 0.17$	0.00 ± 0.07	59.56 ± 0.12	0.1064 ± 0.0004	-0.57	0.97
	VIII	$+2.76 \pm 0.17$	0.00 ± 0.16	59.60 ± 0.12	0.1064 ± 0.0004	-0.58	1.67
967	VII	$+1.49 \pm 0.15$	0.00 ± 0.43	59.70 ± 0.11	0.1048 ± 0.0003	-0.58	1.32
	VIII	$+2.73 \pm 0.16$	0.00 ± 0.10	60.12 ± 0.11	0.1037 ± 0.0003	-0.57	1.25
2602	VII	$+0.17 \pm 0.15$	0.09 ± 0.19	59.18 ± 0.13	0.1036 ± 0.0003	-0.57	1.55
	VIII	$+2.25 \pm 0.16$	0.11 ± 0.22	59.68 ± 0.13	0.1037 ± 0.0003	-0.56	1.63
2652	VII	$+0.04 \pm 0.16$	0.06 ± 0.20	58.10 ± 0.13	0.1122 ± 0.0004	-0.56	1.51
	VIII	$+1.88 \pm 0.17$	0.25 ± 0.23	58.47 ± 0.14	0.1109 ± 0.0004	-0.57	0.85
2702	VII	$+0.41 \pm 0.16$	0.00 ± 0.07	59.51 ± 0.12	0.1056 ± 0.0003	-0.57	1.23
	VIII	$+1.98 \pm 0.16$	0.00 ± 0.07	59.95 ± 0.12	0.1049 ± 0.0003	-0.57	0.60
2752	VII	$+0.26 \pm 0.16$	0.00 ± 0.06	59.31 ± 0.12	0.1067 ± 0.0003	-0.57	1.00
	VIII	$+2.24 \pm 0.17$	0.00 ± 0.08	59.90 ± 0.12	0.1052 ± 0.0003	-0.57	0.91

Table 7.34: *Fit parameters extracted form May 2011 data of the XOR-C algorithm for BCM-Vertical luminosity measurement – Y scans.*

BCID	Scan	$X_0[\mu m]$	$b_X[10^{-4}\,(10^{22}p)^{-2}]$	$\Sigma_X[\mu m]$	$\mu_X^{vis,\,peak}[(10^{22}p)^{-2}]$	$C_{\Sigma_X-\mu_X^{vis,\,peak}}$	χ^2/NDF
81	VII	-2.48 ± 0.17	1.17 ± 0.22	54.97 ± 0.13	0.1162 ± 0.0004	-0.57	1.20
	VIII	-0.20 ± 0.17	1.53 ± 0.23	55.50 ± 0.14	0.1153 ± 0.0004	-0.57	0.88
131	VII	-2.53 ± 0.16	0.08 ± 0.23	59.04 ± 0.13	0.1058 ± 0.0003	-0.55	2.44
	VIII	-0.26 ± 0.17	0.97 ± 0.27	59.54 ± 0.14	0.1048 ± 0.0003	-0.55	1.78
181	VII	-2.43 ± 0.17	0.00 ± 0.15	58.97 ± 0.12	0.1047 ± 0.0004	-0.57	1.87
	VIII	-0.15 ± 0.17	0.84 ± 0.29	59.71 ± 0.15	0.1030 ± 0.0004	-0.54	2.52
231	VII	-2.10 ± 0.16	1.36 ± 0.22	56.37 ± 0.13	0.1103 ± 0.0004	-0.57	1.20
	VIII	$+0.03 \pm 0.16$	1.20 ± 0.22	57.10 ± 0.13	0.1090 ± 0.0004	-0.56	1.04
281	VII	-2.37 ± 0.16	1.02 ± 0.20	56.25 ± 0.13	0.1095 ± 0.0004	-0.56	1.59
	VIII	-0.40 ± 0.16	2.07 ± 0.25	56.65 ± 0.14	0.1080 ± 0.0004	-0.56	1.13
331	VII	-2.00 ± 0.16	0.40 ± 0.19	56.99 ± 0.13	0.1069 ± 0.0004	-0.57	0.73
	VIII	$+0.43 \pm 0.17$	1.52 ± 0.24	56.99 ± 0.14	0.1069 ± 0.0004	-0.57	0.66
817	VII	-1.69 ± 0.16	1.40 ± 0.22	56.81 ± 0.13	0.1064 ± 0.0004	-0.56	0.64
	VIII	$+0.01 \pm 0.16$	0.91 ± 0.20	57.21 ± 0.13	0.1053 ± 0.0004	-0.56	1.24
867	VII	-1.74 ± 0.16	1.35 ± 0.21	56.51 ± 0.13	0.1078 ± 0.0004	-0.57	1.57
	VIII	$+0.24 \pm 0.16$	1.46 ± 0.22	56.40 ± 0.13	0.1068 ± 0.0003	-0.56	1.22
917	VII	-1.95 ± 0.16	0.69 ± 0.22	57.45 ± 0.13	0.1073 ± 0.0004	-0.54	1.60
	VIII	$+0.25 \pm 0.16$	1.03 ± 0.23	57.44 ± 0.13	0.1066 ± 0.0004	-0.56	1.88
967	VII	-1.73 ± 0.15	0.72 ± 0.21	58.30 ± 0.13	0.1048 ± 0.0003	-0.57	1.32
	VIII	$+0.06 \pm 0.15$	1.25 ± 0.24	58.34 ± 0.13	0.1041 ± 0.0003	-0.56	1.12
2602	VII	-3.43 ± 0.15	0.57 ± 0.22	58.40 ± 0.12	0.1060 ± 0.0003	-0.55	2.68
	VIII	-0.67 ± 0.15	0.68 ± 0.23	58.88 ± 0.13	0.1046 ± 0.0003	-0.55	3.42
2652	VII	-3.39 ± 0.16	0.72 ± 0.18	55.13 ± 0.13	0.1130 ± 0.0004	-0.57	1.29
	VIII	-0.81 ± 0.16	0.68 ± 0.19	55.56 ± 0.13	0.1125 ± 0.0004	-0.56	2.21
2702	VII	-3.40 ± 0.16	0.14 ± 0.18	57.03 ± 0.12	0.1067 ± 0.0003	-0.56	2.65
	VIII	-0.45 ± 0.16	0.54 ± 0.21	57.49 ± 0.13	0.1057 ± 0.0003	-0.55	3.53
2752	VII	-3.26 ± 0.16	0.35 ± 0.19	56.73 ± 0.13	0.1081 ± 0.0004	-0.56	0.92
	VIII	-0.80 ± 0.16	0.25 ± 0.20	57.03 ± 0.13	0.1075 ± 0.0004	-0.55	2.20

Table 7.35: *Fit parameters extracted form May 2011 data of the XOR-C algorithm for BCM-Horizontal luminosity measurement – X scans.*

BCID	Scan	$Y_0[\mu m]$	$b_Y[10^{-4}\,(10^{22}p)^{-2}]$	$\Sigma_Y[\mu m]$	$\mu_Y^{vis,\,peak}[(10^{22}p)^{-2}]$	$C_{\Sigma_Y-\mu_Y^{vis,\,peak}}$	χ^2/NDF
81	VII	$+0.68 \pm 0.17$	0.39 ± 0.20	57.16 ± 0.14	0.1142 ± 0.0004	-0.58	2.49
	VIII	$+2.25 \pm 0.17$	0.64 ± 0.23	57.20 ± 0.14	0.1149 ± 0.0004	-0.57	1.62
131	VII	$+0.71 \pm 0.16$	0.00 ± 0.22	58.55 ± 0.12	0.1033 ± 0.0003	-0.57	1.48
	VIII	$+2.18 \pm 0.17$	0.49 ± 0.22	58.70 ± 0.14	0.1023 ± 0.0003	-0.57	2.19
181	VII	$+0.51 \pm 0.17$	0.42 ± 0.23	58.92 ± 0.15	0.1021 ± 0.0004	-0.57	1.58
	VIII	$+2.19 \pm 0.17$	0.17 ± 0.23	59.18 ± 0.15	0.1017 ± 0.0004	-0.56	1.95
231	VII	$+0.84 \pm 0.16$	0.03 ± 0.37	58.44 ± 0.13	0.1092 ± 0.0004	-0.58	0.97
	VIII	$+2.24 \pm 0.16$	0.00 ± 0.05	58.92 ± 0.12	0.1085 ± 0.0003	-0.57	1.61
281	VII	$+0.63 \pm 0.16$	0.08 ± 0.23	59.19 ± 0.14	0.1076 ± 0.0004	-0.56	1.53
	VIII	$+2.30 \pm 0.17$	0.27 ± 0.25	59.47 ± 0.14	0.1077 ± 0.0004	-0.56	2.17
331	VII	$+0.76 \pm 0.17$	0.00 ± 0.05	59.80 ± 0.12	0.1067 ± 0.0004	-0.57	1.45
	VIII	$+2.20 \pm 0.17$	0.09 ± 0.24	59.60 ± 0.14	0.1072 ± 0.0004	-0.57	0.98
817	VII	$+1.40 \pm 0.16$	0.00 ± 0.14	60.19 ± 0.12	0.1060 ± 0.0003	-0.57	0.95
	VIII	$+2.82 \pm 0.16$	0.00 ± 0.06	60.45 ± 0.12	0.1052 ± 0.0003	-0.57	2.51
867	VII	$+1.30 \pm 0.16$	0.00 ± 0.13	60.22 ± 0.12	0.1068 ± 0.0003	-0.57	1.41
	VIII	$+2.36 \pm 0.16$	0.23 ± 0.25	60.18 ± 0.14	0.1067 ± 0.0003	-0.56	0.79
917	VII	$+1.41 \pm 0.17$	0.10 ± 0.23	59.36 ± 0.14	0.1065 ± 0.0004	-0.56	1.74
	VIII	$+2.58 \pm 0.17$	0.22 ± 0.23	59.29 ± 0.14	0.1065 ± 0.0004	-0.57	1.13
967	VII	$+1.58 \pm 0.16$	0.00 ± 0.43	60.05 ± 0.11	0.1033 ± 0.0003	-0.57	1.09
	VIII	$+2.41 \pm 0.16$	0.00 ± 0.19	60.13 ± 0.11	0.1035 ± 0.0003	-0.57	1.01
2602	VII	$+0.15 \pm 0.15$	0.00 ± 0.23	59.22 ± 0.11	0.1037 ± 0.0003	-0.57	1.29
	VIII	$+2.29 \pm 0.15$	0.00 ± 1.70	59.52 ± 0.11	0.1026 ± 0.0003	-0.58	2.36
2652	VII	$+0.18 \pm 0.16$	0.11 ± 0.20	57.79 ± 0.13	0.1121 ± 0.0004	-0.57	1.18
	VIII	$+2.17 \pm 0.17$	0.46 ± 0.24	58.45 ± 0.14	0.1106 ± 0.0004	-0.57	1.32
2702	VII	$+0.30 \pm 0.16$	0.00 ± 0.04	59.31 ± 0.11	0.1053 ± 0.0003	-0.57	1.42
	VIII	$+2.07 \pm 0.16$	0.00 ± 0.34	60.03 ± 0.12	0.1046 ± 0.0003	-0.57	1.77
2752	VII	$+0.27 \pm 0.17$	0.00 ± 0.06	59.44 ± 0.12	0.1059 ± 0.0003	-0.57	2.49
	VIII	$+2.11 \pm 0.17$	0.15 ± 0.25	59.89 ± 0.14	0.1055 ± 0.0004	-0.56	0.32

Table 7.36: *Fit parameters extracted form May 2011 data of the XOR-C algorithm for BCM-Horizontal luminosity measurement – Y scans.*

AND algorithm

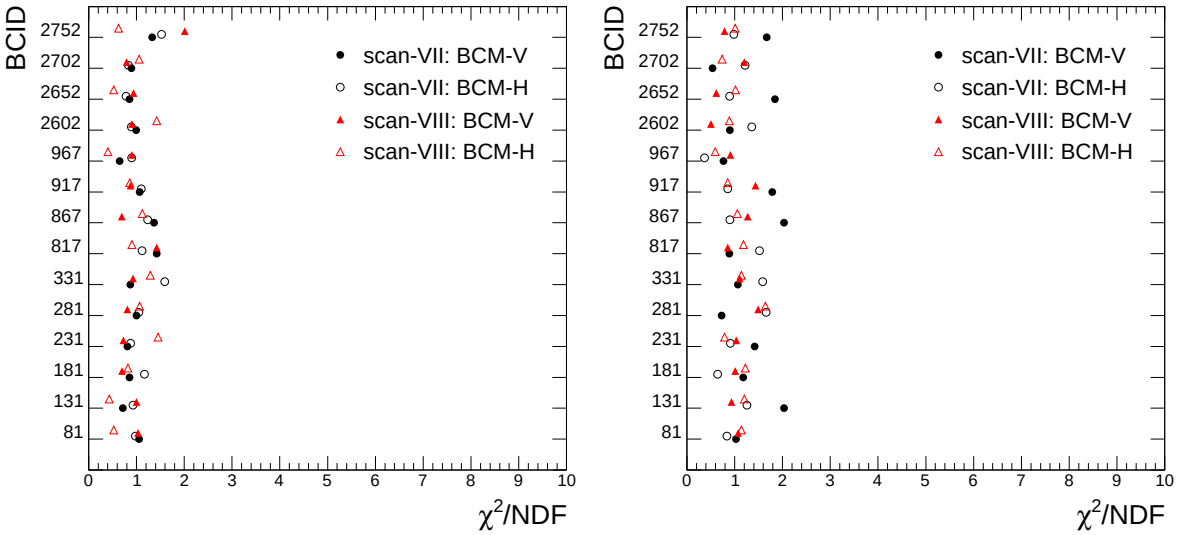

Figure 7.37: *χ^2 evaluation of the x scan (left) and y scan (right) fits for the AND algorithm.*

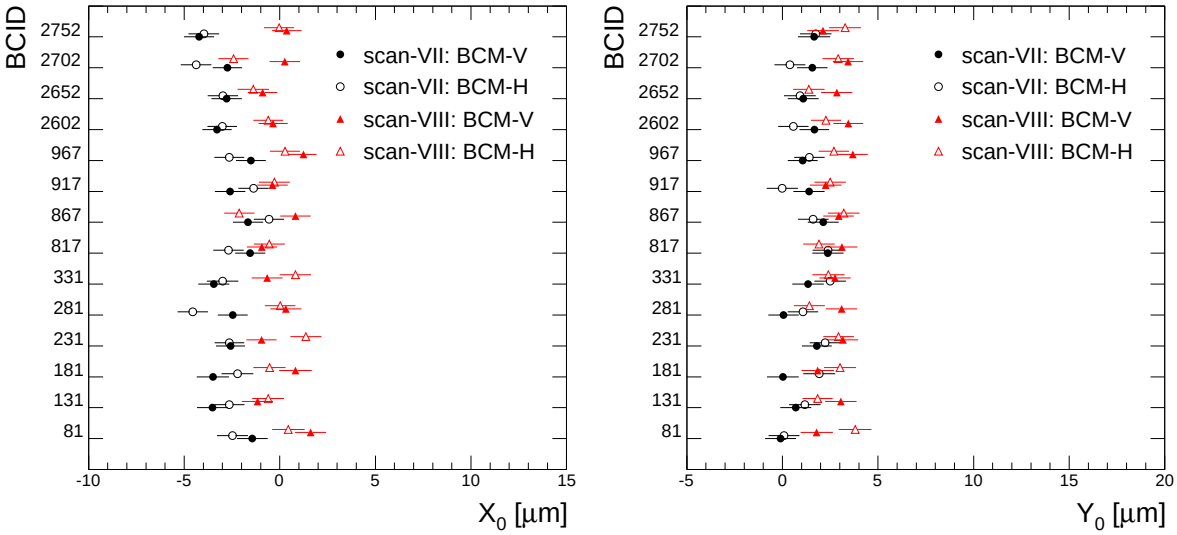

Figure 7.38: *Offset of the centered beams during x scans (left) and y scans (right) for the AND algorithm.*

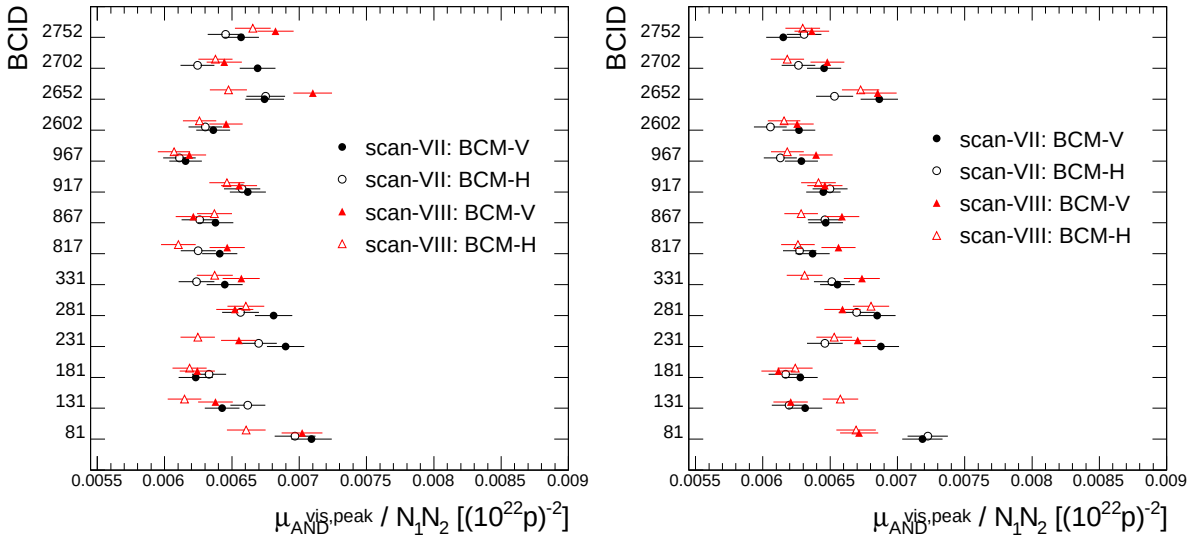

Figure 7.39: *The maximum beam current normalized μ^{vis} during x scans (left) and y scans (right) for the AND algorithm.*

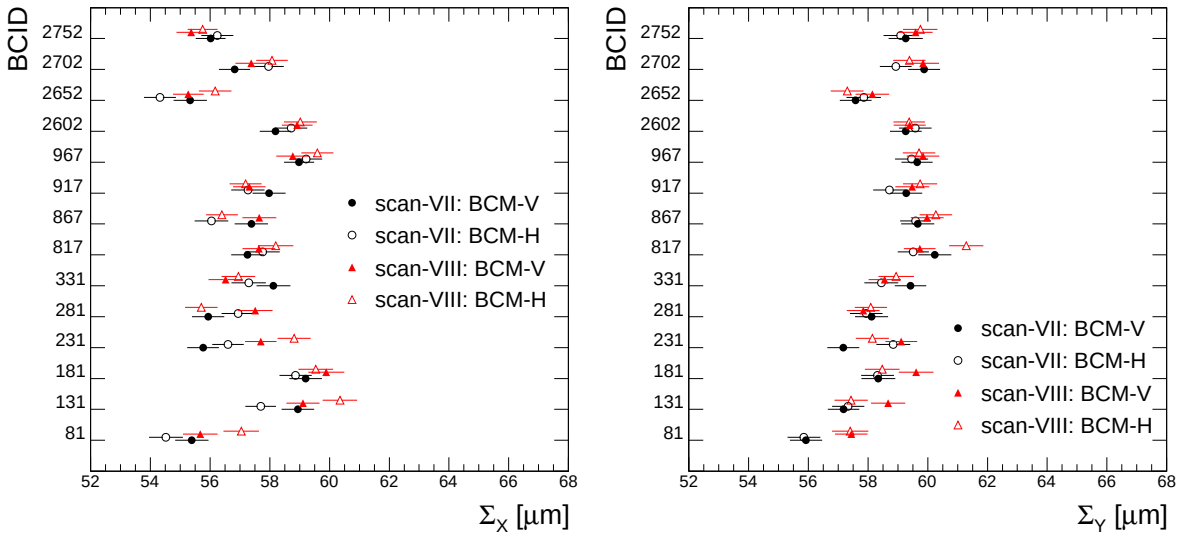

Figure 7.40: *The effective beam width as obtained form the fits of x scans (left) and y scans (right) for the AND algorithm.*

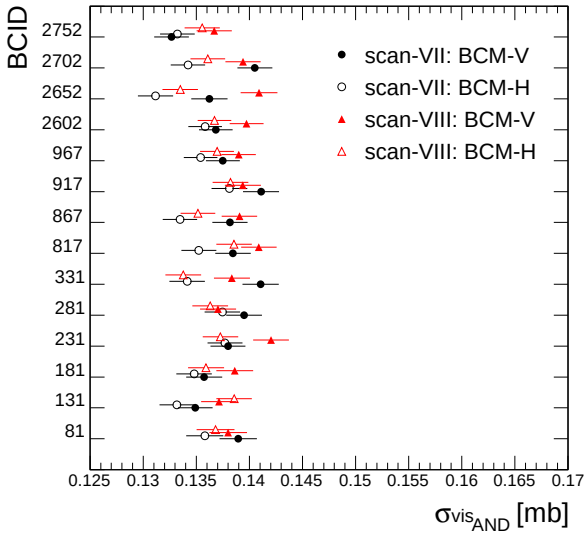

Figure 7.41: *Visible cross-sections for both BCM luminosity measurements, both scans, and all BCIDs. An excelent agreement is obtained for the AND algorithm.*

BCID	Visible cross-section [mb]			
	BCM-Verical		BCM-Horizontal	
	Scan VII	Scan VIII	Scan VII	Scan VIII
81	0.1389 ± 0.0018	0.1380 ± 0.0018	0.1358 ± 0.0017	0.1368 ± 0.0018
131	0.1349 ± 0.0016	0.1371 ± 0.0017	0.1332 ± 0.0016	0.1386 ± 0.0017
181	0.1357 ± 0.0017	0.1386 ± 0.0017	0.1348 ± 0.0017	0.1359 ± 0.0017
231	0.1380 ± 0.0016	0.1420 ± 0.0017	0.1377 ± 0.0017	0.1373 ± 0.0017
281	0.1395 ± 0.0017	0.1370 ± 0.0017	0.1375 ± 0.0017	0.1363 ± 0.0017
331	0.1411 ± 0.0017	0.1383 ± 0.0017	0.1341 ± 0.0017	0.1338 ± 0.0017
817	0.1385 ± 0.0017	0.1409 ± 0.0017	0.1352 ± 0.0016	0.1386 ± 0.0017
867	0.1382 ± 0.0017	0.1391 ± 0.0017	0.1335 ± 0.0016	0.1351 ± 0.0016
917	0.1411 ± 0.0017	0.1394 ± 0.0017	0.1381 ± 0.0017	0.1382 ± 0.0017
967	0.1375 ± 0.0016	0.1390 ± 0.0016	0.1354 ± 0.0016	0.1370 ± 0.0016
2602	0.1368 ± 0.0016	0.1397 ± 0.0016	0.1358 ± 0.0016	0.1367 ± 0.0016
2652	0.1362 ± 0.0017	0.1409 ± 0.0017	0.1312 ± 0.0017	0.1335 ± 0.0017
2702	0.1405 ± 0.0017	0.1394 ± 0.0017	0.1342 ± 0.0016	0.1361 ± 0.0016
2752	0.1327 ± 0.0016	0.1367 ± 0.0017	0.1332 ± 0.0016	0.1355 ± 0.0017
Average	0.1378 ± 0.0004	0.1390 ± 0.0004	0.1350 ± 0.0004	0.1364 ± 0.0004
RMS	0.0023	0.0015	0.0019	0.0015

Table 7.37: *May 2011 vissible cross-section obtained for the AND algorithm.*

BCID	Scan	$X_0[\mu m]$	$\Sigma_X[\mu m]$	$\mu_X^{nr,peak}[(10^{22}p)^{-2}]$	$C_{\Sigma_X-\mu_X^{nr,peak}}$	χ^2/NDF
81	VII	-1.44 ± 0.80	55.39 ± 0.56	0.0071 ± 0.0002	-0.62	1.05
	VIII	$+1.61 \pm 0.82$	55.67 ± 0.58	0.0070 ± 0.0002	-0.63	1.03
131	VII	-3.52 ± 0.81	58.94 ± 0.54	0.0064 ± 0.0001	-0.61	0.72
	VIII	-1.17 ± 0.82	59.11 ± 0.55	0.0064 ± 0.0001	-0.62	1.00
181	VII	-3.50 ± 0.84	59.20 ± 0.54	0.0062 ± 0.0001	-0.60	0.85
	VIII	$+0.82 \pm 0.85$	59.89 ± 0.60	0.0062 ± 0.0001	-0.63	0.70
231	VII	-2.58 ± 0.76	55.77 ± 0.53	0.0069 ± 0.0001	-0.63	0.81
	VIII	-0.96 ± 0.79	57.70 ± 0.53	0.0066 ± 0.0001	-0.62	0.73
281	VII	-2.47 ± 0.78	55.94 ± 0.54	0.0068 ± 0.0001	-0.62	1.00
	VIII	$+0.32 \pm 0.81$	57.51 ± 0.58	0.0065 ± 0.0001	-0.64	0.81
331	VII	-3.45 ± 0.81	58.12 ± 0.57	0.0064 ± 0.0001	-0.63	0.87
	VIII	-0.66 ± 0.80	56.52 ± 0.57	0.0066 ± 0.0001	-0.63	0.93
817	VII	-1.55 ± 0.79	57.25 ± 0.55	0.0064 ± 0.0001	-0.63	1.43
	VIII	-0.93 ± 0.79	57.63 ± 0.55	0.0065 ± 0.0001	-0.63	1.42
867	VII	-1.66 ± 0.79	57.38 ± 0.56	0.0064 ± 0.0001	-0.64	1.37
	VIII	$+0.82 \pm 0.80$	57.65 ± 0.56	0.0062 ± 0.0001	-0.64	0.69
917	VII	-2.60 ± 0.79	57.98 ± 0.55	0.0066 ± 0.0001	-0.63	1.07
	VIII	-0.38 ± 0.80	57.32 ± 0.54	0.0066 ± 0.0001	-0.62	0.88
967	VII	-1.52 ± 0.78	58.98 ± 0.51	0.0062 ± 0.0001	-0.61	0.65
	VIII	$+1.24 \pm 0.78$	58.77 ± 0.55	0.0062 ± 0.0001	-0.64	0.90
2602	VII	-3.29 ± 0.77	58.19 ± 0.53	0.0064 ± 0.0001	-0.63	0.99
	VIII	-0.35 ± 0.76	58.92 ± 0.51	0.0065 ± 0.0001	-0.62	0.90
2652	VII	-2.79 ± 0.80	55.33 ± 0.56	0.0067 ± 0.0001	-0.63	0.85
	VIII	-0.90 ± 0.78	55.27 ± 0.51	0.0071 ± 0.0001	-0.60	0.94
2702	VII	-2.74 ± 0.77	56.82 ± 0.52	0.0067 ± 0.0001	-0.62	0.90
	VIII	$+0.26 \pm 0.79$	57.38 ± 0.53	0.0064 ± 0.0001	-0.61	0.79
2752	VII	-4.22 ± 0.79	56.02 ± 0.50	0.0066 ± 0.0001	-0.59	1.33
	VIII	$+0.36 \pm 0.78$	55.37 ± 0.49	0.0068 ± 0.0001	-0.59	2.01

Table 7.38: *Fit parameters extracted form May 2011 data of the AND algorithm for BCM-Vertical luminosity measurement – X scans.*

BCID	Scan	$Y_0[\mu m]$	$\Sigma_Y[\mu m]$	$\mu_Y^{nr,peak}[(10^{22}p)^{-2}]$	$C_{\Sigma_Y-\mu_Y^{nr,peak}}$	χ^2/NDF
81	VII	-0.10 ± 0.81	55.93 ± 0.54	0.0072 ± 0.0001	-0.61	1.03
	VIII	$+1.79 \pm 0.85$	57.44 ± 0.54	0.0067 ± 0.0001	-0.59	1.07
131	VII	$+0.69 \pm 0.80$	57.18 ± 0.52	0.0063 ± 0.0001	-0.60	2.03
	VIII	$+3.06 \pm 0.82$	58.68 ± 0.57	0.0062 ± 0.0001	-0.62	0.93
181	VII	$+0.02 \pm 0.83$	58.34 ± 0.57	0.0063 ± 0.0001	-0.61	1.18
	VIII	$+1.84 \pm 0.85$	59.61 ± 0.58	0.0061 ± 0.0001	-0.62	1.01
231	VII	$+1.80 \pm 0.78$	57.17 ± 0.53	0.0069 ± 0.0001	-0.62	1.42
	VIII	$+3.17 \pm 0.79$	59.11 ± 0.53	0.0067 ± 0.0001	-0.61	1.03
281	VII	$+0.06 \pm 0.80$	58.12 ± 0.56	0.0068 ± 0.0001	-0.62	0.72
	VIII	$+3.09 \pm 0.82$	57.84 ± 0.55	0.0066 ± 0.0001	-0.61	1.49
331	VII	$+1.34 \pm 0.82$	59.43 ± 0.53	0.0066 ± 0.0001	-0.59	1.07
	VIII	$+2.75 \pm 0.81$	58.56 ± 0.54	0.0067 ± 0.0001	-0.60	1.11
817	VII	$+2.38 \pm 0.82$	60.24 ± 0.56	0.0064 ± 0.0001	-0.62	0.89
	VIII	$+3.11 \pm 0.80$	59.73 ± 0.53	0.0066 ± 0.0001	-0.60	0.86
867	VII	$+2.13 \pm 0.81$	59.66 ± 0.55	0.0065 ± 0.0001	-0.62	2.04
	VIII	$+2.94 \pm 0.80$	59.98 ± 0.55	0.0066 ± 0.0001	-0.62	1.27
917	VII	$+1.39 \pm 0.82$	59.28 ± 0.53	0.0064 ± 0.0001	-0.60	1.79
	VIII	$+2.25 \pm 0.82$	59.48 ± 0.57	0.0065 ± 0.0001	-0.62	1.44
967	VII	$+1.06 \pm 0.78$	59.64 ± 0.52	0.0063 ± 0.0001	-0.62	0.76
	VIII	$+3.69 \pm 0.78$	59.85 ± 0.54	0.0064 ± 0.0001	-0.63	0.91
2602	VII	$+1.67 \pm 0.77$	59.26 ± 0.53	0.0063 ± 0.0001	-0.63	0.90
	VIII	$+3.44 \pm 0.78$	59.40 ± 0.54	0.0063 ± 0.0001	-0.62	0.50
2652	VII	$+1.09 \pm 0.81$	57.59 ± 0.53	0.0069 ± 0.0001	-0.60	1.84
	VIII	$+2.84 \pm 0.81$	58.15 ± 0.56	0.0069 ± 0.0001	-0.62	0.61
2702	VII	$+1.56 \pm 0.80$	59.88 ± 0.54	0.0065 ± 0.0001	-0.62	0.53
	VIII	$+3.43 \pm 0.80$	59.84 ± 0.54	0.0065 ± 0.0001	-0.61	1.20
2752	VII	$+1.65 \pm 0.84$	59.26 ± 0.57	0.0062 ± 0.0001	-0.62	1.67
	VIII	$+2.13 \pm 0.82$	59.59 ± 0.57	0.0064 ± 0.0001	-0.62	0.79

Table 7.39: *Fit parameters extracted form May 2011 data of the AND algorithm for BCM-Vertical luminosity measurement – Y scans.*

BCID	Scan	$X_0[\mu m]$	$\Sigma_X[\mu m]$	$\mu_X^{nr,peak}[(10^{22}p)^{-2}]$	$C_{\Sigma_X-\mu_X^{nr,peak}}$	χ^2/NDF
81	VII	-2.48 ± 0.81	54.52 ± 0.57	0.0070 ± 0.0002	-0.62	0.98
	VIII	$+0.45 \pm 0.84$	57.04 ± 0.59	0.0066 ± 0.0001	-0.63	0.52
131	VII	-2.64 ± 0.79	57.70 ± 0.52	0.0066 ± 0.0001	-0.60	0.93
	VIII	-0.61 ± 0.83	60.35 ± 0.58	0.0061 ± 0.0001	-0.62	0.43
181	VII	-2.21 ± 0.83	58.86 ± 0.54	0.0063 ± 0.0001	-0.60	1.17
	VIII	-0.54 ± 0.85	59.54 ± 0.58	0.0062 ± 0.0001	-0.61	0.82
231	VII	-2.64 ± 0.77	56.60 ± 0.53	0.0067 ± 0.0001	-0.62	0.88
	VIII	$+1.36 \pm 0.81$	58.81 ± 0.55	0.0062 ± 0.0001	-0.62	1.45
281	VII	-4.55 ± 0.80	56.94 ± 0.56	0.0066 ± 0.0001	-0.63	1.05
	VIII	$+0.02 \pm 0.80$	55.71 ± 0.54	0.0066 ± 0.0001	-0.61	1.07
331	VII	-2.99 ± 0.82	57.29 ± 0.58	0.0062 ± 0.0001	-0.63	1.59
	VIII	$+0.81 \pm 0.82$	56.95 ± 0.56	0.0064 ± 0.0001	-0.62	1.29
817	VII	-2.69 ± 0.80	57.76 ± 0.57	0.0062 ± 0.0001	-0.64	1.12
	VIII	-0.55 ± 0.81	58.20 ± 0.59	0.0061 ± 0.0001	-0.65	0.91
867	VII	-0.57 ± 0.79	56.05 ± 0.56	0.0063 ± 0.0001	-0.64	1.24
	VIII	-2.12 ± 0.79	56.40 ± 0.53	0.0064 ± 0.0001	-0.62	1.12
917	VII	-1.37 ± 0.79	57.27 ± 0.56	0.0066 ± 0.0001	-0.63	1.10
	VIII	-0.29 ± 0.81	57.19 ± 0.54	0.0065 ± 0.0001	-0.61	0.86
967	VII	-2.64 ± 0.78	59.22 ± 0.53	0.0061 ± 0.0001	-0.63	0.90
	VIII	$+0.27 \pm 0.79$	59.59 ± 0.54	0.0061 ± 0.0001	-0.62	0.40
2602	VII	-3.01 ± 0.77	58.71 ± 0.54	0.0063 ± 0.0001	-0.63	0.89
	VIII	-0.60 ± 0.78	59.02 ± 0.55	0.0063 ± 0.0001	-0.64	1.42
2652	VII	-2.98 ± 0.80	54.32 ± 0.54	0.0068 ± 0.0001	-0.61	0.78
	VIII	-1.38 ± 0.82	56.17 ± 0.55	0.0065 ± 0.0001	-0.61	0.53
2702	VII	-4.38 ± 0.80	57.96 ± 0.51	0.0062 ± 0.0001	-0.60	0.83
	VIII	-2.43 ± 0.79	58.08 ± 0.53	0.0064 ± 0.0001	-0.61	1.05
2752	VII	-3.98 ± 0.80	56.24 ± 0.53	0.0065 ± 0.0001	-0.61	1.52
	VIII	-0.04 ± 0.78	55.76 ± 0.50	0.0067 ± 0.0001	-0.59	0.63

Table 7.40: *Fit parameters extracted form May 2011 data of the AND algorithm for BCM-Horizontal luminosity measurement – X scans.*

BCID	Scan	$Y_0[\mu m]$	$\Sigma_Y[\mu m]$	$\mu_Y^{nr,peak}[(10^{22}p)^{-2}]$	$C_{\Sigma_Y-\mu_Y^{nr,peak}}$	χ^2/NDF
81	VII	$+0.08 \pm 0.81$	55.85 ± 0.55	0.0072 ± 0.0001	-0.61	0.84
	VIII	$+3.80 \pm 0.86$	57.40 ± 0.61	0.0067 ± 0.0001	-0.63	1.14
131	VII	$+1.17 \pm 0.82$	57.34 ± 0.54	0.0062 ± 0.0001	-0.61	1.25
	VIII	$+1.84 \pm 0.79$	57.44 ± 0.56	0.0066 ± 0.0001	-0.62	1.20
181	VII	$+1.93 \pm 0.84$	58.32 ± 0.55	0.0062 ± 0.0001	-0.60	0.64
	VIII	$+3.01 \pm 0.84$	58.48 ± 0.58	0.0062 ± 0.0001	-0.62	1.22
231	VII	$+2.23 \pm 0.80$	58.85 ± 0.57	0.0065 ± 0.0001	-0.63	0.91
	VIII	$+2.93 \pm 0.80$	58.14 ± 0.55	0.0065 ± 0.0001	-0.62	0.79
281	VII	$+1.07 \pm 0.80$	57.94 ± 0.54	0.0067 ± 0.0001	-0.61	1.66
	VIII	$+1.41 \pm 0.80$	58.09 ± 0.54	0.0068 ± 0.0001	-0.61	1.64
331	VII	$+2.49 \pm 0.82$	58.45 ± 0.57	0.0065 ± 0.0001	-0.62	1.58
	VIII	$+2.40 \pm 0.84$	58.95 ± 0.60	0.0063 ± 0.0001	-0.63	1.14
817	VII	$+2.39 \pm 0.82$	59.51 ± 0.52	0.0063 ± 0.0001	-0.59	1.52
	VIII	$+1.91 \pm 0.83$	61.29 ± 0.57	0.0063 ± 0.0001	-0.62	1.19
867	VII	$+1.61 \pm 0.80$	59.59 ± 0.51	0.0065 ± 0.0001	-0.59	0.90
	VIII	$+3.21 \pm 0.82$	60.27 ± 0.54	0.0063 ± 0.0001	-0.61	1.05
917	VII	-0.01 ± 0.81	58.71 ± 0.54	0.0065 ± 0.0001	-0.61	0.85
	VIII	$+2.50 \pm 0.83$	59.74 ± 0.57	0.0064 ± 0.0001	-0.62	0.85
967	VII	$+1.41 \pm 0.79$	59.46 ± 0.56	0.0061 ± 0.0001	-0.63	0.37
	VIII	$+2.69 \pm 0.79$	59.71 ± 0.54	0.0062 ± 0.0001	-0.62	0.59
2602	VII	$+0.57 \pm 0.79$	59.58 ± 0.55	0.0061 ± 0.0001	-0.63	1.36
	VIII	$+2.28 \pm 0.79$	59.38 ± 0.53	0.0062 ± 0.0001	-0.62	0.89
2652	VII	$+0.91 \pm 0.83$	57.86 ± 0.58	0.0065 ± 0.0001	-0.62	0.89
	VIII	$+1.38 \pm 0.82$	57.30 ± 0.55	0.0067 ± 0.0001	-0.61	1.01
2702	VII	$+0.39 \pm 0.81$	58.93 ± 0.53	0.0063 ± 0.0001	-0.60	1.22
	VIII	$+2.91 \pm 0.82$	59.38 ± 0.54	0.0062 ± 0.0001	-0.61	0.74
2752	VII	$+1.74 \pm 0.82$	59.09 ± 0.57	0.0063 ± 0.0001	-0.62	0.98
	VIII	$+3.27 \pm 0.83$	59.75 ± 0.58	0.0063 ± 0.0001	-0.62	1.01

Table 7.41: *Fit parameters extracted form May 2011 data of the AND algorithm for BCM-Horizontal luminosity measurement – Y scans.*

7.5 Error estimates

This section is devoted to the systematic uncertainties of the vdM calibration. The first few subsections will present the estimations for effects that are BCM specific, while the rest discuss possible systematic influences that apply to all ATLAS luminosity detectors. In the last subsection a short overview is given along with the total uncertainty estimation.

7.5.1 μ-dependence

The first data processing stage is the μ-correction. There are no large uncertainties expected here since the procedure is based only on the assumption that different proton-proton interactions are independent. This gives rise to Poisson distribution for number of proton-proton interactions within bunch crossing and everything else is exact mathematics. This single assumption is not expected to be broken.

Nevertheless estimation should be made and the most reliable approach is to look at the data. One can compare the μ^{vis} extracted from different algorithms. Direct comparison is not valid since values are expected to differ by a factor of relative algorithm efficiencies. To rectify this it is best to multiply μ_A^{vis} with the corresponding visible cross-section σ_A^{vis} and compare the resulting luminosities.

For each run all the luminosity blocks, during which stable beams were declared, were taken into account. For each of these luminosity blocks each filled BCID was analyzed by calculating its corresponding instantaneous luminosity for all algorithms. For the reference the OR algorithm of the BCM-Vertical luminosity was chosen and $L_{A;H/V}/L_{OR;V} - 1$, $L_{OR;V}$ data pairs were histogrammed. For runs with run numbers between 185000 and 188000 the comparison is shown in figure 7.43. The horizontal distribution shows the luminosity span of individual bunches during the analyzed period. If any μ-dependence would not have been included in the μ-corrections performed, it would be seen as $L_{A;H/V}/L_{OR;V}$ variation dependent on μ (effectively $L_{OR;V}$). No such dependence is present in the data shown, indicating consistent μ-corrections between different algorithms. Both directions have additional spread due to statistical uncertainty and due to time jitter. In vertical direction this is the dominant contribution to the distribution width, which is most obvious with AND algorithm. Since no deviations can be observed from the displayed data, the width of distributions can be used as a conservative upper limit. This amounts to $\pm 0.4\%$ of μ-correction uncertainty.

With such procedure possible relative discrepancies in μ-correction can be observed, so additional absolute verification would be nice. Another possibility for a consistency check is to go back to the Monte Carlo simulated data and to look at discrepancies between the data and the linear fit of μ^{vis} as a function of actual $\langle\mu\rangle$. This was shown in figure 6.16. Within statistical uncertainties, there are no points that would deviate from linear model. This enables to set an upper level of possible deviation, and $\pm 0.4\%$ is obtained requiring $\sim 80\%$ confidence level, which agrees with the estimation based on data.

7.5.2 Detector consistency

Another observation can be made in figure 7.43. While the average $L_{A;H/V}/L_{OR;V} - 1$ is constant over different values of $L_{OR;V}$, it does not equal zero. A noticeable systematical deviation can be seen. Ideally this should not be the case, since all algorithms, for both BCM-Vertical and BCM-Horizontal luminosity, have been independently calibrated and should give the same result. The plots for BCM-Vertical (top three scatter plots in figure 7.43) indicate that things are somewhat consistent within a single DPU. AND algorithm data is centered around 0 while XOR-A and XOR-C deviate and are obviously anticorrelated. This would indicate that the sample contamination of single-sided events changed with respect to the run during which vdM was performed, while AND is immune to such a change. Nevertheless this gives a nice estimation of background contamination that should be included in the final uncertainty estimate. However a small surprise appears with the BCM-Horizontal data. Here the background effect seems to be in opposite direction since XOR-A values are smaller than XOR-C values. This either means that the background is different in x and y plane or it indicates some other beam setup non-reproducibility. Additionally, all of the BCM-Horizontal data seems to be shifted with respect to BCM-Vertical-OR. The shift is independent of time and runs, thus pointing to vdM systematics or to some small change that happened right after vdM, particularly for BCM-Horizontal measurement.

Table 7.42 shows the fitted average $L_{A;H/V}$ for different measurements. Since one of the algorithms serves as a baseline for comparison, the additive shift of values is arbitrary and for final estimation an average was taken as a baseline, so the deviations are equally balanced between positive and negative. With this, no measurement deviates more than $\pm 1.0\%$ which is taken as the final estimate on detector consistency and other non-reproducibilities.

Algorithm	BCM-Vertical deviations [%]	BCM-Horizontal deviations [%]
OR	0 (by definition)	$+0.7$
XOR-A	$+0.4$	$+0.6$
XOR-C	-0.4	$+1.2$
AND	-0.1	$+1.5$

Table 7.42: *Fitted average of $L_{A;H/V}$ for different algorithms. Deviations indicate two sources of non-consistency. One seems to be common to both BCM-Vertical and BCM-Horizontal luminosity, while another contribution is specific for BCM-Horizontal luminosity. An estimation of $\pm 1.0\%$ covers all observed deviations.*

7.5.3 Fit model

The next unknown systematic contribution comes from the fit model describing the vdM scan curve. The parametrization were discussed in subsection 7.3.2 and single or double Gaussians with flat background were found to best describe the data. However there is no physics argument to support such a choice since the bunch shape is defined by the magnet fields

of the collider, its RF system, and the particle source. To estimate a potential error, different models were fitted on the data. The entire analysis was performed for each model resulting in new collection of σ^{vis} values. The deviations from values presented in the previous section are shown for OR algorithm in table 7.43. This algorithm provides the best statistics and the shape of the scan curve should be most defined. The largest deviation of $\pm 0.7\%$ is taken as the final estimate. This value was not exceeded when the procedure was repeated in other algorithms.

	BCM-Vertical σ^{vis} deviations [%]				BCM-Horizontal σ^{vis} deviations [%]			
Scans	IV	V	VII	VIII	IV	V	VII	VIII
g	$+0.7$	-0.2	-0.3	$+0.1$	-0.5	-0.6	$+0.2$	-0.1
g+c	-0.2	-0.4	0 by definition		$+0.7$	-0.4	0 by definition	
g+g	$+0.0$	-0.1	$+0.4$	$+0.0$	$+0.2$	$+0.1$	$+0.1$	$+0.3$
g+g+c	0 by definition		$+0.0$	$+0.0$	0 by definition		-0.1	$+0.0$
spline	$+0.3$	$+0.1$	-0.2	-0.1	-0.2	$+0.4$	$+0.1$	-0.2

Table 7.43: *The deviation of extracted calibration values σ^{vis} due to different modeling of the scan curve. The largest deviation of $\pm 0.7\%$ is taken as the uncertainty estimation.*

7.5.4 σ^{vis} consistency

The σ^{vis} values determined for given detector and algorithm should be BCID independent. By comparing these values in the tables 7.37, 7.32, 7.27, 7.22, 7.17, 7.12, 7.7, and 7.2 it is clear that they are scattered more than would be expected from their statistical errors. This BCID dependence is estimated by calculating the RMS values (given in tables) which yields an overall estimation of $\pm 0.4\%$.

7.5.5 Threshold variation

Another possible effect is the variation of the NINO thresholds. Threshold is set by digital-to-analog converter. By combining its characteristics with possible thermal fluctuations a 0.5% of its maximal output represents a very conservative estimation of its fluctuations. A full dynamic range of thresholds spans over $1\,\mathrm{V}$, thus giving $\sim 5\,\mathrm{mV}$ fluctuations. To roughly estimate how much this influences the luminosity a threshold scan was performed, where the hit rate was measured as a function of the threshold. The data is shown in figure 7.42. Below $300\,\mathrm{mV}$ noise strongly dominates, while above this value only collision-induced signals remain. The operational thresholds are set around $400\,\mathrm{mV}$. In this region a maximal trend of $-0.1\%/\mathrm{mV}$ can be observed for the single channel rates. In the case of OR algorithm, where the effect is expected to be biggest, and under the assumption that the channel fluctuations are completely correlated, this would mean less than 0.1% change of efficiency for each mV of fluctuation. Combining with estimated $\sim 5\,\mathrm{mV}$ this results in maximal 0.5% change of efficiency.

Due to limited statistics during the threshold scan, and due to the fact, that the maximal threshold is $1\,\mathrm{V}$, the connection between threshold in mV and the threshold of the most probable signal thr_{PM} (defined in the simulation chapter) is hard to assess. The best estimate would be that thr_{PM} corresponds to $\sim 600\,\mathrm{mV}$. In this case $5\,\mathrm{mV}$ corresponds to $\sim 10^{-2} thr_{PM}$, which can be combined with simulation estimates of BCM luminosity efficiency dependence on threshold, given in table 6.6. It results in 0.1% of efficiency variation, which is even smaller than the estimate from the measured data.

It should be stressed that in the above reasoning the channel fluctuations were assumed to be fully correlated, which is not the case in practise. Additionally the event counting approach makes things more immune against threshold variations as luminosity increases, due to higher multiplicity, and thus higher signal. This supports the statement that the final 0.5% uncertainty estimation is a very conservative one.

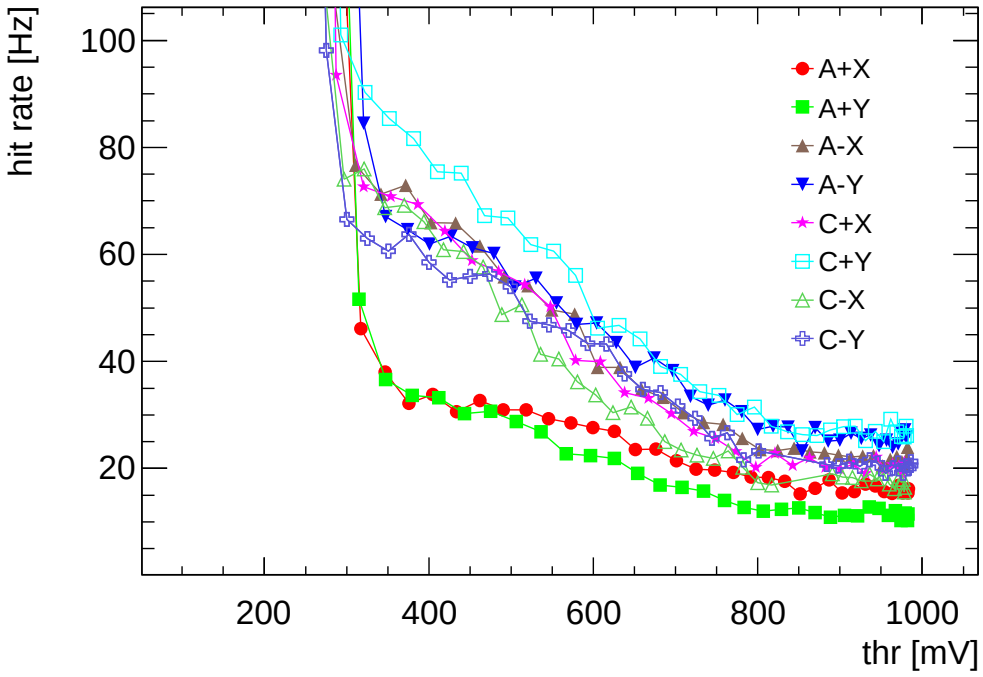

Figure 7.42: *Rates for all eight low threshold channels as a function of threshold. The threshold is set by DAC and the signal is read back by ADC, whose value is used on the horizontal axis.*

7.5.6 Bunch charge product

The product of bunch charges in equation 7.13 turns out to be the dominant contributor to the systematic uncertainty. Since its value can vary from bunch to bunch up to 20%, with bunches having different sizes, the BCID blind luminosity calibration does not make sense. Each bunch must be treaded separately in the calibration analysis, thus requiring also per

bunch measurement of charge product. This way one can also exclude from the analysis the unpaired bunches (those that do not collide), which carry the charge but do not contribute to the luminosity. The task of charge measurement is far from straightforward and more detailed explanation of the technicalities and uncertainty estimation was given by Bunch Current Normalization Working Group in [BC11]. Only a short overview is given here.

The responsibility for bunch charge measurements lies with eight Bunch Current Transformers (BCTs). In order to achieve best precision of the charge measurement for individual bunch two independent measurements are done:

DC Current Transformer (DCCT) can not resolve individual bunches, and is therefore used for measurement of the total charge in of the LHC beam. It provides a high accuracy measurement.

Fast Beam Current Transformers (FBCTs) lack the precision in absolute scale, but provide accurate relative bunch-to-bunch measurement for all 3564 BCIDs in the LHC ring.

Both measurement are then combined, using relative bunch values provided by FBCT and scaling them so that the total charge matches the DCCT measurements. The final measured bunch charge N_i for $\mathrm{BCID} = i$ is then:

$$N_i = \left(N^{DCCT} - N_{ghost}\right) \frac{S_i^{FBCT}}{\sum S_i^{FBTC}}. \tag{7.14}$$

The S_i^{FBCT} are the relative bunch charges measured by FBCT, N_{tot}^{DCCT} is the total charge measured by DCCT, and N_{ghost} is the 'ghost charge'. Ghost charge is a contribution of the bunches filled with less than $\sim 10^8$ protons. Charge of this bunches contributes to the total charge measured by DCCT but they are below the FBCT limit. This reasons the subtraction in equation 7.14. Another detail hides in the N_{tot}^{DCCT}. This quantity is not directly measured but it is calculated as:

$$N_{tot}^{DCCT} = \alpha S^{DCCT} - N_0^{DCCT}, \tag{7.15}$$

where α is the scale factor, S^{DCCT} is the signal observed and N_0^{DCCT} is the baseline offset. Each of these quantities contributes to the final uncertainty:

DCCT baseline offset can drift in time due to various reasons: temperature, electronic pickup in cables,... The easiest way to estimate the possible drift is to compare the offset right before and right after the fill. During these periods there is no beam in the machine and only the offset is measured. The difference in measured values between before and after the fill gives an estimate of the drift. Typically it corresponds to $\pm 0.8 \cdot 10^9$ protons for each beam, regrades of the fill parameters. This indicates that the associated relative error decreases with increasing charge of the beam. The estimated values represents $\pm 0.1\%$ uncertainty which is rather small compared to other contributions.

DCCT scale is another parameter which it must be understood in order to predict variations of N_{tot}^{DCCT}. This absolute scale is determined by observing the detector response to a known current source. According to technical specification given by manufacturer the source

should be accurate to $\pm 0.1\%$, however other effects must also be taken into account. Potential influence can come from detector non-linearities, dependence on the LHC fill pattern, orbit distortions, or measurement non-reproducibility over large time periods. To estimate the entire spectrum of possible contributors many DCCT calibration have been performed during 2010 and 2011. A peak-to-peak deviation of $\pm 2.7\%$ was taken as the overall estimation.

Bunch-to-bunch ratio as measured by FBTC can be compared to the independent measurement of ATLAS beam pick-up timing system whose response is also related to the charge of the passing bunch. Only statistical discrepancy between the two measurements could be observed and this was taken as a systematic uncertainty of the relative bunch charge measurement. It gives $\pm 1.6\%$ uncertainty for October 2010 data and $\pm 1.3\%$ uncertainty for May 2011 data.

Ghost charges and satellite bunches are another contributors to the total charge in the LHC beam. For different reasons some of the accelerated particles can be delayed with respect to the SPS or LHC RF systems, which that capture this charge in the wrong RF bucket. Since each BCID consists of 10 RF buckets the nominal time difference between each of them is $2.5\,\mathrm{ns}$. All of this charge contributes to DCCT measurement. The charge that is in the wrong buckets also contributes to the FBCT measurement for that particular BCID, of coarse if the total measured charge within corresponding $25\,\mathrm{ns}$ exceeds the FBCT sensitivity threshold.

The charge below the FBCT threshold remains undetected and is named *ghost charge*. Its relative portion within different RF buckets was measured during the LHC fill 1783 by the LHC Longitudinal Density Monitors (LDMs) [LD10]. Excluding the nominally filled BCIDs, the total measured charge was 0.18% of the total charge for the beam 1, and 0.40% for the beam 2. Here BCM can contribute its measurement as well. Its good timing resolution enabled monitoring of the the hits registered outside the nominal collisions. During the same fill this resulted in uncertainty estimation of 0.07% for beam 1 and 0.06% for beam 2. An average of LDM and BCM measurement was taken as the best estimate. It should be stressed that the obtained values have large uncertainty and were observed to vary significantly from fill to fill.

Undeliberately filled RF buckets within the same BCID hosts the satellite bunches. These produce luminosity within the same $25\,\mathrm{ns}$ time window, however at slightly different time and at different position. All three quantities: time, position and produced luminosity, are dependent of beam parameters, especially the beam crossing angle. Situation is even more complicated, since the interaction vertex is displaced which changes the detector acceptance, as shown in simulation in chapter 6. This not only varies the bunch charge measurement but in principle also influences the luminosity detector by slightly altering the measured rates. The latter is negligible at the luminosity values being currently measured, while the former could have a significant effect. A study was therefore performed both during 2010 and during 2011 vdM scans [SC11]. Satellite bunches were identified during offline analysis, for which the coverage of the vertexing algorithms was

extended over the $z = \pm 1\,\mathrm{m}$. This covers the $\pm 5\,\mathrm{ns}$ time displacement, thus including four satellite bunches nearest to the nominal bunch. After counting the vertexes, the efficiency obtained form Monte Carlo was take into account. Additional corrections needed to be applied for beam crossing angle and the transversal beam size dependence on the longitudinal position. The upper limit on the bunch charge product uncertainty was estimated to be 0.1%, combining with ghost charge contribution it gives a total of 0.2%.

The overall luminosity uncertain due to bunch charge product measurement is given in table 7.44 and amounts to 3.2% for October 2010 data, and 3.0 for May 2011 data.

Scan number	IV-V	VII-VIII
DCCT baseline offset	0.1%	0.1%
DCCT scale	2.7%	2.7%
Relative bunch population	1.6%	1.3%
Ghost charge & satellite bunches	0.2%	0.2%
Total	3.2%	3.0%

Table 7.44: *Systematic uncertainties of the bunch charge product determination.*

7.5.7 Beam centering

The assumption behind the vdM scan is that the peak luminosity observed during the scan corresponds to the maximum head-on luminosity as set up during the data taking. This assumption is correct only if during the scan the the beam is perfectly centered in the non-scanning plane. Any deviation scales down the scan curve. This contribution can be estimated from the presented results. The beam centering offset X_0 and Y_0 show non-reproducibility on the level of $3\,\mathrm{mum}$. Corresponding variation of the luminosity is 0.1%.

7.5.8 Absolute length scale

The basic idea behind the vdM scan is to determine the luminosity via measurement of beam parameters, which are then used in equation 7.13 to determine the luminosity. To accurately determine the $\Sigma_{X(Y)}$, precise beam separation must be known at every scan point. Any error in the separation scale is taken into luminosity through $\Sigma_{X(Y)}$.

The beam separation is achieved with closed orbit bumps located around the IP. To verify that given magnet settings yield the predicted beam separation an independent measurement is needed, usually called *length scale calibration*. In this measurement the beams are moved over the range $\pm 150\,\mu\mathrm{m}$ in five steps. Though displaced the beams are still partially colliding and thus giving the ATLAS detector possibility to reconstruct primary vertixes form the recorded data. With ID tracking precision and sufficient statistics, the center of the luminous region can be determined very precisely. This is then compared to the beam displacement deduced from the magnets.

Since there are two beams and close orbit bumps can move the beams in two directions, with each direction being steered by its own magnet, there are in principle four different scale correction factors. For all of them the length scan calibration was performed separately and results are given in table 7.45. To cover the data presented in this thesis two length scale calibrations are needed. The first one was done on October 4th, 2010, [C111] covering October 2010 scan data, while the second one occured on May 16th, 2011 [C211] to verify the scale used for May 2011 scan data. Two length scale calibrations were needed due to different β^* in the two periods.

Length scale calibration: October 4th, 2010		
	x-direction	y-direction
Beam 1 correction factor	1.003 ± 0.002	0.997 ± 0.002
Beam 2 correction factor	0.995 ± 0.002	0.999 ± 0.002
Total correction factor	0.999 ± 0.003	0.998 ± 0.003

Length scale calibration: May 16th, 2011		
	x-direction	y-direction
Beam 1 correction factor	1.0010 ± 0.0004	0.9955 ± 0.0003
Beam 2 correction factor	0.9981 ± 0.0003	0.9983 ± 0.0003
Total correction factor	0.9996 ± 0.0003	0.9969 ± 0.0002

Table 7.45: *Results of length scale calibrations for both 2010 and 2011 vdM data at IP1. The values are the ratios between vertex reconstructed and magnet announced beam displacement. Measurements are given for individual beams and for both scan planes with accompanying statistical errors.*

Because the vdM scans were performed by symmetrical movement of the two beams the overall correction factor is the average of the corresponding beam 1 and beam 2 values. These values are consistent with unity so no correction was done to the vdM scan data. For individual beam deviation from unity is within $\pm 0.3\%$. Adding this values in quadrature gives the final estimation of $\pm 0.4\%$ for $\Sigma_X \Sigma_Y$ uncertainty due to length scale error. The same estimation holds for both calibrations.

7.5.9 Beam-position jitter

Another effect coupled to the beam moving is the jitter of the beam under the same movement settings. While the length scale calibration checked the average scale of the displacement, small random deviations from nominal settings always occur. Their magnitude was estimated during length scale calibration by observing the reproducibility of beam centering. The extracted RMS value is $0.8\,\mu\mathrm{m}$ for October 2010 data [C111] and $0.6\,\mu\mathrm{m}$ for May 2011 data [C211]. This jitter causes the points of the vdM scan curve to be sightly misplaced, and by deliberately inducing such a displacement an effect on σ^{vis} can be studied. Though the fit model and RMS values of the jitter are different the σ^{vis} deviations do not

differ significantly when comparing different scans. The biggest change in visible cross-section amounted to 0.4% and this value is used as the final beam-position jitter contribution to systematic uncertainty.

7.5.10 Emittance growth

There is yet another assumption on which vdM procedure relies upon. The beam characteristics are assumed to be constant, i.e. the transverse emittance should not change. This implies constant luminosity and constant beam size, thus constant Σ. The change of these quantities therefore indicates the change of emittance.

Both the increase in Σ and drop of the measured peak values is clearly visible from the results. The observed effect had the same magnitude in both scans for given LHC fill. The same observation was made by measuring the single beam profile with wire scanners and synchrotron light monitors.

The effect is not expected to be large, since the equation 7.13 multiplies the Σ and μ and the increase of the former should cancel the decrease of the latter. To estimate any possible deviations the best quantity to look at is the change in the bunch average value of σ^{vis} and compare it between the two consecutive scans. Looking at the OR algorithm values (because of smallest statistic uncertainty) this gives estimation of 0.36% of maximal variation during October 2011 scans and 0.42% variation during May 2011 scan. This estimates the effect of emittance change between the scans, however a smaller effect is possible due to change within a scan that would distort the vdM scan curve. Same Monte Carlo based simulation can be used as was used for length scale uncertainties, which yield 0.2% effect.

Combining the two estimations and acknowledging the limited statistics over which the σ^{vis} was averaged a conservative estimation of 0.5% was taken as a final estimation, valid for both calibrations.

7.5.11 Transverse correlations

In general the bunch proton density function is described by two-dimensional function $\rho(x, y)$. The data analysis assumed that there are no correlation in the proton density between x and y directions and the distribution function factorizes, enabling independent Σ_X and Σ_Y fitting. If such a correlation exists the effective beam width might be slightly different from the results obtained from fits [LC00].

If the correlation is linear with the correlation coefficient κ and the density distribution is described by a single Gaussian, then the luminosity is simply scaled by factor $(\sqrt{1-\kappa^2})^{-1}$. The correlation was measured with the help of vertex counting. The longitudinal vertex distribution was fitted to the tilted ellipse that is expected with correlation. From the tilt, the value $\kappa \simeq 0.02$ was obtained, indicating the effect on luminosity in the order of 0.02%. This is therefore negligible.

Still keeping linear correlation between x and y proton density distribution, a larger effect can be obtained in cases where the distribution is described by sum of two Gaussians, like in October 2010 data. With the notation used in equation 7.8 when the double Gauss fit model was

given, the product $\Sigma_X \Sigma_Y$ has nonlinear contributions like:

$$\left(\frac{f_1}{\sigma_{1,x}\sigma_{1,y}} + \frac{1-f_1}{\sigma_{2,x}\sigma_{2,y}} \right)^{-1}. \tag{7.16}$$

Such contributions can be factorized if we have a single Gaussian ($f_1 = 1$). If not, this is extra systematic effect that must be estimated. Again the vertex counting was used as a tool to independently check for the two different sub-populations of the bunches. The analysis states a final $\pm 0.9\%$ uncertainty due to correlations. This has been obtained from the October 2010 data, while the May 2011 does not indicate a second Gaussian component. Combined x and y scans fits however show, a maximal 0.4% difference from the uncoupled fits. This is a raw estimations since different correlations were needed to be assumed, however the estimation is consistent with the October 2010 data, which had significant second Gaussian component.

7.5.12 Overall systematic uncertainty of vdM calibration

Combining all contributions a final systematical uncertainty can be determined. Individual contributions are listed in table 7.46. A final estimation are: 3.7% for calibration of 2010 data and 3.4% for calibration of 2011 data.

Contribution	October 2010	May 2011
μ-correction	0.4%	0.4%
Detector consistency	1.0%	1.0%
Fit model	0.7%	0.7%
σ^{vis} consistency	0.4%	0.4%
Threshold variation	0.5%	0.5%
Bunch charge product	3.2%	3.0%
Beam centering	0.1%	0.1%
Absolute length scale	0.4%	0.4%
Beam position jitter	0.4%	0.4%
Emittance growth	0.5%	0.5%
Transverse correlations	0.9%	0.4%
Total	3.7%	3.4%

Table 7.46: *Relative systematic uncertainties of the vdM calibrations (σ^{vis}) in October 2010 and May 2011.*

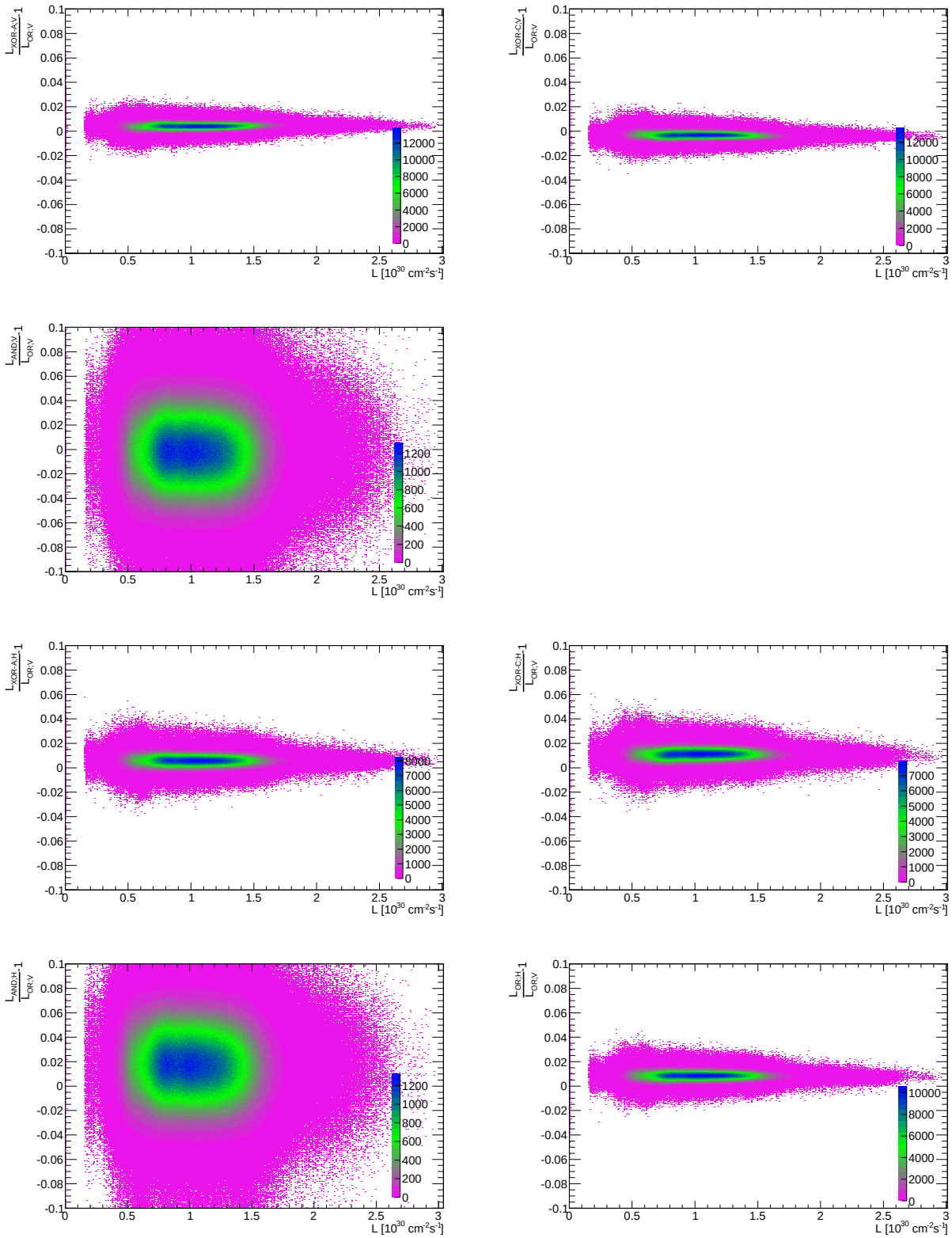

Figure 7.43: *μ-correction comparison of various BCM luminosity algorithms with respect to the BCM-Vertical OR algorithm measurement. All plots indicate stable μ-corrections, though another small systematical uncertanty is observable.*

Chapter 8

Luminosity measurements

8.1 A look into the BCM luminosity measurement performance

Having described the detector functionality and determining the the calibration constants, the time has come for the final treat - the recorded data. In this section the data is presented on an example of ATLAS run 188921. This run started on September 7th 2011 and had 423 colliding bunch pairs. Is has been chosen since it is a typical run that shows all of the interesting BCM features in a clear way.

The different stages of luminosity analysis are shown in figure 8.1. Plots show data for $\mathrm{BCID} = 45$. The start of the luminosity analysis are the raw event-type probabilities shown in upper-left plot. On this data the μ-corrections are applied, giving upper right plot of the same figure. The corrections are significant, a factor ~ 2 is needed in the case of the OR algorithm. The obtained μ_A^{vis} are then multiplied by calibration constants obtained from vdM scans and the bottom plot of figure 8.1 is produced. It shows that all algorithms give the same result, however, being limited to a single bunch, still limits the statistics, especially for the AND algorithm.

The described procedure is repeated for all BCIDs. For filled BCIDs figure 8.2 shows that instantaneous luminosity varies by a factor of 2 between different bunches. Their life time also varies. The right plot of the same figure shows the sum over all bunches. Each point on this figure represents data for a single luminosity block. Consistency equal to that observed in the vdM is obtained, which indicates a problem-free data taking. Notice that the agreement is not perfect for the two luminosity blocks, the one during which beams are brought into collision and for the one during which a beam dump was performed. This is due to the fast changing luminosity. This was assumed to be constant over the basic data building block to perform the μ-corrections.

Another thing that can be offered by BCM are plots assisting in data quality monitoring. If σ^{vis} (used to calibrate the detector) is divided by the proton-proton cross-section (taken from an independent measurement [TS11]) the detector/algorithm efficiency is obtained. Multiplying

μ^{vis} with this efficiency gives the total average number of interactions per bunch crossing $\langle\mu\rangle$. Figure 8.3 represents a histogram of integrated luminosity vs. $\langle\mu\rangle$. At the beginning of the run the average interaction number per bunch crossing reaches values up to 15. This is roughly half of what is expected at LHC design luminosity. The majority of data is recorded later in the run when interactions are less frequent.

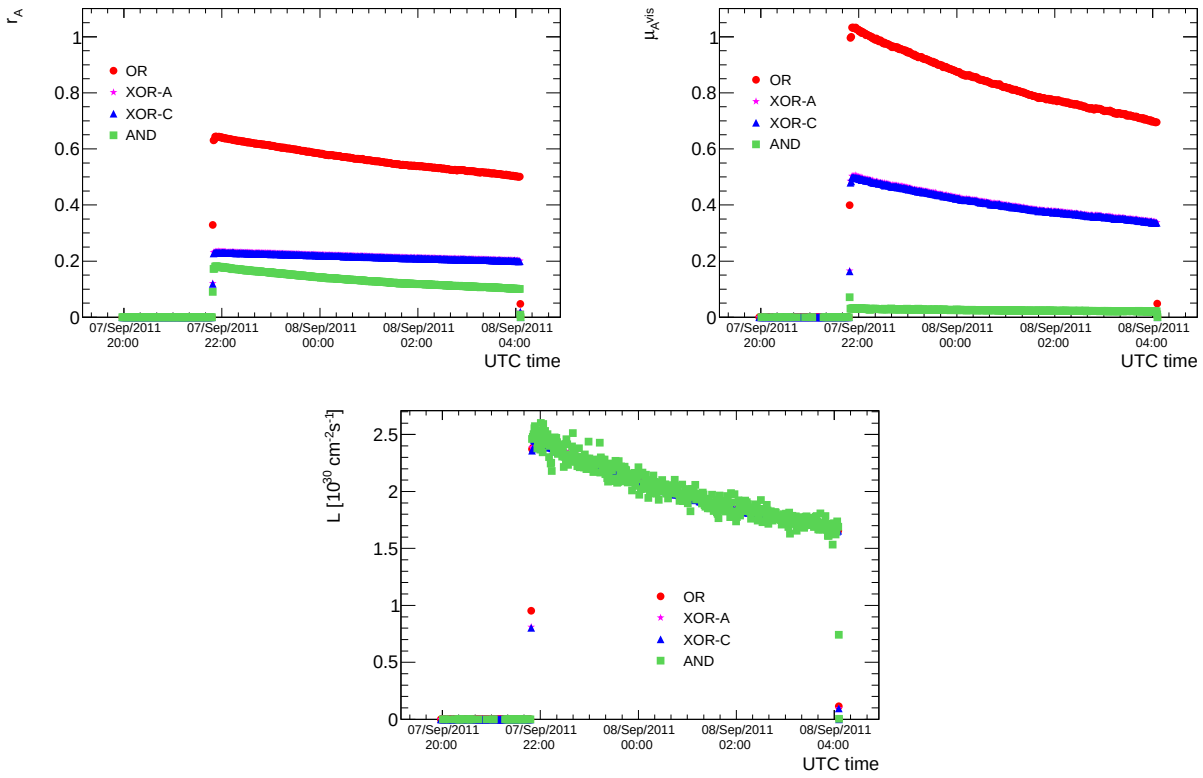

Figure 8.1: *Data processing stages for* BCID $= 45$ *in ATLAS run 188921. Upper left plot shows the recorded event-type probabilities. On these the μ-corrections must be applied and the resulting μ_A^{vis} is shown in upper right plot. Multiplying this with the calibration constants σ_A^{vis} (obtained from vdM) the final instantaneous luminosity is obtained (bottom plot) for this bunch pair. All four algorithms give consistent data, though the and still suffers from low statistics when looking at a single bunch.*

8.1.1 Background seen in the luminosity data

As shown, measuring the luminosity for each bunch separately is BCM's strong suit and nothing demonstrates this better than plots in figure 8.5. Here the entire luminosity maps are plotted. All algorithm again show consistent data and the bunch train structure of the beam is clearly visible. Each such bunch train is followed by the afterglow caused by the beam residuals in the LHC. Though dominant background, accompanied by the random noise, its

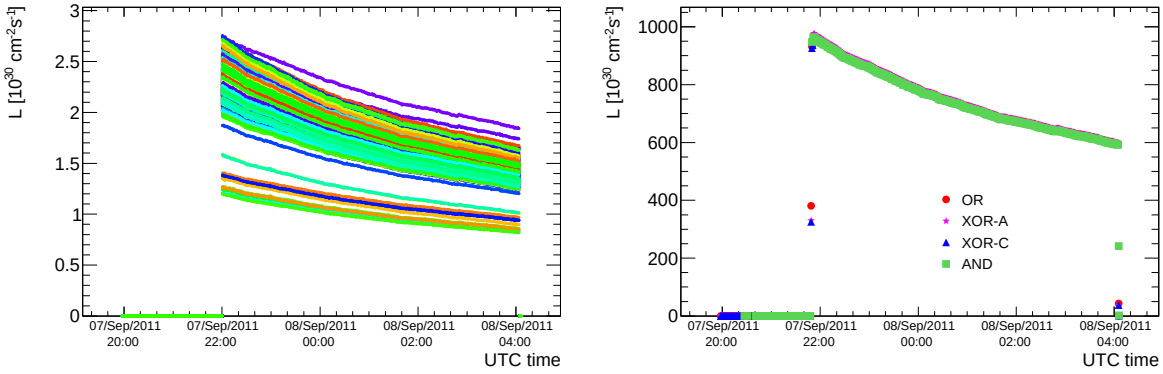

Figure 8.2: *The good BCM timing allows to perform the luminosity measurement for each bunch separately. The collection of all bunch luminosities is shown on the left side. Once BCID mask is applied, and with it the contribution of background in empty BICDs is removed, all the BCID luminosities can be summed and the right plot is obtained. This it the total instantaneous luminosity as a function of time.*

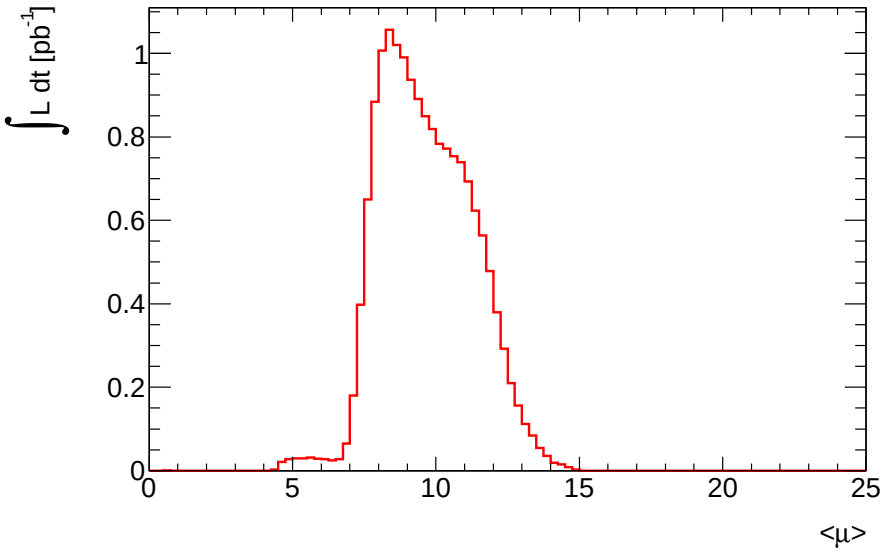

Figure 8.3: *Independent measurement of proton-proton cross-section [TS11] was used and the actual number of interactions per bunch crossing $\langle\mu\rangle$ was be estimated. The plot shows the integrated luminosity (quantity of data) that was available at certain $\langle\mu\rangle$. At the beginning of the fill most of bunch crossings yield around 12 proton-proton interactions, which gradually lowers due to beam losses. The $\langle\mu\rangle \approx 25$ is expected once the design luminosity of LHC is reached.*

relative contribution is in the order of per mill. And this holds true for the OR (upper-left plot) and XOR algorithms.

Another contribution to the background are the unpaired bunches (those that do not collide

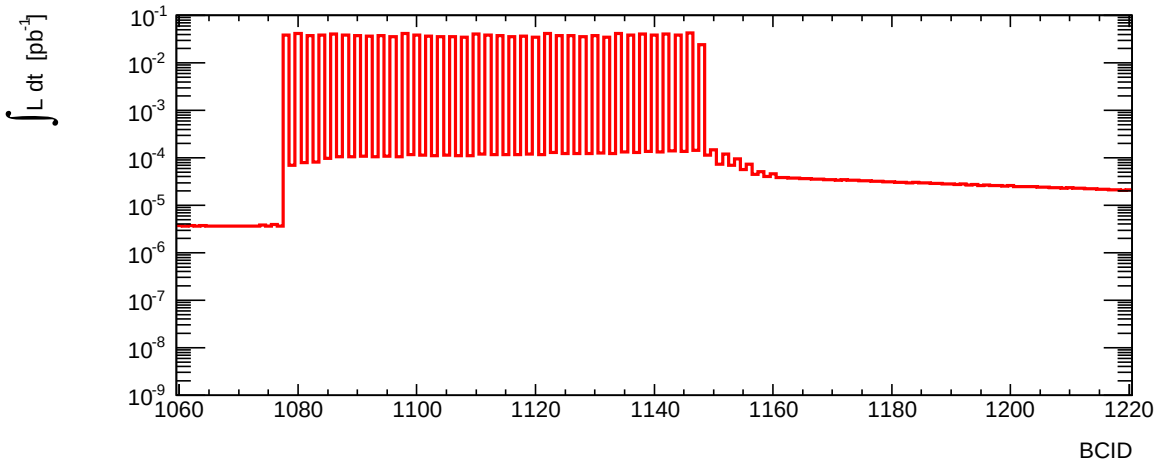

Figure 8.4: *Only a subset of OR luminosity map that spans over a bunch than is displayed. Individual bunches can be distinguished and it is clear that every second one is filled. Form the measurement of the BCIDs in between the filled ones, the contamination of the bunch following the full one can be estimated.*

within ATLAS). This contribution can be seen around $\mathrm{BCID} \sim 1800$ and $\mathrm{BCID} \sim 2700$. These bunches still carry the beam halo and interact with the residual beam gas. Being smaller than the afterglow, their contribution to the measured luminosity is negligible. However BCM XOR-A (bottom-left plots) and XOR-C (bottom-right plot) luminosity measurements show beautifully that this is 'single-sided' background. While only one train is noticeable in each of the XOR algorithms both can be seen in the OR algorithm data. This is not true for the afterglow, which seems to induce mostly uncorrelated hits. This is also the reason why there is hardly any afterglow visible in the AND algorithm data (upper-right plot). The background here is almost completely suppressed by the selectivity of the AND algorithm. This gives a fascinating six orders of magnitude difference between signal and noise. This plot clearly states, that at even higher luminosities than currently achieved, the AND algorithm will provide a superb approach to luminosity measurement. At current luminosities however the OR still has the advantage of being statistically dominant.

A closer look in the BCID range $1060 - 1220$, for the OR algorithm, is offered by the figure 8.4. It clearly shows that within the bunch train every second BCID is filled with the bunch. The BCIDs in between report luminosity roughly three orders of magnitude lower than the filled BCIDs, but that is to be expected. The contamination of the first bunch following the filled one was estimated in section 6.3.5 and values agree.

All the above shows that the OR algorithm has the highest background which contributes roughly 0.1% to the luminosity value. This is negligible contribution compared to the calibration uncertainty. The AND algorithm is practically without noise. The final results are even more clean than the results in plots in figure 8.5 since only filled BCID are summed over, leaving out the rest of the beam's contribution.

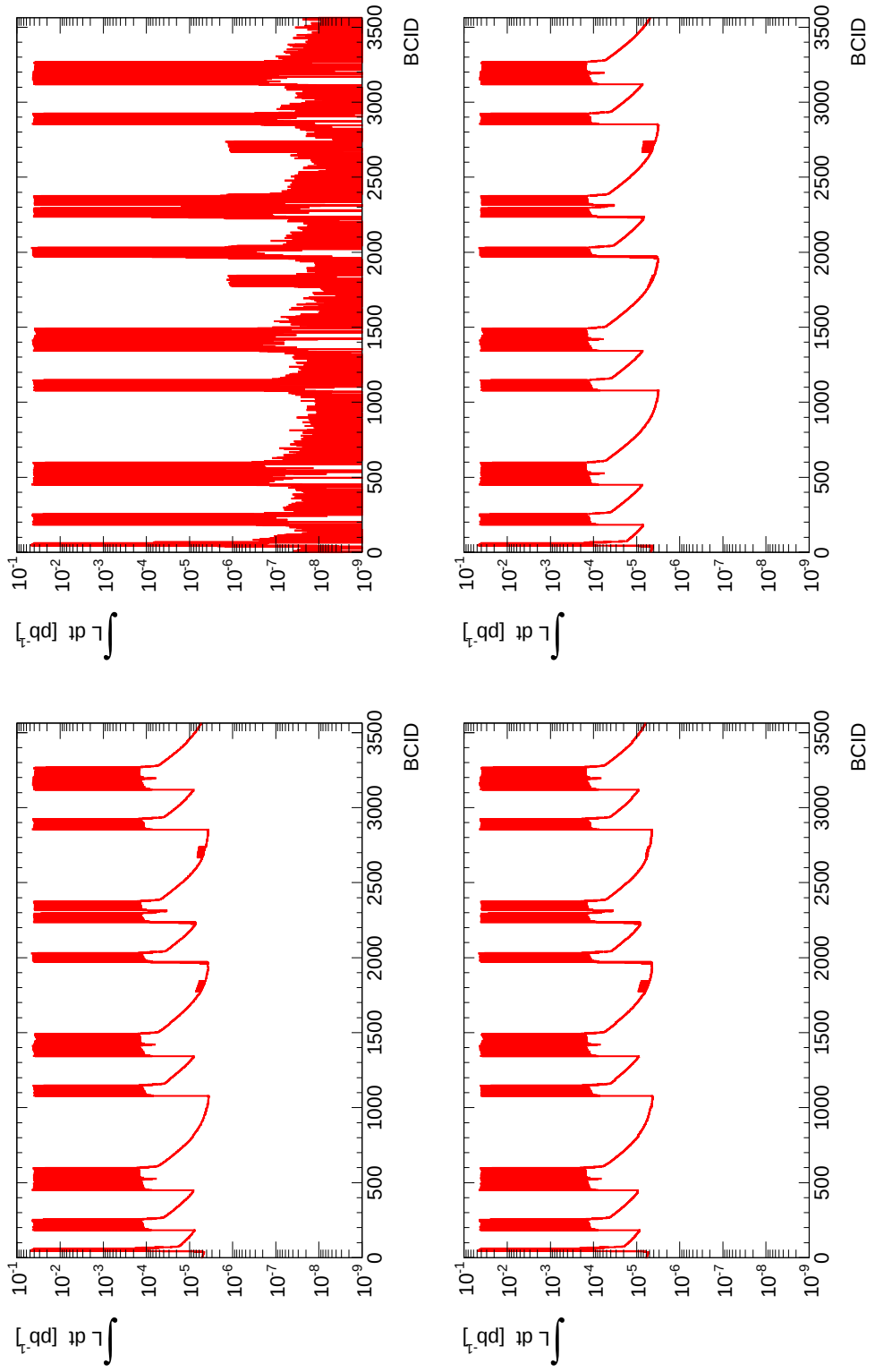

Figure 8.5: *Horizontal axis denotes BICD and extends over all 3564 slots covering the entire LHC beam. Bunch train structure of the beam is clearly visible, as well as the relative strength between signals induced by colliding and by unpaired bunches (around BCIDs 1800 and 2700). Upper-left plots shows the OR data luminosity prediction which is most susceptible to random noise and bunch train afterglow. Both are enormously reduced when AND algorithm is used (upper-right plot), while a direction of noise source can be identified from bottom-left and bottom-right plots which show data for XOR-A and XOR-C.*

8.2 Overview of the recorded data

BCM was completely integrated into the ATLAS luminosity infrastructure by the end of June 2010. Since then, it is stably contributing its measurements which are collected by OLC and recorded into the conditions database. During the entire period it offered a reliable measurements with almost no operational dead time. The most relevant is the 2011 data, since it covers the majority of the accumulated statistics, and additionally, because in May 2011 the BCM was chosen as the ATLAS preferred luminosity measurement device. This means that the official values for ATLAS luminosity reported to LHC and used in physics analysis are based on the BCM data and work presented in this thesis.

A subset of 2011 data is presented in the following plots. First is figure 8.6, showing the agreement between different algorithms. OR algorithm of BCM-Vertical luminosity is take as a reference. Over a two month period the algorithms seem to produce self consistent results, with deviations between them routed in the systematics of vdM scan.

Figure 8.7 shows the peak instantaneous luminosity for individual runs over two month period, while figure 8.8 shows the total integrated luminosity over the same period of time. The analysis of the larger time period is ongoing. The numbers produced so far are consistent with the OLC numbers, as they should since they are based on the same raw data. Maximal deviations observed are much less than $1‰$ which is expected from computational errors. Up to October 28th, 2011, the peak luminosity of $3.65 \cdot 10^{33} cm^{-2} s^{-1}$ was measured in the LHC fill 2256. To determine the total integrated luminosity corresponding to the recorded data up to the same date, ATLAS combined the BCM data with the run parameters from the conditions database (luminosity block numbers during which stable beams were declared, list of filled BCIDs,...). The total value ammounts to $5.19\,\mathrm{fb}^{-1}$ [RSUM].

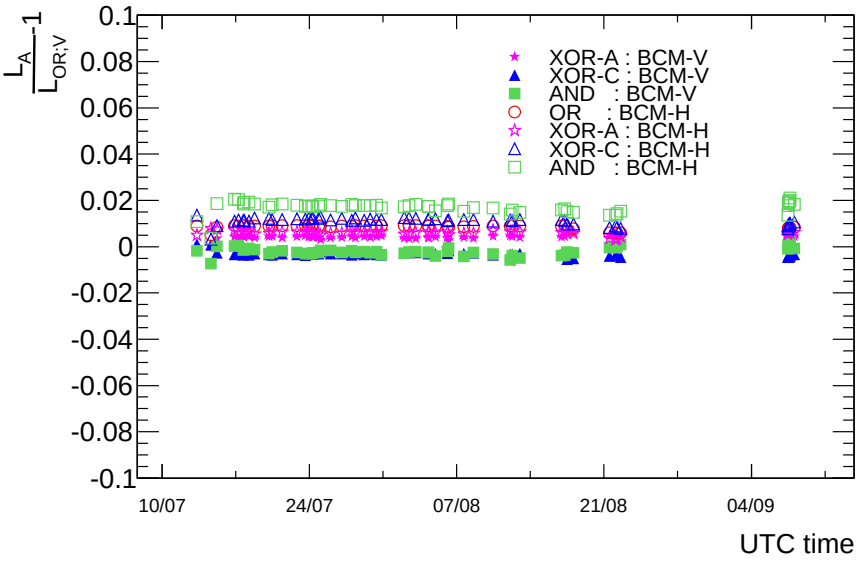

Figure 8.6: *Relative difference of BCM luminosity algorithms with respect to BCM-Vertical-OR. This differences have already been incorporated into the systematical uncertainty of vdM calibrations. They seem to be rather constant with time.*

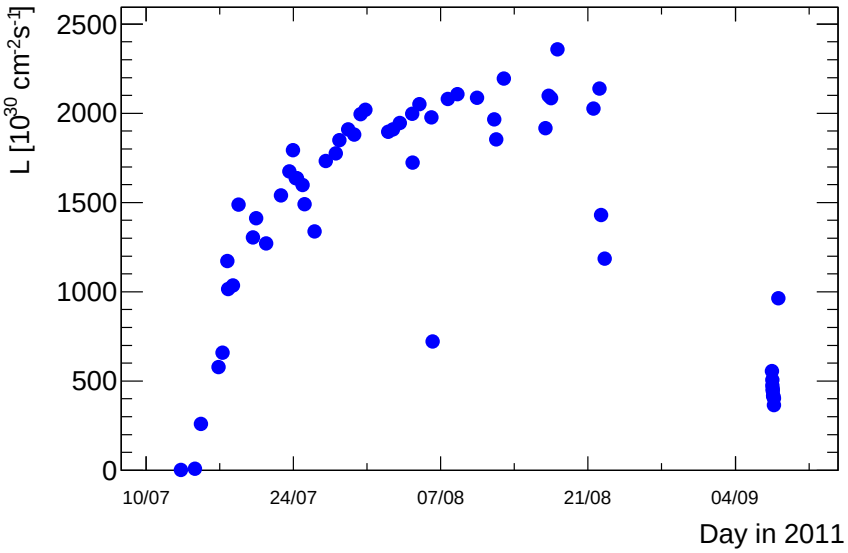

Figure 8.7: *Peak instantaneous luminosity of the runs.*

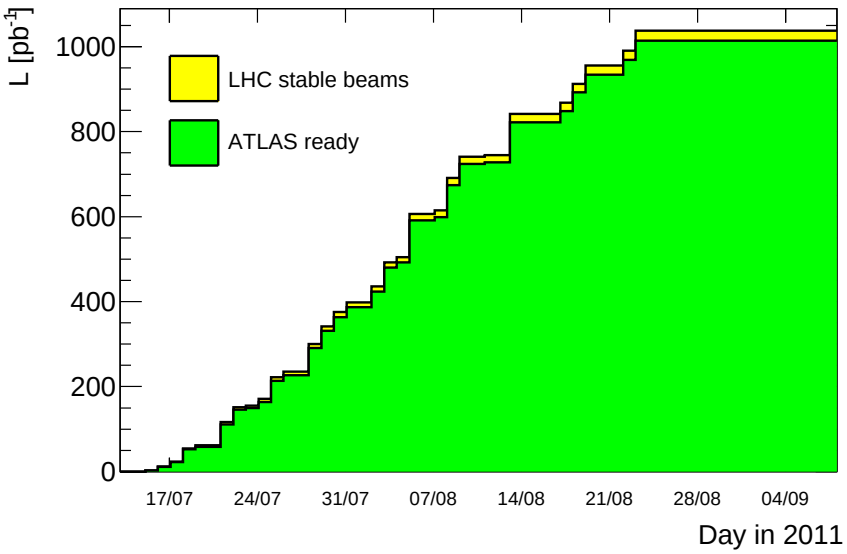

Figure 8.8: *Total accumulated luminosity for ATLAS. A large operational efficiency of the detector time gives only a small discrepancy between LHC delivered and ATLAS ready luminosity.*

Chapter 9

Conclusions

To provide the much needed input of luminosity for the physics analysis, the ATLAS experiment developed a rather complexed luminosity infrastructure. Many sub-detectors contribute information on different time scales and with different precision. Having many independent measurements helps in uncertainty and reliability estimation. All of these measurements are gathered and processed by the central data acquisition service - the Online Luminosity Calculator, which also stores the data for later offline use.

The thesis presents the work done to evaluate, extend and establish BCM as a luminosity monitor. While many detectors can be used for this measurement the BCM offers above average measurement quality. Many reasons are responsible for this. The diamond as a sensor material provides a stable operation with relatively low noise compared to silicon (due to the larger band gap). Additionally it is radiation hard, allowing longer life time of the detector. The high operational bias voltage of $1000\,\mathrm{V}$ allows fast charge collection and short signals. Combined with fast radiation front-end electronics, signals widths of $2\,\mathrm{ns}$ are achieved. Since bunches collide at maximum every $25\,\mathrm{ns}$, this renders the pile-up out of the possible complications.

With timing as its strong suit the BCM can easily eliminate large portion of the background from its measurements already at the early data processing stage. This was implemented with a custom-made firmware operating on a Xilinx FPGA. Fast, luminosity specific, digital processing is implemented, making optimal use of the underlying sensor timing resolution. To register detector hits for each of the 3564 possible bunch positions in the LHC beam, four independent luminosity maps were implemented. Each of these maps is based on different logic that classifies event-types and filters out only the desired hit combinations.

This logic, called *luminosity algorithms*, has been defined with the help of Monte Carlo simulation. Simulation helped to estimate the expected response and assisted in choosing the luminosity algorithms accordingly. The collection of OR, $XOR-A$, $XOR-C$, and AND algorithms was chosen to extend the dynamic range of the BCM over a few orders of magnitude. These algorithms are all based on event-counting, which makes the measurement simpler and thus more robust. The OR algorithm provides the highest statistics and is currently chosen as the preferred algorithm. It was shown that even in this, to background most susceptible algorithm, the background contribution is minimal. The two XOR-based algorithms resemble the OR algorithm in many characteristics and their main asset is that they are selective when

it comes to single sided background. Though to no extra value in luminosity measurement, they help to identify different contributions of background and ease the data quality monitoring. The measurement alternative to OR is the AND algorithm. Being weighted with the burden of smallest statistics it is the most selective one, suppressing the background to hardly a observable level. The luminosity algorithms populate the luminosity maps that are read-out and distributed to the BCM private data stream and to OLC. The implementation allows the read-out without any dead time with rates up to few Hertz, which is more than needed for the luminosity measurement of the long living LHC beams.

Additional asset are two data processing units. The 8 low threshold channels are distributed among these two units in a way that both have A and C side measurement. Signal processing is done completely independent on each of the units. This effectively reduces statistic, especially for the AND algorithm (comparing to the scenario where all eight channels would be processed by the same unit), however it introduces two new assets. First one it the fact that also OR statistics is reduced. Since this is not operational problem it is beneficiary since this means that OR algorithm will saturate at higher luminosities, thus spanning the luminosity range of BCM usability. The second asset is that the system provides two independent measurements. A comparison showed that systems gives a consistent results on a level of 1%. Additionally, doubling your detector means redundancy in case of possible failure.

Theses described the entire structure of both the firmware and the data acquisition software, while the efforts were focused on understanding the detector response as precisely as possible. μ-corrections were developed to correct the observed non-linearity due to pile-up of more and more proton interactions within a single bunch under rising luminosity. The choice of algorithms enabled this corrections to be done analytically, thus avoiding any additional uncertainties. Monte Carlo simulations were performed to verify the measurement procedure and to provide the first estimate of the calibration constants.

The currently valid calibration was done by the van der Meer scans, which measure the effective beam parameters, enabling the calculation of luminosity. Simultaneously the event-type probabilities for luminosity algorithms were measured and comparison against the calculated luminosity yielded the calibration constants. Two such scans were performed. The October 2010 vdM scan calibrated the 2010 data, while the vdM scan in May 2011 calibrated the 2011 data. For both scans the the data was found consistent between the BCM-Horizontal and BCM-Vertical measurements and between different algorithms. Estimations of possible systematical influences to the calibration resulted in total 3.7% and 3.4% of uncertainty estimations for October 2010 and May 2011 calibration respectively.

The BCM was fully incorporated in the ATLAS luminosity framework in June 2010, and since, it performed reliably with almost no operational dead time. The data reveals that the background is in the order of 0.1% for the OR algorithm, while AND algorithm is practically background free. The data shows a stability and reliable performance even over larger time periods. The low background, small systematical uncertainty, and reliability persuaded the ATLAS community that BCM has to offer the best luminosity measurement within ATLAS. In spring 2011 the BCM therefore became the ATLAS preferred luminosity measuring device. Its measurement is used as an official ATLAS value, that is reported to LHC and being the default value for the physics analyses.

Poglavje 10

Povzetek doktorskega dela

10.1 Uvod

Trenutno znanje o fiziki osnovnih delcev je povzeto v teoriji, poimenovani *Standardni model*. Ta predpostavlja dve vrsti osnovnih delcev: kvarke in leptone, z dodatno skupino delcev, ki so odgovorni za nastanek sil. Teorija se je izoblikovala v zgodnjih sedemdesetih letih in je uspešno napovedala veliko različnih pojavov v svetu osnovnih delcev ter prestala desetletja preizkuševanja... vendar še vedno ostaja nepreizkušen drobec – Higgsov delec. Ta zadnji kos sestavljanke Standardnega modela še ni bil opažen. Vendar to ni zadnja sestavljanka v naravi, ki je ostala! Standardni model opisuje le tri izmed štirih osnovnih sil in ne pojasnjuje težnosti. Obstajajo tudi namigi, da Standardni model ne opisuje dobro procesov, kjer je v igri večja energija. Za razlago teh procesov bi bila potrebna kakšna nova teorija....

Da bi se dokopali do odgovorov na ta vprašanja, je bilo predlaganih več poskusov. Veliki hadronski trkalnik (LHC) je le eden izmed teh. Njegov namen je razširiti meje energij, pri katerih lahko nadzorovano opazujemo fizikalne procese. LHC pospešuje protone ali svinčeva jedra v dveh ločenih curkih, ki se križata na štirih mestih. Tukaj pospešeni delci trkajo in detektorji na teh mestih merijo nastale produkte. Izmed šestih detektorjev postavljenih ob LHC obroču sta največja ATLAS in CMS. To sta spektrometra namenjena meritvam velike množice fizikalnih pojavov.

Količina proizvedenih podatkov je sorazmerna s številom trkov delcev, ki jih priskrbi trkalnik. Zaradi tehničnih omejitev in omejenega podatkovnega prostora je le del teh podatkov posnet in dosegljiv za fizikalne analize. Izkoristek snemanja se tako dobi, če količino posnetih podatkov delimo s količino proizvedenih podatkov. Ti količini opisujemo z *luminoznostjo*. Tukaj igra svojo vlogo tudi detektorski sistem za spremljanje kakovosti curka protonov (BCM).

Disertacija opisuje delovanje sistema BCM, ki je le eden izmed detektorjev spektrometra ATLAS. Kot uvod je obrazložen pojem luminoznosti, kar objasni, zakaj je to tako pomembna količina in kako vpliva na fizikalne meritve. Sledi opis trkalnika, kar bralcu skicira izvor luminoznosti in oriše stvari, ki vplivajo nanjo. Razdelki, ki sledijo, se osredotočijo na merilne naprave. Opisan je spektrometer ATLAS kot celota, kjer je posebej izpostavljena infrastruktura za merjenje luminoznosti. Sledi podroben opis sistema BCM, kjer je do potankosti opisana celotna veriga, namenjena merjenju luminoznosti: od algoritmov za obdelavo signalov do

prenosa in shranjevanja podatkov. Predstavljena je tudi simulacija sistema, ki pomaga razumeti zvezo med luminoznostjo in ustreznimi številkami, ki jih poda BCM kot svojo meritev. Simulacija je tudi omogočila prvotno oceno umeritvenih konstant. Ta ocena je bila v veliko pomoč med snovanjem sistema, medtem ko je bila umeritev za merjene podatke narejena s postopkom van der Meera. Tej kalibraciji je namenjeno najobširnejše poglavje, čemur sledi še kratek pregled opravljenih meritev luminoznosti.

10.2 Luminoznost

Večino lastnosti osnovnih delcev se lahko izmeri le posredno. Običajen pristop je opazovanje sipanja delca na tarči. Delec interagira z delci v tarči in končen rezultat, ki ga zazna detektor, je odvisen od merjene količine (npr. mase, spina,...). Iz izmerjenega načina sipanja se tako izlušči željena količina. Samo sipanje določimo s tem, da izmerimo število delcev N na enoto prostorskega kota Ω, ki so se sipali v določeno smer v enoti časa. Ta merjena količina se lahko zapiše kot produkt:

$$\frac{dN}{d\Omega dt} = L\frac{d\sigma}{d\Omega}. \tag{10.1}$$

V gornji enačbi je $\frac{d\sigma}{d\Omega}$ diferencialni sipani presek in opisuje *fizikalni proces*, ki ga merimo. To je končni cilj meritev. Sorazmernostni faktor L se imenuje *luminoznost* in se podaja v enotah $cm^{-2}s^{-1}$ in opisuje *pogoje fizikalnega poskusa*[1]. Integriranje gornje enačbe po prostorskem kotu da pogostost interakcij R:

$$R = \frac{dN}{dt} = L\sigma. \tag{10.2}$$

Če se torej omeji na določen fizikalen proces (konstanten celotni sipalni presek σ) je trenutna luminoznost torej le sinonim za *pogostost interakcij*. Integral gornje enačbe po času bi dal celokupno število interakcij, ki so se zgodile v določenem časovnem obdobju. To predstavlja *količino podatkov* in je torej enakovredno *integrirani luminoznosti* $\mathfrak{L} = \int Ldt$.

Luminoznost je torej lastnost trkalnika. Številu interakcij, ki jih ta proizvede, ustreza *ustvarjena luminoznost*. Zaradi tehničnih omejitev detektor ni sposoben ne izmeriti, ne zapisati končnega stanja vseh teh interakcij. Iz tega razloga se uporablja dodatna količina – *zapisana luminoznost*, ki predstavlja količino proizvedenih podatkov v časovnih obdobjih, ko je bil detektor aktiven in je snemal podatke. Cilj vsakega eksperimenta je torej čim večja zapisana luminoznost, saj več podatkov pomeni manjšo statistično napako.

V nasprotju z večnim lovom za čim večjo zapisano luminoznistjo obstaja optimalna trenutna luminoznost trkalnika. Omejitev hitrosti snemanja, ki jo postavi detektor (določi R v enačbi 10.2), tako prisili v optimalni kompromis med trenutno luminoznostjo (hitrostjo nabiranja podatkov) in številom procesov, ki se jih opazuje (sipalnim presekom σ). Dodatno bi prevelika trenutna luminoznost pomenila tudi preveč hkratnih signalov v detektorju, kar lahko drastično zmanjša, tako njegov izkoristek za sledenje delcem, kot tudi njegovo natančnost. Upoštevajoč lastnosti detektorja, proučevane procese ter količino in kakovost dobljenih

[1] V primeru sipanja na mirujoči tarči je luminoznost kar enaka ploskovnemu pretoku vpadnih delcev

podatkov je razvidno, da skrbno izbrana trenutna luminoznost predstavlja pomembno količino v poskusih sipanja osnovnih delcev.

10.3 Načini merjanja luminoznosti

Da je lažje ločiti različne prispevke k negotovostim meritev, lahko meritve v splošnem razdelimo med *relativne meritve luminoznosti* in *absolutne meritve luminoznosti*. Relativne meritve so lahko zelo natančne, saj jih omejuje le sistematična napaka detektorja. To je možno znižati tudi na nivo $\sim 1\%$. Tem meritvam pa manjka absolutna vrednost in jih je v nekem trenutku potrebno umeriti z absolutno meritvijo. Ta umeritev praviloma prispeva prevladujoči del sistematične napake. Večina absolutnih meritev je zelo omejenih v pogojih pri katerih se lahko izvajajo, zato so uporabljene le za kalibracijo relativnih meritev, kot jih nudi BCM. Te meritve se nato uporabljajo med snemanjem podatkov. Najpomembnejši pristopi k absolutnemu merjenju so:

Sipanje pod majhnimi koti je povezano s totalnim sipalnim presekom preko optičnega teorema [PF95]. Če je ρ razmerje med realno in imaginarno komponento sipane valovne funkcije pod kotom nič, potem se lahko luminoznost izrazi kot (glej dodatek A):

$$L = \frac{1}{16\pi} \frac{R_{tot}^2}{dR_{el}/dp|_{p\to 0}} \left(1+\rho^2\right). \tag{10.3}$$

Z merjenjem celotne pogostosti interakcij R_{tot} in elastičnega sipanja pod majhnimi koti R_{el} se torej lahko izračuna luminoznost. Ta metoda zahteva vrednost dR_{el}/dp pri $p = 0$, torej pri kotu 0, kar zaradi samega curka ni migoče meriti. Tako se večinoma meri v območju majnih kotov, kjer sta prispevka interakcij zaradi močne in elektromagnetne sile približno enaka. V primeru trkalnika LHC je potrebno kote, pod katerimi se opravljajo meritve zmanjšati tudi do $14\,\mu\mathrm{rad}$. Za takšno meritev je potreben namenski zagon LHC-ja z nastavitvami curka, ki zagotovijo, da so povprečni koti pod katerimi se trkajo protoni še dosti manjši. To pa zahteva nizko luminoznost in se torej tak način lahko uporablja le za umerjanje in ni primeren za snemanje podatkov.

Natančno izračunjivi procesi kot so na primer $pp \to ppe^+e^-$ in $pp \to pp\mu^+\mu^-$ predstavljajo drug pristop. Iz posnetih podatkov je možno izluščiti pogostost teh procesov, kar se nato primerja z izračunanim sipalnim presekom. Sorazmernostni faktor (glej enačbo 10.2) je luminoznost. Največja omejitev za hadronski trkalnik, kot je LHC, so izjemno majhne verjetnosti za uporabne kvantno-elektrodinamične procese, kar oteži natančno meritev. Dodatno možnost predstavlja uporaba kvantno-kromodinamičnih procesov, kot je nastanek W in Z bozonov [ZC04]. Ti procesi so najbolje poznani v tej skupini. Privlačna prednost je, da se s tem načinom lahko izmeri luminoznost partonov (kvarkov in gluonov) in ne protonov kot celote.

Lastnosti protonskega curka določajo luminoznost gruče protonov:

$$L = f_r N_1 N_2 \int \rho_1(x,y)\rho_2(x,y)\,dxdy, \tag{10.4}$$

kjer je f_r frekvenca kroženja gruče v trkalniku, N_1 in N_2 sta števili protonov v gručah ki trčita in $\rho_{1/2}$ predstavljata ploskovni porazdelitvi teh protonov znotraj gruč 1 in 2. Da se izogne izračunu teh porazdelitev, je van der Meer predlagal postopek, kjer enega izmed curkov premikamo glede na drugega in opazujemo pogostost izmerjenih interakcij $R_{vdm}(x)$ kot funkcijo razmika curkov x. Iz izmerjene porazdelitve lahko določimo ρ in s tem tudi luminoznost. Ta metoda je kasneje opisana bolj podrobno, saj je uporabljena za umeritev sistema BCM.

Relativne načine merjenj luminoznosti se deli na:

Štetje dogodkov kar je eden najrobustnejših načinov merjenja. Dogodek je definiran kot trk dveh gruč protonov in vsak tak trk ovrednotimo ali ustreza v naprej danim pogojem ali ne. Rezultat meritve je pogostost dogodkov, ki ustrezajo pogojem. Ti pogoji so imenovani *algoritmi luminoznosti*. So lahko zelo različni in bodo natančneje opisani v prihodnjih poglavjih. Primer takšnega algoritma je zahteva, da detektor ne zazna nič. Ker so interakcije med protoni med seboj neodvisne, lahko število takšnih 'praznih' dogodkov n_{det} izrazimo kot:

$$n_{det} = n_{BC}\left(1 - e^{-A_{ec}\cdot L}\right), \tag{10.5}$$

kjer je n_{BC} število trkov gruč in A_{ec} konstanta detektorja odvisna od celotnega sipalnega preseka in izkoristka detektorja. Iz prejšnje enačbe lahko izrazimo luminoznost, vendar se je potrebno zavedati, da napaka meritve narašča z manjšanjem razlike $n_{BC} - n_{det}$.

Štetje delcev lahko odpravi pravkar opisano težavo. Tukaj detektor meri številčnost delcev, ki nastanejo ob trku protonov. Njihovo število M je sorazmerno številu protonov, ki trčijo, torej tudi luminoznosti:

$$M = C \cdot A_{pc} \cdot L. \tag{10.6}$$

Povprečno število delcev na en trk je označeno s C in kostanta detektorja z A_{pc}. Ta način merjenja je uporabljen redkeje, saj zahteva dosti bolj kompleksen detektor.

10.4 Veliki hadronski trkalnik

V velikem hadronskem trkalniku je luminoznost pogojena z lastnostmi protonskih gruč, zato je na mestu nekaj besed o samem trkalniku. LHC pospešuje in vodi delce z električnimi ($\vec{E}$) oz. magnetnimi ($\vec{B}$) polji. Osnovna načela in pregled optike curka delcev je opisan v [BO66]. Gibanje posameznega delca z nabojem e, gibalno količino $\vec{p}$ in hitrostjo $\vec{v}$ opisuje enačba:

$$\frac{d\vec{p}}{dt} = e\left(\vec{E} + \vec{v} \times \vec{B}\right). \tag{10.7}$$

LHC je krožen trkalnik, ki uporablja magnetno polje za ukrivljenje poti delcev ter električno polje za njihovo pospeševanje. Delce pospešuje v dveh ločenih tirnicah, v nasprotnih smereh. Ti tirnici se na štirih mestih križata. Ta križišča so interakcijske točke, kjer prikaja do trkov protonov, in okoli katerih so zgrajeni detektorji. Glavna prednost takšnega krožnega trkalnika

je postopno pospeševanje delcev. Delci krožijo v trkalniku in pridobijo vsak krog le del energije, kar se lahko ponavlja in tako postopoma veča njihovo kinetično energijo. Ta je tako omejena le z magneti, ki morajo biti vedno močnejši, čim večja je energija delcev, da jih obdržijo v krogu.

Za pospeševanje je odgovorna RF komora, ki z vzbujenimi radio-frekvenčnimi valovi pospešuje delce. Ti se v ravnovesnem stanju lahko obdržijo le med posameznimi vali. Curek tako ni zvezen, temveč se razdeli na gruče[2]. Da ima detektor med trki dovolj časa za obdelavo signalov je polno le vsako deseto mesto, kar da 3564 možnih gruč v vsakem izmed obeh curkov LHC-ja.

Za luminoznost je pomembna tudi porazdelitev delcev v ravnini pravokotni na smer potovanja gruče (ρ v enačni 10.4). Ta je definirana s kakovostjo izvora delcev in magnetnim poljem, ki ukrivlja njihov tir v trkalniku. V ta namen se uporabljajo kvadrupolni magneti. Zadnji magnet pred interakcijsko točko poskrbi tudi, da gručo protonov stisne, ji tako poveča gostoto ter posledično poveča tudi verjetnost za interakcijo s protoni nasproti leteče gruče.

Curek protonov se tako v interakcijski toči doliči z dvema parametroma: β^* in ε_N, ki opisujeta kako močno se gruča stisne pred trkom ter njeno prečno strukturo. S tem se lahko izrazi luminoznost (izpeljava je v prilogi B):

$$L_{bb} = \frac{N_1 N_2 f_{rev} \gamma}{4\pi \varepsilon_n \beta^*}. \tag{10.8}$$

10.4.1 LHC in luminoznost

Z lastnostmi curka in s številom možnih gruč je omejena največja možna luminoznost trkalnika. Ta vrednost pa ni edina, ki vpljiva na količino dejansko posnetih podatkov. Eden izmed pomembnih konceptov je *polnilna shema*. Ta določa katere gruče bodo prisotne in katere ne. Upoštevati je treba postopek polnjenja in praznjenja trkalnika. Za to potrebni magneti zahtevajo končen čas za doseg pravilnega magnetnega polja in med vklapljanjem/izklapljanjem ne sme biti prisotnih gruč. Tako je izmed 3564 možnih mest lahko v optimalnem primeru zapolnjenih le 2808. Omeniti je potrebno tudi, da si oba curka delita pot skozi detektor. Če je v curku več kot 156 gruč, se v tem deljenem območju hkrati sreča več kot le en par gruč. Tako bi lahko nastalo več dodatnih neželjenih interakcijskih točk, čemur pa se izogne s premikom curkov tako, da se križata pod majhnim kotom. To pomeni, da tudi gruče trčijo pod tem kotom, kar zmanjša luminoznost za ustrezen geometrijski faktor.

Dodatno je potrebno upoštevati tudi čas, ki je potreben za izbor podatkov, ki se bodo posneli. Za grob izbor je potrebno nekaj deset nanosekund, kar pomeni, da nekaj trkov za izbranim ni možno posneti. To povzroči, da se količina posnetih podatkov ne veča premo sorazmerno z luminoznostjo.

Nazadnje je tukaj potrebno omeniti še izgube. Največji prispevek k manjšanju števila protonov v gručah (vendar zdaleč ne edini) so interakcije, torej luminoznost sama. Upadanje števila protonov pomeni, da so gruče vedno bolj redke in trki gruč dajo vedno manj interakcij med protoni. V določenem trenutku, ko sta curka dovolj oslabljena, je tako najbolje ta curka zavreči in napolniti trkalnik z novima. Optimalen čas je odvisen od izgub in časa, potrebnega, da

[2]Ena gruča je skupek protonov med dvema zaporednima valoma.

se LHC ponovno napolni s protonskimi gručami. Če sta za to potrebni dve uri in je življenjska doba žarka zaradi izgub $14\,\mathrm{h}$, potem je optimalo trkati gruče le $\sim 7\,\mathrm{h}$. To pomeni, da je možno snemati podatke $\sim 80\%$ časa delovanja trkalnika, kar postavlja dodatno omejitev na količino zbranih podatkov.

10.5 Spektrometer ATLAS

Detektor ATLAS je podrobneje opisan v [R199], [R299] in [AT08]. Je spektrometer, namenjen študiju širokega nabora fizikalnih procesov. Je oblike valja, in meri $44\,\mathrm{m}$ v dolžino in $25\,\mathrm{m}$ v višino (premer valja). Protonska curka potujeta po osi valja in trkata v geometrijski sredini. Od znotraj navzven si sledijo naslednji sestavni deli:

Notranji detektor iz ukrivljenosti poti nabitih delcev v magnetnem polju meri njihovo gibalno količino in pomaga pri prepoznavanju elektronov.

Kalorimetri merijo energijo. Ločeni so v dva sklopa, od katerih prvi meri energijo elektronov in fotonov, drugi energijo hadronov.

Mionski sistem v magnetnem polju velikega toroida meri gibalno količino mionov.

Gruče v detektorju trkajo z največjo pogostostjo $40\,\mathrm{MHz}$ in za vsak trk celoten detektor shrani vse merjene podatke v pomnilnik. Teh je veliko preveč za trajno shranjevanje, zato je za eksperiment bistvenega pomena izbor podatkov. Ker je končna pogostost snemanja omejena na $\sim 200\,\mathrm{Hz}$, je potrebno, da prožilni sistem, ki je za to odgovoren, izbere en zanimiv trk protonov izmed več kot milijona zaznanih. To opravi v treh zaporednih stopnjah in tako postopoma zmanjšuje pogostost zanimivih trkov od $40\,\mathrm{MHz}$ na $75\,\mathrm{kHz}$, do končnih $200\,\mathrm{Hz}$. Izbrani podatki se trajno zapišejo in so dostopni fizikom za njihove meritve. Velika količina podatkov postavi tudi ostre zahteve za prenos in obdelavo podatkov. S tem namenom je bil razvit namenski računalniški model, ki je natančneje opisan v [CR05].

10.5.1 ATLAS in luminoznost

Luminoznost para gruč se lahko izrazi iz enačbe 10.2:

$$L = \frac{R}{\sigma} = \frac{\langle \mu \rangle \, f_{rev}}{\sigma}. \tag{10.9}$$

Za drug enačaj je bila izmerjena pogostost R izražena kot produkt frekvence, s katero kroži gruča in povprečne vrednosti števila trkov pri posameznem trku gruče $\langle \mu \rangle$. Slednja predstavlja povprečno število interakcij pri enem trku dveh gruč. To je torej lastnost gruče in z merjenjem količine $\langle \mu \rangle / \sigma$ se lahko določi luminoznost. Samostojna meritev količine $\langle \mu \rangle$ ni smiselna, saj bi bilo zanjo potrebno poznati izkoristek detektorja ε. Prav tako bi se bilo dobro izogniti dodatni meritvi celotnega sipalnega preseka σ. V ta namen sta definirani: *vidno povprečno*

število interakcij μ_{vis} in *vidni presek* σ_{vis}:

$$\mu_{vis} = \langle \mu \rangle \, \varepsilon \tag{10.10a}$$

$$\sigma_{vis} = \sigma\varepsilon. \tag{10.10b}$$

S tem se luminoznost izrazi kot:

$$L = \frac{\langle \mu \rangle \, f_{rev}}{\sigma} = \frac{\langle \mu \rangle \, \varepsilon f_{rev}}{\sigma\varepsilon} = \frac{\mu_{vis} f_{rev}}{\sigma_{vis}}. \tag{10.11}$$

μ_{vis} je neposredno merljiv, neznan pa ostane viden presek σ_{vis}. Ta predstavlja umeritveno konstanto.

Prva ocena umeritvenih konstant je bila dobljena iz Monte Carlo simulacije [AL10]. Njena natančnost je bila ocenjena na $\sim 20\%$, kjer največji delež doprinese nezanesljivost modeliranja različnih komponent sipalnega preseka. Večja natančnost je bila dosežena s postopkom van der Meera. Do oktobra 2011 je bilo opravljenih 7 takšnih meritev, s katerimi je bil umerjen tudi sistem BCM, kar bo natančneje opisano. S to metodo je moč zmanjšati sistematsko napako na nekaj odstotkov.

Opisan pristop je skupen vsem detektorjem, ki merijo luminoznost s pomočjo štetja dogodkov. Tega načina se trenutno v ATLAS-u poslužujemo vsi sistemi z izjemo elektromagnetnega kalorimetra. Ta meri luminoznost s pomočjo ionizacijskega toka. Za dosego željene natančnosti je zato potrebno meriti tok v daljšem časovnem oknu, torej povprečje po veliko dogodkih. Preostali detektorji imajo vsi zadostno časovno ločljivost, da razločijo posamezne trke gruč. Vsi ti sistemi temeljijo na različnih načinih delovanja, od ionizacije, do scintilacij, ter meritev Čerenkove svetlobe. To daje detektorju ATLAS velik nabor neodvisnih meritev, kar omogoči neprestano preverjanje njihovih skladnosti in dosego optimalne natančnosti meritev.

Informacije iz vseh teh sistemov morajo biti obdelane na enoten način. V ta namen je bila znotraj detektorja ATLAS razvita samostojna infrastruktura za obdelavo podatkov. Predpostavlja se, da je luminoznost konstantna znotraj majhnih časovnih oken imenovanih *blok luminoznosti* (angleško Luminosity Block, okrajšano z LB). Celoten čas snemanja podatkov je tako razdeljen na kopico blokov luminoznosti, za vsakega izmed teh pa je v podatkovni bazi zapisana izmerjena luminoznost vseh detektorjev. Teh meritev se je možno poslužiti kasneje pri študiju fizikalnih procesov.

Različni detektorji ponujajo različne meritve. Nekateri posredujejo meritve luminoznosti za vsako gručo posebaj, nekateri pa le vsoto po vseh gručah v LHC curku. Vse te meritve obdela *Kalkulator lumnoznosti*, ki je osrednja enota obdelave podatkov o luminoznosti (glej sliko 10.1). Ta poenoti vse zapise meritev, ter izračuna luminoznost iz surovih podatkov dobljenih iz detektorjev. Končno meritev posreduje bazi podatkov, nadzornim sistemom v kontrolni sobi spektrometra ATLAS, ter kot povratno informacijo tudi samemu trkalniku.

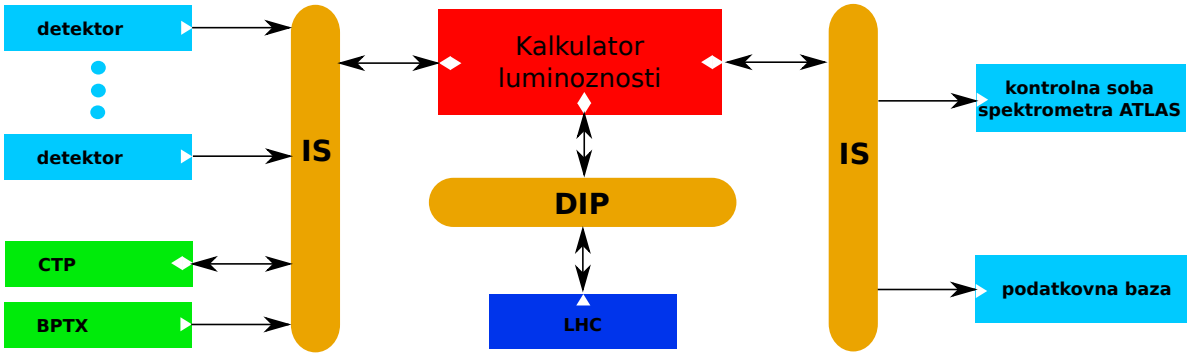

Slika 10.1: *Shema obdelave podatkov o luminoznosti v spektrometru ATLAS. CTP je osrednji procesor prožilnega sistema in določa meje blokov luminoznosti. Dodatni podatek o tem, katere gruče je potrebno vključiti v meritev luminoznosti, prispeva sistem BPTX. IS in DIP predstavljata dva različna protokola za izmenjavo podatkov. IS prevladuje znotraj spektrometra ATLAS, medtem ko se DIP uporablja za izmenjavo informacij s trkalnikom.*

10.6 Sistem za spremljanje kakovosti curka protonov

Eden izmed detektorjev luminoznoti je tudi sistem za spremljanje kakovosti curka protonov [B+08] (angleško Beam Conditions Monitor, okrajšano BCM). Celotna energija curka protonov je že koncem leta 2010 dosegla energijo približno $115\,\mathrm{MJ}$. V primeru, da se v obliki ionizacije, le majhen del te energije nenadzorovano odloži v notranjem delu detektorja, bi ga lahko poškodoval. Da bi se preprečila morebitna nesreča, so bili razviti varnostni sistemi, tako v samem trkalniku, kot tudi v spektrometrih. V ATLAS-u je ta naloga dodeljena detektorju BCM. Kljub temu, da ohranja svoj prvotni namen, je bil BCM razširjen z dodatnimi možnostmi. Ena izmed teh je tudi meritev luminoznosti.

BCM je bil razvit z namenom optimalnega ločevanja med signalom, ki je posledica trkov protonov, in ozadjem. Bistvena razlika med tema dvema prispevkoma je točka nastanka delcev, ki so zaznani v detektorju. V primeru trkov protonov ti delci nastanejo v središču detektorja, medtem ko večina ozadja nastane v trkalniku izven detektorja. Za razločevanje detektor BCM uporablja meritev časa preleta. Dva dela detektorja sta postavljena simetrično, $184\,\mathrm{cm}$ od interakcijske točke, vsak na svoji strani detektorja (glej sliko 10.2). Ti dve strani sta tako kot v spektrometru ATLAS poimenovani stran A in stran C. BCM beleži čas, ko je bil delec zaznan v enem izmed senzorjev. Razlika tako zabeleženih časov v obeh delih detektorja je enaka 0, če so delci nastali v interakcijski točki, oziroma $12.5\,\mathrm{ns}$, če so nastali izven detektorja ATLAS. Tako lahko z dobro časovno ločljivostjo ločimo med signalom trkov protonov in ozadjem.

Detektor je sestavljen iz osmih modulov, po štirih na vsaki strani interakcijske točke. Kot senzorji so uporabljeni $500\,\mu\mathrm{m}$ debeli polikristalinični diamanti kvadratne oblike (velikosti $10\,\mathrm{mm} \times 10\,\mathrm{mm}$). Upravljalna napetost $1000\,\mathrm{V}$ pobere naboj ustvarjen ob preletu delca. Ta signal se nato ojači v dveh stopnjah in prevede v digitalno obliko. Celotna izvedba omogoči električne signale tipične širine $\sim 2\,\mathrm{ns}$, kar je več kot odlično za razlikovanje med trki protonov in ozadjem. Štirje moduli, nameščeni na podporno strukturo vakuumske cevi, po kateri potujeta

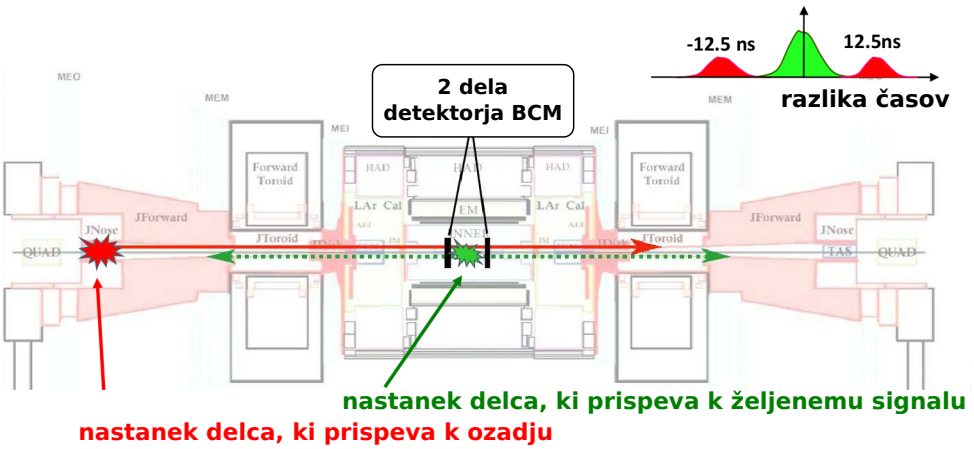

Slika 10.2: *Položaj detektorja BCM znotraj spektrometra ATLAS. Rdeče oznake nakazujejo primer delca, ki predstavlja ozadje k meritvi. Zelene predstavljajo delce, ki nastanejo v interakcijski točki in prispevajo k željenemu signalu. Histogram zgoraj desno nakazuje porazdelitev meritev razlike časa, zaznanega v obeh delih detektorja. Razvidno je, da se lahko z meritvijo časa ločuje ozadje od željenega signala.*

curka protonov, so razvidni na sliki 10.3.

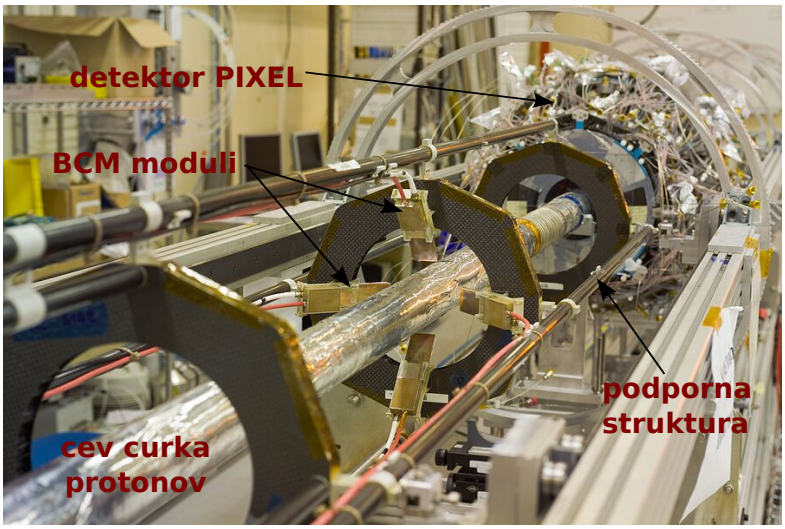

Slika 10.3: *Polovica modulov detektorja BCM, pritrjenih na nosilno strukturo. Razvidna je tudi cev, po kateri je speljan curek protonov, ter detektor PIXEL, ki meri smer nabitih delcev.*

Signal iz vsakega izmed modulov se pred digitalizacijo razcepi na dva dela, katerih amplituda je bila v razmerju $1 : 5$. V želji, da bi BCM pokrival večje dinamično območje, je bilo to razmerje v začetku leta 2011 spremenjeno in sedaj znaša približno $1 : 200$. Z delitvijo signalov je tako mogoče digitalizirati podatke z dvema nivojema proženja. Vsak modul tako

nudi *kanal z nizkim nivojem proženja* in *kanal z visokim nivojem proženja*. Kanali visokega nivoja proženja so idealni za varnostni sistem. Tukaj ni potrebno zaznati posameznih delcev, in je le večja številčnost delcev vredna pozornosti. V nasprotju pa so kanali nizkega nivoja proženja zmožni zaznati posamezne delce, kar se izkoristiti za meritve luminoznosti.

10.6.1 Merjenje luminoznosti

BCM ima svojih osem detektorskih modulov nameščenih tako, da so štirje v skupni vodoravni ravnini, metem ko so preostali štirje v skupni navpični ravnini. Signali iz detektorjev so razdeljeni med dve procesni enoti. Ti dve enoti popolnoma neodvisno obdelujeta podatke. Ena izmed enot obdeluje informacije kanalov nizkega proženja iz modulov, ki so nameščeni v vodoravni ravnini, ter informacije kanalov visokega proženja iz modulov nameščenih v navpični ravnini. Ta procesna enota podaja podatke o luminoznosti, ki so bili poimenovani *BCM-Vodoravna luminoznost*. Druga procesna enota pa podaja meritev, poimenovano *BCM-Navpična luminoznost*. BCM torej nudi dve neodvisni meritvi luminoznosti.

Sam način merjenja temelji na štetju dogodkov. Tukaj je veliko svobode, saj lahko definiramo poljubne algoritme luminoznosti. Za detektor so bili izbrani štirje takšni algoritmi, ki definirajo štiri hkratne meritve znotraj vsake izmed obeh procesnih enot. Izbor je:

algoritem OR šteje dogodke, ko je bilo zaznano v BCM-ju karkoli. Upoštevajo se le signali, ki so bili zaznani v časovnem oknu širokem $12.5\,\mathrm{ns}$. Ta tip dogodkov je seveda najpogostejši, kar pomeni majhno statistično napako. Njegova glavna slabost pa je velika dojemljivost za šum in ozadje, ter nasičenje pri cečjih vrednostih luminoznosti.

algoritem AND ima izboljšano odpornost proti neželjenim signalom. Zahteva namreč, da mora dogodek vsebovati signale tako iz A, kot tudi iz C strani detektorja. Upoštevajo se le signali, ki so bili zaznani v časovnem oknu širokem $12.5\,\mathrm{ns}$. Verjetnost, da šum povzroči dogodek tipa AND je tako zelo zmanjšana. Vendar to povzroči tudi manjši izkoristek za signale, ki so posledica protonskih interakcij, kar pomeni manjšo statistiko. To je največja slabost tega algoritma.

algoritem XOR-C zahteva, da so bili v dogodku zaznani signali le na C strani detektorja. Upoštevajo se le signali, ki so bili zaznani v časovnem oknu širokem $12.5\,\mathrm{ns}$. Takšna zahteva zapostavlja ozadje, ki prihaja iz strani C. Verjetnost, da se zazna na strani C je zanj majša kot za ozadje, ki prihaja iz strani A (za enostransko ozadje je bolj dojemljiva nasprotna stran detektorja). Tak algoritem omogoči oceno ozadja in njegovega vpliva na meritev luminoznosti.

algoritem AND25 postavlja isti pogoj kot algoritem AND, vendar upošteva vse signale znotraj časovnega okna $25\,\mathrm{ns}$, ki pripada enemu trku gruč. Prejšnji algoritmi imajo ožje časovno okno, postavljeno tako, da vključuje čas, ko se zaznajo produkti protonskih interakcij. Ne vključuje pa časa, ko se pričakuje del ozadja. Ta del ozadja je tako izključen iz algoritma AND in vključen v algoritem AND25, kar omogoči oceno njegovega vpljiva na meritev luminoznosti.

Omeniti je potrebno še algoritem XOR-A, ki bi izbiral le dogodke s signali izključno na detektorski strani A. Ta se ne meri, saj ga je možno izračunati. Vsota števila dogodkov vrst XOR-A, XOR-C in AND mora biti namreč po definiciji enaka številu dogodkov vrste OR.

Evidenca števcev različnih vrst dogodkov se nahaja znotraj procesnih enot. Procesna enota poveča ustrezni števec za ena ob vsakem trku gruče. Tabela teh števcev za vse gruče se imenuje *tabela luminoznosti*. Tako imata obe procesni enoti po štiri takšne tabele. Te se preko računalniške mreže prenesejo na osebni računalnik vsake $0.8\,\mathrm{s}$. Ta sešteva iste števce iz zaporednih tabel, ki jih dobi znotraj trajanja bloka luminoznosti. Ko je tega bloka konec, sporoči vsoto (za vsako gručo posebej) preko komunikacijskega protokola IS Kalkulatorju luminoznosti. Hkrati, vsake $0.8\,\mathrm{s}$, se Kalkulatorju luminoznosti sporoči tudi vsota vseh števcev v prebrani tabeli luminoznosti. To omogoča hiter nadzor nad luminoznostjo, ki je predvsem v pomoč pri optimizaciji nastavitev trkalnika.

Tako dobljeni podatki se preko Kalkulatorja luminoznosti shranjujejo v uradni bazi podatkov spektrometra ATLAS. Hkrati se ti podatki tudi zapisujejo v zasebne BCM datoteke. Prav ta podatkovni tok je uporabljen v obdelavi podatkov, ki sledi. Vanj se namreč zapisujejo najpodrobnejši podatki in vsebuje merjene podatke za vse štiri algoritme luminoznosti za obe procesni enoti.

10.7 BCM odziv na luminoznost in simulacija

Čeprav za razlago končnih meritev ni uporabljena nobena vrednost, ocenjena z Monte Carlo simulacijo, se je simulacija izkazala za bistven pripomoček med snovanjem detektorja. Dala je potrditev načina merjenja ter ponudila začetno oceno umeritvenih konstant.

Simulacija je pomagala razumeti bistven del meritve – zvezo med luminoznostjo in izmerjenimi verjetnostmi za različne vrste dogodkov, ki jih poda BCM. Kadar se uporablja štetje dogodkov, se namreč luminoznost, ki je definirana na območju $[0, \infty)$ preslika v verjetnost, da zaznamo določeno vrsto dogodka, torej v območje $[0, 1]$. Zveza med obema količinama očitno ni premo sorazmerna, jo pa je moč izraziti v analitični obliki. Naj bodo verjetnosti za dogodke vrst OR, XOR-A, XOR-C in AND pri trku enega para protonov označene z ε_{OR}, ε_{XOR-A}, ε_{XOR-C} in z ε_{AND}. To so parametri sistema, s katerimi se lahko izrazijo pričakovane verjetnosti r_A, kjer A predstavlja poljuben algoritem luminoznosti. Postopna izpeljava je podana v dodatku C, končni izrazi pa so:

$$r_{OR} = 1 - e^{-\langle\mu\rangle\varepsilon_{OR}} \tag{10.12a}$$

$$r_{XOR} = e^{-\langle\mu\rangle\varepsilon_{OR}} \left(e^{\langle\mu\rangle\varepsilon_{XOR}} - 1\right) \tag{10.12b}$$

$$r_{AND} = 1 - e^{-\langle\mu\rangle\varepsilon_{OR}} \left(e^{\langle\mu\rangle\varepsilon_{XOR-C}} + e^{\langle\mu\rangle\varepsilon_{XOR-A}} - 1\right) \tag{10.12c}$$

Edina predpostavka je neodvisnost interakcij med protonskimi pari. To pomeni, da je število interakcij pri trku gruč porazdeljeno po Poissonovi porazdelitvi, ter se jih opiše z že znano količino $\langle\mu\rangle$. Monte Carlo ocena verjetnosti r_A je prikazana na sliki 10.4.

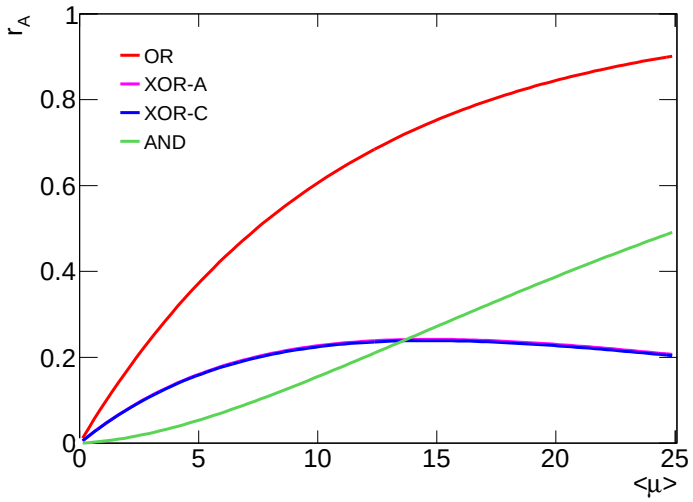

Slika 10.4: *Monte Carlo ocena pogostosti dogodkov, ki ustrezajo različnim algoritmom luminoznosti. Vrednost* $< \mu >= 25$ *približno ustreza največji luminoznosti, ki bi jo naj sčasoma dosegel trkalnik LHC (*$10^{34}\,\mathrm{cm}^{-2}\mathrm{s}^{-1}$*).*

10.7.1 μ-popravki

Procesni enoti BCM-ja podata število preštetih dogodkov N_A in število prehodov gruč N_E. Z njima se izračuna:

$$r_A = \frac{N_A}{N_E}. \tag{10.13}$$

Ta količina je torej izmerjena in cilj je iz enačb 10.12 izraziti $\langle\mu\rangle$, ki bo razkril luminoznost. Obrate teh enačb je mogoče izraziti analitično. Postopna izpeljava je podana v dodatku D. V namen krajšega zapisa se označi $r_0 = 1 - r_{OR}$ in vidno število interakcij za različne algoritme luminoznosti so:

OR algoritem je najpreprostejši:

$$\mu_{OR}^{vis} = -\ln\left[r_0\right], \tag{10.14}$$

XOR algorithma sta oba opisana z:

$$\mu_{XOR}^{vis} = \ln\left[1 + \frac{r_{XOR}}{r_0}\right]. \tag{10.15}$$

Razvidno je, da potrebujemo tako OR, kot XOR meritev, da se določi vidno število interakcij za algoritem luminoznosti XOR.

AND algoritem uporablja izraz:

$$\mu_{AND}^{vis} = \ln\left[\frac{r_0}{\frac{r_0}{r_0+r_{XOR-A}} + \frac{r_0}{r_0+r_{XOR-C}}}\right]. \tag{10.16}$$

V dodatku D so podane tudi ocene za nezanesljivost količin μ_A^{vis}. Tukaj je potrebno poudariti, da so r_{OR}, r_{XOR-A}, r_{XOR-C} in r_{AND} medsebojno korelirani in bi morale biti njihove vrednosti pri večkratnem merjenju porazdeljene v skladu z multinomsko porazdelitvijo. Ta podaja tudi korelacije med temi količinami, ki jih je potrebno upoštevati pri oceni napak.

Če so poznane umeritvene konstante σ_A^{vis}, se s tako določenimi μ_A^{vis} lahko izračuna luminoznost z enačbo 10.11.

10.7.2 Simulacija detektorja BCM

Simulacija detektorja BCM je bila opravljena v računalniškem okolju ATHENA, ki je skupaj z celotno arhitekturo obdelave simuliranih podatkov podrobneje opisano v [CR05]. Okvirni potek simulacije bi lahko opisali s koraki:

- naključen izbor procesov, ki se lahko dogodijo med trkom dveh protonov;
- sledenje nastalim produktom med njihovo potjo skozi spektrometer ATLAS in napovedovanje sledi, ki jih pustijo v različnih detektorjih;
- digitalizacija nastalih sledi, ki napove končen odziv detektorja.

Simulacija se izvaja za celoten spektrometer hkrati in del te simulacije je tudi BCM. Da se je lahko enakopravno vključil v celoten proces simulacije je bilo potrebno ustvariti nekaj programske kode, ki:

- opiše geometrijo detektorja in lastnosti materialov, ki so uporabljeni;
- obravnava potovanje delcev skozi diamantni senzor;
- digitalizira njegov odziv na delce, ki so ga preleteli in v detektorju pustili nekaj energije.

Funkcionalne podrobnosti vseh teh korakov simulacije so izčrpno opisane v razdelku 6.3.2 in jim tukaj ne bo posvečeno več pozornosti. Bistvenega pomena je le to, da je končen rezultat simulacije oblikovno enak merjenim podatkom, kar da simulaciji veliko napovedno vrednost.

10.7.3 Napoved izkoristkov pri meritvah luminoznosti

Glaven cilj simulacije je bil napovedati izkoristek detektorja pri meritvah luminoznosti, oziroma določitev umeritvenih konstant σ_A^{vis}. Pri simuliranju posameznih interakcij med dvema protonoma se je upoštevala Poissonova porazdelitev teh interakcij pri večkratnem trkanju gruč. Skladno s to porazdelitvijo je pri dani luminoznosti (danem $\langle\mu\rangle$) naključno izbrano število interakcij. Izbrano število interakcij je bilo vzetih iz simuliranega vzorca in naloženih 'druga čez drugo', s čimer se je simuliralo več hkratnih interakcij. Digitalizirani podatki so razkrili kateremu izmed algoritmov luminoznosti pripada tak dogodek in ustrezno število se poveča za ena. Ta postopek se ponavlja čimvečkrat za izbrano vrednost $\langle\mu\rangle$, čemur sledijo ponovitve za drugače izbrane vrednosti. Ocenjene so bile vrednosti r_A za $\langle\mu\rangle$ je 0.2, 0.4, 0.6, 0.8, 1, 2, 4, 6, 8, 10, 12, 14, 16, 18, 20, 22, in 25. Z dobljenimi r_A se je rokovalo kot z izmerjenimi podatki,

torej opravljeni so bili μ-popravki. Odvisnost tako dobljenih μ_A^{vis} od znanega parametra $\langle\mu\rangle$ je prikazana na sliki 10.5. Črte na sliki prikazujejo prilagojene linearne funkcije na simulirane podatke. Njihova strmina je enaka izkoristku za posamezne meritve luminoznosti. Ti izkoristki so bili ocenjeni na: $9.32\% \pm 0.04\%$ v primeru algoritma OR, $4.55\% \pm 0.02\%$ v primeru algoritma XOR-A, $4.51\% \pm 0.02\%$ v primeru algoritma XOR-C, ter $0.27\% \pm 0.02\%$ v primeru algoritma AND.

Iz simulacije je bilo ocenjenih tudi nekaj drugih lastnosti, ki so bile pomembne predvsem za ocenitev sistematskih napak simulacije in končnih meritev:

- iz simulacije je razvidno, da je več kot polovica delcev, zaznanih v detektorju BCM, sekundarnih delcev. To so delci, ki ne nastanejo ob interakciji protonov (primarni delci), ampak kot posledica interakcij primarnih delcev z materialom v detektorju. To nakazuje, da je razumevanje porazdelitve materiala v detektorju ključnega pomena za simulacijo.

- ocenjen je bil trend spreminjanja izkoristkov za algoritme luminoznosti v odvisnosti od nivoja proženja. Ta podatek je uporabljen pri študiju možne negotovosti meritev luminoznosti zaradi nihanj nivoja proženja.

- ocenjeno je bilo, da je v primeru algoritma OR približno 1% luminoznosti opažen v časovnem intervalu, ki pripada naslednji gruči protonov. Razlog so zakasneli delci. Pojav je dvakrat manjši v primeru XOR algoritmov, ter neopazen v primeru algoritma AND.

Celotna simulacija je tako potrdila pravilnost celotnega postopka merjenja in podala tudi ocene za njeno natančnost. Te ocene je potrebno razumeti kot dokaj okvirne, saj je bila nezanesljivost Monte Carlo metode ocenjena na $\sim 20\%$.

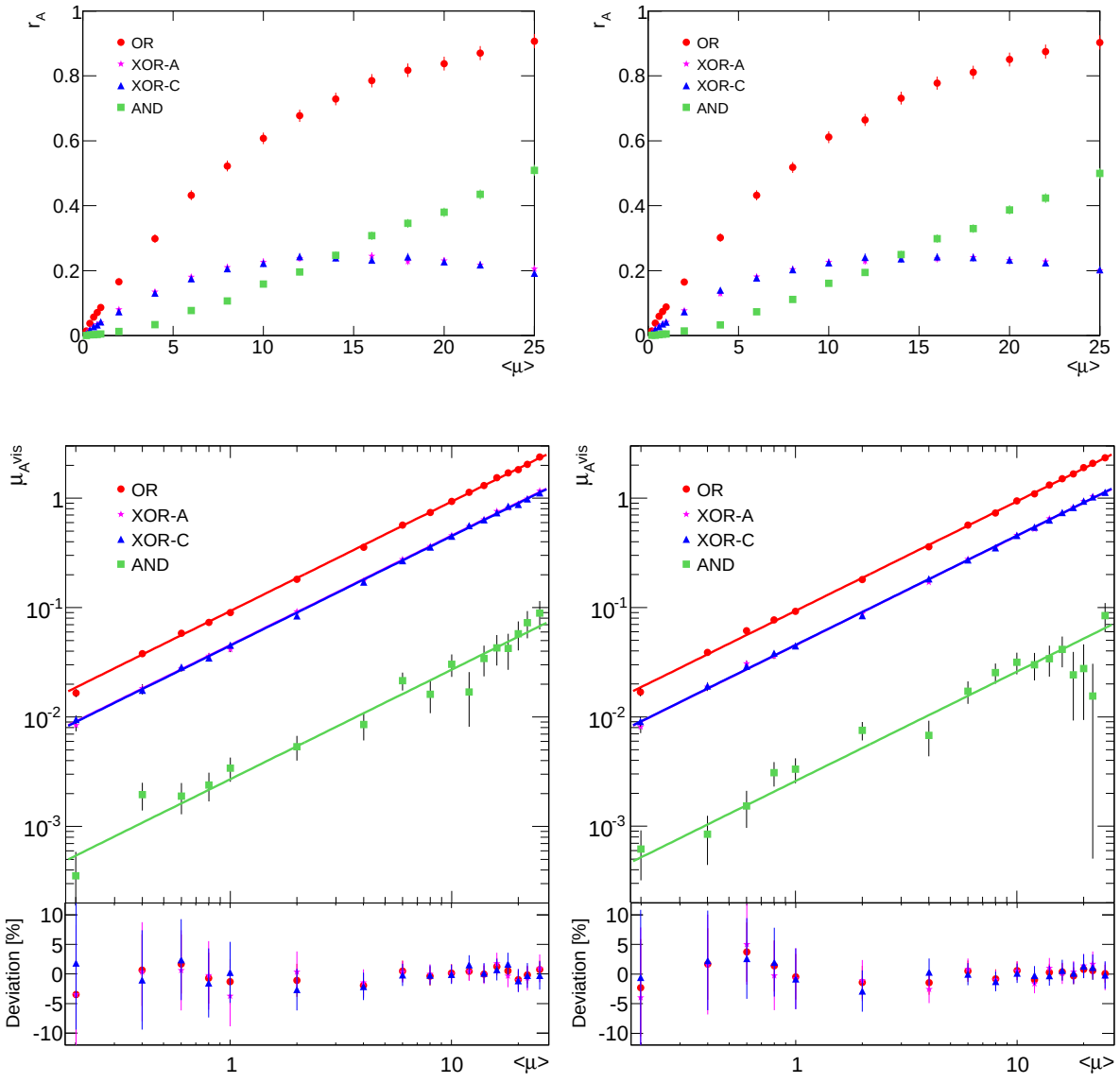

Slika 10.5: *Simulirane verjetnosti za dogodke r_A, ki ustrezajo različnim algoritmom luminoznosti (zgoraj), ter vidno povprečno število interakcij na trk gruč (spodaj). Leva grafa prikazujeta napoved za BCM-Navpično meritev luminoznosti, medtem ko desna grafa prikazujeta napoved za BCM-Vodoravno meritev luminoznosti. Prikazana so tudi odstopanja simuliranih podatkov od prilagojenih krivulj, razen za algoritem AND.*

10.8 Umerjanje detektorja BCM za meritve luminoznosti

Za uporabo meritev luminoznosti v fizikalnih analizah je protrebno določiti umeritvene konstante in s tem luminoznost natančneje, kot to zmore simulacija. V ta nemen so bile opravljene posebne meritve imenovane postopki Van der Meera. Cilj teh je izmeriti lastnosti žarka tako, da lahko z enačbo 10.4 izračunamo luminoznost. To vrednost se primerja s hkrati izmerjenimi μ_A^{vis} in sorazmernostni faktorji so vidni preseki za različne algoritme σ_A^{vis}.

10.8.1 Postopek van der Meera

Postopek van der Meera (vdM) poteka tako, da postopoma razmikamo curka v ravnini, pravokotni na njuno smer. Razmak označimo z δ. Curka se razmikata korakoma. Kadar ju magneti premikajo, se merjenje opusti in se nadaljuje zgolj v intervalih, ko sta curka na miru. Temu sledi ponoven premik in ponovno merjenje pri novem razmiku. Meri se lahko katerokoli količino, ki je premo sorazmerna z luminoznostjo. V namen splošnosti enačb je ta označena z $R(\delta)$. V primeru detektorja BCM temu ustreza vidno število interakcij μ_A^{vis}. Postopek je potrebno ponoviti dvakrat, v obeh smereh, pravokotnih na smer curka. Značilna meritev je prikazana na sliki 10.6. Če se omeji na smer x, potem je najbolje definirati *efektivno širino curka* Σ_x:

$$\Sigma_x\left(\rho_1,\rho_2\right) = \frac{1}{\sqrt{2\pi}}\frac{\int R_x(\delta)\,d\delta}{R_x(0)}. \tag{10.17}$$

S prilagajanjem izbranega nastavka se tako lahko določi maksimalno vidno število interakcij $\mu^{vis,peak}$ ter integral pod krivuljo. Torej tudi Σ_x. Enak postopek se ponovi tudi v smeri y in z dobljenima Σ_x in Σ_y se lahko izračuna luminoznost kot:

$$L = \frac{f_{rev}N_1N_2}{2\pi\Sigma_x\Sigma_y}. \tag{10.18}$$

Primerjava te enačbe z enačbo 10.11 razkrije umeritvene konstante:

$$\sigma_A^{vis} = 2\pi\Sigma_x\Sigma_y\frac{\mu_A^{vis,peak}}{N_1N_2}, \tag{10.19}$$

Tukaj je potrebno poudariti glavno prednost tega umeritvenega postopka: ne zahteva ne poznavanja izkoristka detektorja in ne celotnega preseka za sipanje protonov! Njegova pomanjkljivost pa je potreba po posebnem upravljanju s curki, kar ni primerno za običajno snemanje podatkov in se torej lahko ta postopek kalibracije uporablja le izjemoma.

10.8.2 Analiza podatkov in rezultati

Disertacija predstavlja rezultat štirih izmed osmih opravljenih meritev van der Meera. Meritvi označeni kot *vdM-IV* in *vdM-V* sta bili opravljeni oktobra 2010 in sta umerili detektor za isto leto. Sprememba razmerja amplitud signala po delitvi med kanaloma nizkega in visokega proženja v začetku leta 2011 je spremenila izkoristek detektorja. Tako je bilo potrebno ponovno

umerjanje. To je bilo ponovno izvedeno z dvema meritvama: *vdM-VII* in *vdM-VIII*, in sicer maja 2011. Oba sklopa meritev se najbolj razlikujeta po številu gruč, ki so bile v trkalniku. Oktobra jih je znotraj spektrometra ATLAS trkalo 6, medtem ko jih je maja trkalo 14.

Za vsako meritev sta bila opravljena postopka v smeri x in y, iz česar sta bila določeni vrednosti Σ_x in Σ_y. Ti sta bili dobljeni kot parametri prilagajanja krivulj na merjene podatke. Pri obdelavi podatkov oktobra 2010 je bila prilagajana vsota dveh Gausovih funkcij in konstante, ki je opisovala ozadje meritev. Izjema je le algoritem AND, za katerega je zadostovala le ena Gausova funkcija brez kakršnega koli ozadja. To nakazuje čistost algoritma AND, ki je posledica njegove velike izbirčnosti. Za opis podatkov maja 2011 je bila potrebna le ena Gausova funkcija s konstantnim ozadjem, ki je bilo ponovno izvzeto iz prilagajanja na podatke algoritma AND.

S prilagajanji so tako bile določene količine, potrebne za izračun vidnega sipalnega preseka. Kot primer so na sliki 10.7 prikazane te umeritvene konstante za algoritem OR, za oba sklopa meritev.

Vrednosti vidnih sipalnih presekov so za BCM-Navpično in BCM-Vodoravno meritev luminoznosti zbrane v tabeli 10.1 in tabeli 10.2.

algoritem	Vidni sipalni presek [mb]			
	BCM-Navpično		BCM-Vodoravno	
	vdM-IV	vdM-V	vdM-IV	vdM-V
OR	4.573 ± 0.007	4.569 ± 0.006	4.599 ± 0.007	4.589 ± 0.006
XOR-A	2.193 ± 0.005	2.185 ± 0.004	2.196 ± 0.005	2.193 ± 0.004
XOR-C	2.240 ± 0.005	2.249 ± 0.004	2.267 ± 0.005	2.264 ± 0.004
AND	0.132 ± 0.001	0.131 ± 0.001	0.132 ± 0.001	0.132 ± 0.001

Tabela 10.1: *Umeritvene konstante za leto 2010 za vse štiri algoritme luminoznosti.*

algoritem	Vidni sipalni presek [mb]			
	BCM-Navpično		BCM-Vodoravno	
	vdM-VII	vdM-VIII	vdM-VII	vdM-VIII
OR	4.709 ± 0.002	4.729 ± 0.002	4.662 ± 0.002	4.681 ± 0.002
XOR-A	2.286 ± 0.002	2.295 ± 0.002	2.251 ± 0.002	2.261 ± 0.002
XOR-C	2.282 ± 0.002	2.293 ± 0.002	2.275 ± 0.002	2.283 ± 0.002
AND	0.1378 ± 0.0004	0.1390 ± 0.0004	0.1350 ± 0.0004	0.1364 ± 0.0004

Tabela 10.2: *Umeritvene konstante za leto 2011 za vse štiri algoritme luminoznosti.*

10.8.3 Ocena sistematske negotovosti meritev

Prispevke k sistematski negotovosti se lahko razdeli med tiste, ki izhajajo iz lastnosti detektroja BCM in tiste, ki so skupni vsem detektorjem znotraj spektrometra ATLAS, ki merijo

luminoznost. Izvori negotovosti znotraj detektorja BCM so:

μ-popravki , ki so sicer analitično izrazljivi in pogojeni le s predpostavko o neodvisnosti večih interakcij protonov znotraj gruče. Negotovost je bila kljub temu ocenjena iz primerjave podatkov različnih algoritmov, ter odstopanj od premosorazmernega modela, ki je bil uporabljen za izračun izkoristka v simulaciji.

skladnost meritev med BCM-Navpično in BCM-Vodoravno meritvijo. Rezultati, ki temeljijo na različnih algoritmih luminoznosti bi morali na koncu napovedati isto luminoznost. Primerjava je bila opravljena čez dalše časovno obdobje (dveh mesecev) in je pokazala, da obstajajo majhna odstopanja, vendar se ne spreminjajo s časom. Največja razlika med rezultati različnih algoritmov je bila dodana v končno oceno sistematske napake.

model prilagajanih krivulj nima teoretične fizikalne podlage in je bil izbran tako, da opiše merjene podatke. Celotna analiza je bila opravljena na podlagi večih drugih krivuljah. Razlike v končnih vidnih presekih σ_A^{vis} so bile največje v primeru algoritma OR in so bile dodane v sistematsko napako.

skladnost umeritve gruč je dodatna mera za neponovljivost, ki jo prispeva sam trkalnik. Iz slike 10.7 je razvidno, da vse gruče ne dajo popolnoma iste umeritve. Tako je bila v oceno napake dodana tudi razmetanost dobljenih vrednosti za posamezne gruče.

spremembe nivoja proženja povzročijo spremembo izkorista detektorja. S pomočjo simulacije in ocene spreminjan nivoja proženja je bil vključen tudi ta prispevek.

Negotovosti, ki pestijo vse detektorje luminoznosti so:

negotovost produkta zasedenosti gruč $N_1 N_2$ v enačbi 10.19. Za število protonov znotraj gruč je potrebna neodvisna meritev [BC11]. Meri se s kombinacijo dveh detektorjev, kjer eden izmed njiju natančno izmeri razmerja števil protonov med gručami, madtem ko drug poskrbi za absolutno umeritev. Celotna negotovost, te dokaj kompleksne meritve je vključena v napako umeritve luminoznosti.

poravnava žarkov se izvede pred začetkom snemanja podatkov z namenom optimizirati luminoznost. Ta poravnava ima določeno mero neponovljivosti, ki prispeva k negotovosti meritve luminoznosti.

umeritev razdalje med curki je še en dodaten prispevek. Razmak je namreč določen z nastavitvami magneta, ki skrbi za premik curkov. Te nastavitve morajo biti povezane z dejansko razdajo med curkoma. Negotovost te povezave pa lahko prispeva k napaki.

stresanje položaja curkov je posledica majhnih razlik v položaju curkov, vsakič ko se uporabijo iste nastavitve za magnete, ki ju premikajo. To je moč opaziti, če se primerja njun nazivni razmak pri katerem je luminoznost največja. Ta razmak se na nivoju $< 1\,\mu\mathrm{m}$ spreminja med zaporednimi vdM meritvami in dodatno prispeva k neponovljivosti.

širjenje gruč protonov je posledica interakcij, ki so jim protoni podvrženi ob trku gruč. Protoni ene gruče morajo potovati skozi električno polje nabitih protonov druge gruče, kar ščasoma povečuje velikost gruč. To povzroči nekonstanten Σ_x tekom vdM meritev. Vpliv je bil ocenjen iz izmerjenih podatkov ter iz Monte Carlo simulacije.

prečne korelacije med porazdelitvijo gostote protonov znotraj gruče so bile pri analizi podatkov zanemarjene. Oceniti se jih da z opazovanjem porazdelitve rekonstruiranih točk interakcij protonov. Takšne korelacije preprečijo, da bi enačbo 10.4 razčlenili v x in y smeri, kot je to bilo strorjeno, in dodajo nove člene v izraz.

Velikost vseh prispevkov k sistematski negotovosti je podana v tabeli 10.3.

Prispevek	Oktober 2010	Maj 2011
μ-popravki	0.4%	0.4%
skladnost meritev	1.0%	1.0%
model prilagajanih krivulj	0.7%	0.7%
skladnost umeritve gruč	0.4%	0.4%
spremembe nivoja proženja	0.5%	0.5%
negotovost produkta zasedenosti gruč	3.2%	3.0%
poravnava žarkov	0.1%	0.1%
umeritev razdalje med curki	0.4%	0.4%
stresanje položaja curkov	0.4%	0.4%
širjenje gruč protonov	0.5%	0.5%
prečne korelacije	0.9%	0.4%
Celotna negotovost	3.7%	3.4%

Tabela 10.3: *Relativna vrednost sistematske napake umeritev za podatke iz oktobra 2010 in maja 2011.*

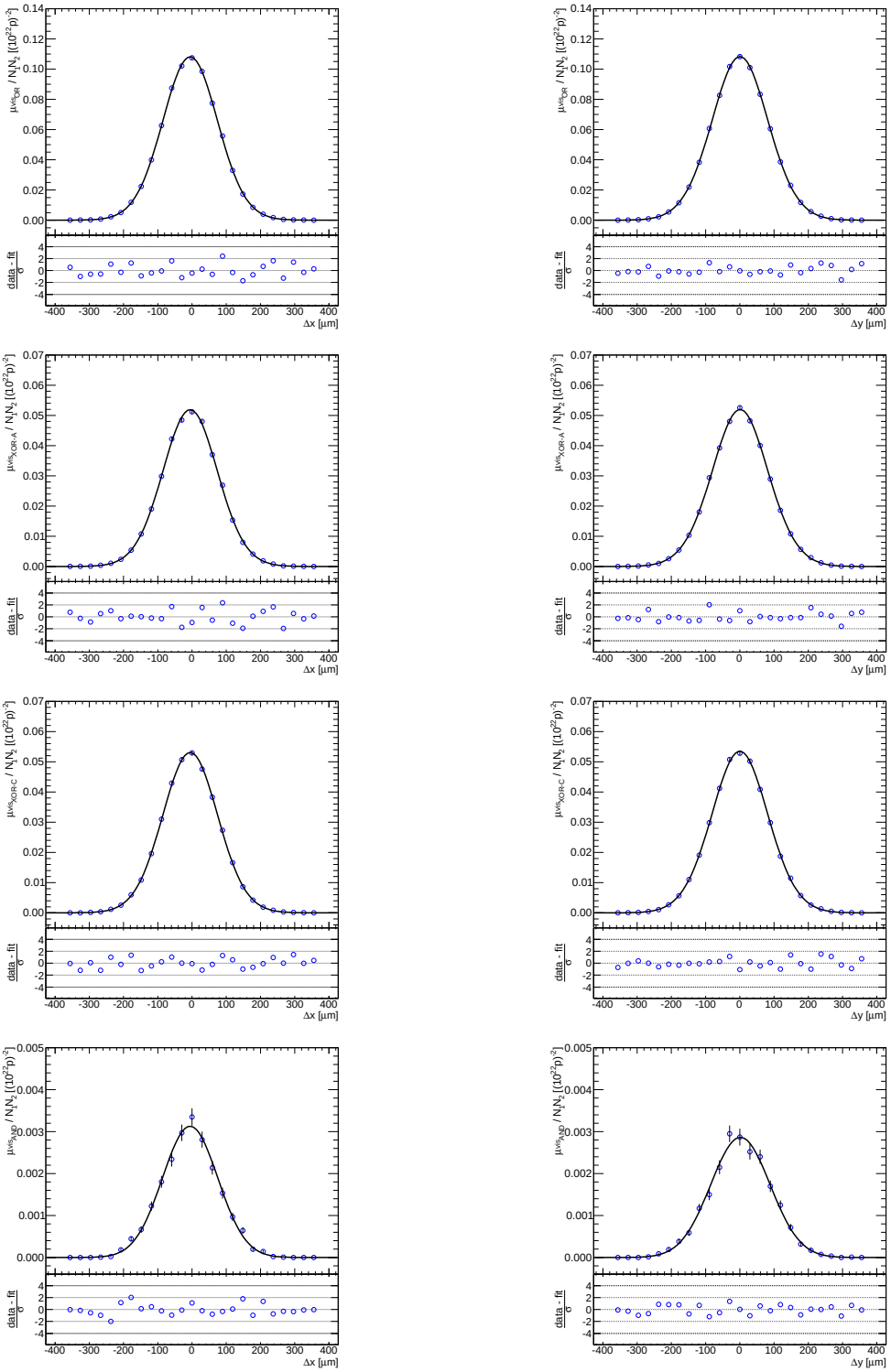

Slika 10.6: *Primer van der Meer meritev za prvo gručo v trkalniku. Levi stolpec prikazuje meritve pri razmikanju curkov v smeri x, medtem ko desni stolpec prikazuje rezultat razmikanja žarkov v smeri y. Vrstice predstavljajo različne algoritme luminoznosti. Od zgoraj navzdol si sledijo: OR, XOR-A, XOR-C in AND. Ta nabor meritev predstavlja najmanjši potreben nabor, da se umeri detektor.*

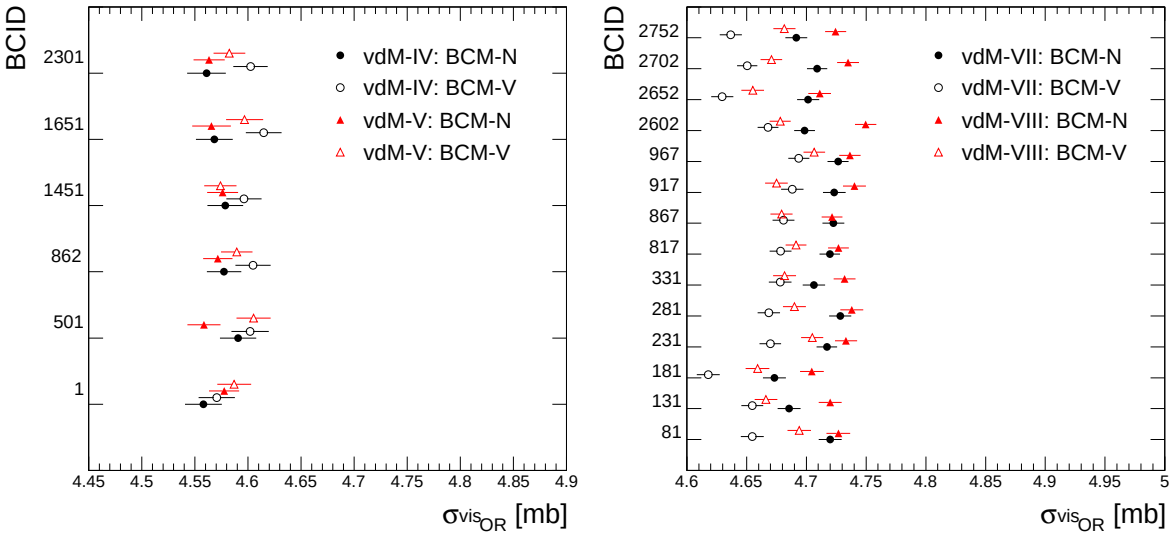

Slika 10.7: *Umeritvene konstante, določene za vsako posamezno gručo za: vdM meritev oktobra 2010 (levo) in vdM meritev maja 2011 (desno). Vrednosti se nanašajo na algoritem OR. BCID predstavlja zaporedno številko gruče v curku trkalnika. Meritvi BCM-Navpična in BCM-Vodoravna sta okrajani z BCM-N in BCM-V.*

10.9 Meritve luminoznosti

Zadnja pozornost naj bo namenjena posnetim podatkom. Kot značilen primer, ki lepo ponazori dosti zanimivih lastnosti detektorja BCM, sledijo predstavljeni podatki snemanja označenega s številom 188921. To se je začelo 7. septembra 2011 med katerim je bilo 423 trkajočih se gruč. Na sliki 10.8 je prikazana meritev trenutne luminoznosti čez celoten čas snemanja. To je končni rezultat meritev in časovni integral predstavlja količino podatkov, kot jih LHC nudi spektrometru ATLAS.

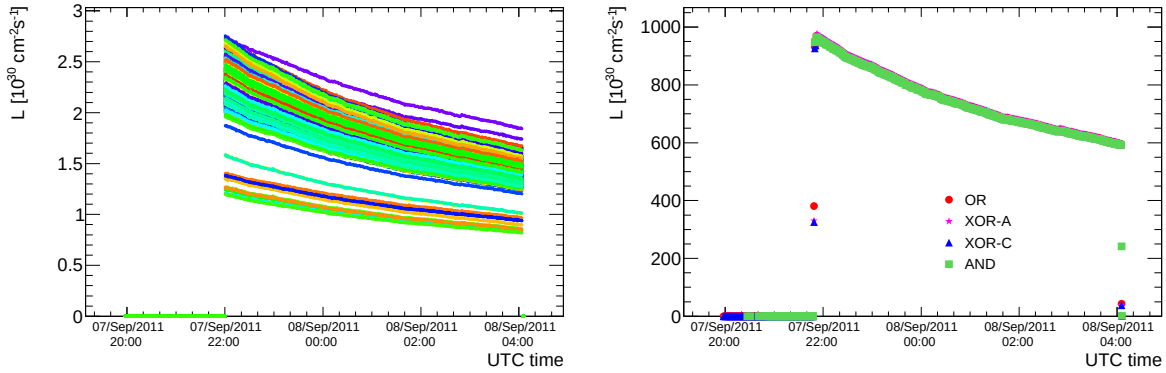

Slika 10.8: *Dobra časovna ločljivost dovoljuje detektorju BCM merjenje luminoznosti vsake gruče posebaj. Nabor meritev vseh gruč je prikazan na leven grafu. Vsota po vseh gručah, ki trkajo, da skupno luminoznost, ki jo nudi LHC spektrometru ATLAS (desno).*

Po mnenju avtorja je najizjemnejša slika 10.9, saj ponazarja izjemno kvaliteto detektorja BCM! Slika prikazuje celotne tabele luminoznosti za vse štiri algoritme. Navpične osi grafov so enake, tako je moč prečudovito videti čistost signala v primeru algoritma AND. Ozadje je zanj še dodatne tri rede velikosti manjše kot v primeru algoritma OR. Tudi v tej, najbolj onesnaženi meritvi, je ozadje manjše od tisočinke vrednosti merjene količine. Opaziti je zaporedja polnih gruč, ki trkajo v spektrometru ATLAS, ter gruč ki nimajo para s katerim bi trčile (okolica $\mathrm{BCID} \sim 1800$ in $\mathrm{BCID} \sim 2700$). Te *osamele gruče* interagirajo s preostalim plinom v vakuumski cevi in tako, sicer zanemarljivo, prispevajo k ozadju. Opaziti je tudi, da sta oba sklopa teh gruč vidna v meritvah algoritma OR, medtem ko je v meritvah algoritmov XOR možno opaziti le po en sklop gruč. To nakazuje, da so ustrezne gruče v dveh nasprotno vrtečih se curkih.

Takšne meritve nudi BCM spektrometru ATLAS vse od junija 2010, ko je bil v popolnosti vključen vanj. Skozi celoten čas je prispeval zanesljivo in natančno meritev, zaradi česar je bil spomladi 2011 izbran za najboljši detektor luminoznosti. Posledično so njegove meritve tiste, ki se posredujejo trkalniku, ter hkrati predstavljajo privzeto vrednost luminoznosti v številnih meritvah fizikalnih procesov.

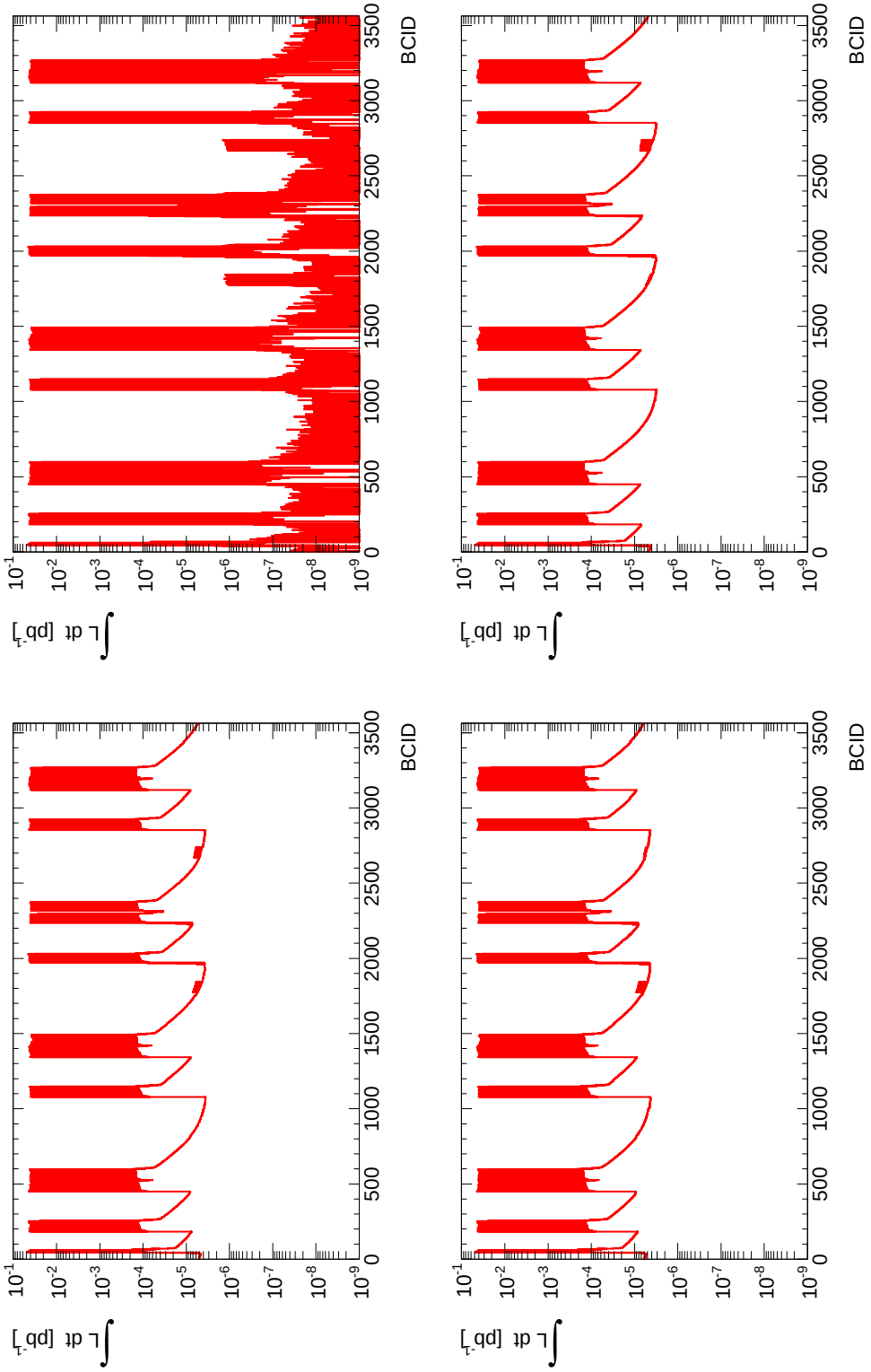

Slika 10.9: *Vodoravna os je označena z BCID-jem, ki predstavlja zaporedno mesto gruč v curku LHC-ja in pokriva vseh 3564 možnih vrednosti. razvidna so zaporedja polnih gruč, kot tudi razmerja prispevkov signala in različnih vrst ozadja. Zgornji-levi graf predstavlja meritve algoritma OR, zgornji-desni meritve algoritma AND, spodnji-levi meritve algoritma XOR-A in spodnji-desni meritve algoritma XOR-C.*

10.10 Zaključek

Da zagotovi meritev luminoznosti, ki je ključna za kvantitativne meritve mnogih fizikalnih procesov, je spektrometer ATLAS razvil merjenje luminoznosti z dokaj kompleksno zgradbo. Informacije prispeva več detektorjev, ki so med seboj neodvisni, kar pripomore k lažji oceni napake in omogoči dodaten nenehen nadzor nad kakovostjo podatkov.

Disertacija je predstavila opravljeno delo, ki je bilo potrebno za vključitev sistema za nadzor curka protonov v spektrometer ATLAS, predvsem kot merilca luminoznosti. Njegova edinstvena zasnova, ki temelji na čistosti in dobri časovni določenosti signala (ki ga prispevajo diamantni senzorji in elektronika) je omogočila, da hkrati s svojo osnovno nalogo varovanja spektrometra ponudi tudi meritev luminoznosti. Ena izmed potrebnih prednosti za opravlanje te naloge se skriva tudi v namesko zasnovanem procesiranju podatkov, ki obdeluje podatke v časovnem oknu $25\,\mathrm{ns}$. To omogoči meritve lastnosti posameznih gruč.

Skladno s smernicami, ki jih je nakazala Monte Carlo simulacija se BCM poslužuje večih algoritmov za merjenje luminoznosti. Algoritmi OR, XOR-A, XOR-C in AND mu med drugim omogočajo celo oceno prispevkov različnih ozadij h končni meritvi. Zelo različna izbirčnost algoritmov OR in AND je botrovala temu, da je BCM lahko prispeval svoj delež že pri meritvah v začetku snemanja podatkov, ko je bila luminoznost izjemno majna. Hkrati pa je pripravljen na vrednosti te količine, ki predstavljajo mejo zmožnosti trkalnika LHC.

Kot detektorju z dvema ločenima pod-sistemoma je olajšana tudi ocena sistematičnih nezanesljivosti. Primerjava je pokazala, da pod-sistema nudita meritve, ki se skladajo v mejah 1% relativne natančnosti. Podvojevanje meritev pa hkrati predstavlja dodatno robustnost celotnega sistema, v primeru neželjenih napak.

V predstaljenem besedilu je bila opisana celotna zgradba detektorja, obdelave in prenosa podatkov potrebnih za meritev luminoznosti. Z Monte Carlo simulacijo je bil preverjen celoten postopek merjenja, ocenjeni prispevki k sistematični negotovosti meritve, ter podana prva ocena umeritvenih konstant. Te so bile kasneje dobljene na podlagi merjenih podatkov s pomočjo van der Meer postopka. Umeritev je bila opravljena za BCM-Navpično in BCM-Vodoravno meritev luminoznosti, oboje za leti 2010 in 2011. Ustrezni sistematski nezanesljivosti znašata 3.7% in 3.4%.

Kot detektor, ki je popolnoma vgrajen v spektrometer ATLAS, je BCM prispeval meritev luminoznosti od junija 2010 dalje. Iz samih podatkov je razvidno, da je ozadje k meritvi manjše od 0.1%. Podatki tudi kažejo na stabilnost in zanesljivost meritev, kar je botrovalo izboru njegovih meritev kot uradnih meritev luminoznosti spektrometra ATLAS. Kot tak prispeva k številnim meritvam različnih fizikalnih procesov.

Bibliography

[A04] F. Anghinolfi et al., NINO: an ultra-fast and low–power front–end amplifier and discriminator ASIC for the multi-gap resistive plate chambers, *NIMA*, 533:183–187, 2004.

[AA08] K.S. Cranmer, The ATLAS Analysis Architecture, *Nuclear Physics B*, 177-178, 2008

[AD03] RD42 Collaboration W. Adam et al. The development of diamond tracking detectors for the LHC, *NIMA*, 541:79–86, 2003.

[ADS] ATLAS Data Summary, `https://atlas.web.cern.ch/Atlas/GROUPS/DATAPREPARATION/DataSummary/`

[AF08] The ATLAS collaboration, ATLAS Forward Detectros for Measurement of Elastic Scattering and Luminosity, *CERN/LHCC*,2008-004

[AL10] The ATLAS collaboration, Luminosity Determination Using the ATLAS Detector, ATLAS-CONF-2010-060

[AMI] ATLAS Metadata Interface, `http://ami.in2p3.fr/opencms/opencms/AMI/www/`

[AS10] The ATLAS collaboration, Luminosity Determination Using the ATLAS Detector, ATLAS-CONF-2010-060

[AT08] The ATLAS collaboration, The ATLAS Experiment at the CERN Large Hadron Collider, *JINST*, 3:1–422, 2008.

[ATLA] ATLAS experiment, `http://www.atlas.ch/`

[B+08] W. Trischuk et al., The ATLAS Beam Conditions Monitor, *JINST*, 3, P02004 (2008)

[BC11] Alice, A et al, LHC Bunch Current Normalisation for the October 2010 Luminosity Calibration Measurements, CERN-ATS-Note-2011-016 PERF March, 2011

[BG] BCM geometry description code, `https://svnweb.cern.ch/trac/atlasoff/browser/InnerDetector/InDetDetDescr/BCM_GeoModel`

[BI10] B. Todd, and B. Puccio, Beam interlock system and safe machine parameters system: 2010 and beyond. BIS - BIC - SMP, CERN, 2010

[BO66] B. de Raad, A. Minten, and E. Keil, Lectures on beam optics, Geneva: CERN, 66-21, 1966

[C111] The ATLAS collaboration, Updated Luminosity Determination in pp Collisions at $\sqrt{s} = 7\,\mathrm{TeV}$ using the ATLAS Detector, ATLAS-CONF-2011-011, March, 2011

[C211] The ATLAS collaboration, Luminosity Determination in pp Collisions at $\sqrt{s} = 7\,\mathrm{TeV}$ using the ATLAS Detector in 2011, ATLAS-CONF-2011-116, August, 2011

[CR05] The ATLAS Collaboration, Atlas Computing: Technical Design Report, CERN, 2005.

[DCS] ATLAS Detector Control System, `https://twiki.cern.ch/twiki/bin/viewauth/Atlas/DetectorControlSystemMainPage`

[DDB] ATLAS Detector description database, `http://atlas.web.cern.ch/Atlas/GROUPS/SOFTWARE/OO/php/DDDB/`

[E6] Element Six Ltd., King's Ride Park, Ascot, Berkshire, SL5 8BP, Unite Kingdom.

[FOT] FOTEC, Viktor Kaplan Str. 2, A-2700 Wr. Neustadt, Austria.

[G4] Geant4 toolkit, `http://geant4.cern.ch/`

[GL] Generators in Athena, `https://twiki.cern.ch/twiki/bin/view/AtlasProtected/McGeneratorsForAtlas`

[GM05] J. Boudreau, and V. Tsulaia, The GeoModel Toolkit for Detector Description, 2005

[GR09] Branco, M., Zaluska, E., de Roure, D., Lassnig, M. and Garonne, V., Managing very large distributed data sets on a data grid. Concurrency and Computation: Practice and Experience, 22: 1338-1364. doi: 10.1002/cpe.1489

[GU00] G. Barrand et al., Gaudi - A Software Architecture and Framework for building HEP Data Processing Applications, *International Conference on Computing in High Energy Physics (CHEP)*, 2000

[ID08] I. Dolenc, Development of Beam conditions monitor for ATLAS experiment, Ph.D. thesis, University of Ljubljana, 2008

[IS97] S. Kolos, IS User's Guide, CERN, Geneva 1997

[ISE] Iseg Spezialelektronik GmgH, D-01454 Radeberg/OT Rossendorf Germany.

[LC00] Y. Cai, Luminosity of asymetric e^+e^- collider with coupling lattices, SLAC-PUB-8479, 2000

[LD10] A. Jeff et al., Design for a Longitudinal Density Monitor for LHC, MOPE055, *Proc. International Particle Acceleration Conference (IPAC'10)* Kyoto, Japan, 2010

[LHC1] LHC Page-1, `http://op-webtools.web.cern.ch/op-webtools/vistar/vistars.php?usr=LHC3`

[LP07] H. Burkhard et al., Absolute Luminosity from Machine Parameters, Geneva: CERN, 2007.

[LR04] O. S. Brüning et al., LHC Design Report., Geneva: CERN, 2004.

[LZ11] M. Schott, Determination of integrated Luminosity via W/Z Boson Production at the ATLAS Detector, ATL-PHYS-PROC-2011-026

[MH68] S. van der Meer, Calibration of the Effective Beam Height at the ISR., CERN-ISR-PO-68-31, 1968.

[O+11] S. Maettig, The Online Luminosity Calculator of ATLAS, CERN, ATL-DAQ-PROC-2011-009

[OK98] R. Jones, L. Mapelli, Y. Ryabov, and I. Solovev, The OKS persistent in-memory object manager *IEEE trans. Nucl. Sci.* 45 1958, 1998

[PA98] D. Ritson, W. Chou, Minimizing the Pacman Effect on the Closed Orbit, *Part. Accel.: 59* , pp. 157-167, 1998

[PF95] M. E. Peskin, D. V. Schroeder, An Introduction to Quantum Field Theory, Westview Press, October 1995

[PV] PVSS System, `http://j2eeps.cern.ch/wikis/display/EN/PVSS+Service`

[PYT] PYTHIA generator, `http://home.thep.lu.se/~torbjorn/Pythia.html`

[R199] ATLAS detector and physics performance: Tehnical Design Report, vol. I, CERN-LHCC-99-014

[R299] ATLAS detector and physics performance: Tehnical Design Report, vol. II, CERN-LHCC-99-015

[RD42] CERN RD42 collaboration, CVD Diamond Radiation Detector Development

[RF03] R. Bailey and P. Collier, Standard Filling Schemes for Various LHC Operation Modes, LHC-Project-note-323, 2003.

[RSUM] ATLAS Run Summary, https://atlas.web.cern.ch/Atlas/GROUPS/DATAPREPARATION/DataSummary/2011/

[RT] ROOT - A Data Analysis Framework, http://root.cern.ch/drupal/

[SC11] The ATLAS collaboration, Upper Limits on the Charge in Satellite Bunches for October 2010 LHC Luminosity Calibration, ATLAS-CONF-2011-049, 2011

[SP01] J. Bohm et al., Power supply and power distribution system for ATLAS silicon strip detectors, Stockholm, September 2001, (CERN-2001-005).

[TG98] The ATLAS Collaboration, First-Level Trigger Technical Design Report, *CERN/LHCC*, 98-14, June 1998

[TS11] The ATLAS collaboration, Measurement of the inelastic proton-proton cross-section at $\sqrt{s} = 7$ TeV with the ATLAS detector, 2011, *Nature Publishing Group*, 10.1038/ncomms1472

[VM07] H.Burkhardt and P. Grafstrom, Absolute Luminosity From Machine Parameters, LHC-PROJECT-Report-1019, CERN, 2007

[VM10] S. M. While, R Alemany-Fernandez, H.Burkhardt, M. Lamont, First Luminosity Scan in the LHC, http://accelconf.web.cern.ch/AccelConf/IPAC10/papers/mopec014.pdf, CERN, 2010

[VP1] Virtual Point 1, http://atlas-vp1.web.cern.ch/atlas-vp1/

[WF05] Steven Weinberg, The Quantum Theory of Fields, Vol. I., *Cambridge University Press*, 2005

[XIL] XILINX, Inc., http://www.xilinx.com/

[XV4] XILINX, Virtex 4 specification, http://www.xilinx.com/support/documentation/virtex-4_data_sheets.htm

[ZC04] C. Anastasiou, L. Dixon, K. Melnikov, and F. Petriello, High-precision QCD at hadron colliders: Electroweak gauge boson rapidity distributions at next-to-next-to leading order, *Phys. Rev. D69*, 94008, 2004

[ZC08] S. White, The ATLAS zero degree calorimeter, *Nucl. Instr. Meth. A*, 177-178, 2008

[ZH94] S. Zhao., Characterization of the Electrical Properties of Polycrystalline Diamond Films., PhD thesis, Ohio Stat University, 1994.

Appendix A

Optical theorem

Optical theorem is a theorem from general scattering theory. For the purpose of completeness, an intuitive explanation of this theorem is given below. For more formal derivation see [PF95] and [WF05].
Since for luminosity determination the total cross-section is needed, one must ignore the underlying processes and observe the scattering as a whole. In the simplest picture of a fixed target, and incident beam along z direction, the amplitude can be written as:

$$\psi(r,\theta) = e^{ikz} + f(\theta)\frac{e^{ikr}}{r}. \tag{A.1}$$

The distance between the target and the point of measuring is denoted by r, and θ denotes the

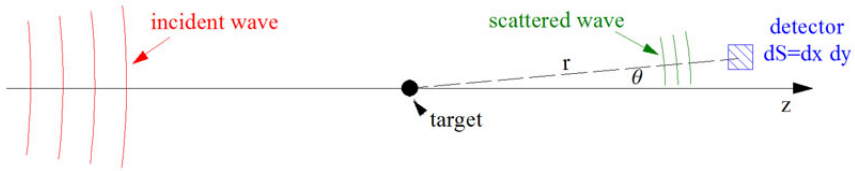

Figure A.1: *Detecting low angle scattering with the detector of surface $dS = dx\,dy$.*

scattering angle (see figure A.1). The first term represents the incident beam, approximated as a plain wave, and the second term describes the scattered wave. If our detector is close to the incident beam and far from the target (small θ), approximation can be made:

$$r = \sqrt{x^2+y^2+z^2} \approx z + \frac{x^2+y^2}{2z}. \tag{A.2}$$

Detector sees the probability density:

$$|\psi(r,\theta)|^2 \approx 1 + 2\Re\left[\frac{f(\theta)}{z}e^{ik(x^2+y^2)/2z}\right]. \tag{A.3}$$

Here another approximation is needed. If one measures really close to the beam than substitution $f(\theta) \rightarrow f(0)$ is justifiable. When integrating this probability density over the detector surface S its response is obtained:

$$\int |\psi(r,\theta)|^2 \, dS = S - \frac{4\pi}{k} \Im \left[f(0) \right] . \tag{A.4}$$

The incident beam wave function is normalized to unity density flux. Therefore the first term is just the flux of incident beam. Because of the second term, the actually observed flux is smaller. Conservation of probability density demands that this degradation equals the scattering losses. Therefore the total cross-section of the target can be written as:

$$\sigma_{tot} = \frac{4\pi}{k} \Im \left[f(0) \right] , \tag{A.5}$$

which is called *optical theorem*.

Appendix B

Luminosity formula for LHC

Assuming LHC beam has a Gaussian radial profile and is spherically symmetrical around the beam direction, one can write normalized particle density distribution as:

$$\rho(r) = \frac{1}{2\pi\sigma^2} e^{-\frac{r^2}{2\sigma^2}}, \tag{B.1}$$

where r is distance from the center of the beam and σ is its width. From this probability for proton interaction can be calculated:

$$\mathscr{P}_{pp} = \int_0^{2\pi} \int_0^{\infty} \rho_1(r)\rho_2(r) r \, dr \, d\varphi. \tag{B.2}$$

Indexes denote quantities for beams 1 and 2 respectively. If there are N_1 and N_2 protons in colliding bunches of equal sizes the probability for an interaction is

$$\mathscr{P}_{bb} = \frac{N_1 N_2}{4\pi^2\sigma^4} \int_0^{2\pi} \int_0^{\infty} e^{-\frac{2r^2}{2\sigma^2}} r \, dr \, d\varphi = \frac{N_1 N_2}{4\pi\sigma^2} \int_0^{\infty} \frac{2r}{\sigma^2} e^{-\frac{2r^2}{2\sigma^2}} \, dr = \frac{N_1 N_2}{4\pi\sigma^2}. \tag{B.3}$$

The expression for luminosity differs only by a factor of bunch revolution frequency f_{rev}. However the width of the beam depends on collider optics and it is customary to express it with parameters of a collider. In short, the link is:

$$\sigma = \sqrt{\frac{\varepsilon_n \beta^*}{\gamma}}, \tag{B.4}$$

where ε_n is the normalized emittance, β^* is the value of beta function at the interaction point, and the γ is a relativistic factor. These parameters are explained in more detail section 3.1. The final expression for single bunch luminosity is:

$$L_{bb} = \frac{N_1 N_2 f_{rev} \gamma}{4\pi\varepsilon_n \beta^*}. \tag{B.5}$$

Of coarse a sum should taken over all colliding bunch pairs if the total collider luminosity is required.

Appendix C

Event-type probabilities

Given the probabilities ε_{OR}, ε_{XOR-A}, ε_{XOR-C}, and ε_{AND} that describe event-type outcome of a single proton-proton collision the measurements can be predicted. A simple analytical calculation suffice, where multiple proton-proton collisions are assumed within the bunch crossing.

OR algorithm

If for a single proton-proton collision a probability for OR event is ε_{OR}, than the probability that OR is detected when i proton-proton collisions are overlaid is:

$$\varepsilon_{OR;i} = 1 - (1 - \varepsilon_{OR})^i. \tag{C.1}$$

The logic is that EMPTY event-type is the opposite of OR event-type, and in order to get EMPTY with of i interactions all of them separately must result in EMPTY event-type. This is for i interactions, however their number is random but obeying Poissonian distribution $\mathcal{P}$. Thus, if we have a bunch where on average $\langle\mu\rangle$ interactions occur we must convolve the above expression with a Poisson distribution:

$$\begin{aligned} r_{OR} &= \sum_{i=0}^{\infty} \mathcal{P}(i;\langle\mu\rangle)\varepsilon_{OR;i} = \sum_{i=0}^{\infty} \frac{\langle\mu\rangle^i e^{-\langle\mu\rangle}}{i!} \left(1 - (1-\varepsilon_{OR})^i\right) \\ &= \sum_{i=0}^{\infty} \frac{\langle\mu\rangle^i e^{-\langle\mu\rangle}}{i!} - \sum_{i=0}^{\infty} \frac{\langle\mu\rangle^i e^{-\langle\mu\rangle}}{i!}(1-\varepsilon_{OR})^i \end{aligned} \tag{C.2}$$

Since Poissonian distribution is normalized to unity, the first term equals 1. For the second a general formula

$$\sum_{i=0}^{\infty} P(i;N)x^i = e^{-N(1-x)} \tag{C.3}$$

can be used, resulting in:

$$r_{OR} = 1 - e^{-\langle\mu\rangle\varepsilon_{OR}}. \tag{C.4}$$

XOR algorithms

With additional parameter ε_{XOR} one can calculate probability for XOR event-type when i interactions occur. The XOR can result from j underlying XOR interactions and $i-j$ EMPTY interactions, where j can range from 1 (there must be at least one) to i. Acknowledging additional binomial statistics one can write:

$$\varepsilon_{XOR;i} = \sum_{j=1}^{i} \binom{i}{j} \varepsilon_{XOR}^{j} (1-\varepsilon_{OR})^{i-j}. \tag{C.5}$$

Again this needs to be convolved with Poisonnian to get the measured event-type probability:

$$r_{XOR} = \sum_{i=0}^{\infty} \mathcal{P}(i;\langle\mu\rangle)\varepsilon_{XOR;i} = \sum_{i=0}^{\infty} \frac{\langle\mu\rangle^{i} e^{-\langle\mu\rangle}}{i!} \sum_{j=1}^{i} \binom{i}{j} \varepsilon_{XOR}^{j} (1-\varepsilon_{OR})^{i-j}. \tag{C.6}$$

From standard mathematics repertoire another binomial formula is needed:

$$\sum_{j=0}^{i} \binom{i}{j} a^{j} b^{i-j} = (a+b)^{i}. \tag{C.7}$$

With it:

$$\begin{aligned} r_{XOR} &= \sum_{i=0}^{\infty} \frac{\langle\mu\rangle^{i} e^{-\langle\mu\rangle}}{i!} \left((\varepsilon_{XOR} + 1 - \varepsilon_{OR})^{i} - (1-\varepsilon_{OR})^{i} \right) \\ &= e^{-\langle\mu\rangle\varepsilon_{OR} + \langle\mu\rangle\varepsilon_{XOR}} - e^{-\langle\mu\rangle\varepsilon_{OR}} \\ &= e^{-\langle\mu\rangle\varepsilon_{OR}} \left(e^{\langle\mu\rangle\varepsilon_{XOR}} - 1 \right) \end{aligned} \tag{C.8}$$

The subtraction of term $(1-\varepsilon_{OR})^{i}$ in the first line is because we sum j from 1 onwards, so $j=0$ must be subtracted. To produce the second line the equation C.3 was again used. The expression holds for both $XOR-A$ and $XOR-C$ algorithm.

AND algorithm

The rate for AND algorithm turns out to be most easily calculated, since the union of XOR-A, XOR-C, and AND event-type samples gives OR event-type sample. Thus:

$$\begin{aligned} r_{AND} &= r_{OR} - r_{XOR-A} - r_{XOR-C} \\ &= 1 - e^{-\langle\mu\rangle\varepsilon_{OR}} \left(e^{\langle\mu\rangle\varepsilon_{XOR-C}} + e^{\langle\mu\rangle\varepsilon_{XOR-A}} - 1 \right). \end{aligned} \tag{C.9}$$

Appendix D

μ-corrections

The measurable event-type probabilities r_A (A denotes arbitrary luminosity algorithm) are a function of corresponding μ^{vis} (visible average number of interactions). Since the interest lies with μ_A^{vis} values, they should be extracted from r_A expressions.

OR algorithm

Starting with equation

$$r_{OR} = 1 - e^{-\mu_{OR}^{vis}}, \tag{D.1}$$

the μ_{OR}^{vis} is extracted by logarithm:

$$\mu_{OR}^{vis} = -\ln\left[r_0\right], \tag{D.2}$$

where $r_0 = 1 - r_{OR}$ has been introduced to shorten the notation. The errors are propagated:

$$\sigma^2_{\mu_{OR}^{vis}} = \left|\frac{\partial \mu_{OR}^{vis}}{\partial r_0}\right|^2 \sigma^2_{r_0} = \left(\frac{\sigma_{r_0}}{r_0}\right)^2. \tag{D.3}$$

XOR algorithm

For XOR algorithm the start expression is

$$r_{XOR} = e^{-\mu_{OR}^{vis}}\left(e^{\mu_{XOR}^{vis}} - 1\right), \tag{D.4}$$

where both μ_{XOR}^{vis} and μ_{OR}^{vis} contribute. Equation D.1 can be inverted to $e^{-\mu_{OR}^{vis}} = r_0$, which can be used to substitute the μ_{OR}^{vis} by the measured r_0:

$$r_{XOR} = r_0\left(e^{\mu_{XOR}^{vis}} - 1\right) \tag{D.5}$$

$$e^{\mu_{XOR}^{vis}} = 1 + \frac{r_{XOR}}{r_0} \tag{D.6}$$

$$\mu_{XOR}^{vis} = \ln\left[1 + \frac{r_{XOR}}{r_0}\right]. \tag{D.7}$$

... deriving the XOR μ-correction. The next is the error propagation:

$$\sigma^2_{\mu^{vis}_{XOR}} = \left|\frac{\partial\mu^{vis}_{XOR}}{\partial r_0}\right|^2 \sigma^2_{r_0} + \left|\frac{\partial\mu^{vis}_{XOR}}{\partial r_{XOR}}\right|^2 \sigma^2_{r_{XOR}} + 2\left|\frac{\partial\mu^{vis}_{XOR}}{\partial r_0}\frac{\partial\mu^{vis}_{XOR}}{\partial r_{XOR}}\right| Cov_{r_0;r_{XOR}}, \quad \text{(D.8)}$$

with extra correlation term. Since the algorithms cover all possibilities of event-types, the combination of r_A measurements should obey multinomial distribution. For it the covariances are known:

$$Cov_{r_A;r_B} = -Nr_Ar_B, \quad \text{(D.9)}$$

where N is the number of times the experiment has been repeated, in case of luminosity measurement the number of times the bunches collided. It also holds for any algorithm that:

$$\sigma^2_A = Nr_A\left(1 - r_A\right). \quad \text{(D.10)}$$

Performing the derivations and inserting the expression for variances and covariances one obtains:

$$\sigma^2_{\mu^{vis}_{XOR}} = \sqrt{\frac{1}{N}\frac{r_0r_{XOR} - 4r_0r^2_{XOR} + r^2_{XOR}}{r_0\left(r_0 + r_{XOR}\right)^2}}. \quad \text{(D.11)}$$

The result is valid for both XOR variants. In the next lines, wherever the -A or -C index is omitted it implies that the expression holds for either of the two.

AND algorithm

The calculation again start with the expression for measured probability:

$$r_{AND} = 1 - e^{-\langle\mu\rangle\varepsilon_{OR}}\left(e^{\langle\mu\rangle\varepsilon_{XOR-C}} + e^{\langle\mu\rangle\varepsilon_{XOR-A}} - 1\right). \quad \text{(D.12)}$$

Like in the case of XOR the μ^{vis}_{OR}, and here also the μ^{vis}_{XOR-A} and μ^{vis}_{XOR-C} must be substituted with the corresponding r_A measurements. Equation D.6 should be used to do the substitution for XOR, while the OR substitution remains identical to one performed for XOR calculation. After few trivial steps one gets the final result:

$$\mu^{vis}_{AND} = \ln\left[\frac{r_0}{\frac{r_0}{r_0+r_{XOR-A}} + \frac{r_0}{r_0+r_{XOR-C}}}\right]. \quad \text{(D.13)}$$

The expression for AND does not require the r_{AND} measurement, since the four r_A measurement are interdependent and one can be expressed with the other three. The error propagation starts with:

$$\begin{aligned}\sigma^2_{\mu^{vis}_{AND}} = &\left|\frac{\partial\mu^{vis}_{AND}}{\partial r_0}\right|^2 \sigma^2_{r_0} + \left|\frac{\partial\mu^{vis}_{AND}}{\partial r_{XOR-A}}\right|^2 \sigma^2_{r_{XOR-A}} + \left|\frac{\partial\mu^{vis}_{AND}}{\partial r_{XOR-C}}\right|^2 \sigma^2_{r_{XOR-C}} + \\ &+2\left|\frac{\partial\mu^{vis}_{AND}}{\partial r_0}\frac{\partial\mu^{vis}_{AND}}{\partial r_{XOR-A}}\right| Cov_{r_0;r_{XOR-A}} + 2\left|\frac{\partial\mu^{vis}_{AND}}{\partial r_0}\frac{\partial\mu^{vis}_{AND}}{\partial r_{XOR-C}}\right| Cov_{r_0;r_{XOR-C}} + \\ &+2\left|\frac{\partial\mu^{vis}_{AND}}{\partial r_{XOR-A0}}\frac{\partial\mu^{vis}_{AND}}{\partial r_{XOR-C}}\right| Cov_{r_{XOR-A};r_{XOR-C}}.\end{aligned} \quad \text{(D.14)}$$

Again equations D.10 and D.9 must be used for variations and covariations. The rest is differentiation... and final equation is obtained:

$$\sigma_{\mu^{vis}_{AND}} = \sqrt{\frac{1}{N_E} \frac{r_{XOR-A} r_{XOR-C} + r_0^2 \left(1 - r_{XOR-A} - r_{XOR-C}\right) - r_0 r_{XOR-A} r_{XOR-C} - r_0^3}{r_0 \left(r_0 + r_{XOR-A}\right) \left(r_0 + r_{XOR-C}\right)}}. \tag{D.15}$$

Appendix E

Outside dimensions of BCM modules

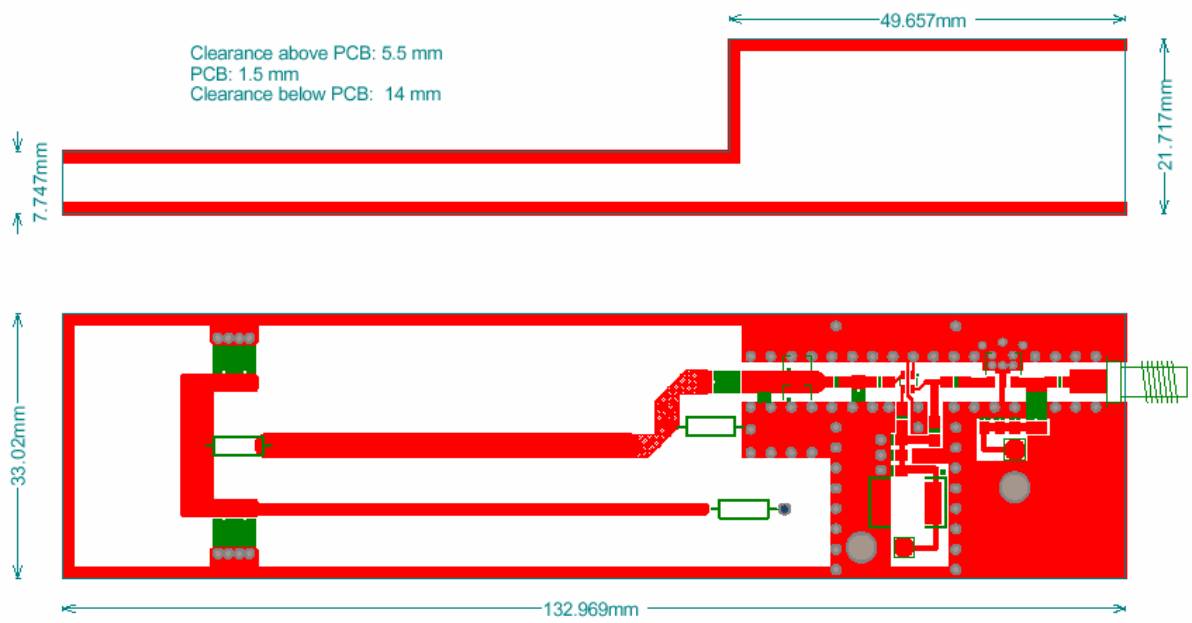

Figure E.1: *Outside dimensions for BCM modules marked F40x.*

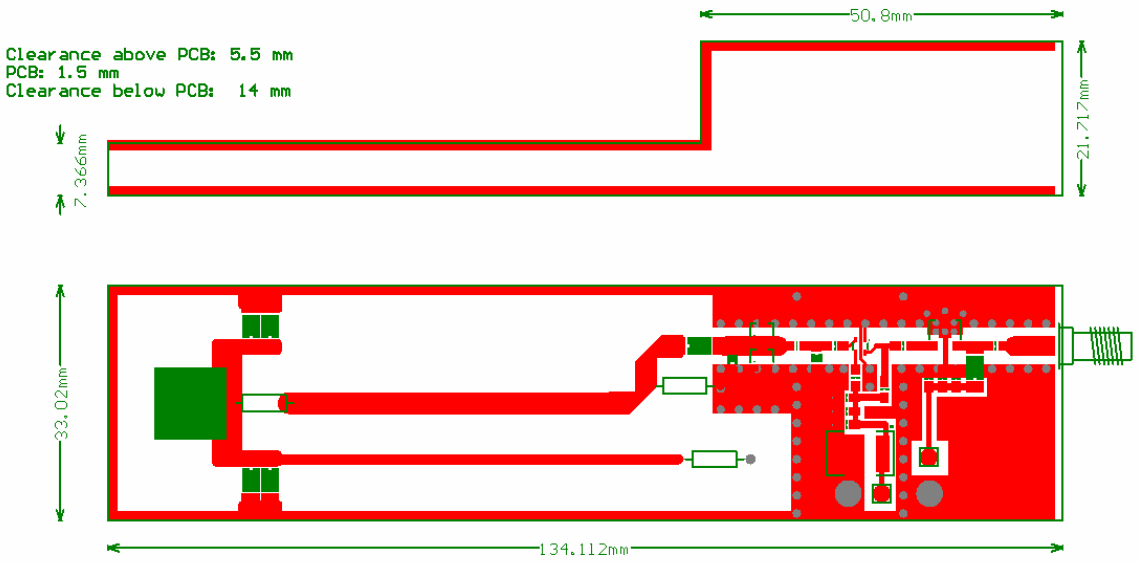

Figure E.2: *Outside dimensions for BCM modules marked F42x.*

Appendix F

BCM GeoModel parameters

BCM parameters from ATLAS Detector Description Database are presented in the table F.1. All quantities are in the default ATLAS GeoModel units: mm, degrees, and MeV.

Parameter	Modules							
	0	1	2	3	4	5	6	7
TRANS_X	95.744	0	-95.744	0	95.744	0	-95.744	0
TRANS_Y	0	95.744	0	-95.744	0	95.744	0	-95.744
TRANS_Z	1882.4	1882.4	1882.4	1882.4	-1882.4	-1882.4	-1882.4	-1882.4
ROT_X	0	0	0	0	180	180	180	180
ROT_Y	45	45	45	45	-45	-45	-45	-45
ROT_Z	0	90	180	270	0	90	180	270
DIAM_TRANS_Y	0	0	0	0	0	0	0	0
DIAM_TRANS_Z	-59.785	-59.785	-59.785	-59.785	-59.785	-59.785	-59.785	-59.785
DIAM_DIAM_X	0.2	0.2	0.2	0.2	0.2	0.2	0.2	0.2
DIAM_DIAM_Y	0	0	0	0	0	0	0	0
DIAM_DIAM_Z	-0.4	-0.4	-0.4	-0.4	-0.4	-0.4	-0.4	-0.4
DIMESION_Z	0.4	0.4	0.4	0.4	1.4	1.4	1.4	0.4
OFF_H	34.86	34.86	34.86	34.86	34.86	34.86	34.86	34.86
OFF_I	29.509	29.509	29.509	29.509	29.509	29.509	29.509	29.509
OFF_J	20.205	20.205	20.205	20.205	20.205	20.205	20.205	20.205

Table F.1: *BCM geometry parameters for GeoModel as written in the Detector Description Database. The all dimensions are in mm while the values of angles are in degrees.*

Spodaj podpisani Boštjan Maček izjavljam, da je disertacija rezultat mojega samostojnega raziskovalnega dela.

Boštjan Maček

Ljubljana, 2011